

(NASA-TM-79582) VERY LONG BASELINE
INTERFEROMETRY APPLIED TO POLAR MOTION,
RELATIVITY AND GEODESY Ph.D. Thesis -
Maryland Univ. (NASA) 387 p HC A17/MF A01

N78-27690

Unclas
CSCL 08F G3/46 25707



Technical Memorandum 79582

Very Long Baseline Interferometry Applied to Polar Motion, Relativity and Geodesy

CHOPO MA

MAY 1978

National Aeronautics and
Space Administration

Goddard Space Flight Center
Greenbelt, Maryland 20771



UNIVERSITY OF MARYLAND
DEPARTMENT OF PHYSICS AND ASTRONOMY
COLLEGE PARK, MARYLAND

APPROVAL SHEET

Title of Thesis: Very Long Baseline Interferometry applied to
Polar Motion, Relativity, and Geodesy

Name of Candidate: Chopo Ma
Doctor of Philosophy, 1978

Thesis and Abstract approved:

Jean-Paul Richard
Associate Professor
Department of Physics and Astronomy

Date Approved:

VITA

Name: Chopo Ma

Permanent Address: 90 La Salle Street
New York, New York 10027

Degree and date to be conferred: Ph. D. May, 1978

Date of birth: [REDACTED]

Place of birth: [REDACTED]

Secondary education: Bronx High School of Science, New York, New York

Collegiate institutions:

| | | | |
|------------------------|-----------|--------|-----------|
| Harvard College | 1964-1967 | A. B. | June 1967 |
| University of Maryland | 1967-1968 | | |
| University of Maryland | 1970-1978 | Ph. D. | May 1978 |

Major: Physics

Publications:

T. A. Clark, L. K. Hutton, C. Ma, I. I. Shapiro, J. J. Wittels,
D. S. Robertson, H. F. Hinteregger, C. A. Knight, A. E. E. Rogers,
A. R. Whitney, A. E. Niell, G. M. Resch, W. J. Webster. "An Unusually
Strong Radio Outburst in Algol: VLBI Observations" Ap. J. 206, L:07, 1976

D. M. Gibson, M. Viner, S. Peterson, T. Clark, L. Hutton, C. Ma, W. Webster,
H. Hinteregger, A. Rogers, I. Shapiro, A. Whitney, J. Wittels, A. Niell,
G. Resch. "An Extraordinary Radio Outburst in Algol: Flux and Structure
Observations" B. A. A. S. 7, 498, 1975

J. W. Ryan, T. A. Clark, R. Coates, C. Ma, D. S. Robertson, B. E. Corey,
C. C. Counselman, I. I. Shapiro, J. J. Wittels, H. F. Hinteregger,
C. A. Knight, A. E. E. Rogers, A. R. Whitney, J. M. Moran. "Precision
Surveying Using Very Long Baseline Interferometry" GSFC X-922-77-242, 1977

J. J. Wittels, I. I. Shapiro, H. F. Hinteregger, C. A. Knight,
A. E. E. Rogers, A. R. Whitney, T. A. Clark, C. Ma, L. K. Hutton,
D. S. Robertson, B. O. Ronnang, O. E. H. Rydbeck, A. E. Niell, G. M. Resch.
"A High Declination Search at 8 GHz for Compact Radio Sources" submitted
to The Astronomical Journal

Positions held:

Teaching assistant - University of Maryland, 1967-1968, 1971
Research assistant - University of Maryland, 1971-1978

ABSTRACT

Title of thesis: Very long baseline interferometry applied to polar motion, relativity, and geodesy

Chopo Ma, Doctor of Philosophy, 1978

Thesis directed by: Associate Professor Jean-Paul Richard

The causes and effects of diurnal polar motion are described. An algorithm is developed for modeling the effects on very long baseline interferometry observables. Five years of radio-frequency very long baseline interferometry data from stations in Massachusetts, California, and Sweden are analyzed for diurnal polar motion. It is found that the effect is larger than predicted by McClure. Corrections to the standard nutation series caused by the deformability of the earth have a significant effect on the estimated diurnal polar motion scaling factor and the post-fit residual scatter.

Simulations of high precision very long baseline interferometry experiments taking into account both measurement uncertainty and modeled errors are described. It is found that the Wide-Band Optical Very Long Baseline Interferometer may be useful in studying gravitational deflection near Jupiter. A selection is made between two three-station networks for monitoring polar motion. The effects of scheduling and the number of sources observed on estimated baseline errors are discussed. It is found that a moderate number of sources should yield the best results. A comparison of actual and simulated experiments indicates that the present variability of real data is not well predicted.

VERY LONG BASELINE INTERFEROMETRY
APPLIED TO
POLAR MOTION, RELATIVITY, AND GEODESY

by
Chopo Ma

Dissertation submitted to the Faculty of the Graduate School
of the University of Maryland in partial fulfillment
of the requirements for the degree of
Doctor of Philosophy
1978

敬
愛 獻
的 給
雙
親

ACKNOWLEDGEMENTS

I would like to thank the large cast of characters that made this production possible.

First, Prof. J. P. Richard for his patience, Dr. T. A. Clark for taking me in out of the cold, and Mr. J. W. Ryan for his unfailing good humor.

My advisors, Prof. Richard and Dr. Clark, and the members of my committee, Profs. C. C. Counselman, D. G. Currie and W. C. Erickson, for keeping my nose to the grindstone and making this a different piece of work than it might have been.

George Kaplan for invaluable discussions of the physical and political complexities of nutation and polar motion.

The past and present members, willing and unwilling, of the VLBI groups at Maryland, Goddard, Haystack, MIT, JPL, Onsala, and NRAO, too numerous to list but not forgotten, and the supporting staff of the participating observatories, particularly the Haystack computer operators, without whom no data would have been available.

Dr. D. S. Robertson for editing most of the data into a useful form and developing the VLBI3 program. May it now fade away.

Dr. A. R. Whitney for the care and feeding of the HP 21MX and discussions of the Mark III that is to be.

The swing and grave shifts of the Goddard 360/91 for allowing me a private queue and pushing through my altogether too numerous computer runs.

J. Hodge for the drawings, E. Fisher for typing the equations, and

W. Moran for providing an alternate printer in time of need.

My roommates, Gerry Marandino, Bob Braunstein, and Bob McCann, for their support over the seemingly interminable years.

Part of this research at the University of Maryland was supported by the National Aeronautics and Space Administration under grant NSG 5035 and by the Computer Science Center. The experiments described were supported in part by the National Science Foundation under grant EAR76-22615, the Advanced Research Projects Agency under contract 23601-71-0092 mod 2, the U. S. Geological Survey under contract 14-08-001-14148, and the National Aeronautics and Space Administration under contracts NAS 7-100 and NAS5-22843 and grant NGR22-009-839. Haystack Observatory is partially supported by the National Science Foundation under grant GP-25865. The VLBI program at the Onsala Space Observatory is supported in part by the Swedish National Science Research Council and the Swedish Board for Technical Development. The Owens Valley Radio Observatory is operated by the California Institute of Technology.

TABLE OF CONTENTS

| Chapter | page |
|---|-------------|
| DEDICATION | ii |
| ACKNOWLEDGEMENTS | iii |
| LIST OF TABLES | x |
| LIST OF FIGURES | xiii |
| INTRODUCTION | 1 |
| CHAPTER I. PRINCIPLES OF VERY LONG BASELINE INTERFEROMETRY | 4 |
| A. The VLBI observables | 4 |
| B. Basic geometry and apparatus of VLBI | 4 |
| C. Dependence of VLBI observables on geometry | 10 |
| D. Dependence of VLBI observables on the propagation medium | 18 |
| E. Dependence of VLBI observables on instrumentation | 21 |
| F. Measurement uncertainties of the VLBI observables | 23 |
| G. VLBI instrumentation systems | 25 |
| CHAPTER II. PHYSICAL MODELS USED IN HIGH PRECISION INTERFEROMETRY | 27 |
| A. The VLBI reference frames | 28 |
| B. Description of various time and time-like quantities | 32 |
| C. Expressions for theoretical values of the VLBI observables | 35 |
| D. Models which determine the baseline orientation | 38 |
| 1. Precession | 39 |
| 2. Nutation | 42 |
| 3. Diurnal rotation | 44 |
| 4. Diurnal polar motion | 46 |
| 5. Polar motion | 50 |
| 6. Time derivatives of the coordinate transformations | 51 |

| | | |
|--|---|-----|
| E. | Perturbations of the observation geometry | 52 |
| 1. | Solid earth tides | 53 |
| 2. | Antenna structure | 59 |
| 3. | Relativistic gravitational deflection | 62 |
| 4. | Ocean loading | 64 |
| F. | Propagation medium models | 65 |
| 1. | Atmosphere | 65 |
| 2. | Ionosphere | 67 |
| 3. | Corona | 69 |
| G. | Basic geometrical derivatives | 70 |
| 1. | Site coordinate derivatives | 70 |
| 2. | Source position derivatives | 71 |
| CHAPTER III. MEASUREMENT OF DIURNAL POLAR MOTION | | 73 |
| A. | Nomenclature of polar motion | 73 |
| B. | Causes and effects of diurnal polar motion | 78 |
| C. | Implementation of diurnal polar motion | 92 |
| D. | Effect of diurnal polar motion on VLBI delay observable | 103 |
| E. | Observations and data preparation | 113 |
| F. | Estimation of diurnal polar motion | 130 |
| 1. | Clock parameterization | 134 |
| 2. | Residual behavior | 136 |
| 3. | Effect of phase variation | 138 |
| 4. | Significance test | 143 |
| G. | Comparison with literature | 145 |
| H. | Interpretation of the diurnal polar motion scaling factor | 147 |
| 1. | Solid earth tides | 147 |
| 2. | Nutation | 151 |

| | |
|---|------------|
| 3. Core-mantle interactions | 159 |
| 4. Other effects | 161 |
| 5. Conclusions | 162 |
| CHAPTER IV. SIMULATION OF HIGH PRECISION INTERFEROMETRIC | |
| EXPERIMENTS | 163 |
| A. Statistical theory | 163 |
| 1. Least squares covariance analysis | 164 |
| 2. Enlarged parameter set | 168 |
| 3. Errors and error models | 169 |
| 4. The effect of model errors on unadjusted parameters . . . | 172 |
| B. Measurement of the relativistic light bending parameter . . . | 175 |
| 1. Occultations by Jupiter | 176 |
| 2. Algorithms for modeling the light deflection parameter . . | 177 |
| 3. Observations at Jupiter's stationary point | 182 |
| 4. Observations at Jupiter's maximum velocity point | 192 |
| 5. Observations at intermediate velocity | 192 |
| 6. Simulations using three parameters | 194 |
| 7. Baseline errors | 196 |
| 8. Conclusions | 198 |
| C. A comparison of two networks for measuring polar motion | |
| and UT1 | 200 |
| 1. Introduction | 200 |
| 2. Simulation configuration | 204 |
| 3. Comparison of networks using low duty cycle schedules . . | 208 |
| 4. Comparison of networks using 24 hr schedules | 213 |
| 5. Comparison of networks using low duty cycle schedules and | |
| complete adjustment | 215 |

| | | |
|----|--|-----|
| 6. | Effect of diurnal polar motion and solid earth tides . . . | 218 |
| 7. | Conclusions | 220 |
| D. | The effect of scheduling on baseline parameter errors | 220 |
| 1. | Introduction | 220 |
| 2. | Simulation parameters | 221 |
| 3. | Three and four source schedules | 231 |
| 4. | Six to nine source schedules | 236 |
| 5. | Eleven source schedules | 246 |
| 6. | Haystack-Goldstone schedule | 252 |
| 7. | Baseline length optimized schedule | 253 |
| 8. | Conclusions | 253 |
| E. | Comparison of actual and simulated experiments | 254 |
| | CONCLUSION | 264 |
| A. | Summary | 264 |
| B. | Remaining problems | 264 |
| 1. | Instrumentation and physical effects | 265 |
| 2. | Data and experiment integration structure | 266 |
| C. | Future projects and possibilities | 267 |
| | APPENDIX A. Mark III instrumentation | 270 |
| 1. | Mark III field system | 270 |
| 2. | Mark III processor | 276 |
| | APPENDIX B. Mark III experiment integration and data base system . | 281 |
| 1. | Data base structure | 282 |
| 2. | Experiment scheduling | 288 |
| 3. | Observations | 292 |
| 4. | Evaluation of VLBI observables | 294 |
| 5. | Estimation of parameters | 297 |

| | |
|---|-----|
| 6. Archiving data | 305 |
| APPENDIX C. User guide to the data base handler | 307 |
| APPENDIX D. Experiment simulation program (ESTIM) | 333 |
| APPENDIX E. Experiments scheduled | 349 |
| APPENDIX F. Measurement of solid earth tides from gravimeter data . | 352 |
| REFERENCES CITED | 359 |

LIST OF TABLES

| Table | page |
|---|-------------|
| II.1 Diurnal angular momentum polar motion coefficients | 49 |
| III.1 Periods of diurnal polar motion | 102 |
| III.2 Antenna and receiver information for diurnal polar motion data | 121 |
| III.3 Number of observations by experiment and baseline for diurnal polar motion data | 122 |
| III.4 Number of observations by source and combined data set for diurnal polar motion data | 126 |
| III.5 Estimate of diurnal polar motion scaling factor | 131 |
| III.6 Effect of phase on adjusted diurnal polar motion scaling factor using Set D and 8 terms in each clock polynomial . . | 140 |
| III.7 Diurnal polar motion scaling factor with phase corrected . . | 142 |
| III.8 F value significance tests for adjustment of diurnal polar motion scaling factor | 144 |
| III.9 Fortnightly diurnal polar motion | 146 |
| III.10 Effect of solid earth tide on diurnal polar motion scaling factor | 149 |
| III.11 Proposed values for nutation coefficients (Melchior 1972) . | 155 |
| III.12 Effect of nutation corrections on diurnal polar motion scaling factor | 156 |
| III.13 Diurnal polar motion scaling factor with nutation corrected | 158 |
| IV.1 Parameters for Jupiter occultation simulations | 183 |
| IV.2 Observation period parameters for Jupiter occultations . . . | 184 |
| IV.3 Errors for relativity parameter, Dec 8-11, 1 source schedule | 186 |

| | | |
|-------|--|-----|
| IV.4 | Errors for relativity parameter, Dec 8-11, 3 source schedule | 188 |
| IV.5 | Errors for relativity parameter, Dec 8-11, 3 site schedules | 191 |
| IV.6 | Errors for relativity parameter, March 20 | 193 |
| IV.7 | Errors for relativity parameter, Oct 12 | 195 |
| IV.8 | Errors for relativity parameter, Oct 12, 3 site schedules | 195 |
| IV.9 | Errors in relativity parameter with 3 parameter modeling of gravitational deflection for 1 source, 1 baseline schedules | 197 |
| IV.10 | Sources used for estimation of site coordinates | 197 |
| IV.11 | Errors in site coordinates for 1 km N-S baseline | 199 |
| IV.12 | Station configurations for wobble/UT1 simulations | 205 |
| IV.13 | Baseline components for wobble/UT1 simulations | 207 |
| IV.14 | Sources used for wobble/UT1 simulations | 207 |
| IV.15 | Unadjusted parameter errors for wobble UT1 simulations . . . | 207 |
| IV.16 | Summary of errors from schedules WRD00, WRD01, WRD02, and WRD03 | 211 |
| IV.17 | Summary of errors from schedules WDF00, WDF01, WDF02, and WDF03 | 212 |
| IV.18 | Errors from wobble/UT1 schedules WRD24 and WDF24 | 214 |
| IV.19 | Westford-Richmond-Fort Davis four day estimate of wobble/UT1 | 216 |
| IV.20 | Westford-Fort Davis-Fairbanks four day estimate of wobble/UT1 | 217 |
| IV.21 | Errors from schedule WRD00 at 5-day intervals - earth tide and diurnal polar motion modeled errors | 219 |
| IV.22 | Errors from schedule WDF00 at 5-day intervals - earth tide and diurnal polar motion modeled errors | 219 |
| IV.23 | Station configurations for schedule tests | 222 |
| IV.24 | Baseline components for schedule tests | 222 |

| | | |
|-------|---|-----|
| IV.25 | Sources used for schedule tests | 222 |
| IV.26 | Sources used in schedules A - M | 226 |
| IV.27 | Baseline errors for Haystack-Pioneer/Goldstone schedules with measurement uncertainty determined by source and receiving parameters - full set of parameter adjustments . . | 229 |
| IV.28 | Baseline errors for Haystack-Pioneer/Goldstone schedules with constant noise added to all observations - full set of parameter adjustments | 230 |
| IV.29 | Baseline errors for Haystack-Pioneer/Goldstone schedules adjusting only site coordinates and clocks | 234 |
| IV.30 | Individual experiment statistics for Haystack - OVRO observations from 76/09/29 - 76/10/14 | 255 |
| IV.31 | Individual source statistics for Haystack - OVRO observations from 76/09/29 - 76/10/14 | 257 |
| IV.32 | Haystack - OVRO observations: average measurement uncertainties over good data points and normalizing errors . | 259 |
| IV.33 | Comparison of actual and simulated parameter formal errors for baseline length, longitude, and latitude from Haystack - OVRO observations using delay only | 261 |
| F.1 | Fit to 400 gravity data points beginning 75/220 18:00 . . . | 355 |
| F.2 | Fit to 236 gravity data points beginning 75/220 18:00 . . . | 355 |
| F.3 | Fit to 175 gravity data points beginning 75/230 14:00 . . . | 355 |
| F.4 | Fit to 400 gravity data points beginning 75/220 18:00 . . . | 355 |
| F.5 | Fit to 900 gravity data points beginning 75/241 17:00 . . . | 357 |

LIST OF FIGURES

| Figure | page |
|---|-------------|
| I.1 Basic VLBI geometry | 5 |
| I.2 VLBI geometry on a rotating (earth) platform | 7 |
| I.3 Geometry of intersecting telescope axes | 17 |
| I.4 Geometry of nonintersecting telescope axes | 17 |
| III.1 Poles and axes of the earth | 74 |
| III.2 Diurnal polar motion epicycle | 82 |
| III.3 Poincot's representation of the free motion of a rigid earth | 86 |
| III.4 Poincot's representation of the forced motion of a rigid earth | 86 |
| III.5 Diurnal polar motion over several days | 82 |
| III.6 Diurnal polar motion in a deformable earth | 90 |
| III.7 Equators and arcs relevant to diurnal polar motion | 95 |
| III.8 Delay signature of diurnal polar motion for 3C 84 over two weeks | 105 |
| III.9 One year envelope of delay signature | 107 |
| III.10 Zero-crossing UT time for delay signature over one year . . | 108 |
| III.11 One day delay signature for sources at different right ascensions | 109 |
| III.12 One day delay signature for sources at different right ascensions for time that the sources are visible | 110 |
| III.13 One day delay signature for sources at different declinations | 111 |
| III.14 One day delay signature for sources at different declinations for time that the sources are visible | 112 |

| | | |
|--------|--|-----|
| III.15 | One day delay signature for north-south baseline | 114 |
| III.16 | Delay signatures for sources observed on Sep. 29, 1976 | 115 |
| III.17 | Delay signatures for sources observed on Oct. 04, 1976 | 116 |
| III.18 | Delay signatures for sources observed on Oct. 09, 1976 | 117 |
| III.19 | Delay signatures for sources observed on Oct. 11, 1976 | 118 |
| III.20 | Delay signatures for sources observed on Oct. 14, 1976 | 119 |
| IV.1 | Geometry of the three-parameter Jupiter deflection model | 179 |
| IV.2 | Mutual visibility for Westford-Richmond-Fort Davis | 209 |
| IV.3 | Mutual visibility for Westford-Fort Davis-Fairbanks | 210 |
| IV.4 | Mutual visibility for Haystack-Pioneer/Goldstone | 225 |
| IV.5 | Comparison of schedules A, B, and C | 232 |
| IV.6 | Comparison of schedules D, E, F, G, H, and I | 238 |
| IV.7 | Comparison of schedules J and K | 247 |
| A.1 | Mark III field system | 271 |
| A.2 | Mark III tape format | 274 |
| A.3 | Mark III processor internal block diagram | 277 |
| A.4 | Mark III processor external block diagram | 278 |
| B.1 | Mark III information flow | 289 |
| B.2 | CALC section block diagram | 300 |
| B.3 | CALC block diagram | 303 |
| D.1 | ESTIM block diagram | 334 |

INTRODUCTION

Very-long-baseline-interferometry (VLBI) was first developed (Brotten et al 1967, Bare et al 1967, Moran et al 1967, Currie et al 1974) for studies of source structure and size. The technique has since been applied to several other fields: 1) radio astrometry (Counselman 1976, Clark et al 1976, Gubbay et al 1974, Rogers et al 1973, Cohen 1972), 2) relativity (Counselman et al 1974), 3) geodesy (Rogers et al 1978, Ong et al 1976, Thomas et al 1976, Whitney et al 1976, Coates et al 1975, Shapiro et al 1974, Hinteregger et al 1972), 4) polar motion and UT1 (Shapiro et al 1974, Moran 1973), and 5) geophysics (Robertson 1975). New equipment such as the Mark III system (Coates et al 1975 and appendix A) and the Wide-band Very Long Baseline Optical Interferometer (Currie 1977) promise to increase the versatility of VLBI while refined analytical methods should yield better scientific results.

This thesis addresses two general areas: 1) the development of models for the analysis of VLBI observations and 2) the applicability of VLBI to the study of various phenomena.

As VLBI measurements become more precise, the need for correct physical models grows more acute. The motion of the observing stations through space is quite complex. At the crudest level they spin in a circle as the earth rotates about its axis. Complications quickly enter however. The direction of the axis in space changes, the position of the axis in the earth changes, and the rotation rate

changes. The earth responds to tidal forces and the stations move accordingly. All these effects must be correctly separated and modeled if the observations are to be properly interpreted at the milliarcsecond or several centimeter level. I have been particularly concerned with diurnal polar motion or dynamic variation of latitude and I have used VLBI data to investigate this phenomenon in order to develop a better model for the overall rotation of the earth.

As VLBI equipment improves in sensitivity, resolution, reliability and cost, the technique can be applied to new areas or to better measurements in existing areas. It is useful to know how well measurements can be made before undertaking an experimental program. For example, optical observations do not suffer from the same set of problems as do microwave observations. Can optical observations then perform a more precise test of relativity? Unless unlimited time is available, it is also desirable to put the time to its best use by optimizing the observations for the parameters of ultimate interest. For example, many observations have been primarily for astronomical purposes. An observing schedule could be designed for geodetic parameters instead. Both questions, what can be done and how to do it best, may be approached through experiment simulation and error analysis. The effect of small model errors on precise measurements can also be studied. I have investigated several areas, applying to them an augmented covariance analysis that includes the effect of certain systematic errors.

Chapter 1 describes the fundamentals of VLBI observations. In

Chapter II I describe the coordinate systems and physical models used in data analysis and experiment simulation. Compact analytical expressions for the models and parameter partial derivatives are given. I derive expressions for the solid earth tides and diurnal polar motion which have particular applicability to the present analysis.

Chapter III describes my study of diurnal polar motion based on five years of VLBI observations. I define the nomenclature and give a detailed description of the phenomenon and its effects. The implementation of a diurnal polar motion model is also described. My work with experiment simulations is described in chapter IV. The statistical theory is first summarized. The core of the chapter discusses three studies: 1) estimating the relativistic light bending parameter with optical observations near Jupiter, 2) precise monitoring of polar motion and UT1 with radio frequency VLBI, and 3) the effect of observing schedules on the precision of baseline parameter estimates. The last section of the chapter compares several actual experiments with simulations. The appendices contain information about the Mark III VLBI system (the instrumentation, data base structure and software), details of the experiment simulation program, and a gravimeter study of solid earth tides.

Chapter I.

PRINCIPLES OF VERY LONG BASELINE INTERFEROMETRY

This chapter describes the basis for Very Long Baseline Interferometry. The observables are defined and the fundamental geometry and apparatus are reviewed. Complications of geometry, propagation media, and instrumentation are sketched in anticipation of the detailed models given in chapter II.

A. The VLBI observables

The primary VLBI observable for geodetic and astrometric studies is the measured time interval between the arrival of a radio signal at one end of the interferometer and its arrival at the other end. This interval is called the delay and its time derivative is the delay rate observable. From a sufficient set of these data as functions of time, the geometry of the interferometer baseline and the position of the observed radio sources can be determined.

B. Basic geometry and apparatus of VLBI

The basic geometry of a VLBI interferometer is shown in figure I.1. Each observing station receives and records independently the signals from a radio source. The time of arrival of the signals in terms of the local clocks is also recorded. In the simplest case the signal from the source is a single plane wave and the observing sites

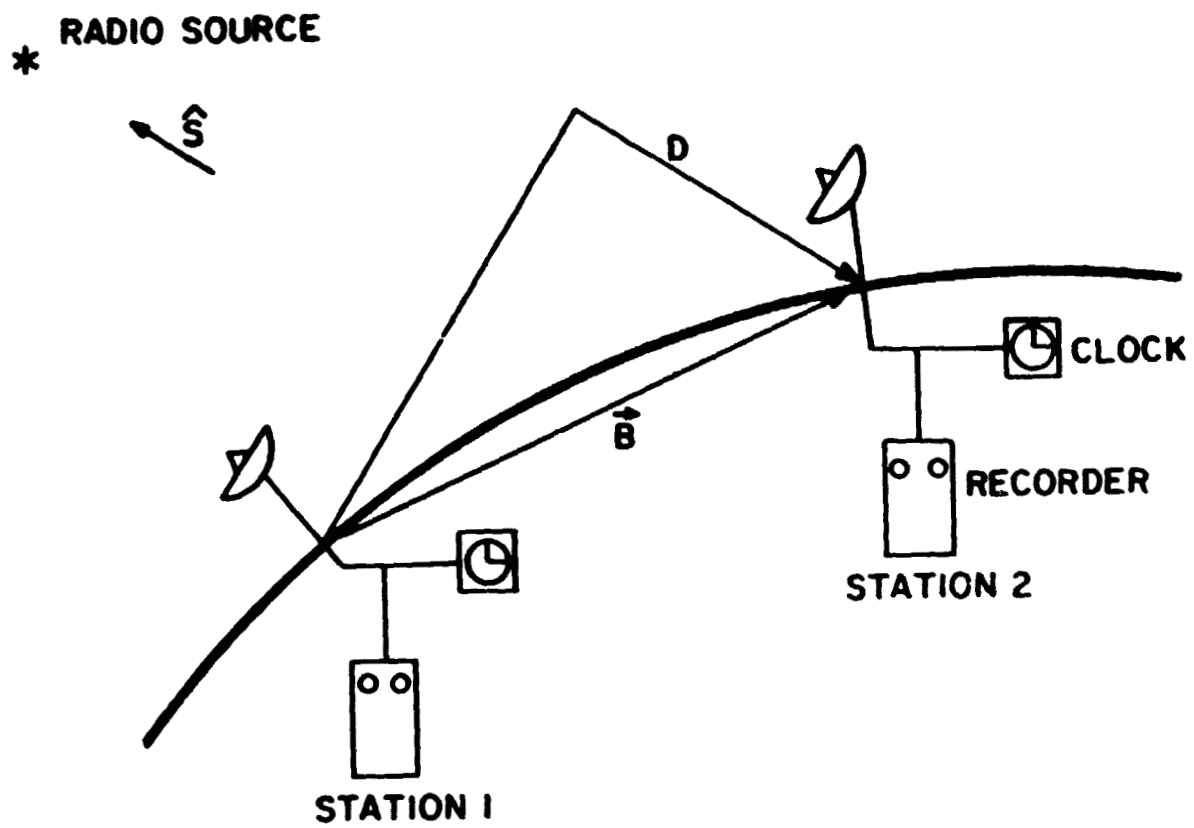


Fig. 1.1 Basic VLBI geometry

JRH
10-77

are fixed in space. The difference in recorded arrival time is then a direct measure, in light-time, of the component of the interferometer baseline in the direction of the source. Measuring delays from sources located orthogonally in space completely determines the baseline length and orientation. For a source emitting continuous random signals, some portion of the wave train is recorded by each station. If the two receiving and recording systems have the same bandwidth and no noise, the signals recorded will be identical in shape but displaced in time. The difference in arrival time is the time offset required to make the wave forms coincide. The delay can then be found by cross-correlating the two signals and determining the point of maximum correlation. The case of an interferometer on a rotating platform is illustrated in figure I.2. Two additional factors must now be taken into account. As the interferometer rotates in space, the projected baseline in the direction of the source changes with time, introducing the delay rate observable. As the stations move, the signals recorded by each station are Doppler shifted. These effects must be removed before the recordings can be correlated to determine the delay observable.

VLBI instrumentation can be divided into several sub-systems:

- 1) antenna, 2) receiver, 3) frequency standard, 4) recorder,
- 5) calibration, and 6) correlator.

Antennas used for VLBI have varied in size from the 305-m bowl at Arecibo, Puerto Rico to a portable 9-m surplus Army dish of the Jet Propulsion Laboratory. The sites have been distributed geographically as widely as Australia and the Crimea. The observations which ar

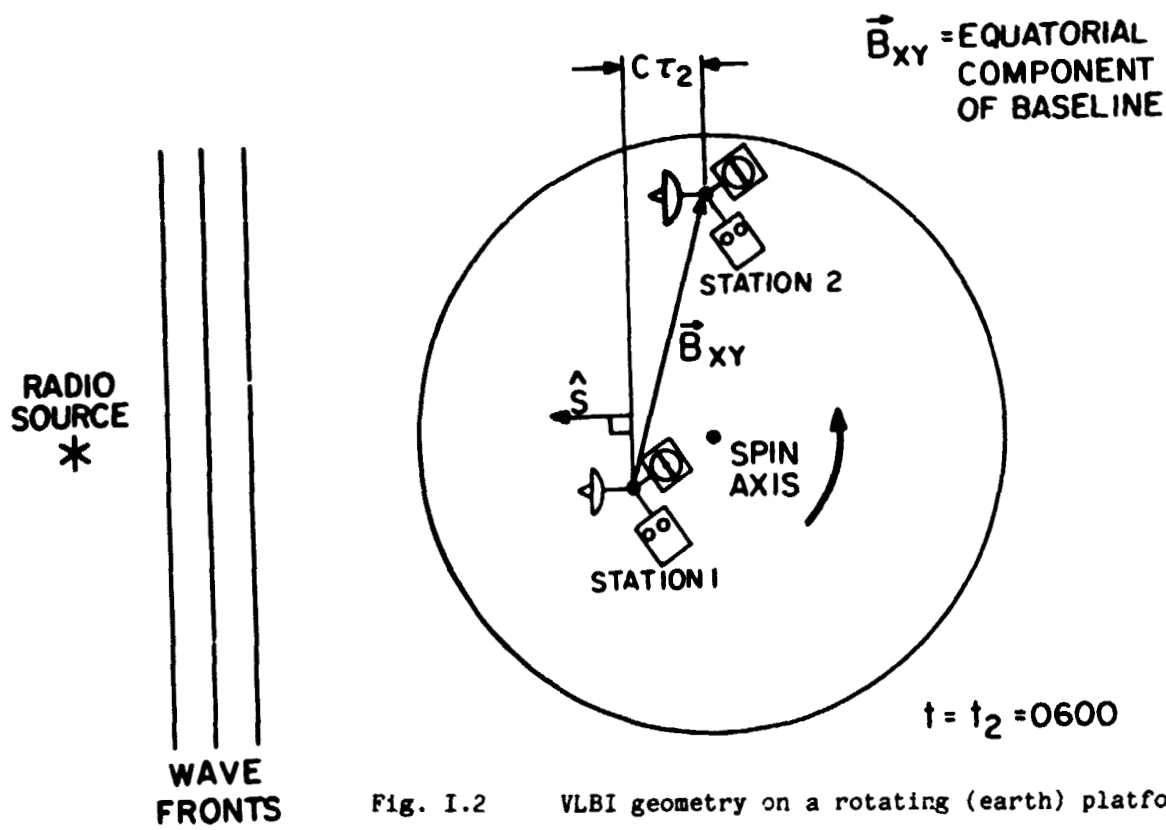
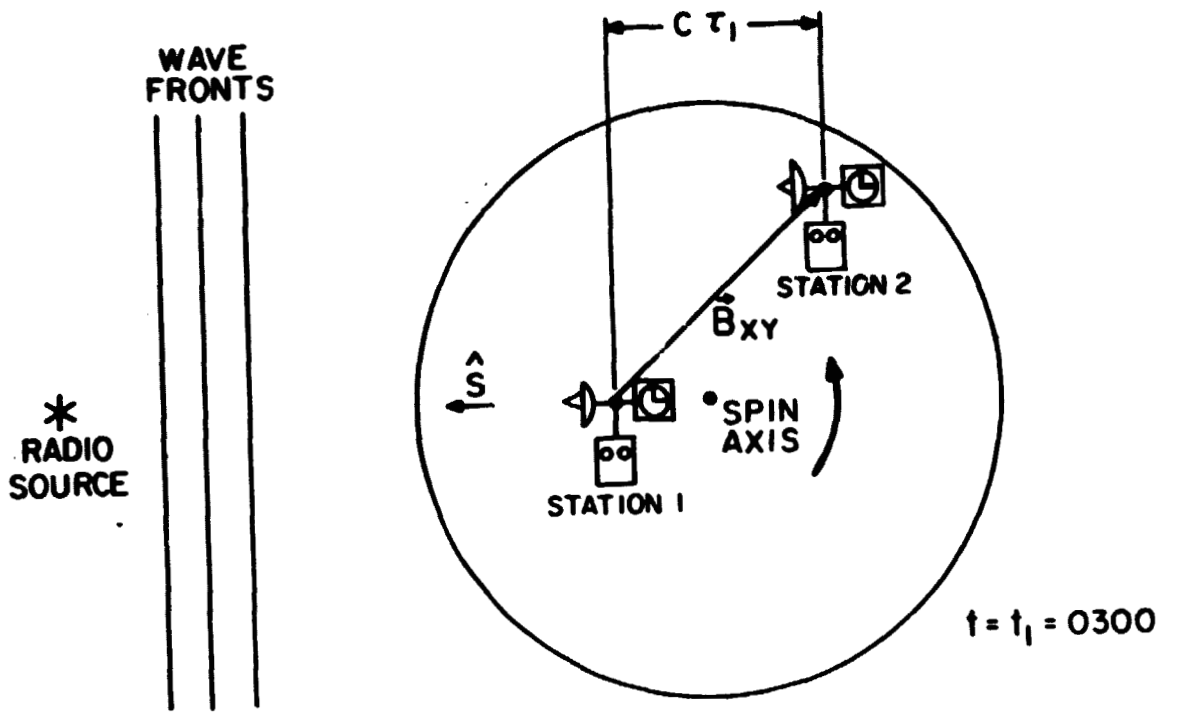


Fig. I.2 VLBI geometry on a rotating (earth) platform

JRH
10-77

described in chapter III were recorded at the Haystack Observatory in Massachusetts, the Mars antenna at the Goldstone tracking complex of the Deep Space Network in California, the Onsala Space Observatory in Sweden, and the Owens Valley Radio Observatory (OVRO) in California. An antenna may have a significant impact on VLBI observations depending on the mount geometry, slew rate (the speed at which the antenna can be moved from source to source), collecting area, and efficiency at the observing frequency. The first two factors affect the sequence of sources that can be observed while the latter two affect the list of sources.

The front end receiver electronics are usually provided by the observatory operating the antenna. The least noisy receivers use maser amplifiers with X band (8 GHz) receiver temperatures as low as 30 deg K at Goldstone and S band (2 GHz) temperatures as low as 17 deg K. Haystack has used a cooled parametric amplifier operating as low as 70 deg K while the OVRO uncooled paramp has operated at 120 deg K. The observing bandwidth has ranged from 26 MHz at Goldstone to 400 MHz at Haystack and OVRO. The noise of the receivers on an interferometer puts a lower limit on the source flux that can be observed while the observing bandwidth influences the measurement uncertainty of the VLBI observables.

Commercial rubidium and cesium beam clocks and hydrogen masers have been used as VLBI frequency standards. Rubidium clocks have fractional frequency stabilities of parts in 10^{11} while hydrogen masers can be two or more orders of magnitude better. Two time scales

are important. Over periods of a few minutes frequency stability must be adequate to provide sufficient integration time for extracting the VLBI observables. Over periods from several hours to a day, the frequency standard must function as a stable clock for recording signal arrival times.

Calibration systems have been used to monitor the electronics and the ambient environmental conditions. Measurement of internal dispersion and cable lengths has been provided by phase calibrators. Sensors for pressure, humidity and temperature and radiometers to measure water vapor content have gathered data for calibrating the effects of the atmosphere.

Several incompatible recording systems exist. The Mark I records a bandwidth of 360 kHz on computer tape drives. Each data tape is limited to three minutes. The widely used Mark II system records a bandwidth of 2 MHz using modified Ampex or IVC video tape decks. The practical advantage of using video recorders is the ability to record continuously for several hours on a single reel of tape. The disadvantage is greater complexity and poorer processing consistency for the delay observable. The Mark III system under development uses an instrumentation drive to record as many as 28 tracks of up to 2 MHz each on a 9600-ft reel. Depending on the recorded bandwidth and number of tracks, a tape may last from 13 minutes to several days.

There are three special purpose correlators for the two operational recording systems. The Mark I processor is located at the

Haystack Observatory. Mark I data have also been reduced on the IBM 360/91 at the Goddard Space Flight Center (GSFC). Two Mark II processors have been built, one at the National Radio Astronomy Observatory (NRAO) in Charlottesville, Virginia and the other at the California Institute of Technology. The design of the three correlators is dissimilar and there have been difficulties comparing the delay and correlation output from the different processors. A skeletal Mark III correlator exists at the Haystack Observatory.

C. Dependence of VLBI observables on geometry

Since the delay and delay rate observables are dependent on the relative geometry of the stations and sources, it is helpful to describe the observing geometry in somewhat greater detail. From figure I.1 the geometrical delay is

$$T_g = \frac{-\vec{B} \cdot \vec{S}}{c} \quad \text{I.C.1}$$

where B is the baseline vector from station 1 to station 2, S is a unit vector pointing in the direction of the source, and c is the velocity of light. (In the following discussion of geometrical effects, the speed of light is set to unity.) In a reference system where the source coordinates are fixed, the vector B will change in orientation but not in norm as the earth rotates. For simplicity, assume the coordinate axes are arranged so that the z -axis is in the direction of the earth's instantaneous spin axis. The baseline vector can be separated into two parts, a polar (z) component parallel to the spin

axis and an equatorial (xy) component perpendicular to the spin axis.

Then

$$\begin{aligned} T_g &= -(\vec{B}_z + \vec{B}_{xy}) \cdot (\vec{S}_z + \vec{S}_{xy}) \\ &= -(b_z s_z + \vec{B}_{xy} \cdot \vec{S}_{xy}) \end{aligned} \quad \text{I.C.2}$$

where b_z and s_z are the norms of the polar components. By definition, the polar component cannot change with the earth's diurnal rotation.

Therefore part of the geometric delay is constant and depends only on the z-component of the baseline vector and the source declination. As the earth rotates, the equatorial component of the baseline is carried around on a platform and its projection in the direction of the source has a sinusoidal behavior

$$\vec{B}_{xy} \cdot \vec{S}_{xy} = b_{xy} s_{xy} \sin(Wt + p) \quad \text{I.C.3}$$

where b_{xy} and s_{xy} are the norms of B_{xy} and S_{xy} , respectively, W is the earth's rotation rate, t is time, and p is the phase angle at a reference epoch. Therefore the total geometric delay is

$$T_g = -(b_z s_z) - (b_{xy} s_{xy} \sin(Wt + p)) \quad \text{I.C.4}$$

The time derivative of the geometric delay (the delay rate) depends only on the equatorial components of the baseline and source vectors and is given by

$$\frac{dT_g}{dt} = -W b_{xy} s_{xy} \cos(Wt + p) \quad \text{I.C.5}$$

There are several physical phenomena which complicate the geometry of a VLBI observation. These are described in general terms below. Details of how the effects are modeled are given in chapter II.

The conventional celestial coordinate system is defined with the origin at the earth's center of mass, the z-direction aligned parallel to the spin axis and the x-direction pointing toward the intersection of the equator and the orbital plane through which the earth passes at the vernal equinox. The presence of other bodies in the solar system causes this coordinate system to change orientation slowly with respect to a reference frame defined by sources sufficiently distant to have undetectable motion when viewed by an unaccelerated observer. The gravitational force of the sun and moon on the earth's equatorial bulge causes luni-solar precession of the spin axis by 50.3 arcsec per year. Astronomical nutation caused largely by the behavior of the moon's orbit superimposes shorter quasi-periodic motions up to 9 arcsec with a principal period of 18.6 years. The other planets cause a slow rotation of the earth's orbital plane, moving the intersection with the equator and decreasing the obliquity, the angle between the orbital plane and the equatorial plane. These motions result in an apparent change in source position as viewed from the instantaneous earth-centered celestial coordinate system and affect VLBI observables accordingly. A change in declination affects the constant part of the geometric delay and the amplitude of the diurnal sinusoids in delay and rate. A change in right ascension affects the phase of the diurnal sinusoids. Since the observed sources are most probably fixed in an

inertial reference frame, it is conceptually simpler to reduce the observations in a fixed coordinate system, currently defined by the orientations of the mean spin axis and mean orbital plane of the epoch 1950.0. The transformation from the instantaneous celestial coordinate system to the reference coordinate system is a set of coordinate rotations characterized by three parameters: the precession constant, and nutations in obliquity and longitude. The motion of the earth along its orbit, which causes stellar aberration, is treated by defining the origin of the reference coordinate system at the solar system barycenter and translating appropriately.

The location of a place on the earth is measured in a terrestrial coordinate system defined by a reference pole and the meridian of Greenwich. Munk and Macdonald (1960) contains the standard discussion of nomenclature. The terrestrial system does not coincide with the celestial coordinate system described above because the spin axis moves relative to the physical surface of the earth and because the Greenwich meridian rotates once per day. The angle about the z-axis between the terrestrial and celestial coordinate systems is measured by apparent sidereal time, the angle between the Greenwich meridian and the celestial x-axis. This angle does not increase uniformly with time as measured by atomic clocks but has periodic variations and an irregular secular drift. If the time broadcast by international time services (universal coordinated time or UTC) is converted assuming uniform rotation to the equivalent sidereal time, there may be a discrepancy of up to 0.9 seconds from the actual apparent sidereal time (BIH annual report). Normally the offset is kept less than 0.7 sec or 10 arcsec.

The effect on the delay observable may be as much as 100 nsec.

The motion of the spin axis with respect to the reference pole fixed to the earth's crust is called polar motion or wobble. There are two distinguishable components of polar motion: 1) the 1-year component caused by the forced motion of the spin axis about the principal moment of inertia axis and 2) the Chandler wobble of 1.2-year period related to the damped Eulerian free precession modified by the elastic deformation of the earth. The amplitude of these terms is about 0.2 arcsec. Over a period of six years the mean position of the spin axis is nearly constant but there may be a small secular drift. In addition to long period polar motion, the existence of diurnal polar motion with an amplitude of 0.02 arcsec has been theorized by Woolard (1953) and McClure (1973). The effect of polar motion is to vary the orientation of the terrestrial system with respect to the celestial system about the x and y-axes, causing a further change in observatory positions. The maximum effect on the delay observable is 20 nsec. Three parameters can be used to characterize polar motion. The slowly moving spin pole position averaged over several days is related to the reference pole by two orthogonal angular distances. These distances describe conventional polar motion. Diurnal polar motion can be described by a factor which scales the magnitude of the displacement. Diurnal polar motion is discussed in detail in chapter III.

The transformation from the terrestrial coordinate system to the instantaneous celestial coordinate system is a set of coordinate

rotations involving apparent sidereal time, long period polar motion and diurnal polar motion.

The tidal potential of the moon and sun causes a solid earth tide. If the earth were fluid, the maximum displacement of the surface would be 76 cm (Melchior 1966). Actual displacements are estimated to be up to 36 cm. There is also a small (3 cm) effect of ocean tides on solid earth displacements (Farrell 1970). As the water in the ocean moves, the load of its weight and its gravitational force on the continents varies. The total tidal displacement is dependent on the relative positions of a station, the moon, the sun and the oceans. Consequently, both baseline length and orientation vary with time. The effect on the VLBI observables is quite complicated. Good models of solid earth tides and ocean loading are desirable even though the effect on delay is less than 2 nsec. The radial and horizontal displacements caused by the solid earth tides are characterized by two Love numbers. Because the ocean loading model is quite different from the solid earth tide model, the ocean tide must be treated separately. Each component of the ocean loading tide can be represented by a magnitude and phase offset, both of which are specific to each station. The phase offset is the phase lag or lead relative to the solid earth tide of the same frequency.

The arrival time of a signal must be defined with respect to some fixed geometrical point within the observing telescope. A convenient point is the intersection of the fixed telescope axis with the plane perpendicular to it containing the moving axis. However, the signal is

recorded as arriving at a fixed interval after it reaches the feed horn of the receiver. If the axes of the telescope intersect (figure I.3), the feed horn of the (ideal) telescope maintains a constant distance from the fixed reference point. The difference in time along the actual ray path to the feed and the ray path directly to the reference point is a constant and the recorded arrival time will have a constant offset. The effect on the delay observable will also be constant while the delay rate is unaffected. If the telescope axes do not intersect (figure I.4), there is a distance between the moving axis and the reference point which the signal must cross. This additional distance is given by

$$\Delta A = D \sin (\theta)$$

I.C.6

where D is the offset between the axes and θ is the angle between the fixed axis and the direction the telescope is pointed. The signal is recorded earlier by both the constant difference between the ray paths to the feed and to the moving axis and by the varying projection of the offset in the direction at which the dish is pointed. Both delay and delay rate may be affected. Since the axis offset may be several meters, the effect can be substantial. In a real telescope, there also are changes in the ray path to the feed resulting from thermal expansion, gravitational loading, wind pressure, etc. Removing these effects requires a detailed model of the telescope structure and has not been done to date. The magnitude of the effects should be under 2 cm.

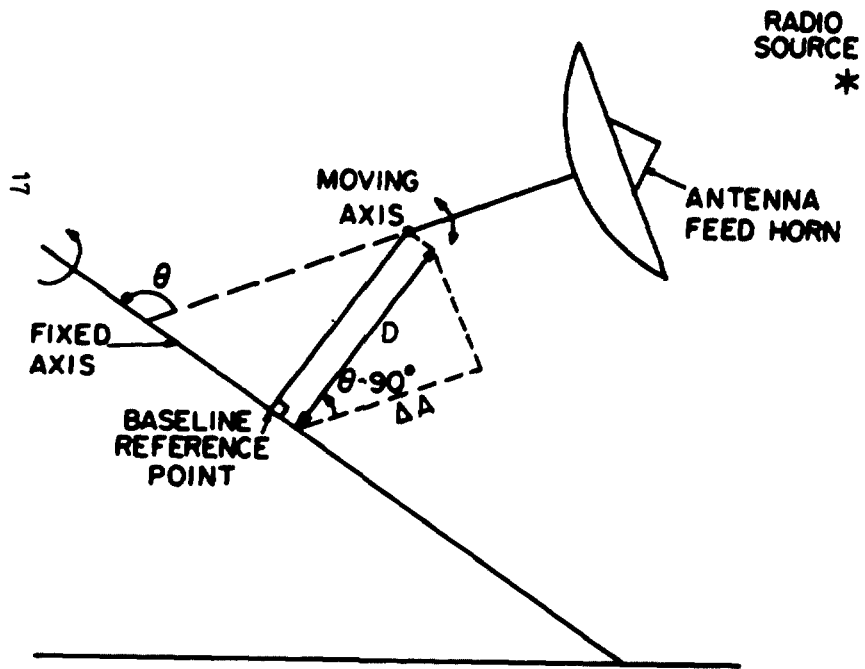


Fig. I.4 Geometry of nonintersecting telescope axes

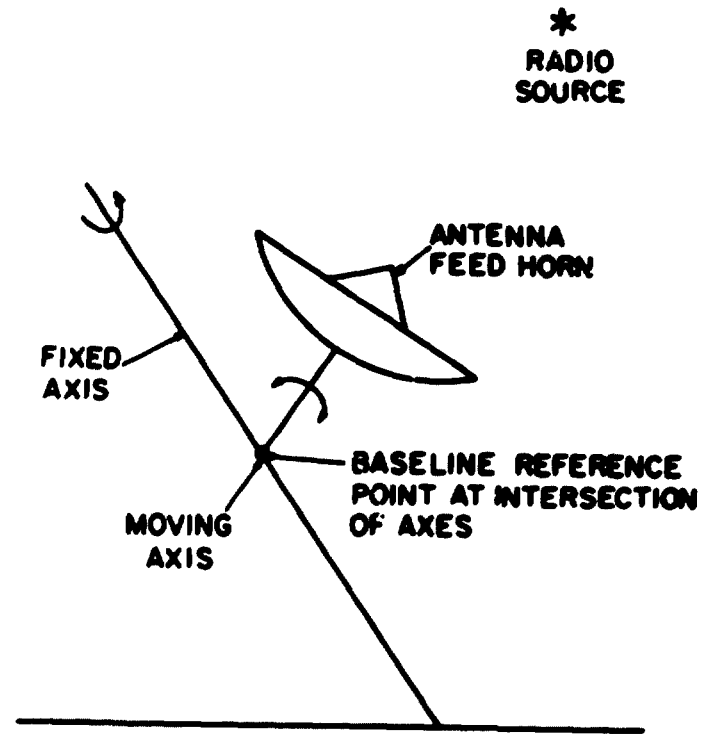


Fig. I.3 Geometry of intersecting telescope axes

While the sources used in VLBI geodesy are far enough away to make actual angular movement unlikely, there can be a small apparent change in position resulting from complex milliarcsec source structure. The apparent source position can depend on the interferometer resolution, which changes as the baseline component perpendicular to the source vector changes over a day. The apparent position will move if the source has an asymmetric distribution of components. Likewise, as the source evolves and different areas radiate, the apparent position may shift even if no overall physical displacement occurs. These effects, which should be less than 0.3 nsec in delay for the most complex source commonly observed, can be minimized using detailed source structure maps to calculate the apparent source position changes.

D. Dependence of VLBI observables on the propagation medium

If the medium is dispersive, there are two velocities associated with wave propagation, group velocity and phase velocity. Both group delay and phase delay can be extracted from the raw VLBI data. The phase delay has ambiguities spaced at $1/f$ where f is the observing frequency. These ambiguities arise from the spacing of the interferometer fringes on the sky and the inability to determine the absolute fringe on which the observed source is located. Since the ambiguities are about 0.1 nsec and are therefore quite difficult to resolve, phase delay is generally not used for geodetic and astrometric studies. It has only been useful when observing a single source or a few closely located sources where the fringe phase can be continuously

extrapolated from one data point to the next.

The group delay is given by

$$\tau = \frac{d\phi}{d\omega}$$

I.D.1

where ϕ is the fringe phase or phase of the cross-correlation function and ω is frequency over the observing bandwidth. Ambiguities in the group delay occur if the observing bandwidth is sampled at discrete frequencies, a technique called bandwidth synthesis. The ambiguity is $\frac{1}{\Delta f_{\min}}$ where Δf_{\min} is the smallest frequency interval used provided that the other spacings are integer multiples of the minimum spacing. Since group delay ambiguities in past Mark I data have ranged from 1 microsec to 40 nsec, it has been possible to correct for them with increasingly accurate a priori geometry.

The retardation effect of the propagation medium can be divided into four areas, the dry component of the troposphere, the wet component, the ionosphere, and the solar corona. In each case the effect on the delay observable is simply the difference in the signal delays at the two observing stations.

The dry component of the troposphere introduces a signal delay of approximately 7 nsec at the zenith. Since the dry atmosphere is relatively uniform and the delay depends almost entirely on the mass along the line of sight, it is possible to model the dry atmosphere from surface meteorological data. The atmosphere can also be modeled

approximately by using a single zenith thickness parameter and scaling the effect by a function of the elevation angle of the observed source. Time variations can be introduced by using different zenith parameters for different periods.

The effect of water vapor in the troposphere is typically between 10% and 15% of the dry component but changes markedly with time and direction. The effect on VLBI observables cannot be modeled from surface conditions because of the patchy distribution of water in the atmosphere. It is necessary to make direct measurements of water content in the observing direction in order to remove the effect. Some work along these lines has been done with microwave radiometers at 19 GHz and 22 GHz (Moran 1976, Resch 1975).

Charged particles in the ionosphere cause a frequency-dependent signal delay. At 8 GHz the equivalent daytime zenith delay is typically 0.3 nsec while the nighttime effect is an order of magnitude lower. Group delay and phase delay are affected with opposite sign. Complications can arise when observing in the direction of dawn or dusk and when the ionosphere is disturbed by solar storms. Simple analytical models have not proved useful and corrections using satellite Faraday rotation data have led to only marginal improvements. Since the ionosphere signal delay is given by

$$T_{\text{ion}} = \frac{k}{f^2}$$

I.D.2

where k is a scaling factor and f is the observing frequency, it is

possible to remove the effect by observing simultaneously at different frequencies. New delay and delay rate observables which are free of ionospheric effects can be derived from their respective values at different frequencies.

Like the ionosphere, the solar corona retards a radio signal because of its charged particle content. It is possible to model the effect as some function of the separation of the source unit vector from the sun. However, when the coronal effect becomes large enough to be a significant error, short term fluctuations near the sun often degrade the data beyond recovery. The multi-frequency technique used to eliminate the ionospheric delay can simultaneously remove the coronal effect.

E. Dependence of VLBI observables on instrumentation

The instrumentation used in VLBI can be divided in two parts for the purpose of discussing its effect on the VLBI observables. One part is the frequency standard which provides both time and mixing frequencies. The other part is the electronics which takes the signal from the telescope feed horn to magnetic tape.

Since the delay observable is directly related to the recorded time of signal arrival, any deviation by a station clock will appear immediately in the delay. The hydrogen masers presently used in VLBI have measured laboratory stabilities of a few parts in 10^{14} , corresponding to an error of less than 5 nsec per day. If both clocks

of a VLBI baseline have linear drifts, then the effect on the delay observable can be parameterized by an offset and a net clock rate. The delay rate is only affected by the second term. The offset is necessary since it is generally not possible to synchronize two widely separated clocks to better than a few microseconds.

Hydrogen masers in field use, however, have been found to be affected by external masses of metal, barometric pressure, temperature, and poorly diagnosed internal illnesses. The masers at Goldstone and NRAO have had variations up to parts in 10^{12} but are typically stable to parts in 10^{14} . Common problems include long term non-linear drifts and discontinuities in phase and rate. A simple but uninformative method of treating poorly behaved clocks is to use a polynomial of the form

$$T_c = a_0 + a_1 t + a_2 t^2 + \dots \quad \text{I.E. 1}$$

where T_c is the clock contribution to the delay from a station, a_0 is the clock offset, a_1 is the rate, and t is an appropriate measure of time. Discontinuities can be handled by using separate polynomials on both sides of the break. The number of polynomials and the number of terms in each is at present a matter of judgment and experience. The behavior of poorly controlled clocks has not been systematic enough to permit a better physical model.

The rest of the instrumentation affects the observables in a manner somewhat analogous to the propagation medium. As signals pass

through the cables and active elements in the receiver and recorder electronics, they are subject to retardation and dispersion. Both effects can be monitored using a phase calibrator signal injected at the feed. The phase calibrator signal is extracted at each frequency used in sampling the observing bandwidth. Its phase in each frequency channel is used to correct dispersion. The arrival time associated with a signal is derived directly from the phase calibrator injected with that signal. Consequently the delay observable is affected not by the delay getting the signal from the feed horn to magnetic tape but by variations in the time interval required for the phase calibrator signal to go from the station frequency standard to the feed. Cable length calibration techniques used at Haystack and NRAO indicate that such variations can be several tenths of nanoseconds and is probably a result of cable stretching and thermal expansion.

F. Measurement uncertainties of the VLBI observables

Whitney (1974) gives expressions for the measurement uncertainties of the VLBI delay and delay rate observables. His analysis includes the case of digitized recording with discrete sampling of the observing bandwidth which applies to the Mark I observations discussed in chapter III.

The measurement standard deviation of the delay observable is given by

$$S(\text{delay}) = \frac{1}{\omega_s \text{SNR}} \quad \text{I.F.1}$$

where

ω_s = standard deviation of the observing frequencies used to
sample the observing bandwidth

SNR = signal to noise ratio

$$= \frac{2\rho}{\pi} \sqrt{2BT} \quad \text{I.F.2}$$

B = recorded bandwidth

T = integration time

$$\rho = \gamma\sqrt{K} \quad \text{I.F.3}$$

γ = fringe visibility

= 1 for a completely unresolved source

$$K = \frac{T_{a1}T_{a2}}{(T_{a1} + T_{s1})(T_{a2} + T_{s2})} \quad \text{I.F.4}$$

T_{a1}, T_{a2} = source antenna temperatures

T_{s1}, T_{s2} = system noise temperatures

$$T_a = \frac{FEA}{2k}$$

F = source flux density

E = antenna efficiency

A = collecting area

k = Boltzmann's constant

The standard deviation of the delay rate observable is given by

$$S(\text{delay rate}) = \frac{\sqrt{12}}{\omega_s T \text{ SNR}} \quad \text{I.F.5}$$

where

ω_{rms} = root-mean-square of the sampling frequencies

In practice the delay rate uncertainty is dominated by the fractional stability of the station frequency standards and atmospheric fluctuations.

G. VLBI instrumentation systems

Three different VLBI systems are discussed in chapters III and IV. These are Mark I, Mark III, and WOVLBI.

Mark I is the only fully realized system of the three and was developed by groups at NRAO, MIT and Haystack Observatory. The instrumentation and algorithms have been described by Whitney et al (1976), Whitney (1974), Hinterreger (1972), and Rogers (1970). Mark I has provided useful data since 1968 but will eventually be completely replaced by Mark III.

The Mark III VLBI system is being designed and built as a cooperative effort by groups at GSFC, Haystack Observatory, NRAO, and MIT. Improvements in the recording and processing hardware should contribute to generating data for both celestial and terrestrial studies which is a factor of ten better than what is now possible. In addition, the equipment should be more reliable and easier to operate than either Mark I or Mark II. A further description of the Mark III system can be found in appendix A. The recorder and processor were

tested in Sept. 1977 on a Massachusetts to West Virginia baseline using up to 24 of 28 possible tracks. A number of strong and weak sources were observed over a 40-hr period. Preliminary results indicate that the Mark III fringe amplitudes agree to 1% with Mark I data taken simultaneously.

The WOVLBI (Wide-band Optical Very Long Baseline Interferometer) was designed and is being built by the Quantum Electronics group at the University of Maryland under the leadership of Prof. D. G. Currie. An earlier model has been used on the 200-inch telescope at Palomar Mountain and the 100-inch telescope at Mt. Wilson to observe stars as faint as sixth magnitude. The operational principles of the WOVLBI are completely different from the radio-frequency systems. A description of the apparatus and its capabilities can be found in Currie (1976, 1977).

Chapter II.

PHYSICAL MODELS USED IN HIGH PRECISION INTERFEROMETRY

This chapter describes the models used in analysis of VLBI experiments. The algorithms are implemented in three computer programs. CALC is part of the Mark III system and is described in appendix B. VLBI3 is an older parameter estimation program. A modified version of VLBI3 was used to obtain the results discussed in chapter III. ESTIM is the experiment simulation and error analysis program and was used in the work described in chapter IV.

The physical models used to determine the theoretical values of the delay and delay rate observables can be divided into three groups: 1) those that determine the orientation of the baseline with respect to the fundamental VLBI reference frame, 2) those that involve perturbations to the simple observing geometry, and 3) those related to the propagation medium. Each group will be treated in a separate section. The chapter begins with a discussion of coordinate systems and time followed by expressions for the VLBI observables.

The following notation will generally be used. $R_i(\theta)$ represents the rotation of the coordinate system by the angle θ about the i -axis. The positive angular direction is counterclockwise as viewed along the axis in toward the origin. The symbol \dot{A} represents the time derivative of the quantity A . $A \cdot B$ is the scalar product of vectors A and B while $A \times B$ is the vector cross product.

A. The VLBI reference frames

An ideal coordinate reference frame for VLBI observations would be an inertial frame defined with respect to radio sources sufficiently distant to be "fixed" in position. Adopted positions of the fundamental sources would define the orientation of the system and positions of the "fixed" sources would be independent of epoch. Any apparent changes in positions would be related to errors in the theory of the earth's motion. For historical and practical reasons the actual coordinate system used is somewhat different.

The fundamental coordinate system used in the present analysis of VLBI observations is a quasi-inertial reference frame whose origin is at the solar system barycenter and whose orientation is defined by the mean equinox and equator of the reference epoch 1950.0 (Julian date 243 3282.423). The z-axis is perpendicular to the mean equator of 1950.0 and is positive northward. The x-axis points at the intersection of the mean equator and the mean ecliptic of 1950.0 in the direction of the ascending node of the ecliptic on the equator (the vernal equinox or the first point in Aries). The y-axis completes a right-handed cartesian system.

The choice of the 1950.0 epoch to orient the coordinate system is dictated by conventional usage since source positions are commonly reduced to the 1950.0 system. The reference epoch will soon be changed to 2000.0, however. The fundamental system of stars to which the

1950.0 epoch coordinate system is referenced is the FK4 catalogue published in 1963. The use of the FK4 catalogue requires the application of Newcomb's expressions for the precessional elements which describe the movement of the mean celestial pole and the mean ecliptic pole. The extent to which Newcomb's precession constant (5025.64 arcsec per century at epoch 1900) differs from the physically correct value will be reflected in an identical deviation of the fundamental coordinate system from an inertial reference frame. The positions of truly fixed sources determined at different epochs would appear to drift when reduced to the reference epoch. However, the conventional precessional elements must be used if VLBI source coordinates are to be easily, if somewhat misleadingly, compared with results from other techniques.

In theory a fundamental optical coordinate system can be defined by fixing three values, the declination of two stars and the right ascension of one of them. The fact that the bright, nearby stars used in fundamental catalogs have detectable proper motions is a serious complication. The fundamental system for VLBI observations does not have the same restrictions. For any VLBI observation the declination of a source contributes a constant of the form $B_p \sin(\text{declination})$ where B_p is the polar component of the baseline. Therefore a source at the celestial pole defines B_p completely. The declination of each source always enters directly into the subsequent analysis with the same terrestrial scaling factor. The origin of right ascension, on the other hand, enters equally into the observations of all the sources and cannot be separated from an offset in time. The absolute right

ascension origin in an optical fundamental system can be obtained in theory by observations of the sun, although in practice the observed motions of the planets, whose positions relative to the ecliptic may be derived from celestial mechanics, are used. As neither the sun nor the planets are suitable for VLBI observations, the right ascension of one observed source must be assumed. At present the 1950.0 right ascension of 3C 273B is fixed at 12 hr 26 min 33.246 sec based on a lunar occultation observed by Hazard et al (1963). Given a sufficiently long set of VLBI observations of fixed sources, however, it would be possible to estimate both the precession constant (Walter 1977) and the position of the mean ecliptic pole, thus freeing the VLBI fundamental system from the optical system.

The transformation from geocentric origin to solar system barycentric origin is accomplished by use of a planetary ephemeris. Presently the output of the Planetary Ephemeris Program (PEP) developed at Lincoln Laboratory is used. The positions of the eight planets, the earth-moon barycenter and the moon are tabulated on magnetic tape. The tabular points are interpolated to give the position, velocity, and acceleration of the earth's center in the solar system barycentric coordinates for a given observation epoch.

At first glance it would seem that the terrestrial system for station coordinates should be defined by the earth's spin axis and barycenter and an arbitrary origin of longitude. The spin axis defines both declination and the polar baseline component while the barycenter enters in the transformation to the solar system barycentric system.

However the spin axis is not fixed with respect to the physical surface and the barycenter is not exactly determined. Consequently the station coordinates would vary with time. It is therefore necessary to adopt a more stable system even though such a system is not so closely related to the dynamics of the earth's motion. The IAU Colloquium No. 26 on Reference Coordinate Systems for Earth Dynamics is an exhaustive discussion of the problem. Two conventions are used in the the present analysis. The system used in the VLBI3 program is a left-handed, cylindrical coordinate system defined by the z-axis in the direction of the Conventional International Origin (CIO) and the x-axis in the Greenwich meridian. The CIO pole is defined by the adopted latitudes of the five observatories in the International Latitude Service (ILS) based on observations during 1900-1905. The origin of the three-dimensional VLBI3 system is defined by the adopted coordinates of the 37-m antenna at the Haystack Observatory (71 deg 29' 19.201" west, 42 deg 37' 23.00" north, 145 m elevation) on the North American Datum. The newer convention used in the CALC program is a right-handed cartesian system whose z-axis and x-axis are defined as above but whose origin is defined by the adopted coordinates of the Mars antenna in the Goldstone Tracking complex ($x = -.2356197569+7$ m, $y = -.46413427130+7$ m, $z = .36770530000+7$ m). The Goldstone position is based on space tracking data from the Jet Propulsion Laboratory and is more closely tied to the earth's barycenter. In both cases the coordinates refer to the intersection of the respective telescopes' pointing axes. It should be noted that the correctness of the adopted coordinates will not affect the baseline length since only a shift of origin is involved. An error in east-west orientation will appear as a

fixed rotation of the baseline about the z-axis, which is indistinguishable from an offset in time.

B. Description of various time and time-like quantities

Within the quasi-inertial fundamental VLBI coordinate system, epochs (time of occurrence) are defined and time intervals measured in coordinate time. The coordinate time second is defined to be the time required for 9192631770 cycles of the transition between two hyperfine levels $F=4, m_F=0$ and $F=3, m_F=0$ of the fundamental state $^2S_{1/2}$ of the atom of cesium-133 in zero magnetic field as observed by a physical clock at the mean position and velocity of the earth in a heliocentric reference frame. Coordinate time (CT) epoch is defined to be

$$CT = A1 + 32.15 \text{ sec} + e_{\text{periodic}} \quad \text{II.B.1}$$

where A1 is atomic time kept by the United States Naval Observatory (USNO), 32.15 sec is an offset to make coordinate time agree with the previous definition of ephemeris time, and e_{periodic} are diurnal, monthly, and annual terms relating to the changing gravitational potential and velocity experienced by a clock on the surface of the earth. The expressions for e_{periodic} are taken from Robertson (1975) and Moyer (1971).

$$e_{\text{periodic}} = \frac{\vec{V}_{ec} \cdot \vec{X}_r}{c^2} \quad \text{II.B.2}$$

$$-1.658 \times 10^{-3} \sin(ea)$$

$$-1.672 \times 10^{-6} \sin(me) \quad (\text{seconds})$$

$$\begin{aligned}
 \text{ea} &= \text{eccentric anomaly of the earth-moon barycenter} \\
 &= \text{ma} + e \sin(\text{ma}) \qquad \text{II.B.3}
 \end{aligned}$$

$$\begin{aligned}
 \text{ma} &= \text{mean anomaly of the earth-moon barycenter} \\
 &= 6.248291 + 1.990967871 \times 10^{-7} t_{50} \quad (\text{radians}) \qquad \text{II.B.4}
 \end{aligned}$$

$$\begin{aligned}
 e &= \text{eccentricity of the heliocentric earth-moon barycenter orbit} \\
 &= 0.01672
 \end{aligned}$$

$$\begin{aligned}
 \text{me} &= \text{mean elongation of the moon from the sun} \\
 &= 2.51841 + 2.462600818 \times 10^{-6} t_{50} \quad (\text{radians}) \qquad \text{II.B.5}
 \end{aligned}$$

$$t_{50} = \text{time in seconds since 1950.0 (Julian date 2433282.423)}$$

where v_{ec} is the velocity of the earth's center in the VLBI coordinate system and X_r is the position of the clock in the terrestrial system. The first term has a diurnal signature, the second annual, the third monthly. The latter two are referred to later as the long period terms (LPT). A nearly annual microsecond contribution due to Jupiter has been neglected.

There are three other concepts which fall under the category of time which should be distinguished. The first is the conventional epoch now designated by UTC (coordinated universal time) which is distributed by various national time services. The time interval is determined from the ensemble average of a number of cesium standards throughout the world. Both the interval and the epoch are coordinated by the Bureau International de l'Heure (BIH). In the United States both the National Bureau of Standards and USNO maintain UTC. In practice VLBI measurements use UTC epoch derived from UTC(USNO) as

propagated by LORAN and portable clock comparisons.

The second concept is time interval and frequency as used during a VLBI experiment. The frequency standards now used are hydrogen masers. The epoch of the nominal start of an observation is marked relative to UTC as kept at the station using the maser as a clock. The epoch associated with an individual data bit is actually a time interval relative to the nominal start time as determined from the maser. This time is referred to in this chapter as atomic time (AT) and is the only physically realized time.

The third concept is time as related to the orientation of the earth with respect to the sun and the "fixed" stars, universal time and sidereal time, respectively. Universal time was originally tied to the mean diurnal motion of the sun defined by Newcomb as

$$UT = 12 \text{ hr} + \text{Greenwich hour angle of the mean equinox of date} \quad \text{II.B.6} \\ -(18 \text{ hr } 38 \text{ min } 45.836 \text{ sec} + 86 \text{ 40184.542 sec } T_u + 0.929 \text{ sec } T_u^2)$$

where T_u is the number of tropical centuries since Jan 0.5 1900 (Julian date 241 5020.0). The Greenwich hour angle can be determined operationally by observations of stars from a fundamental catalogue. Continual improvement of mechanical and later atomic clocks led to the recognition that the observed position of stars is measurably affected by the variations in the position of the earth's spin axis, which determines the celestial pole and conventional true equator of date, and by variations in the rotation rate, secular, seasonal, and

irregular. The distinction is now drawn between UT0, UT1, and UT2. UT0 is obtained from direct astronomical observations and is dependent on observatory location. UT1 is UT0 corrected for polar motion and hence represents the actual angular position of the earth. The operational difficulties in determining UT1 are discussed in chapter IV. UT2 is UT1 corrected by an empirical formula for the seasonal variation in rotation rate but is now obsolete.

In practice time is kept by atomic clocks at a uniform rate and broadcast as UTC. By international agreement since 1972, a leap second is intercalated as needed at the end and/or middle of the calendar year to keep UTC within 0.9 sec of UT1. Values for UTC-UT1 are calculated by the BIH from data of a large number of observatories and distributed monthly. The angular orientation of the earth at any epoch can then be determined from Newcomb's formula and interpolation of the tabulated UTC-UT1 values.

C. Expressions for theoretical values of the VLBI observables

The expressions used for delay (τ) and delay rate ($\dot{\tau}$) in the CALC and VLBI3 programs are taken from Robertson (1975). The delay is defined as the interval of time measured by the physical station clocks between the arrival of a signal at station 2 of an interferometer and its arrival at station 1, i.e., $\tau = t(2) - t(1)$ where $t(2)$ and $t(1)$ are the respective observed arrival times. The following notation is used.

$\dot{}$ = first derivative with respect to coordinate time

$\ddot{}$ = second derivative with respect to coordinate time
 R = solar system barycentric position of the earth's center
 R_1 = geocentric position of first station
 R_2 = geocentric position of second station
 S = unit vector in the direction of the observed source
 τ_A = delay from propagation media
LPT = Long Period Terms from expression for CT

Then with the speed of light set to unity,

$$\tau_0 = (R_1 - R_2) \cdot S - [(\dot{R} + \dot{R}_2) \cdot S][(R_1 - R_2) \cdot S][1 - (\dot{R} + \dot{R}_2) \cdot S] \quad \text{II.C.1}$$

$$- \frac{1}{2} [(\ddot{R} + \ddot{R}_2) \cdot S][(R_1 - R_2) \cdot S]^2 + \tau_A$$

$$\tau = \tau_0 - \dot{R} \cdot [R_2 - R_1] - [\ddot{R} \cdot R_2 + \dot{R} \cdot \dot{R}_2] \tau_0 + (\text{LPT}) \tau_0 \quad \text{II.C.2}$$

$$\dot{\tau}_0 = (\dot{R}_1 - \dot{R}_2) \cdot S - [(\dot{R} + \dot{R}_2) \cdot S][(\dot{R}_1 - \dot{R}_2) \cdot S] \quad \text{II.C.3}$$

$$- [(\ddot{R} + \ddot{R}_2) \cdot S][(R_1 - R_2) \cdot S] + [(\dot{R}_1 - \dot{R}_2) \cdot S][(\dot{R} + \dot{R}_2) \cdot S]^2$$

$$+ 2[(R_1 - R_2) \cdot S][(\dot{R} + \dot{R}_2) \cdot S][(\ddot{R} + \ddot{R}_2) \cdot S]$$

$$- \frac{1}{2} [(\ddot{R} + \ddot{R}_2) \cdot S][(R_1 - R_2) \cdot S]^2$$

$$- [(\ddot{R} + \ddot{R}_2) \cdot S][(R_1 - R_2) \cdot S][(\dot{R}_1 - \dot{R}_2) \cdot S] + \dot{\tau}_A$$

$$\dot{\tau} = \frac{d\tau}{dAT} \quad \text{II.C.4}$$

$$= \dot{\tau}_0 - [\ddot{R} \cdot (R_2 - R_1) + \dot{R} \cdot (\dot{R}_2 - \dot{R}_1)](1 + \dot{\tau}_0) - [\dot{R} \cdot \ddot{R}_2] \dot{\tau}_0$$

It should be noted that the above expressions are derived

relativistically in the quasi-inertial fundamental VLBI reference frame and hence implicitly include the effects of annual, elliptic and diurnal aberration. The aberration caused by the earth's orbital velocity is accounted for exactly by use of the instantaneous velocity vector rather than a circular approximation. Since the day numbers conventionally used in reducing positions from apparent to mean place specifically ignore the small E-terms caused by orbital eccentricity, source positions derived from VLBI data will differ from conventional positions (conventional - VLBI) by (adapted from Mueller 1969)

$$(\Delta\alpha, \Delta\delta) = (\Delta C, \Delta D) E \quad \text{II.C.5}$$

where

$$\Delta C = e\chi \cos w_s \cos \epsilon \quad \text{II.C.6}$$

$$\Delta D = e\chi \cos w_s \quad \text{II.C.7}$$

$$E = \begin{pmatrix} \cos \alpha \sec \delta & \tan \epsilon \cos \delta - \sin \alpha \sin \delta \\ \sin \alpha \sec \delta & \cos \alpha \sin \delta \end{pmatrix} \quad \text{II.C.8}$$

α = right ascension

δ = declination

ϵ = true obliquity

w_s = longitude of perihelion

χ = aberration constant = 20.496 arcsec

e = earth's orbital eccentricity = 0.01673

The value of the elliptic aberration changes very slowly and does not exceed 0.343 arcsec.

In CALC and VLBI3 the complete expansions for τ and $\dot{\tau}$ are used. However, the station vectors R_1 and R_2 are computed operationally in the terrestrial reference frame rather than in the quasi-inertial solar system barycentric frame where the earth position vector R is computed. The various vectors are then added in a Euclidean rather than in a relativistic manner. The problem of correctly calculating the barycentric station vectors on a translating, rotating, gravitational earth is quite complicated. Some initial studies indicate that the discrepancy between Euclidean and relativistic addition affects the delay observable by less than 50 picoseconds. ESTIM uses only the first term from τ_0 and $\dot{\tau}_0$.

D. Models which determine the baseline orientation

The models which are related to the orientation of the baseline can be treated as simple coordinate rotations. These are precession, nutation, diurnal rotation, polar motion (or wobble), and diurnal polar motion. The baseline in the fundamental VLBI coordinate system is given by

$$B_{1950.0} = P N S D W B_{\text{terrestrial}} \quad \text{II.D.1}$$

where P is the precession matrix from mean equator and equinox of date to mean of 1950.0, N is the nutation matrix from conventional true equator and equinox of date to mean of date, S is the diurnal rotation matrix about the instantaneous spin axis, D is the diurnal polar motion

matrix, and W is the polar motion matrix from the CIO pole to the conventional spin axis. The application of these five rotation matrices gives the baseline components in fundamental 1950.0 VLBI coordinate system.

1. Precession

The precession matrix P transforms from the coordinate system of the mean equator and equinox of date to the system of the mean equator and equinox of 1950.0. P is given by (ESAENE 1961)

$$P = R_z(\zeta_0)R_y(-\theta)R_z(z) \quad \text{II.D.1.1}$$

where

$$\zeta_0 = (2304''.250 + 1''.396 t_0)t + 0''.302 t^2 + 0''.018 t^3 \quad \text{II.D.1.2}$$

$$z = \zeta_0 + 0''.791 t^2 + 0''.001 t^3 \quad \text{II.D.1.3}$$

$$\theta = (2004''.682 - 0''.853 t_0)t + 0''.426 t^2 + 0''.042 t^3 \quad \text{II.D.1.4}$$

$90^\circ - \zeta_0$ = right ascension of ascending node of the mean equator of date on the equator of 1950.0

$90^\circ + z$ = right ascension of ascending node of the mean equator of 1950.0 on the mean equator of date

θ = inclination of the mean equator of date with respect to the mean equator of 1950.0

t_0 = time between epoch 1900 Jan 0.5 and epoch 1950.0

t = time between epoch 1950.0 and epoch of observation

t_0, t in units of tropical centuries of 36524.21988 ephemeris days

1900 Jan 0.5 = Julian date 241 5020.0

1950.0 = Julian date 243 3282.423

The ESTIM program uses the coefficients given above. As implemented in the programs VLBI3 and CALC, the coefficients are reduced to epoch 1950.0 as follows (Ash 1972):

$$\zeta_0 = 2304''.948 \, t + 0''.302 \, t^2 + 0''.179 \, t^3 \quad \text{II.D.1.5}$$

$$z = 2304''.948 \, t + 1''.093 \, t^2 + 0''.0192 \, t^3 \quad \text{II.D.1.6}$$

$$\theta = 2004''.255 \, t - 0''.426 \, t^2 - 0''.0416 \, t^3 \quad \text{II.D.1.7}$$

The precession matrix is computed differently in the three programs. In ESTIM the time argument is UTC at the start of an observation. In VLBI3 the individual elements of the product rotation matrix

$$\begin{pmatrix} \cos \zeta_0 \cos \theta \cos z & \cos \zeta_0 \cos \theta \sin z & \cos \zeta_0 \sin \theta \\ -\sin \zeta_0 \sin z & +\sin \zeta_0 \cos z & \\ -\sin \zeta_0 \cos \theta \cos z & -\sin \zeta_0 \cos \theta \sin z & -\sin \zeta_0 \sin \theta \\ -\cos \zeta_0 \sin z & +\cos \zeta_0 \cos z & \\ -\sin \theta \cos z & -\sin \theta \sin z & \cos \theta \end{pmatrix} \quad \text{II.D.1.8}$$

are calculated using CT as the time argument. In CALC the individual rotation matrices are calculated using CT and then multiplied.

The partial derivative of the precession matrix with respect to the precession constant is derived from the following expressions (Lieske 1967).

$$\zeta_0 = [2304''.948 + \frac{1}{2}(h \cos \epsilon_0 - h_0 \cos \epsilon_{00})]t + 0''.302 t^2 + 0''.0179 t^3 \quad \text{II.D.1.9}$$

$$z = [2304''.948 + \frac{1}{2}(h \cos \epsilon_0 - h_0 \cos \epsilon_{00})]t + 1''.093 t^2 + 0''.0192 t^3 \quad \text{II.D.1.10}$$

$$\vartheta = [2004''.255 + (h \sin \epsilon_0 - h_0 \sin \epsilon_{00})]t - 0''.426 t^2 - 0''.416 t^3 \quad \text{II.D.1.11}$$

t = time between epoch 1950.0 and epoch of observation
in units of tropical centuries

h_0 = nominal value of the precession constant at epoch 1950.0
= 5026.75" per century

ϵ_{00} = nominal value of the mean obliquity of the ecliptic
at epoch 1950.0
= 23 deg 26' 44.84"

h = actual precession constant

ϵ_0 = actual mean obliquity

$$\frac{\partial \zeta_0}{\partial h} = \frac{\partial z}{\partial h} = \frac{t}{2} \cos \epsilon_0 \quad \text{II.D.1.12}$$

$$\frac{\partial \vartheta}{\partial h} = t \sin \epsilon_0 \quad \text{II.D.1.13}$$

VLBI3 calculates the partial derivative of the precession matrix with respect to the precession constant term by term. CALC calculates the partial derivative of each rotation matrix with respect to the

appropriate matrix multiplications. ESTIM does not calculate a partial derivative matrix.

2. Nutation

The nutation matrix N transforms from the coordinate system defined by the "true" equator and equinox of date to the system defined by the mean equator and equinox of date. The astronomical nutation series computed by Woolard (1953) assumes a rigid earth, in which case the spin axis and the angular momentum vector point in almost the same direction. The departure is never more than $0.0007''$ or 2 cm at the surface. For a deformable earth McClure (1973) calculates that the departure may be as much as 21 cm. External torques strictly speaking affect the motion of the angular momentum vector rather than the spin axis if the two differ. Woolard calculates the effect of both the Eulerian and luni-solar diurnal separation between the angular momentum and spin axes but drops the terms in preparing the final nutation tables. Hence, to be more correct, the conventional "true" equator should be described as the equator perpendicular to the slowly moving (with respect to the earth's surface) angular momentum vector. N is given by (Mueller 1969)

$$N = R_x(-\epsilon_0)R_z(\Delta\psi)R_x(\epsilon_0 + \Delta\epsilon) \quad \text{II.D.2.1}$$

where

$$\begin{aligned} \epsilon_0 &= \text{mean obliquity of date} \\ &= 84428''.26 - 46''.845 t - 0''.0059 t^2 - 0''.00181 t^3 \quad \text{II.D.2.2} \end{aligned}$$

$\Delta\epsilon$ = nutation in obliquity

$\Delta\psi$ = nutation in longitude

$\epsilon_0 + \Delta\epsilon$ = true obliquity of date

t in units of Julian centuries of 36525 days since 1900 Jan 0.5

There are 69 terms in Woolard's series for $\Delta\psi$ and 40 terms for $\Delta\epsilon$. For convenience the values are tabulated as functions of CT on the PEP ephemeris tape used by CALC and VLBI3 and are interpolated to the CT epoch of observation. CALC uses the three rotation matrices to compute the complete nutation matrix. ESTIM also uses the three matrices but computes only the two largest terms in Woolard's series. VLBI3 uses the following first order approximation for N:

$$\begin{pmatrix} 1 & \Delta\psi \cos \epsilon & \Delta\psi \sin \epsilon \\ -\Delta\psi \cos \epsilon & 1 & \Delta\epsilon \\ -\Delta\psi \sin \epsilon & -\Delta\epsilon & 1 \end{pmatrix} \quad \text{II.D.2}$$

The nutation constant ($9.210''$) is the largest term in Woolard's series for the nutation in obliquity (ESAENA 1961).

$$\Delta\epsilon = (9.210'' + 0.0001 t) \cos \Omega \dots \quad \text{II.D.2.4}$$

Ω = longitude of the mean ascending node of the lunar orbit
on the ecliptic measured from the mean equinox of date

$$\begin{aligned} &= 259^\circ 10' 59''.79 - 5 \text{ rotations} = 134^\circ 8' 31''.23 t \\ &\quad + 7''.48 t^2 + 0''.0080 t^3 \end{aligned} \quad \text{II.D.2.5}$$

t = time from 1900 Jan 0.5 in units of Julian centuries of

36525 days

The partial derivative of the nutation matrix with respect to the nutation constant is

$$R_x(-\epsilon_0)R_z(\Delta\psi) \begin{pmatrix} 0 & 0 & 0 \\ 0 & -\sin \epsilon & \cos \epsilon \\ 0 & -\cos \epsilon & -\sin \epsilon \end{pmatrix} \cos \Omega \quad \text{II.D.2.6}$$

where $\epsilon = \epsilon_0 + \Delta\epsilon$. The nutation partial derivative is not currently implemented.

3. Diurnal rotation

The diurnal rotation matrix S conventionally rotates from the terrestrial coordinate system aligned with the x-axis in the Greenwich meridian and the z-axis along the spin axis to the instantaneous celestial system defined by the x-axis aligned with the true equinox of date. If the spin axis and the angular momentum axis are collinear, the rotation involved is purely about the single z-axis. In the more precise model where the two vectors are not collinear, the rotation is about the spin axis. An additional rotational angle must be included to account for the difference between the coordinate system defined by the instantaneous spin axis and the system defined by the angular momentum vector (which defines the conventional true of date equator). For convenience and clarity, this additional rotation is included in the diurnal polar motion matrix and is discussed in section II.D.4.

The diurnal rotation matrix S is given by (ESAENA 1961)

$$S = R_z(-GAST) \quad \text{II.D.3.1}$$

where

$$\begin{aligned} GAST &= \text{Greenwich apparent sidereal time} \\ &= \text{Greenwich mean sidereal time at 0hr UT} \quad \text{II.D.3.2} \\ &\quad + W_d UT1 + \Delta\psi \cos \epsilon \end{aligned}$$

$$GMST = 6 \text{ hr } 38 \text{ min } 45.836 \text{ sec} + 8640184.542 \text{ sec } t + 0.0929 \text{ sec } t^2 \quad \text{II.D.3.3}$$

$$W_d = 1.00273 79092 65 + 0.589 \cdot 10^{-6} t \text{ (sidereal sec per UT sec)} \quad \text{II.D.3.4}$$

t = time since 1900 Jan 0.5 in units of Julian centuries

$$UT1 = UTC - (UTC - UT1) \quad \text{II.D.3.5}$$

$\Delta\psi$ = nutation in longitude

ϵ = true obliquity of date

= mean obliquity of date + nutation in obliquity

$$= \epsilon_0 + \Delta\epsilon$$

GMST and W_d are calculated with 0 hr UTC as the time argument. In VLBI3 UTC - UT1 is calculated through a series of differences: A1 - UTC, TAI - A1, and TAI - UT1. TAI is International Atomic Time coordinated by the BIH. A1 - UTC is now a stepwise function which is changed periodically by 1 second as UTC is adjusted to stay with 0.9 sec of UT1. TAI - A1 is fixed at -0.3439 sec. TAI - UT1 is interpolated to the epoch of observation from five day tabular values distributed as circular D of the BIH. CALC uses the difference

UTC - UT1 interpolated from circular D. ESTIM ignores the UTC - UT1 offset in the observation geometry. $\Delta\psi \cos \epsilon$ is the equation of the equinoxes and represents the difference between mean and apparent sidereal time. $\Delta\psi$ is tabulated on the PEP ephemeris tape used by VLB3 and CALC. ESTIM uses a truncated time series for $\Delta\psi$ in which only the largest term appears (ESAENA 1961):

$$\Delta\psi = -(17''.2327 - ''01737 t) \sin \Omega \quad \text{II.D.3.6}$$

t = time since 1900 Jan 0.5 in units of Julian centuries

The partial derivative of the diurnal rotation matrix with respect to the UTC - UT1 offset is given by

$$\begin{pmatrix} -\sin(\text{GAST}) & \cos(-\text{GAST}) & 0 \\ -\cos(\text{GAST}) & -\sin(-\text{GAST}) & 0 \\ 0 & 0 & 0 \end{pmatrix} \omega_d \quad \text{II.D.3.7}$$

4. Diurnal polar motion

The diurnal polar motion matrix D transforms from the coordinate system defined by the slowly moving conventional spin pole to the system aligned with the instantaneous angular momentum pole. Two separate types of rotations are necessary. Rotations about the x-axis and y-axis translate the coordinate system z-axis from the slowly moving spin pole to the instantaneous angular momentum pole. A rotation about the z-axis corrects for the angular separation between the instantaneous spin pole and the instantaneous angular momentum

pole. Following the derivation shown in section III.C, D is given by

$$D = R_z(-\delta\psi \cos \epsilon) R_x(-(H_y + y_E)) R_y(H_x + x_E) \quad \text{II.D.4.1}$$

where

$\delta\psi$ = distance along the mean ecliptic of date from the equator
normal to the instantaneous angular momentum vector
to the equator normal to the instantaneous spin axis

ϵ = angle between the mean ecliptic of date and the
equator normal to the instantaneous angular momentum vector
= conventional true obliquity of date

H_x, H_y = position of the instantaneous angular momentum pole
with respect to the slowly varying spin pole

$$x_E = - \left(1 - \frac{A}{C}\right) \left(1 - \frac{k}{k_s}\right) x_{\text{slowly moving spin pole position}} \quad \text{II.D.4.2}$$

$$y_E = - \left(1 - \frac{A}{C}\right) \left(1 - \frac{k}{k_s}\right) y_{\text{slowly moving spin pole position}} \quad \text{II.D.4.3}$$

C = largest principal moment of inertia
= 8.040+44 gm-cm²

A = smaller principal moment of inertia
= 8.013+44 gm-cm²

k = tidal effective Love number
= 0.29

k_s = secular Love number
= 0.937

It should be noted that the conventional spin pole position is reported in a left-handed coordinate system by the BIH and that all the above expressions apply to a right-handed coordinate system. Therefore

$y(\text{slowly varying}) = -y(\text{BIH}).$

The seven largest of the 135 terms in the time series for H and $\delta\psi$ calculated by McClure (1973) are listed in table II.1. The error in neglecting the remainder of the terms is at most 0.0006". The sine series for H gives the x-component. The cosine series gives the y-component. $\delta\psi \sin \epsilon$ is computed from a sine series. The astronomical arguments for the series are the same as for H except that the P argument of Greenwich mean sidereal time is dropped. CALC computes the diurnal polar motion matrix D given above. ESTIM ignores diurnal polar motion in computing the observation geometry. VLBI3 calculates the quantities H and $\delta\psi \cos \epsilon$ and adjusts the conventional wobble values and apparent sidereal time.

$$\text{WOBX}_{\text{corrected}} = \text{WOBX} + (H_x + x_E) \quad \text{II.D.4.4}$$

$$\text{WOBY}_{\text{corrected}} = \text{WOBY} - (H_y + y_E) \quad \text{II.D.4.5}$$

$$\text{GAST}_{\text{corrected}} = \text{GAST} + \delta\psi \cos \epsilon \quad \text{II.D.4.6}$$

The negative sign in WOBY is required by the left-handed BIH system.

The diurnal polar motion scaling parameter is a multiplicative factor scaling the diurnal polar motion rotation matrix. It is discussed further in section III.C. The partial derivative of the diurnal polar motion matrix with respect to the scaling factor is, to first order,

Table II.1 Diurnal angular momentum polar motion coefficients

| Tidal argument code number | Coefficients of | | | | | | Coefficient for H | Coefficient for $\delta\psi \sin\epsilon$ |
|-------------------------------|-----------------|----|----|----|---|----|----------------------|--|
| | P | l | l' | F | D | O | | |
| 135.655 | 1 | -1 | 0 | -2 | 0 | -2 | -.0009149 | .00038502 |
| 145.545 | 1 | 0 | 0 | -2 | 0 | -1 | -.0008659 | .00041647 |
| 145.555 | 1 | 0 | 0 | -2 | 0 | -2 | -.0045924 | .00201046 |
| 163.555 | 1 | 0 | 0 | -2 | 2 | -2 | -.0019980 | .00093797 |
| 165.555 | 1 | 0 | 0 | 0 | 0 | 0 | .0019037 | -.00086146 |
| 165.555 | 1 | 0 | 0 | 0 | 0 | 0 | .0040934 | -.00185233 |
| 165.565 | 1 | 0 | 0 | 0 | 0 | -1 | .0008113 | -.00042084 |

P = Greenwich mean sidereal time

l = 296.10460 8 + 13.06499 24465 d + .00068 90 D2 + .00000 0295 D3 deg

l' = 358.47583 3 + .98560 02669 d - .00001 12 D2 - .00000 0068 D3 deg

F = 11.25088 9 + 13.22935 04490 d - .00024 07 D2 - .00000 0007 D3 deg

D = 350.73748 6 + 12.19074 91914 d - .00010 76 D2 + .00000 0039 D3 deg

O = 259.18327 5 - .05295 39222 d + .00015 57 D2 + .00000 0046 D3 deg

d = days since 1900 Jan 0.5

D = units of 10000 days since 1900 Jan 0.5

D2 = D²₃

D3 = D³₃

$$\begin{pmatrix} 0 & -\delta\psi \cos \epsilon & -(H_x + x_E) \\ \delta\psi \cos \epsilon & 0 & -(H_y + y_E) \\ H_x + x_E & H_y + y_E & 0 \end{pmatrix} \quad \text{II.D.4.7}$$

CALC computes the partial derivative by dividing all the terms of D by the scaling parameter and setting the diagonal terms to zero. ESTIM and VLBI3 calculate the first order derivative matrix directly.

5. Polar motion

The polar motion matrix W transforms from the CIO terrestrial system to the system with the z-axis aligned with the slowly moving spin pole. W is given by

$$W = R_x(-y_s)R_y(x_s) \quad \text{II.D.5.1}$$

where x_s and y_s are the angular displacements of the spin axis from the CIO pole as measured in the right-handed geographic coordinate system. The values are interpolated from the five day tabular points contained in the BIH circular D. Since the BIH uses a left-handed coordinate system for $x(\text{BIH})$ and $y(\text{BIH})$, the sign of the y-component must be changed. CALC forms the matrix

$$W = R_x(+y_{\text{BIH}})R_y(+x_{\text{BIH}}) \quad \text{II.D.5.2}$$

VLBI3 uses the first order approximation:

$$\begin{pmatrix} 1 & 0 & -x_{BIH} \\ 0 & 1 & y_{BIH} \\ x_{BIH} & -y_{BIH} & 1 \end{pmatrix}$$

II.D.5.3

ESTIM ignores polar motion in calculating the observation geometry.

The partial derivative of the polar motion matrix with respect to the x and y spin pole displacements are $R_x(y_{BIH}) \frac{\partial R_y(x_{BIH})}{\partial x_{BIH}}$ and $\frac{\partial R_x(y_{BIH})}{\partial y_{BIH}} R_y(x_{BIH})$, respectively. CALC uses the product matrices to calculate the partial derivatives. ESTIM and VLBI3 use first order approximations:

$$\frac{\partial W}{\partial x_{BIH}} = \begin{pmatrix} 0 & 0 & -1 \\ 0 & 0 & 0 \\ 1 & 0 & 0 \end{pmatrix} = \frac{\partial W}{\partial x_s} \quad \text{II.D.5.4}$$

$$\frac{\partial W}{\partial y_{BIH}} = \begin{pmatrix} 0 & 0 & 0 \\ 0 & 0 & 1 \\ 0 & -1 & 0 \end{pmatrix} = -\frac{\partial W}{\partial y_s} \quad \text{II.D.5.5}$$

6. The time derivative of the coordinate transformations

The time derivative of the complete rotation matrix from terrestrial to the fundamental 1950.0 VLBI coordinate system is approximated by ignoring all time variations except for diurnal rotation about the spin axis.

$$\dot{\hat{S}} = \dot{\hat{R}}_z(-\text{GAST}) \frac{d\text{GAST}}{d\text{CT}} \quad \text{II.D.6.1}$$

$$\dot{\hat{R}}_z(-\text{GAST}) = \begin{pmatrix} -\sin(-\text{GAST}) & \cos(-\text{GAST}) & 0 \\ -\cos(-\text{GAST}) & -\sin(-\text{GAST}) & 0 \\ 0 & 0 & 0 \end{pmatrix} \quad \text{II.D.6.2}$$

CALC computes $d(\text{GAST})/d\text{CT}$ by

$$\frac{d\text{GAST}}{d\text{CT}} = W_d \frac{d\text{UT1}}{d\text{AT}} \frac{d\text{AT}}{d\text{CT}} + \frac{d\Delta\psi}{d\text{CT}} \cos \epsilon - \Delta\psi \sin \epsilon \frac{d\epsilon}{d\text{CT}} \quad \text{II.D.6.3}$$

W_d = diurnal rotation rate

$\frac{d\text{UT1}}{d\text{AT}}$ and $\frac{d\Delta\psi}{d\text{CT}}$ are computed by numerical differentiation of the tabulated quantities. $\frac{d\epsilon}{d\text{CT}}$ is calculated from the time series for ϵ assuming $\frac{dt}{d\text{CT}}$ is unity, where t is the conventional time argument. $\frac{d\text{AT}}{d\text{CT}}$ is computed by differentiating the expression for CT.

VLBI3 uses the expression

$$\frac{d\text{GAST}}{d\text{CT}} = W_d - W_d \frac{d(\text{UTC} - \text{UT1})}{d\text{CT}} + \frac{d\Delta\psi \cos \epsilon}{d\text{CT}} \quad \text{II.D.6.4}$$

where $\frac{d(\text{UTC} - \text{UT1})}{d\text{CT}}$ is found by numerical differentiation.

ESTIM uses $\frac{d\text{GAST}}{d\text{CT}} = W_d$

E. Perturbations of the observation geometry

The effects which perturb the simple geometric model are solid

earth tides, antenna structure, deflection caused by solar gravitation, and ocean loading.

1. Solid earth tides

The solid earth tides resulting from the lunar and solar tidal potentials modulate the positions of the VLBI observing stations. The topocentric tidal displacement is given by (Melchior 1966)

$$\begin{aligned} \Delta t &= (\Delta t_1, \Delta t_2, \Delta t_3) \\ &= \left(\frac{H}{g} U_t, \frac{L}{g \cos \phi} \frac{\partial U_t}{\partial \lambda}, \frac{L}{g} \frac{\partial U_t}{\partial \phi} \right) \end{aligned} \quad \text{II.E.1.1}$$

where t_1 , t_2 , and t_3 are linear displacements in the radial, eastward, and northward directions, H and L are the two Love numbers, λ is the site east longitude, and ϕ is the site geodetic latitude. g is the surface acceleration of gravity and U_t is the tidal potential.

The exact expression for U_t is given by

$$U_t = GM \left[\frac{1}{p} - \frac{\mathbf{R} \cdot \mathbf{A}}{r^3} - \frac{1}{r} \right] \quad \text{II.E.1.2}$$

where

p = distance from the site to the disturbing body

R = vector from the earth's center to the disturbing body

r = norm of R

A = vector from the earth's center to the site

G = gravitational constant

M = mass of the disturbing body

This expression includes implicitly all tidal harmonics and is used directly in the CALC program with the geocentric lunar and solar positions interpolated from the PEP ephemeris tape. The conventional development of the tidal potential explicitly separates the second degree and third degree harmonics, which are reduced by a factor of 60. Separate Love numbers are applied to each degree of harmonics. Since the tides of different harmonics have differing spatial characteristics, they are affected by different aspects of the earth's structure. The Love numbers which scale the tide are therefore also different. Application of the second order Love numbers to the exact expression, as is done in CALC, leads to a theoretical error which is of negligible practical importance. However, Love numbers estimated from this expression are consequently not strictly comparable to other data.

The partial derivatives of the tidal potential with respect to latitude and longitude necessary for calculating the horizontal displacements are given by

$$\frac{\partial U_t}{\partial(\phi, \lambda)} = GM \left(\frac{P \cdot \frac{\partial A}{\partial(\phi, \lambda)}}{p^3} - \frac{R \cdot \frac{\partial A}{\partial(\phi, \lambda)}}{r^3} \right) \quad \text{II.E.1.3}$$

$$\begin{aligned} P &= \text{vector from the site to the disturbing body} \\ &= R - A \end{aligned}$$

In the terrestrial coordinate system the cartesian coordinates of the

site are given by

$$\begin{aligned} (c_1, c_2, c_3) &= A && \text{II.E.1.4} \\ &= \{(N+h)\cos\phi\cos\lambda, (N+h)\cos\phi\sin\lambda, (N[1-e^2]+h)\sin\phi\} \end{aligned}$$

where

$$\begin{aligned} N &= \text{radius of curvature in the prime vertical} \\ &= R_e (1 - e^2 \sin^2\phi)^{-1/2} && \text{II.E.1.5} \end{aligned}$$

R_e = equatorial radius of the earth = 6378.145 km

e^2 = square of the ellipsoid eccentricity = $6.716912701 \times 10^{-3}$

h = site height above the ellipsoid

Then,

$$\begin{aligned} \frac{\partial(c_1, c_2, c_3)}{\partial\phi} &= (-c_3 \cos\lambda, -c_3 \sin\lambda, R_e \cos\phi) && \text{II.E.1.6} \\ &\text{ignoring second order terms} \end{aligned}$$

$$\frac{\partial(c_1, c_2, c_3)}{\partial\lambda} = (-c_2, c_1, 0) \quad \text{II.E.1.7}$$

are the necessary derivatives of A with respect to latitude and east longitude. The tidal displacements can be transformed from the topocentric to the terrestrial coordinate system by

$$(\Delta c_1, \Delta c_2, \Delta c_3) = R_z(-\lambda)R_y(\phi)(\Delta t_1, \Delta t_2, \Delta t_3) \quad \text{II.E.1.8}$$

and to the 1950.0 VLBI reference frame by

$$(\Delta x, \Delta y, \Delta t) = \text{PNSDW}(\Delta c_1, \Delta c_2, \Delta c_3)$$

II.E.1.9

The tidal displacements at the epoch of observation are added to the fixed site coordinates to give the instantaneous site coordinates in the fundamental VLBI coordinate system.

The additional site velocity due to tidal distortions is given by

$$(\Delta t_1, \Delta t_2, \Delta t_3) = \left(\frac{H}{g} \dot{U}_t, \frac{L}{g \cos \phi} \frac{\partial \dot{U}_t}{\partial \lambda}, \frac{L}{g} \frac{\partial \dot{U}_t}{\partial \phi} \right) \quad \text{II.E.1.10}$$

$$\dot{U}_t = \text{GM} \left[-\frac{P \cdot \dot{P}}{p^3} + \frac{R \cdot \dot{R} - \dot{R} \cdot A - R \cdot \dot{A}}{r^3} + \frac{3(R \cdot A)(R \cdot \dot{R})}{r^5} \right] \quad \text{II.E.1.11}$$

$$\frac{\partial \dot{U}_t}{\partial (\phi, \lambda)} = \text{GM} \left[\frac{P \cdot \frac{\partial \dot{A}}{\partial (\phi, \lambda)} + \dot{P} \cdot \frac{\partial A}{\partial (\phi, \lambda)}}{p^3} - \frac{3 P \cdot \frac{\partial A}{\partial (\phi, \lambda)}}{p^5} (P \cdot \dot{P}) \right. \\ \left. - \frac{R \cdot \frac{\partial \dot{A}}{\partial (\phi, \lambda)} + R \cdot \frac{\partial A}{\partial (\phi, \lambda)}}{r^3} + \frac{3 R \cdot \frac{\partial A}{\partial (\phi, \lambda)}}{r^5} (R \cdot \dot{R}) \right] \quad \text{II.E.1.12}$$

The time derivative of the vector from the earth's center to the site is found by

$$\dot{A} = \text{PNSDW}(c_1, c_2, c_3) \quad \text{II.E.1.13}$$

while the lunar and solar time derivatives are interpolated from the PEP ephemeris tape.

The earth tide model used in ESTIM and VLBI3 is based on the

harmonic expansion of the tidal potential of Melchior (1966). Only the eleven largest terms are used.

$$\begin{aligned}
 U_t = K[& \cos^2 \phi \{ a_1 \cos(2H_l + p_1) + a_2 \cos(2H_l - \mu + w + p_2) \\
 & + a_3 \cos(2H_s + p_3) + a_4 \cos(2[S + \lambda] + p_4) \} \\
 & + \sin 2\phi \{ a_5 \cos(S + \lambda + p_5) + a_6 \cos(H_l - \mu + p_6) \\
 & + a_7 \cos(H_s - \sigma + p_7) \} \\
 & - \left(\frac{3}{2} \sin^2 \phi - \frac{1}{2} \right) \{ a_8 + a_9 \cos(\mu - w) + a_{10} \cos 2\mu \\
 & + a_{11} \sin 2\sigma \}]
 \end{aligned}
 \tag{II.E.1.14}$$

where

$$K = 26.7 \text{ cm}$$

| | |
|------------------|-------------------------|
| $a_1 = 0.908$ | $p_1 = 0$ |
| $a_2 = 0.174$ | $p_2 = 0$ |
| $a_3 = 0.423$ | $p_3 = 0$ |
| $a_4 = 0.115$ | $p_4 = 0$ |
| $a_5 = 0.531$ | $p_5 = -90 \text{ deg}$ |
| $a_6 = 0.377$ | $p_6 = +90 \text{ deg}$ |
| $a_7 = 0.176$ | $p_7 = +90 \text{ deg}$ |
| $a_8 = 0.739$ | |
| $a_9 = 0.083$ | |
| $a_{10} = 0.156$ | |
| $a_{11} = 0.073$ | |

S = Greenwich sidereal time

$$H_l = \text{lunar hour angle} = S - \mu + \lambda \tag{II.E.1.15}$$

$$H_s = \text{solar hour angle} = S - \sigma + \lambda \tag{II.E.1.16}$$

λ = site east longitude

μ = mean longitude of the moon

$$= 4.719967 + 8399.709 t \quad (\text{radians}) \quad \text{II.E.1.17}$$

σ = mean longitude of the sun

$$= 4.881628 + 628.3319 t \quad (\text{radians}) \quad \text{II.E.1.18}$$

w = longitude of the lunar perigee

$$= 5.835152 + 71.01803 t \quad (\text{radians}) \quad \text{II.E.1.19}$$

t = time in Julian centuries since 1900 Jan 0.5

The values of the Love numbers H and L used in VLBI3 are 0.584 and 0.045, respectively (Melchior 1966, p. 300). CALC uses Love numbers derived by Dahlen (1976) from seismic earth models: 0.60967 for H and 0.085 for L . ESTIM does not correct the geometry for solid earth tides.

Since the Love numbers are simply scaling factors for the tidal displacements, the partial derivatives in the topocentric system are simple.

$$\frac{\partial \Delta t}{\partial H} = \left(\frac{U_t}{g}, 0, 0 \right) \quad \text{II.E.1.20}$$

$$\frac{\partial \Delta t}{\partial L} = \left(0, \frac{1}{g \cos \phi} \frac{\partial U_t}{\partial \lambda}, \frac{1}{g} \frac{\partial U_t}{\partial \phi} \right) \quad \text{II.E.1.21}$$

The partial derivatives of the delay observable with respect to the Love numbers is then

$$\frac{\partial \tau}{\partial H} = -(PNSDW)R_z(-\lambda)R_y(\phi) \left(\frac{\Delta t_1(1) - \Delta t_1(2)}{H}, 0, 0 \right) \cdot S \quad \text{II.E.1.22}$$

$$\frac{\partial \tau}{\partial L} = -(PNSDW)R_z(-\lambda)R_y(\phi) \left(0, \frac{\Delta t_2(1) - \Delta t_2(2)}{L}, \frac{\Delta t_3(1) - \Delta t_3(2)}{L} \right) \cdot S \quad \text{II.E.1.23}$$

where (1) and (2) refer to station 1 and station 2 of an interferometer.

2. Antenna structure

The actual geometry of observation depends on the type of mount used by an antenna. Since the reference point defined to be the station location, i.e., the intersection of the telescope pointing axes (figure I.3), does not coincide with the point at which a time is associated with a received signal, i.e., at the feed horn where the phase calibrator is injected, there is a receiving time offset. The offset depends on the difference in signal travel time along two paths, one directly from the source to the reference point (the direct path), the other reflected (perhaps several times) from the dish surface to the feed horn. As the telescope points in various directions and is subject to different static loading, wind, and thermal distortions, the shape of the reflecting surface and the exact position of the feed in the ray path will change. The change in ray path is rather difficult to model but should not be more than a few centimeters. If the physical dish geometry is assumed to be completely rigid, the effect of different mounting systems can be simply modeled. If the pointing axes

of the telescope intersect, the path length difference between the direct path and the reflected path will be independent of source position and will be indistinguishable from a clock offset. If the axes do not intersect (figure I.4), the reference point is defined to be the intersection of the fixed axis with the plane perpendicular to the fixed axis containing the moving axis. There will then be a varying distance along the direct path given by $\Delta A = D \sin(\theta)$ where D is the axis offset and θ is the angle between the source and the fixed axis.

There are four commonly used axis configurations. In a topocentric (radial, eastward, northward) coordinate system, the fixed axis direction is given by $F =$

| | | |
|--------------------|----------------------------------|----------|
| equatorial | ($\sin \phi$, 0, $\cos \phi$) | II.E.2.1 |
| az-el | (1, 0, 0) | II.E.2.2 |
| x-y pointing north | (0, 0, 1) | II.E.2.3 |
| x-y pointing east | (0, 1, 0) | II.E.2.4 |

where p is the latitude of the telescope. The geometrical topocentric source unit vector is given by

$$S_t = [PNSDW R_z(-\lambda)R_y(\phi)]^{-1} S_{1950.0} \quad \text{II.E.2.5}$$

$$= (S_{t1}, S_{t2}, S_{t3})$$

Since the actual pointing direction is required, the geometric zenith angle must be corrected for refraction (Smart 1965).

z = geometrical zenith angle

$$= \frac{\pi}{2} - \sin^{-1} S_{tl} \quad \text{II.E.2.6}$$

z_c = refracted zenith angle

$$= z + 2.826172873 \cdot 10^{-4} \tan z \quad \text{II.E.2.7}$$
$$- 3.23855539 \cdot 10^{-7} \tan^3 z \quad (\text{radians})$$

Then

S_{tr} = topocentric unit vector to the refracted source position

$$= (\cos z_c, \sin z_c \sin a, \sin z_c \cos a) \quad \text{II.E.2.8}$$

where a is the source azimuth angle. The additional path length along the direct path is given by

$$\Delta A = D \sin \{ \cos^{-1} (F \cdot S_{tr}) \} \quad \text{II.E.2.9}$$

$$\Delta \dot{A} = \frac{-DF \cdot \frac{dS_{tr}}{dt}}{\tan \{ \cos^{-1} (F \cdot S_{tr}) \}} \quad \text{II.E.2.10}$$

D = axis offset

Then the effects on the delay and delay rate are

$$\Delta \tau = \frac{\Delta A(2) - \Delta A(1)}{c} \quad \text{II.E.2.11}$$

$$\Delta \dot{\tau} = \frac{\Delta \dot{A}(2) - \dot{A}(1)}{c} \quad \text{II.E.2.12}$$

where (2) and (1) refer to station 2 and station 1 of an interferometer. CALC uses the full algorithm given above. VLBI3 handles the equatorial and az-el cases only using specialized algorithms. ESTIM does not apply an axis offset correction to the geometry and neglects the refraction correction in calculating the partial derivative.

Since the axis offset acts as a scaling factor for the path length change, the partial derivatives of the delay and delay rate with respect to the axis offset at each site are

$$\frac{\partial \tau}{\partial D} = (+/-) \frac{\Delta A}{cD} \quad \text{II.E.2.13}$$

$$\frac{\partial \dot{\tau}}{\partial D} = (+/-) \frac{\Delta \dot{A}}{cD} \quad \text{II.E.2.14}$$

+ for station 2

- for station 1

3. Relativistic gravitational deflection

The gravitational potential of sun bends the path taken by signals coming from the source and consequently causes an apparent change in position. An expression is given by Shapiro (1967).

η = difference in angle of arrival

$$= (1 + \gamma) \frac{r_s}{r_e} \tan \frac{\theta}{2} \quad \text{II.E.3.1}$$

where

γ = bending parameter

= 1 for Einstein

r_s = gravitational radius of the sun

= $1.4766252 \times 3 \text{ m}$

r_e = heliocentric observer distance

θ = source - sun - observer angle

The correction applied to the source position by CALC is

$$\Delta S = \frac{(1 + \gamma) \frac{r_s}{r_e} \tan \frac{\rho}{2} [S \times (S \times R_s)]}{|S \times (S \times R_s)|} \quad \text{II.E.3.2}$$

where

$$\rho = \pi - \cos^{-1}(S \cdot R_s) \quad \text{II.E.3.3}$$

S = source position unit vector

R_s = geocentric sun position unit vector

$\frac{S \times (S \times R_s)}{|S \times (S \times R_s)|}$ defines a unit vector in the plane containing the source and sun vectors perpendicular to the source vector and pointing away

from the sun. The effect on the delay and delay rate is

$$\Delta \tau = \frac{-B \cdot \Delta S}{c} \quad \text{II.E.3.4}$$

$$\Delta \dot{\tau} = \frac{-B \cdot \Delta \dot{S}}{c} \quad \text{II.E.3.5}$$

where B is the baseline vector.

The partial derivatives of delay and rate with respect to the deflection parameter are the effects divided by $1 + \gamma$.

4. Ocean loading

The algorithm for ocean loading is not yet implemented.

For the O1 and M2 ocean tides, the amplitude of ocean loading displacement and phase lag relative to the corresponding solid earth tides can be calculated for a specific site using the methods of Farrell (1970). Two assumptions must be made to extend these results to other tidal components. First, the response of the earth is assumed to be identical for all tidal components in a given frequency band, either diurnal or semidiurnal. Second, the ocean tide components other than O1 and M2 are assumed to scale as the corresponding solid earth tides. With these two assumptions the ocean loading displacement for a given site and epoch can be calculated. For each frequency band the effect of other (not O1 or M2) tidal components is found by scaling the amplitudes relative to either O1 or M2 by the corresponding solid earth tide amplitudes. The phase lag is assumed to be the same as for O1 or M2, depending on the frequency band. With the scaled amplitude and calculated phase lag, the displacement effect for a given site and epoch for each tidal component can be computed from the corresponding solid earth tide component. The total ocean loading displacement at a particular site and epoch is found by summing the effects from the individual tidal components.

F. Propagation medium models

There are two models which are directly related to the signal delay caused by the propagation medium, the atmosphere and ionosphere models. The effect of the corona is modeled somewhat differently.

1. Atmosphere

The atmosphere contributes two components to the refractivity and hence to propagation delay: a dry term from the displacement polarization of all the air molecules and a wet term from the dipole moment of the water molecules. The additional path length arising from the dry term is strictly proportional to the surface pressure (Moran 1976).

$$L_d = 77.6 R/gm P_0 \text{ (cm)}$$

II.F.1.1

where

R = universal gas constant = 8.3144+7 erg/mole

g = local acceleration of gravity (cm/sec^2)

m = molecular weight of dry air = 28.966

P_0 = dry component pressure millibars

= total pressure - partial pressure of water vapor

The wet term path length depends on the integrated water vapor content along the line of sight. Since the water vapor is not well mixed in the atmosphere, this contribution is difficult to estimate

from surface data. Studies done with microwave radiometers measuring the brightness temperatures at 19 GHz and 22 GHz indicate that the wet term path length can be measured to 0.4 cm (Moran 1976). The magnitude is approximately 1% to 15% of the dry component.

A modified cosecant law is used in both CALC and VLBI3 to scale the zenith path length to other elevation angles.

$$L = \frac{L_z}{\sin \theta} \frac{0.00143}{\tan \theta + 0.0045} \quad \text{II.F.1.2}$$

where

L_z = zenith path length

= 7 nsec nominal

θ = elevation angle

$$= \sin^{-1} S_{t1} \quad \text{II.F.1.3}$$

S_t = topocentric source unit vector

The constants are best fit values from ray tracing through a standard atmosphere (Chic 1970).

ESTIM user a simple cosecant law: $L = \frac{L_z}{\sin \theta}$

The time derivative of the atmosphere delay is

$$\dot{L} = -\frac{L^2}{L_z} \dot{\theta} \left[\cos \theta - \frac{.00143}{[(\tan \theta + .0045) \cos \theta]^2} \right] \quad \text{II.F.1.4}$$

$$\dot{\theta} = \frac{\dot{s}_{t1}}{\cos \theta} \quad \text{II.F.1.5}$$

Then the effects on delay and delay rate are

$$\Delta\tau = \frac{L(2) - L(1)}{c} \quad \text{II.F.1.6}$$

$$\Delta\dot{\tau} = \frac{\dot{L}(2) - \dot{L}(1)}{c} \quad \text{II.F...7}$$

where (2) and (1) refer to station 2 and station 1 of an interferometer.

Since the zenith path length is a simple scaling factor, the partial derivative of the observables with respect to the atmosphere parameter is the modeled effect on the observable divided by the parameter value with the appropriate sign (+ for station 2, - for station 1).

2. Ionosphere

The ionosphere has not been successfully modeled. While the ionosphere path delay may vary by a factor of ten from day to night, the total effect at X band is no more than 10% of the dry atmosphere path length. In past analyses of VLBI data part or all of the ionosphere has been absorbed into the atmosphere zenith path length adjustment. A model requiring dual frequency data has been implemented but the available data at a second frequency have not been good enough to be useful.

Since the charged particle path length is given by

$$\tau_{\text{ion}} = \frac{k}{f^2} \quad \text{II.F.2.1}$$

where

k = charged particle scaling factor

f = observing frequency

then,

$$\tau_1 = \tau_{\text{geometric}} + \frac{k}{f_1^2} \quad \text{II.F.2.2}$$

$$\tau_2 = \tau_{\text{geometric}} + \frac{k}{f_2^2} \quad \text{II.F.2.3}$$

τ_1, τ_2 = observed delays at two frequencies f_1 and f_2

$$\tau_1 - \tau_2 = k \left(\frac{1}{f_1^2} - \frac{1}{f_2^2} \right) \quad \text{II.F.2.4}$$

$$k = (\tau_1 - \tau_2) \frac{(f_1 f_2)^2}{f_1^2 - f_2^2} \quad \text{II.F.2.5}$$

Therefore,

$$\tau_{\text{geometric}} = \tau_1 - \frac{\tau_1 - \tau_2}{1 - \left(\frac{f_1}{f_2}\right)^2} \quad \text{II.F.2.6}$$

This new delay should be free of all effects caused by charged particles in the line of sight to the observed source. Both ionospheric and coronal effects should be removed.

3. Corona

The corona is also a propagation medium effect. However, it is presently treated as a change in the apparent position of the source rather than an additional delay. The model implemented in CALC and VLBI3 is included for completeness but is invariably not used since almost all VLBI observations are some distance from the sun.

$$\Delta S = \left(\frac{a}{I^2} + \frac{b}{I^6} \right) \left(\frac{1}{f^2} \right) \frac{S \times (S \times R_s)}{|S \times (S \times R_s)|} \quad \text{II.F.3.1}$$

where

ΔS = change in apparent position

a, b = parameters of electron density

f = observing frequency

I = impact parameter in units of solar radii

$$= \frac{r_e \sin \rho}{S}$$

II.F.3.2

$$\rho = \pi - \cos^{-1}(S \cdot R_s)$$

S = source position unit vector

R_s = geocentric sun position unit vector

The sign of the correction is positive for group delay and negative for phase delay.

G. Derivatives with respect to site and source coordinates

1. Site coordinate derivatives

The partial derivatives of the observables with respect to cartesian site coordinates are particularly simple.

$$\frac{\partial \tau}{\partial \mathbf{x}} = - \left(\text{PNSDW} \frac{\partial \mathbf{B}}{\partial \mathbf{x}} \right) \cdot \mathbf{s} \quad \text{II.G.1.1}$$

$$\frac{\partial \dot{\tau}}{\partial \mathbf{x}} = - \left(\text{PNSDW} \frac{\partial \mathbf{B}}{\partial \mathbf{x}} \right) \cdot \mathbf{s} \quad \text{II.G.1.2}$$

$$\frac{\partial \mathbf{B}}{\partial x_1} = (+/-)(1, 0, 0) \quad \text{II.G.1.3}$$

$$\frac{\partial \mathbf{B}}{\partial x_2} = (+/-)(0, 1, 0) \quad \text{II.G.1.4}$$

$$\frac{\partial \mathbf{B}}{\partial x_3} = (+/-)(0, 0, 1) \quad \text{II.G.1.5}$$

where (x_1, x_2, x_3) are the cartesian terrestrial coordinates and \mathbf{B} is the baseline vector. The sign is determined by whether the site is the second or first station of the baseline. This formulation appears in CALC and ESTIM.

The partial derivatives of the baseline with respect to cylindrical coordinates are given by

$$\frac{\partial \mathbf{B}}{\partial \mathbf{r}} = \left(\frac{x_1}{r}, \frac{x_2}{r}, 0 \right) \quad \text{II.G.1.6}$$

$$\frac{\partial B}{\partial \lambda} = \{ (+/-)x_2, x_1, 0 \} \quad \text{II.G.1.7}$$

$$\frac{\partial B}{\partial z} = (0, 0, 1) \quad \text{II.G.1.8}$$

where

r = cylindrical radius

λ = (west/east) longitude

z = polar coordinate

x_1, x_2 = cartesian coordinates

The cylindrical derivatives are used in VLBI with west longitude.

They also appear in ESTIM using east longitude to maintain a right-handed system.

2. Source position derivatives

The partial derivatives of the observables with respect to source right ascension (α) and declination (δ) are

$$\frac{\partial r}{\partial(\alpha, \delta)} = -PNSDWB \cdot \frac{\partial S}{\partial(\alpha, \delta)} \quad \text{II.G.2.1}$$

$$\frac{\partial \dot{r}}{\partial(\alpha, \delta)} = -PNSDWB \cdot \frac{\partial \dot{S}}{\partial(\alpha, \delta)} \quad \text{II.G.2.2}$$

$$\frac{\partial S}{\partial \delta} = \begin{pmatrix} -\sin \delta \cos \alpha \\ -\sin \delta \sin \alpha \\ \cos \delta \end{pmatrix} \quad \text{II.G.2.3}$$

$$\frac{\partial S}{\partial \alpha} = \begin{pmatrix} -\cos \delta \sin \alpha \\ \cos \delta \cos \alpha \\ 0 \end{pmatrix}$$

II.G.2.4

Chapter III.

MEASUREMENT OF DIURNAL POLAR MOTION

The precision of recent interferometric data requires more accurate models of small effects in order to extract the most useful information. One effect which has not been extensively studied is diurnal polar motion. This chapter gives an estimate for magnitude of diurnal polar motion and discusses possible interpretations.

A. Nomenclature of polar motion

Because the subject of polar motion has suffered from confusing usage, a number of terms will be defined and described. Polar motion refers to the secular and periodic change in position of a pole with respect to the surface of the earth. A pole is a point on the surface usually defined by the intersection of an axis or vector with the surface. In contrast, astronomical nutation (hereafter simply nutation) is the periodic motion of vectors or axes in inertial space, in practice with respect to the "fixed" stars. While nutation and some polar motions arise from related causes, the points of view are quite different. Polar motion takes place in a rotating terrestrial reference frame. Nutation is seen in an inertial celestial reference frame.

There are three axes and four poles of interest. These are shown in figure III.1. PG, PF, PS, and PH are points on the surface. The

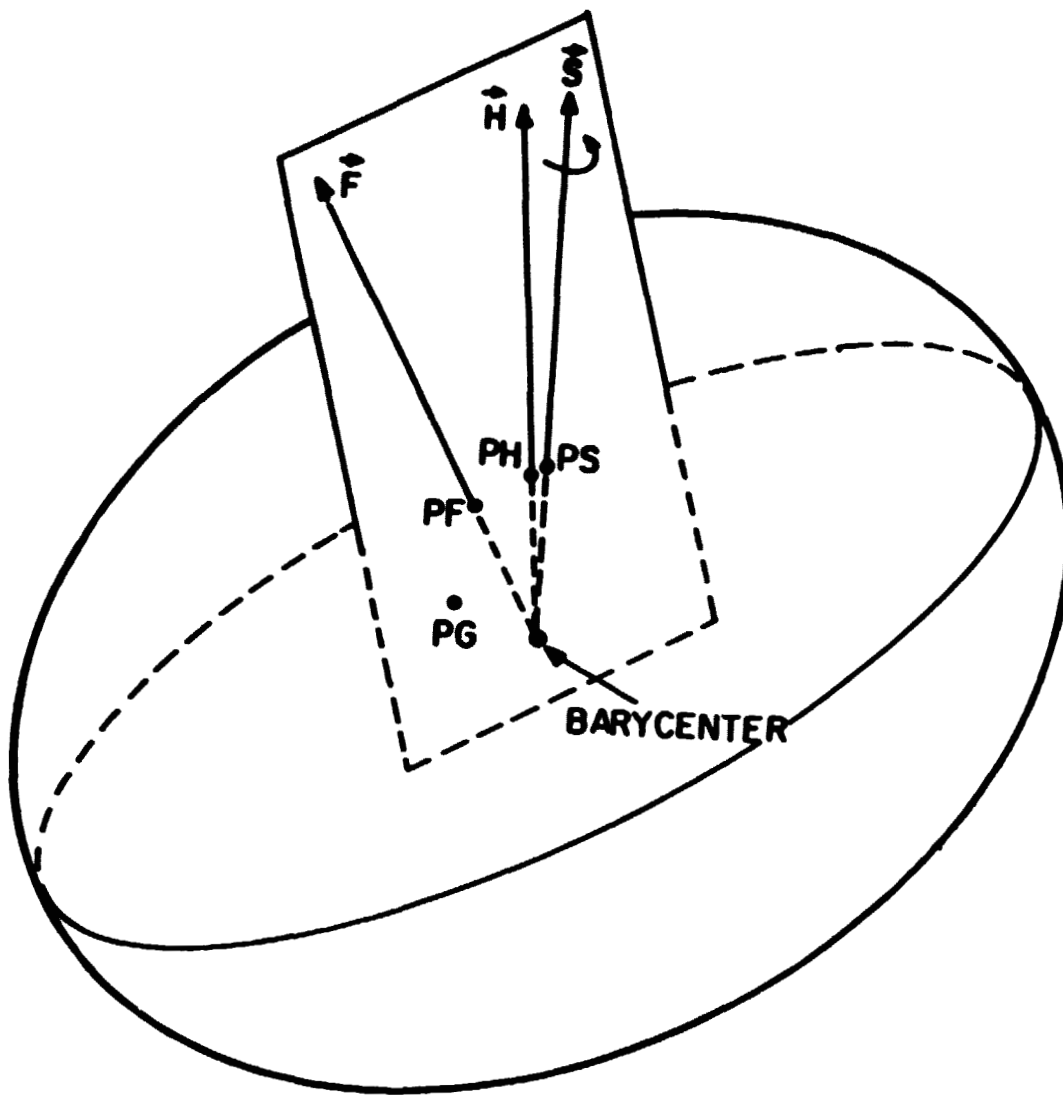


Fig. III.1 Poles and axes of the earth

JRH
10-77

geographic pole PG is an arbitrary point on the surface. By definition the geographic pole does not undergo polar motion. Through general acceptance it is a point determined by the International Latitude Service (now the International Polar Motion Service) which was the mean spin pole position from 1900 to 1905. The spin pole PS is the intersection of the surface with the instantaneous spin vector S. The terms spin vector and spin axis will be used somewhat interchangeably, the axis being the direction defined by the vector. At any instant, the points on the spin axis are stationary. All other points rotate about the spin axis with an angular velocity equal to the magnitude of S. The angular momentum pole PH is the intersection of the instantaneous angular momentum vector H with the surface. The angular momentum axis is likewise the direction of the angular momentum vector. The angular momentum is taken about the barycenter such that

$$H = \sum r \times mv \qquad \text{III.A.1}$$

where

r = vector from the barycenter to a mass element

m = mass of element

v = linear velocity of mass element

The principal axes of a body are the orthogonal directions which define a coordinate system in which the moment of inertia tensor is diagonal. For a oblate spheroid like the earth the moment of inertia is equal about two axes and larger about the third. The latter axis is called the axis of figure F. The intersection of the axis of figure and the surface is the pole of figure PF. All axes pass through the

barycenter. If otherwise unspecified, the terms axis and pole will mean any of the axes or poles described above.

At any instant a given pole has some displacement from some reference pole. The displacement can be expressed in cartesian or polar coordinates. The direction of pole displacement (or simply the pole direction) is the direction of the displacement vector. The magnitude of the displacement vector will be termed the magnitude of polar motion. Magnitude is usually given in angular units but may also be expressed in the linear equivalent at the surface. At a later instant the pole of interest will have a different displacement vector from the reference pole. The term direction of polar motion refers to the direction of change in displacement from one instant to the next.

Associated with each axis is an equator, the intersection of the surface with the plane perpendicular to the axis passing through the barycenter. The spin equator corresponds to the conventional definition of the true equator of date. The equator normal to the angular momentum axis will be called the dynamical equator. The equator of the axis of figure will be called the equator of figure or, less rigorously, the terrestrial equator. In the celestial reference frame an equator is the intersection of the specified equatorial plane with the celestial sphere.

Polar motion falls into two ranges of periods, approximately one day and a year or longer. The latter will be called long period motion or wobble. There are two distinguishable components of long period

motion, annual and Eulerian. The annual component is related to continuous redistribution of mass in meteorological and geophysical processes. Eulerian or Chandler motion is the polar motion that occurs in the absence of external torques. In the following discussion the annual long period motion is ignored. The position of the spin pole along the path of long period motion as determined from data spanning and averaged over several days will be called the slowly moving pole position. In the general literature the unqualified term polar motion means this motion of the slowly moving pole.

Diurnal polar motion is the motion of the spin, angular momentum, or figure pole with periods close to one day. It has been referred to as Oppolzer terms and dynamical variation in latitude, the first from the earliest mathematical expression, the latter from a resultant effect.

The latitude of an observatory is the angle between the local vertical or normal and an equatorial plane. The astronomic latitude, for example, is defined by the plumb line vertical and the spin equatorial plane. The declination of a source is the complement of the angle between the source and the spin axis as seen in the celestial reference frame. Since polar motion reflects a change in the direction of an axis with respect to the surface on which the observatory is fixed, polar motion usually causes a change in latitude. No latitude change occurs when the direction of polar motion is normal to the plane containing the old axis and the observatory. Polar motion taken in isolation has no direct effect on declination. As long as the spin

axis is unchanged in the celestial reference frame declinations remain the same. Declinations are, however, changed by nutation.

B. Causes and effects of diurnal polar motion

Diurnal polar motion is caused by lunar and solar torques acting on the equatorial bulge of the earth. The change in angular momentum caused by the torques manifests itself as precession and nutation when considered in the inertial celestial reference frame. In the rotating terrestrial reference frame the change in angular momentum is seen as diurnal polar motion.

The simplest case is that of a rigid, rotating, oblate spheroid inclined with respect to a perturbing body. Consider a body-fixed coordinate frame aligned with the principal axes. Let z be along the axis of figure and let x and y form a right-handed system. The moment of inertia is then

$$I = \begin{pmatrix} A & 0 & 0 \\ 0 & A & 0 \\ 0 & 0 & C \end{pmatrix} \quad \text{III.B.1}$$

where $A < C$. Suppose that the perturbing body is in the northern hemisphere at a position $R(r, \theta, \phi)$, where r is the radial distance, θ is the longitude, and ϕ is the co-latitude. Suppose also that the distance, co-latitude, and mass of the perturbing body and the moments of inertia of the spheroid are such that the resulting precession is

much slower than the spheroid's rotation. Then both r and ϕ are essentially constant. θ changes at a constant rate as the perturbing body moves around (as seen in the rotating body-fixed reference frame). The force on the equatorial bulge from the perturbing body is given by

$$F = \nabla V \quad \text{III.B.2}$$

where V is the gravitational potential of the spheroid. Since the perturbing body is in the northern hemisphere, the force is upward.

$$F = F \hat{k} \quad \text{III.B.3}$$

where

$$\hat{i}, \hat{j}, \hat{k} = \text{unit vectors in the body-fixed system}$$

The torque is

$$\begin{aligned} L &= R \times F & \text{III.B.4} \\ &= f R \sin \theta \hat{i} \\ &= f \sin \theta \hat{i} - f \cos \theta \hat{j} + 0 \hat{k} \end{aligned}$$

$$f = 3GM(C-A) \frac{z}{r^5}$$

G = gravitational constant

M = mass of perturbing body

z = distance of perturbing body above equatorial plane of figure

$$\theta = \omega t$$

ω = angular frequency of the perturbing body

= -(angular frequency of the spheroid)

Applying Euler's equations,

$$L_1 = I_{11}\dot{\omega}_1 + (I_{33} - I_{22})\omega_2\omega_3 \quad \text{III.B.5}$$

$$L_2 = I_{22}\dot{\omega}_2 + (I_{11} - I_{33})\omega_3\omega_1$$

$$L_3 = I_{33}\dot{\omega}_3 + (I_{22} - I_{11})\omega_1\omega_2$$

where

L_1, L_2, L_3 = components of torque

$\omega_1, \omega_2, \omega_3$ = components of angular velocity or spin

$\dot{\omega}_1, \dot{\omega}_2, \dot{\omega}_3$ = time derivatives of $\omega_1, \omega_2, \omega_3$

Then,

$$f \sin \omega t = A\dot{\omega}_1 + (C - A)\omega_2\omega_3 \quad \text{III.B.6a}$$

$$-f \cos \omega t = A\dot{\omega}_2 + (A - C)\omega_3\omega_1 \quad \text{III.B.6b}$$

$$0 = C\dot{\omega}_3 + (A - A)\omega_1\omega_2 \quad \text{III.B.6c}$$

From eq. III.B.6c ω_3 is constant. Differentiating eq. III.B.6a with respect to time,

$$f\omega \cos \omega t = A\ddot{\omega}_1 + (C - A)\dot{\omega}_2\omega_3 \quad \text{III.B.7}$$

$\ddot{\omega}_1$ = second time derivative of ω_1

From eq. III.B.6b

$$\dot{\omega}_2 = \frac{1}{A} [(C - A)\omega_3\omega_1 - f \cos \omega t] \quad \text{III.B.8}$$

Substituting $\dot{\omega}_2$ into III.B.7 and rearranging,

$$\ddot{\omega}_1 + \omega_1 \left[\omega_3 \left(\frac{C-A}{A} \right) \right]^2 = \frac{f}{A} \left[\omega_3 \left(\frac{C-A}{A} \right) + \omega \right] \cos \omega t \quad \text{III.B.9}$$

Eq. III.B.9 has the form of an undamped forced harmonic oscillator. The equation for ω_2 , the y-component of the spin vector, takes the same form. Consequently, the equations for the x and y-components of the spin vector indicate that the spin vector undergoes oscillatory motion about the axis of figure.

There are two components of this spin polar motion as shown in figure III.2. The smaller forced motion is superimposed on the larger free motion resulting in an epicyclical total polar motion. The axes are shifted to indicate the arbitrary nature of the geographic pole.

The free Eulerian motion has a frequency

$$\omega_0 = \omega_3 \frac{C-A}{A} \quad \text{III.B.10}$$

and an amplitude γ_0 that can only be determined from initial conditions. The period is 300 days for the rigid earth where $(C-A)/A$ is 0.0033. The direction of polar motion about the pole of figure is counterclockwise as viewed from the north.

The forced diurnal motion has a frequency ω and a spin amplitude of

Fig. III.2 Diurnal polar motion epicycle

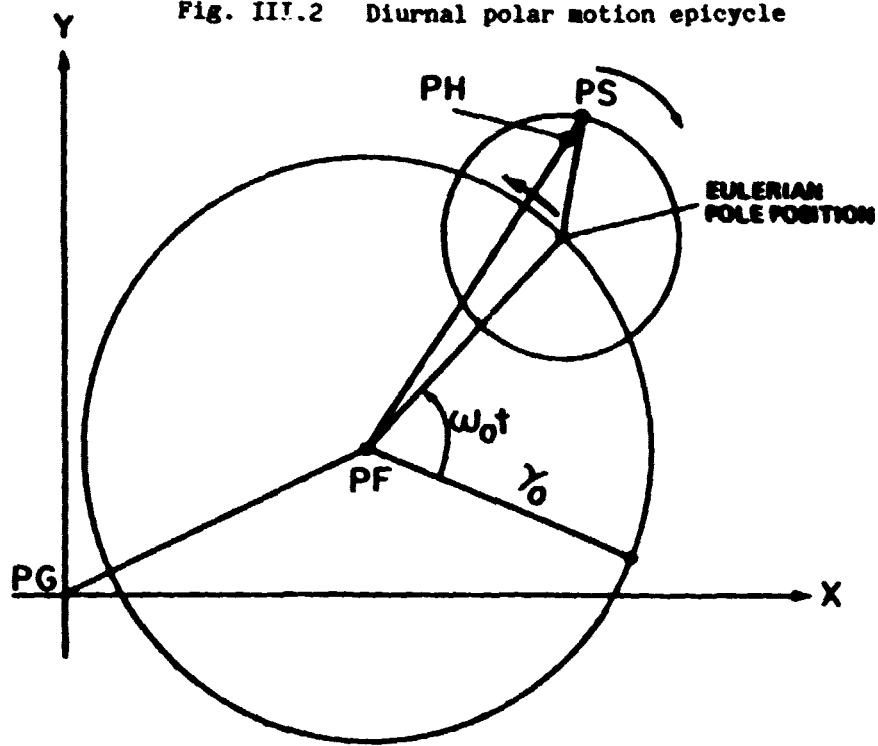
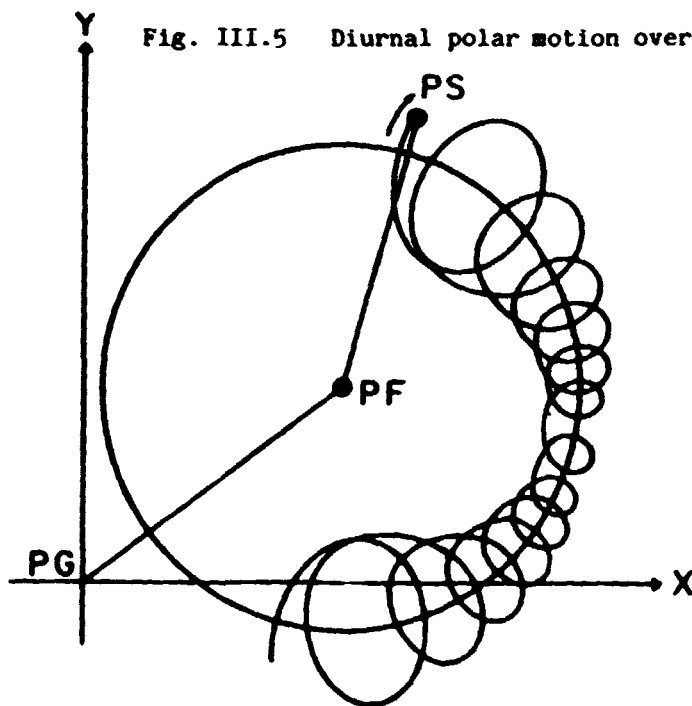


Fig. III.5 Diurnal polar motion over several days



$$S = \frac{f}{A\omega^2} \left[\omega_3 \left(\frac{C-A}{A} \right) + \omega \right] \quad \text{III.B.11}$$

Since $(C-A)/A \ll 1$ and ω_3 is essentially equal to ω , the amplitude reduces to

$$\begin{aligned} S &= \frac{f}{A\omega} & \text{III.B.12} \\ &= 3GM \left(\frac{C-A}{A} \right) \frac{z}{r^5} \frac{1}{\omega} \end{aligned}$$

The angular magnitude of the spin polar motion is S/ω or approximately 0.01 arcsec for the rigid earth. The direction of diurnal polar motion about the slowly moving pole position is clockwise viewed from the north. Since the earth rotates in a counterclockwise direction in space when viewed from the north, the direction of the instantaneous pole is essentially constant in the space-fixed reference system.

The direction cosines of the spin vector S with the principal axes are

$$\begin{aligned} \cos(\omega, X) &= \frac{\omega_1}{\omega} & \text{III.B.13} \\ \cos(\omega, Y) &= \frac{\omega_2}{\omega} \\ \cos(\omega, Z) &= \frac{\omega_3}{\omega} = \gamma \end{aligned}$$

where γ is the angular magnitude of the spin polar motion. The corresponding direction cosines for the angular momentum vector H are

$$\cos(H, X) = \frac{A\omega_2}{H} \quad \text{III.B.14}$$

$$\cos(H, Y) = \frac{A\omega_2}{H}$$

$$\cos(H, Z) = \frac{A\omega_3}{H}$$

Because the direction cosines for S and H are different, S and H cannot be parallel and are separated by an angle ν where

$$\sin \nu = \frac{C-A}{A} \sin \gamma \cos \gamma \left(\sin^2 \gamma + \frac{C^2}{A^2} \cos^2 \gamma \right)^{-1/2} \quad \text{III.B.15}$$

The axis of figure F, S, and H all lie in a plane with the angular momentum between the other two as shown in figure III.1. Since both γ and ν are small, eq. III.B.15 can be reduced to

$$\frac{\nu}{\gamma} = \frac{C-A}{C} \quad \text{III.B.16}$$

indicating that H is much closer to S than to F. Consequently as PS undergoes polar motion, PH also moves but with a slightly different magnitude and direction. The H pole direction is the same as the S pole direction relative to the pole of figure but different relative to the slowly moving Eulerian pole as shown in figure III.2.

The separation between S and H is a direct consequence of the separation between S and F. The latter separation is inevitable if an external torque is present. However, the observed magnitude of separation between S and F depends not on the external perturbing bodies but on the initial conditions, which are of a geophysical

nature.

The kinematics of the various motions is illustrated in figure III.3 using Poincot's construction. A cone fixed in the body is centered about F and has a semi-aperture γ . A cone fixed in space is centered about H with a semi-aperture ν . The spin vector lies along the line of contact between the cones. Rotational motion of the body is characterized by a continuous rolling without slipping of the larger body cone around the smaller space cone. With each diurnal rotation the line of contact returns to the same point on the space cone but to a different point on the body cone, thus reflecting polar motion about the pole of figure.

As an aside it might be pointed out that the angular separation between S and H means that there must be diurnal nutation of the spin vector, a diurnal change of direction of the spin vector as viewed in the inertial reference frame.

In the absence of an external torque the semi-apertures of the cones are constant and only Eulerian polar motion occurs. An external torque causes daily modulations $\Delta\gamma$ and $\Delta\nu$ resulting in diurnal polar motion. In addition the spin vector must move in space as it follows the change in angular momentum. The kinematics is shown in figure III.4. A cone of semi-aperture $\Delta\gamma$ fixed in the earth at an angle γ_0 from the axis of figure rolls on a space-fixed cone of semi-aperture ϵ_1 , where ϵ_1 is the obliquity of the ecliptic. The spin vector again lies along the line of contact and the small body cone

Fig. III.3 Poinot's representation of the free motion of a rigid earth

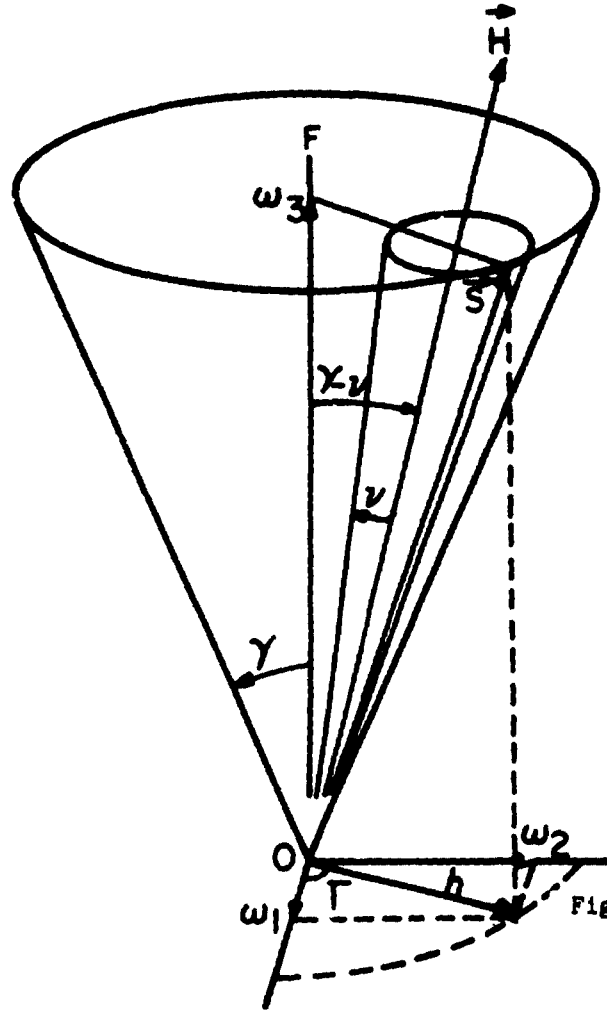
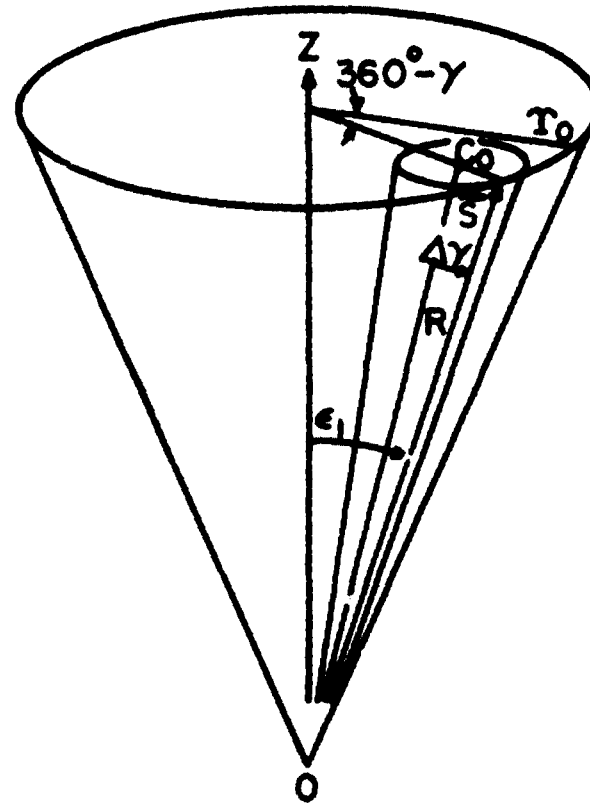


Fig. III.4



Poinot's representation of the forced motion of a rigid earth

makes one revolution in approximately a day.

An expression for diurnal polar motion on a rigid earth can be found in Woolard (p.157-162, 1953). Because the external torque of the perturbing bodies depends on their mass, distance, and declination, expansions of the lunar and solar ephemerides are necessary for a complete development of the corresponding diurnal polar motions. However, the additional complications may be thought of as caused by new fictitious perturbing bodies with characteristic masses, distances, declinations, and angular velocities. The principal fictitious bodies can be constructed from circular lunar and solar orbits. Ignoring fine details, the declinations of the moon and sun are zero twice a month and twice a year, respectively. Since the magnitude of diurnal polar motion is proportional to the height of the perturbing body above the equatorial plane, diurnal polar motion vanishes when the perturbing body is on the equator, i.e., semimonthly and semiannually. Consider then a space-fixed coordinate system with the z-axis parallel to the body-fixed z-axis. There are four fictitious bodies necessary. Two bodies B1 and B2 with masses M1 and M2, respectively, are fixed in space at $(r_1, \theta_1, \varphi_1)$ and $(r_2, \theta_2, \varphi_2)$. These cause the constant lunar and solar torques arising from the obliquity of the ecliptic. The two bodies contribute to a single diurnal polar motion with a period of exactly one sidereal day. A third body B3 with mass M1 at $(r_1, \theta_3, \varphi_1)$ revolves about the space-fixed z-axis with a semimonthly period. Whenever $\theta_3 = 180$ deg, the torques of bodies B1 and B3 cancel, causing the amplitude of lunar diurnal polar motion to be zero. In the same manner B4 with mass M2 revolves about the z-axis at $(r_2, \theta_4, \varphi_2)$ with a

semiannual period, causing semiannual cancellation of the solar diurnal polar motion. Since B₃ and B₄ revolve slowly compared to the angular velocity of the earth, their angular velocities in the earth-fixed system are only slightly different from the angular velocities of the fixed bodies (B₁ and B₂) so that the periods of their associated polar motions are still close to one sidereal day. The net polar motion is shown in figure III.5. The magnitude of diurnal polar motion varies as various perturbations interfere.

The effects described above apply strictly only to a rigid earth. A deformable earth behaves in a more complex manner because it distorts in response to centrifugal and tidal forces.

Spin polar motion changes the direction of centrifugal forces acting on the mass elements of the earth. The elasticity of the earth allows a mass redistribution towards the continuously changing spin equator as the structural centripetal force balances the changing centrifugal force. The major result is to increase the period of the Eulerian motion since the pole of figure is forced to move towards the spin pole.

The effects of tidal forces can be divided into two parts. First, the diurnal solid earth tide changes the position of the pole of figure. The amplitude of the diurnal tide is maximum when the perturbing body is at the limits of its declination. The tide is greatest at (+/-) 45 deg latitude and has nodal lines at the equator and at the meridians 90 deg away from the meridian of the perturbing

body. The earth is divided into quadrants by the nodal lines. The quadrants directly under and opposite the perturbing body are raised while the other two are depressed. The axis of figure therefore tilts away from the direction of the perturbing body. As the meridian of the perturbing body changes, the pole of figure undergoes a corresponding diurnal polar motion relative to the geographic pole.

Second, the potential field of the earth changes as mass is redistributed. The tidal deformation itself and the variations in density give rise to a new potential characterized by the Love number k . The sum of the original and induced potentials determines the external torque. In the terrestrial reference frame the result is to reduce the apparent external torque and thus reduce the magnitude of the diurnal spin and angular momentum polar motions.

McClure (1973) and Federov (1958) present analyses of diurnal polar motion in a deformable earth. McClure calculates complete series for the diurnal polar motion of the spin, angular momentum, and figure poles. Using a value of 0.29 for Love k he finds that the maximum magnitude of figure pole motion is 60 m. The three poles remain in a single plane as shown in figure III.6. Federov only discusses the angular momentum polar motion and derives results similar to McClure's.

The effect of diurnal polar motion on precise measurements has not been discussed extensively in the literature. McCarthy (1976), for example, assumes Woolard's results when correcting his data. Atkinson (1975) and Jeffreys (1963) point out that astronomers invariably assume

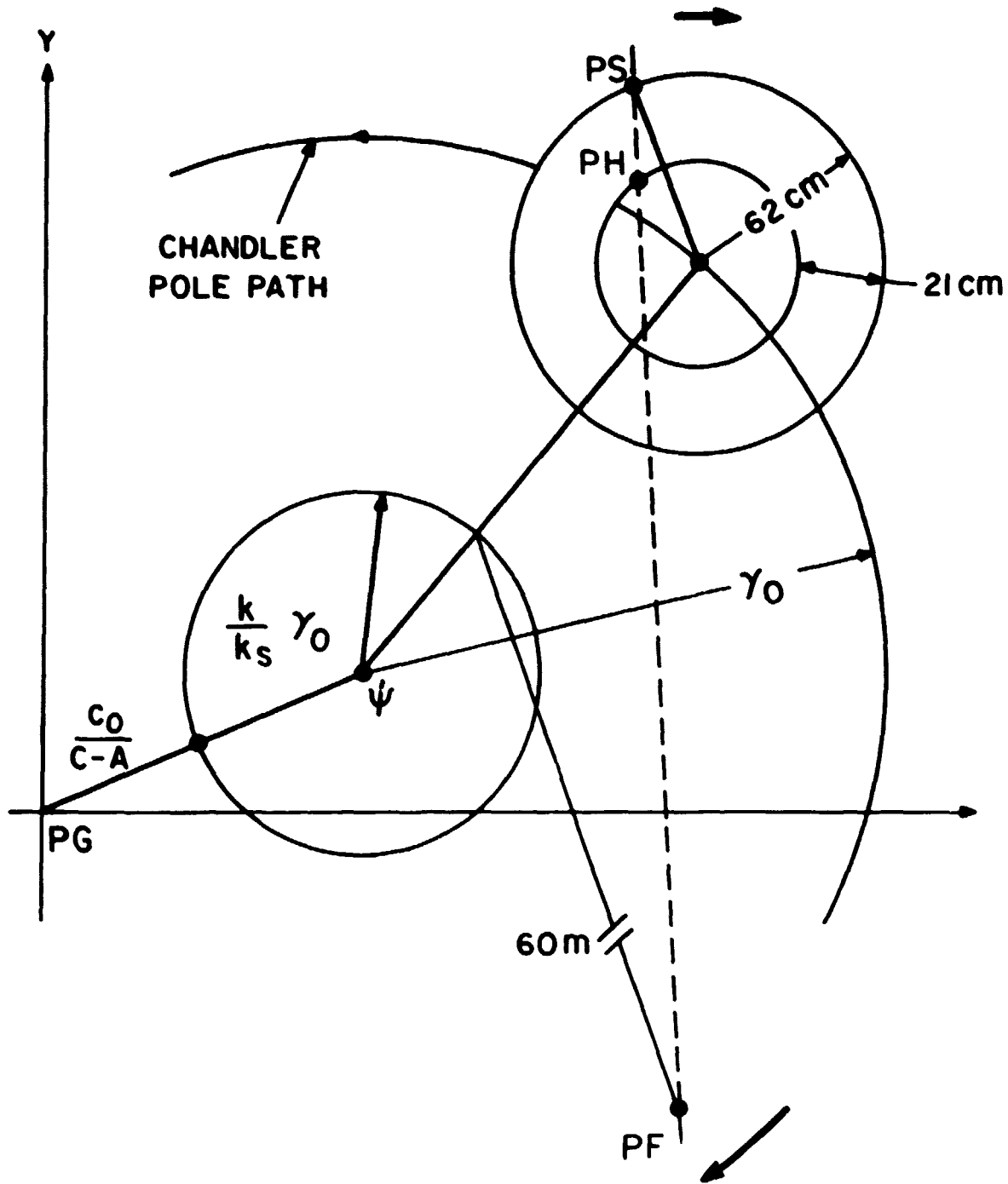


Fig. III.6 Diurnal polar motion in a deformable earth

that stars rotate about "the" spin axis during a night. The traditional celestial coordinate system is based on this belief. However, conventional astronomical angular observations, particularly fundamental observations, are done in a purely topocentric coordinate system oriented by local vertical and a fixed azimuth. The position of the spin axis in the celestial frame cannot be measured by a single observation but must be inferred, usually from zenith angles. The zenith angle of a star is definitely affected by polar motion. Atkinson indicates that diurnal polar motion will cause a systematic bias in fundamental declination observations. Jeffreys states that in the half day required to measure upper and lower transit diurnal polar motion may be as much as the standard error in the solutions and more than the error tolerated in the calculation of the celestial spin axis position.

The proper approach for handling the subtleties of diurnal polar motion, especially in a deformable earth, is the subject of some debate. Most workers undoubtedly ignore the effect and adhere to the conventional spin axis in thought and deed. Atkinson (1973) gives corrections to the coefficients of Woolard's nutation series to adjust observations to the pole of figure instead of the spin pole. Jeffreys also favors using the axis of figure. The primary objection to this method, at least as stated by these authors, is that the pole of figure is not a fixed point on the surface but moves considerably under tidal distortions. If what they mean by pole of figure is the geographic pole the case is perhaps more secure. However, the geographic pole is now entirely arbitrary and has no physical relationship to the

celestial position of any axis of interest. Federov prefers the angular momentum vector and its pole for theoretical correctness and simplicity. External torques apply directly to changes in the angular momentum vector. He points out that a redefinition of declination related to the dynamical equator is necessary for complete consistency. McClure takes an eclectic view and gives a number of approaches involving the spin, angular momentum, and figure poles.

The important point is that the purpose of all precession, nutation, polar motion, and diurnal rotation transformations is to relate the geographic coordinate system aligned with the geographic pole to a celestial coordinate system whose orientation is fixed at some epoch. The connection between the two systems takes place where an axis or vector intersects the earth's surface at its corresponding pole. In the celestial reference frame the vector may have a complicated motion caused by precession and nutation. In the terrestrial reference frame the pole may migrate almost haphazardly. As long as the celestial and terrestrial motions can be separately measured or modeled the choice of spin, angular momentum or figure is immaterial. The choice of angular momentum for the analysis of VLBI data is discussed in the next section.

C. Implementation of diurnal polar motion

McClure's model of diurnal polar motion is used for two reasons. First, it is more comprehensive than Federov's model. McClure gives a complete tidal component expansion and considers the behavior of all

three poles. He also includes the effect of the separation between the spin vector and the angular momentum vector. Second, the algorithm was available for computer application, albeit in a faulty form.

One of McClure's transformations from the celestial frame to the geographic system is

$$\begin{aligned}
 X_{\text{terrestria}} &= R_y(-m_1)R_x(-m_2)R_y\left(-\frac{H_1}{C\Omega} + m_1\right)R_x\left(\frac{H_2}{C\Omega} - m_2\right) \quad \text{III.C.1} \\
 &R_z(\text{GAST} + \delta\psi_{\text{rD}} \cos \epsilon_{\text{HD}}) \\
 &R_x(-\epsilon_{\text{HD}})R_z(-\Delta\psi_{\text{HD}})R_x(\epsilon_0) \\
 &R_z(-z)R_y(\zeta)R_z(-\zeta_0)X_{\text{mean of epoch}}
 \end{aligned}$$

where

R_x, R_y, R_z = rotation matrices about the respective axes

m_1, m_2 = x and y coordinates of the instantaneous spin pole in a right-handed terrestrial coordinate system

$\frac{H_1}{C\Omega}, \frac{H_2}{C\Omega}$ = x and y coordinates of the instantaneous angular momentum pole in the same system

$\delta\psi_{\text{rD}}$ = distance along the mean ecliptic of date from the equator normal to the instantaneous angular momentum vector to the equator normal to the instantaneous spin axis

ϵ_{HD} = angle between the mean ecliptic of date and the equator normal to the instantaneous angular momentum vector

$\Delta\psi_{\text{HD}}$ = distance along the mean ecliptic of date from the mean equator of date to the equator normal to the instantaneous

angular momentum vector

ϵ_0 = mean obliquity of date

z, θ, ζ_0 = precessional angles

The arcs and equators in the celestial frame are shown in figure III.7.

This set of rotations transforms in stages from the geographic pole to the spin pole

$$R_y(-m_1)R_x(m_2) \quad \text{III.C.2}$$

then from the spin pole to the angular momentum pole

$$R_y\left(-\frac{H_1}{C\Omega} + m_1\right)R_x\left(\frac{H_2}{C\Omega} - m_2\right) \quad \text{III.C.3}$$

The angular momentum pole is associated with the angular momentum vector in space. Then,

$$R_z(\text{GAST} + S\psi_{TD} \cos \epsilon_{HP}) \quad \text{III.C.4}$$

aligns the x-axis with the true vernal equinox of date and

$$R_x(-\epsilon_{HD})R_z(-A\psi_{HD})R_x(\epsilon_0) \quad \text{III.C.5}$$

accounts for nutation. Finally, precession is represented by

$$R_z(-z)R_y(\theta)R_z(-\zeta_0) \quad \text{III.C.6}$$

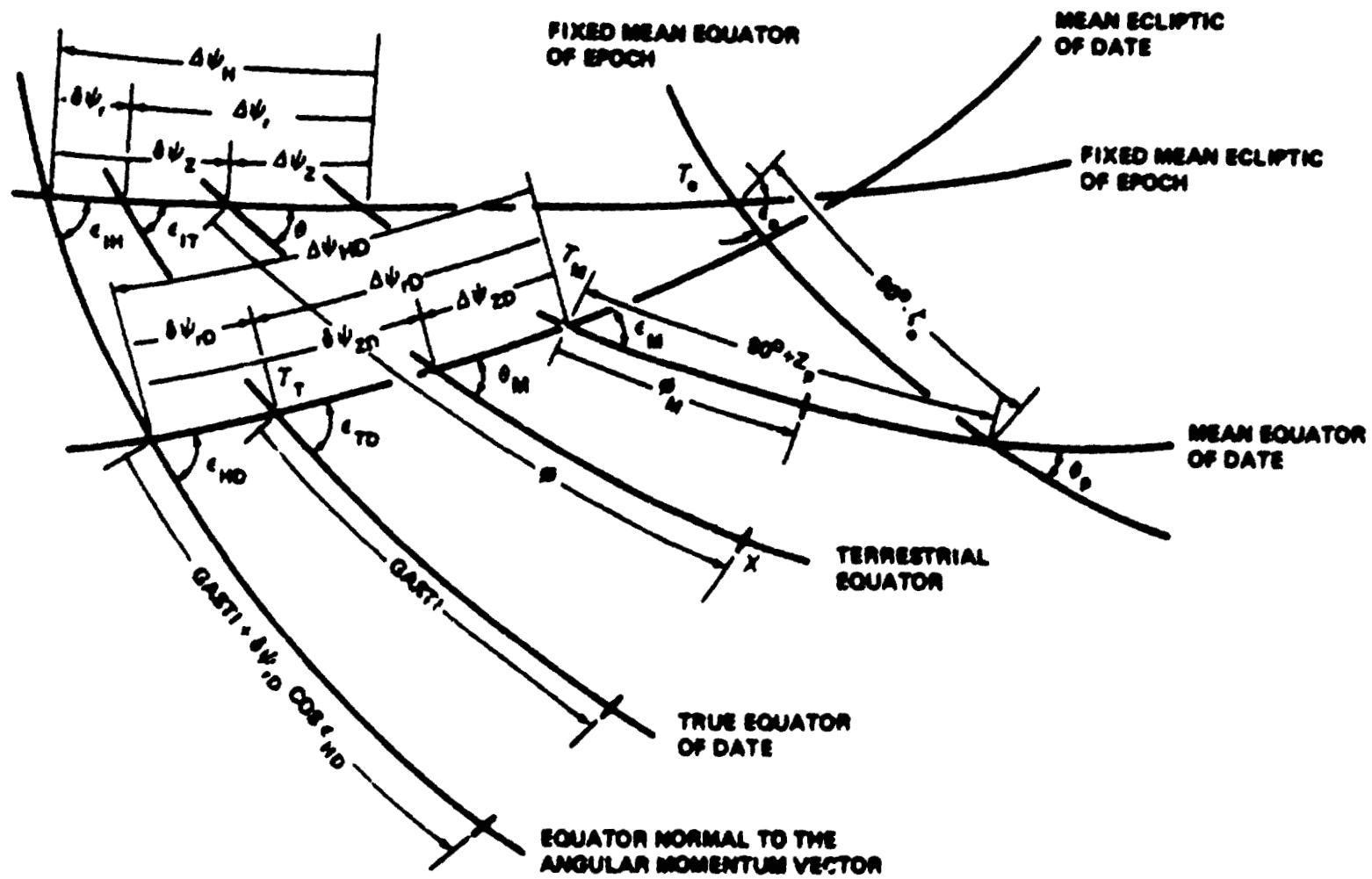


Fig. III.7 Equators and arcs relevant to diurnal polar motion

There are several reasons for using this particular transformation. First, by relatively simple modifications the actual irregular motion of the slowly moving pole can be included. Second, angular momentum is more closely related to the dynamics of the earth than is spin or the axis of figure. Angular momentum is not affected by diurnal nutation. Third, Woolard's nutation series can be used. Woolard integrates Poisson's equations to find the motion of the angular momentum vector. He then calculates corrections to be added in order to reach the positions of the spin axis and the axis of figure. McClure points out that the spin axis corrections are lost in rounding in Woolard's table 26, which is the standard nutation series coefficients. Consequently, the coefficients apply more properly to the position of the angular momentum vector than to that of the spin axis. Likewise the conventional true equator of date is more properly called the dynamical equator.

The transformation from geographic to spin pole can be divided into diurnal and long period (LP) parts.

$$R_y^{(-m_1)} R_x^{(m_2)} = R_y^{(-m_1 \text{ Eulerian})} R_x^{(m_2 \text{ Eulerian})} \quad \text{III.C.7}$$

$$R_y^{(-m_1 \text{ diurnal})} R_x^{(m_2 \text{ diurnal})}$$

where $R_y^{(-m_1 \text{ Eulerian})} R_x^{(m_2 \text{ Eulerian})}$ moves from the geographic pole to the slowly moving pole position.

The transformation from the spin pole to the the angular momentum pole can also be divided into a diurnal part and a slowly varying

Eulerian part. The diurnal transformation can be written

$$R_y(-H_{1d} + m_{1d})R_x(H_{2d} - m_{2d}) = R_y(-H_{1d})R_y(m_{1d})R_x(H_{2d})R_x(-m_{2d}) \quad \text{III.C.8}$$

where

H_{1d}, H_{2d} = displacement of the instantaneous angular momentum pole relative to the slowly moving pole

m_{1d}, m_{2d} = displacement of the instantaneous spin pole relative to the slowly moving pole

The form of the Eulerian separation is

$$\left(m - \frac{H}{\Omega}\right) = \left(1 - \frac{A}{C}\right)\left(1 - \frac{k}{k_s}\right)m_0(\cos \sigma t + i \sin \sigma t) \quad \text{III.C.9}$$

C, A = principal moments of inertia of the earth

k, k_s = Love numbers

$m_0(\cos \sigma t + i \sin \sigma t)$ = observed slowly moving pole displacement from the six-year mean spin pole

Since the rotations are small, a first order approximation is possible.

Rotations III.C.2. and III.C.3 can be rewritten using III.C.7, III.C.9,

and III.C.8 as

$$\begin{aligned} R_y(-m_1)R_x(m_2)R_y\left(-\frac{H_1}{\Omega} + m_1\right)R_x\left(\frac{H_2}{\Omega} - m_2\right) & \quad \text{III.C.10} \\ & = R_v(-m_{1E})R_x(m_{2E})R_v(-m_{1d})R_x(m_{2d}) \\ & \quad \left(1 - \frac{A}{C}\right)\left(1 - \frac{k}{k_s}\right)R_v(-m_{1E})R_x(m_{2E}) \\ & \quad R_v(-H_{1d})R_y(m_{1d})R_x(H_{2d})R_x(-m_{2d}) \end{aligned}$$

$$= R_y(-m_{1E})R_x(m_{2E}) \\ \left(1 - \frac{A}{C}\right) \left(1 - \frac{k}{k_s}\right) R_y(-m_{1E})R_x(m_{2E})R_y(-H_{1d})R_x(H_{2d})$$

The term $R_y(-m_{1E})R_x(m_{2E})$ is the conventional polar motion matrix which is designated by W in section II.D.5. The term $R_y(-H_{1d})R_x(H_{2d})$ is the diurnal motion of the instantaneous angular momentum pole about the slowly moving pole position.

The term $R_z(\text{GAST} + \delta\psi_{rD} \cos \epsilon_{HD})$ from III.C.4 can be exactly separated into two rotations:

$$R_z(\text{GAST})R_z(\delta\psi_{rD} \cos \epsilon_{HD}) \quad \text{III.C.11}$$

The first rotation is the conventional rotation by the Greenwich apparent sidereal time in order to align the x-axis with the true vernal equinox. The second is a correction needed because the rotation about the z-axis is about the angular momentum axis rather than the spin axis.

Therefore the first two lines of eq. III.C.1 from mean of epoch to geographic (rotations III.C.2, III.C.3, and III.C.4) can be written as

$$W \left(1 - \frac{A}{C}\right) \left(1 - \frac{k}{k_s}\right) R_y(-m_{1E})R_x(m_{2E}) \quad \text{III.C.12} \\ R_y(-H_{1d})R_x(H_{2d}) \\ R_z(\delta\psi_{rD} \cos \epsilon_{HD})R_z(\text{GAST})$$

After combining rotations to first order about each axis and dropping terms which can be included elsewhere (W and R_z (GAST)), the diurnal polar motion matrix D in the direction from terrestrial to mean of epoch (opposite of the rotations used above) is given by

$$D = R_z(-\delta\psi_{rD} \cos \epsilon_{HD}) R_x(-H_{2d} - y_E) R_y(H_{1d} + x_E) \quad \text{III.C.13}$$

where

$$x_E = - \left(1 - \frac{A}{C}\right) \left(1 - \frac{k}{k_s}\right) x_{\text{slowly moving pole position}}$$

$$y_E = - \left(1 - \frac{A}{C}\right) \left(1 - \frac{k}{k_s}\right) y_{\text{slowly moving pole position}}$$

Strictly speaking, the use of the conventional slowly moving pole is incorrect. McClure's expressions for the Eulerian motions apply about a mean pole position while the CIO pole, which is the origin for long period polar motion, is no longer coincident with the present six-year mean pole position. There has been a secular motion of the six-year mean pole of about $0.003''$ to $0.006''$ per year in the direction of 285 deg east longitude (Poma et al 1976). Since $(1 - A/C) (1 - k/k_s)$ is 0.0023 only a small error (less than 1.5 cm) is involved.

McClure uses all the second degree diurnal tidal terms in Doodson's development to calculate diurnal polar motion. The seven largest terms in the time series for H_d and $\delta\psi_{rD} \sin \epsilon_{HD}$ are used in the present implementation. The error in neglecting the remainder of the 135 terms is at most $0.0006''$.

$$\begin{aligned}
H_{1d} = & -.0009149 \sin(w - w_1 - 2w_3 - 2w_5) & \text{III.C.14} \\
& -.0008659 \sin(w - 2w_3 - w_5) \\
& -.0045924 \sin(w - 2w_3 - 2w_5) \\
& -.0019980 \sin(w - 2w_3 + 2w_4 - 2w_5) \\
& +.0019037 \sin(w) \\
& +.0040934 \sin(w) \\
& +.0008113 \sin(w - w_5)
\end{aligned}$$

$$\begin{aligned}
H_{2d} = & -.0009149 \cos(w - w_1 - 2w_3 - 2w_5) & \text{III.C.15} \\
& -.0008659 \cos(w - 2w_3 - w_5) \\
& -.0045924 \cos(w - 2w_3 - 2w_5) \\
& -.0019980 \cos(w - 2w_3 + 2w_4 - 2w_5) \\
& +.0019037 \cos(w) \\
& +.0040934 \cos(w) \\
& +.0008113 \cos(w - w_5)
\end{aligned}$$

$$\begin{aligned}
\delta\ddagger \text{ sine} = & -.00038502 \sin(+ w_1 + 2w_3 + 2w_5) & \text{III.C.16} \\
& -.00041647 \sin(+ 2w_3 + w_5) \\
& -.00201046 \sin(+ 2w_3 + 2w_5) \\
& -.00093797 \sin(+ 2w_3 - 2w_4 + 2w_5) \\
& +.00086146 \sin() \\
& +.00185233 \sin() \\
& -.00042084 \sin(- w_5)
\end{aligned}$$

H_{1d} , H_{2d} , $\delta\ddagger \text{ sine}$ in arcseconds

w = Greenwich mean sidereal time

w_1 = mean anomaly of the moon
 w_3 = mean argument of the latitude of the moon
 w_4 = mean elongation of the moon from the sun
 w_5 = longitude of the mean ascending node of the lunar orbit on
the ecliptic

Since each term in the series for H_3 includes an argument ω , Greenwich mean sidereal time, the period for H_3 is close to a sidereal day. The terms for $\delta \ddagger \text{ sine}$ do not include the w argument for Greenwich mean sidereal time. Therefore the correction in rotation III.C.11 for the separation of spin and angular momentum changes with periods longer than a day.

Table III.1 shows the characteristic periods associated with each term in the series for H_3 and $\delta \ddagger \text{ sine}$ in the order in which they appear in eq. III.C.14-16. The tidal argument number is a notation devised by Doodson to classify tidal components by increasing speed and is used by McClure to organize his tables. The terrestrial periods apply to the terms of H_3 . The celestial periods are those for the terms in $\delta \ddagger \text{ sine}$. The fact that the arguments for H_3 and $\delta \ddagger \text{ sine}$ differ only by w means that the two sets of periods are directly related. The beat frequency between a term in H_3 and the two precessional terms, which have only the argument w , is the same as the corresponding celestial frequency. Since the semimonthly and semiannual terms have the largest coefficients, the envelope of the magnitude of diurnal polar motion will have these periods.

Table III.1 Periods of diurnal polar motion

| Tidal argument number | terrestrial period | | | celestial period |
|--------------------------|--------------------|-----|-----|------------------|
| | hr | min | sec | |
| 135.655 | 26 | 52 | 05 | 9.1 solar days |
| 145.545 | 25 | 49 | 23 | 13.6 solar days |
| 145.555 | 25 | 49 | 08 | 13.7 solar days |
| 163.555 | 24 | 03 | 54 | semiannual |
| 165.555 | 23 | 56 | 03 | solar precession |
| 165.555 | 23 | 56 | 03 | lunar precession |
| 155.565 | 23 | 55 | 51 | 6798 solar days |

To estimate its magnitude, diurnal polar motion is characterized by a single parameter which scales the rotations in the diurnal polar motion matrix D . See section II.D.4. Both the magnitude of polar motion and the correction for spin-angular momentum separation are scaled together. The direction of the diurnal pole relative to the slowly moving pole is not affected or adjusted. A scaling factor of unity corresponds to the model of McClure.

D. Effect of diurnal polar motion on the VLBI delay observable

The effect of diurnal polar motion on delay rate will not be considered here. As is explained in section III.E, the delay rate observable has not been particularly helpful in estimating diurnal polar motion from VLBI data.

The simple effects of polar motion on delay depend on four parameters: 1) the projection of the baseline on the plane containing the reference pole, the pole of interest and the barycenter (hereafter called the pole plane), 2) the projection of the source unit vector on the pole plane, 3) the projection of the baseline on the plane perpendicular to the source vector, and 4) the displacement of the pole of interest from the reference pole. The effect of polar motion is maximum when all the relevant parameters are at their maximum value, i.e., when the baseline is perpendicular to the source vector and both lie in the pole plane. The effect is scaled by the magnitude of the pole displacement.

Long period polar motion and diurnal polar motion have quite different signatures because their geometries affect the parameters differently. For wobble the baseline projection on the pole plane is essentially fixed for the period of a day. For diurnal polar motion the projection changes as the pole plane rotates about the reference pole axis. When viewed in the celestial reference frame, the pole plane of long period polar motion rotates once about the spin axis in space during a day and the source vector projection changes depending on the source declination. The pole plane for diurnal polar motion changes slowly in space so that the source vector projection on the pole plane is constant over a day. The projection of the baseline on the plane perpendicular to the source vector has a behavior orthogonal to that of delay and is not different for the two modes of polar motion. The last factor, the displacement of the pole, changes very slowly for long period polar motion and more rapidly with a strong semi-monthly period for diurnal polar motion. An effect which is not at all present in long period polar motion is the third rotation in the diurnal polar motion matrix necessitated by the separation of the spin and angular momentum. Diurnal polar motion causes effects which are akin to UT1 variations.

The basic signature of diurnal polar motion in delay is a nearly diurnal sinusoid caused by the changing projection of the baseline on the pole plane. The effect on 3C 84, a mid-latitude source, with the Haystack-OVRO baseline is shown in figure III.8 for Sept. 29 to Oct. 15, 1976. The horizontal scale is time. The vertical scale, also used for succeeding plots, is (+/-) 0.5 nsec. The fortnightly envelope

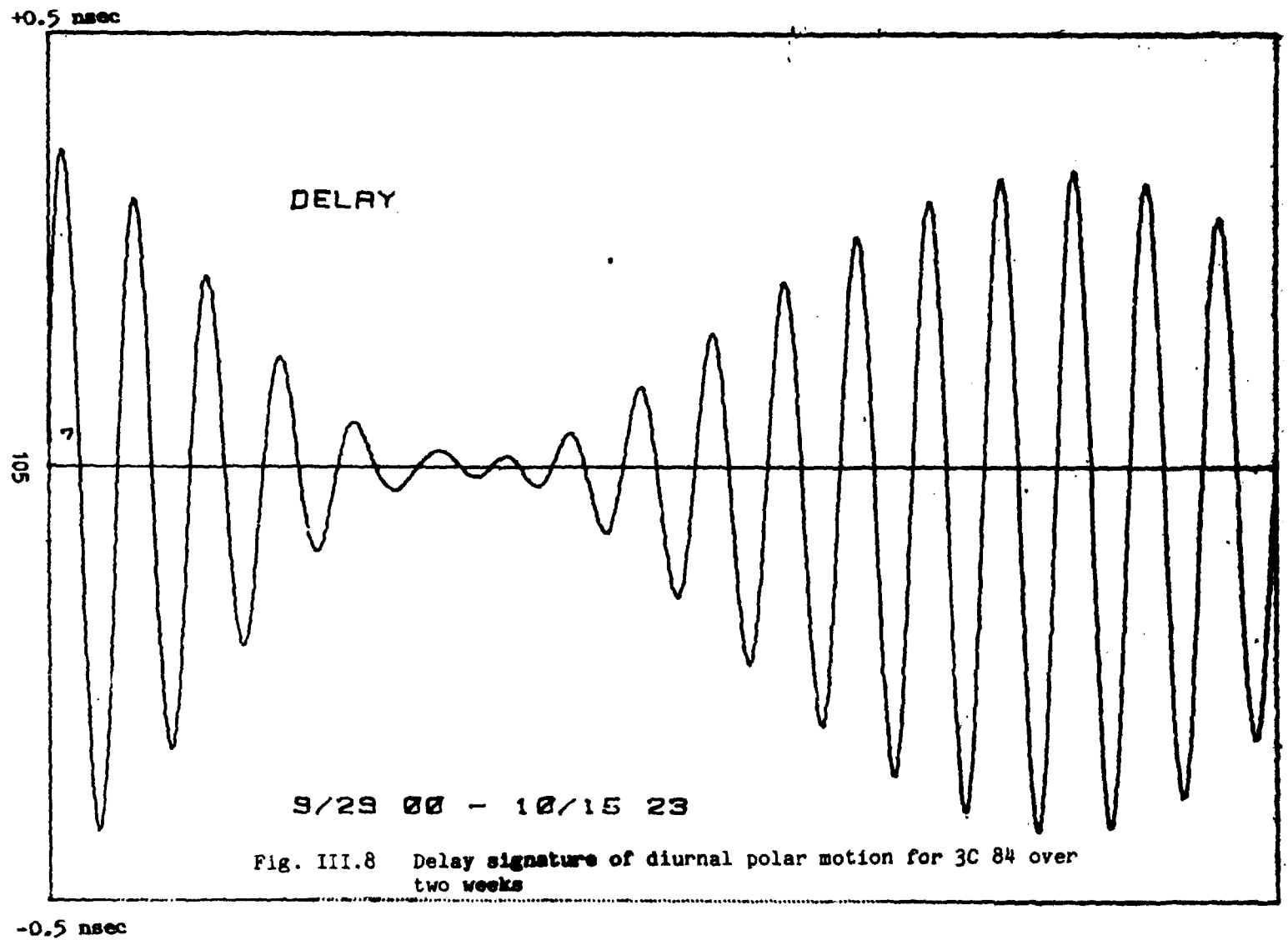


Fig. III.8 Delay signature of diurnal polar motion for 3C 84 over two weeks

is quite obvious. There is an apparent null because the time interval is near the autumnal equinox when the solar polar motion magnitude is zero. Figure III.9 shows the envelope over a year while figure III.10 shows the UT time of the positive-going zero crossing for the same interval. The Haystack-OVRO baseline is used for most of the following examples.

The dependence of the effect on source and baseline geometry is more complicated than for long period polar motion. Because the celestial orientation of the pole plane changes slowly over a day, the effect on sources at different right ascensions is different. The source vector projection on the pole plane changes with right ascension. Figure III.11 shows the effects for sources with 45 deg declination at various right ascensions on an arbitrary day. Figure III.12 shows only that part of the day for which the sources are visible.

The dependence on the declination for sources at a fixed right ascension is also complicated. Figure I shows the signature for several sources at 0 hr right ascension for the same arbitrary day. The effect is not monotonic with declination. Since diurnal polar motion is modeled by rotations about three axes instead of two, its effect changes character with declination. At high declinations the motion of the pole is dominant. Near the equator the correction to the rotation about the z-axis becomes more important in the diurnal signature. Figure III.14 shows the same sources during their visible intervals. The equatorial source has the shortest period of

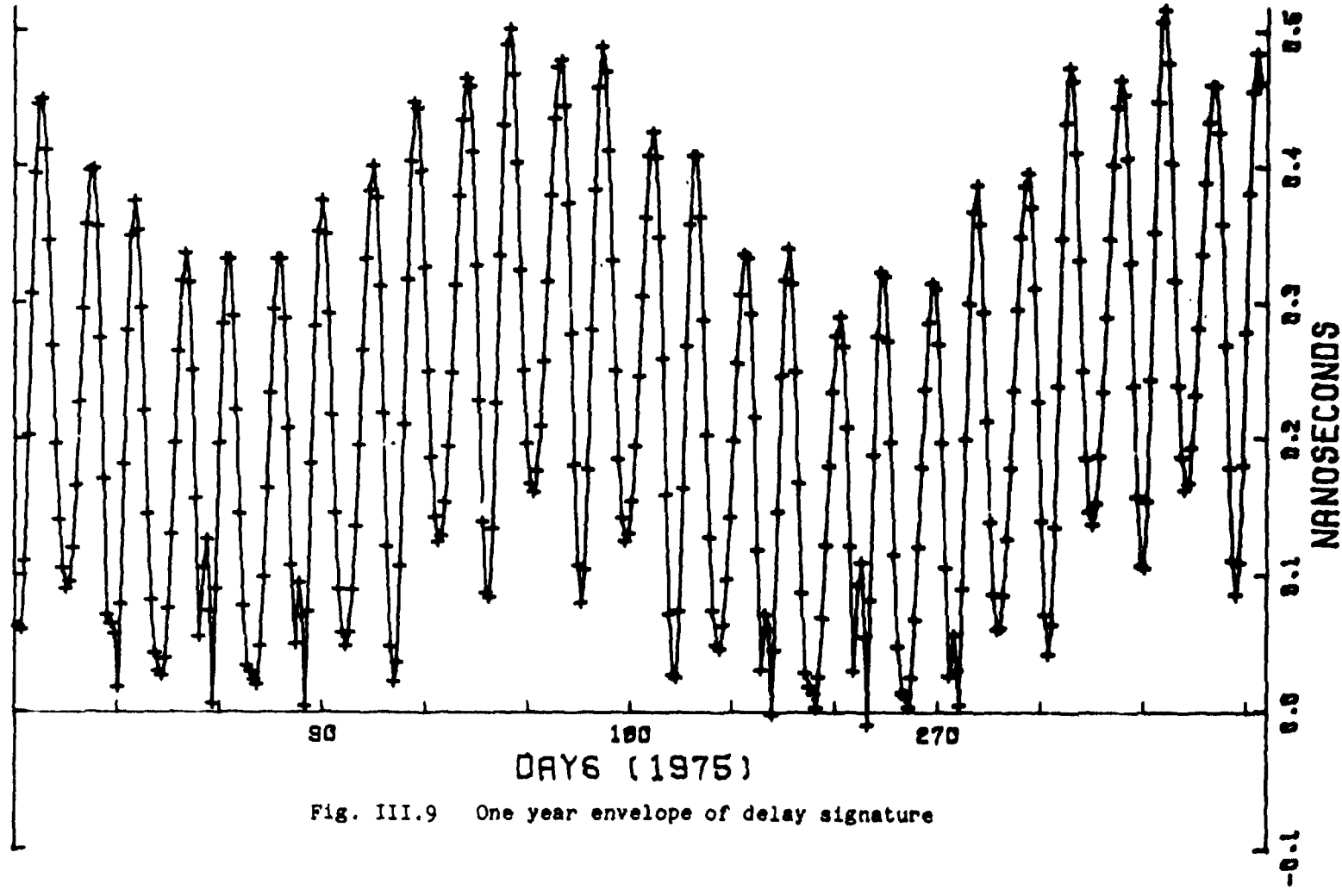
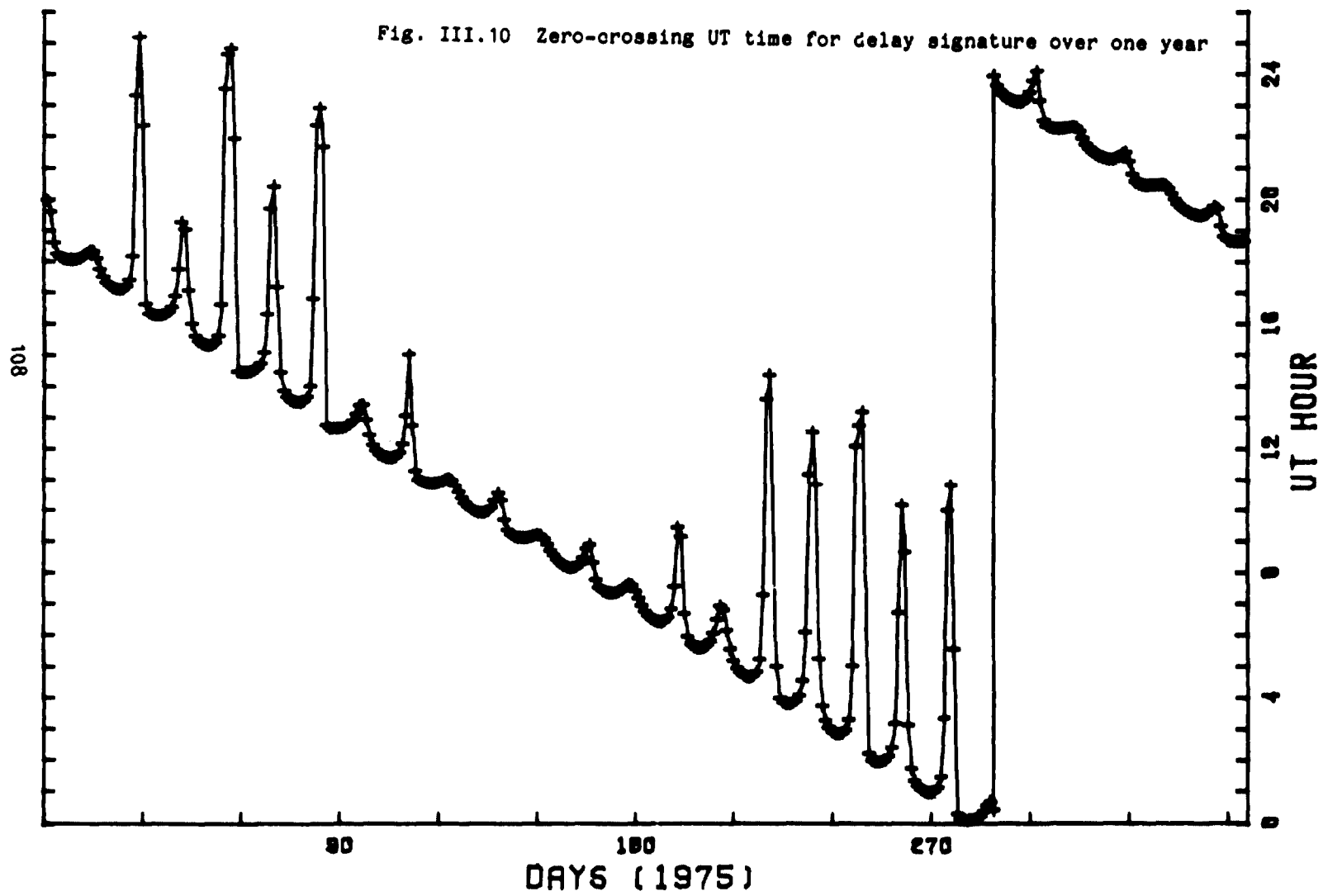


Fig. III.9 One year envelope of delay signature

Fig. III.10 Zero-crossing UT time for delay signature over one year



+0.5 nsec

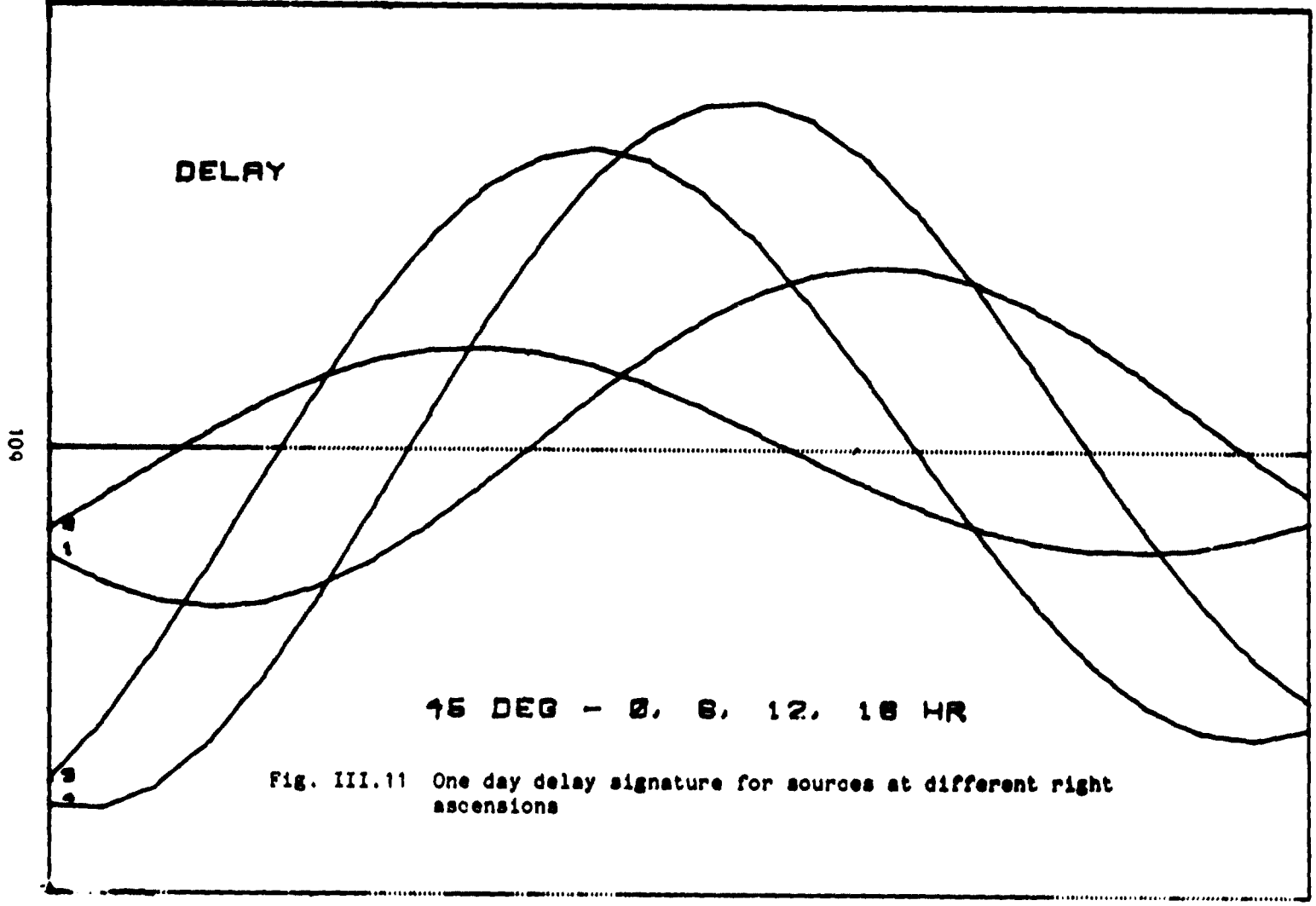
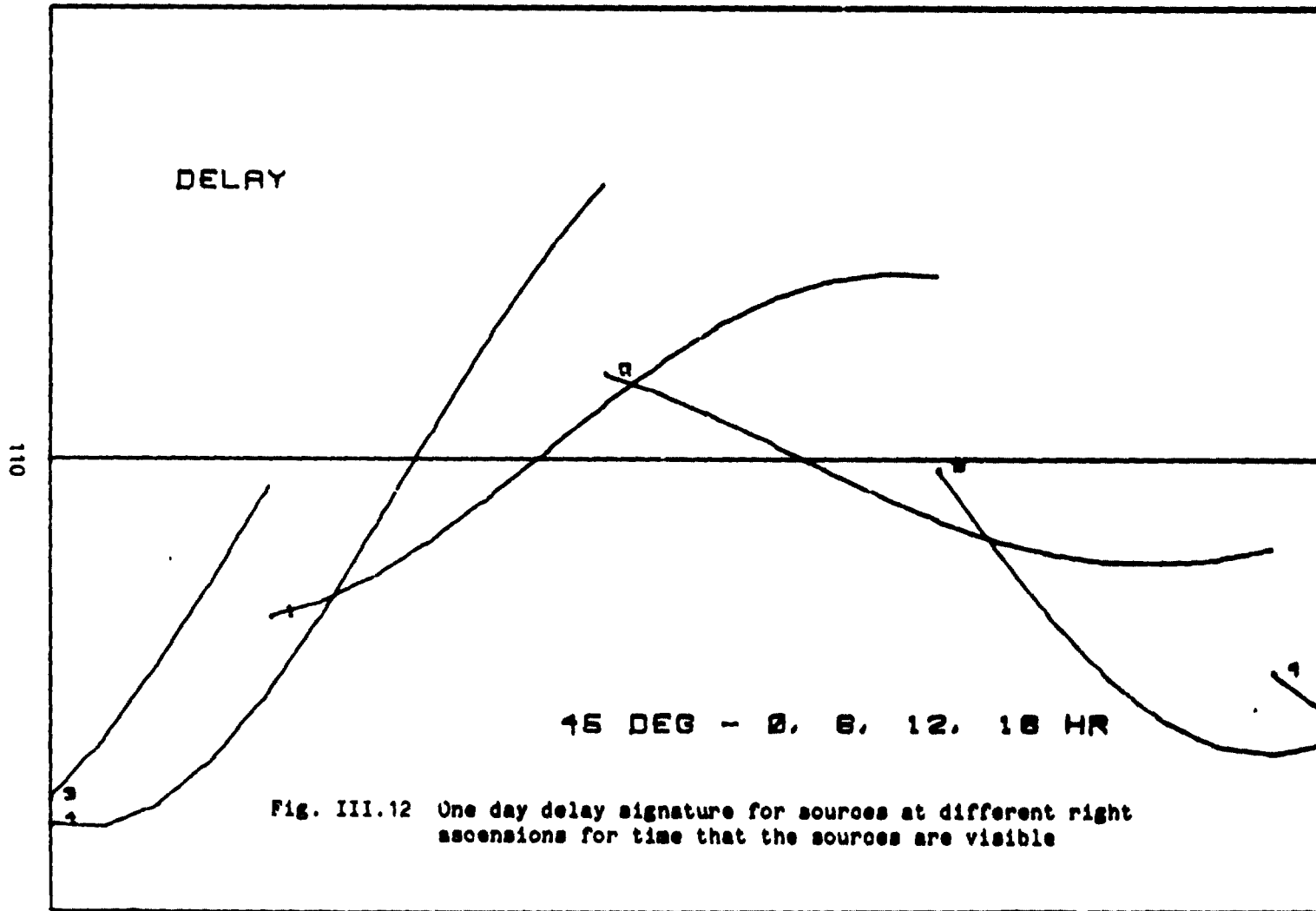


Fig. III.11 One day delay signature for sources at different right ascensions

- .5 nsec

+0.5 nsec



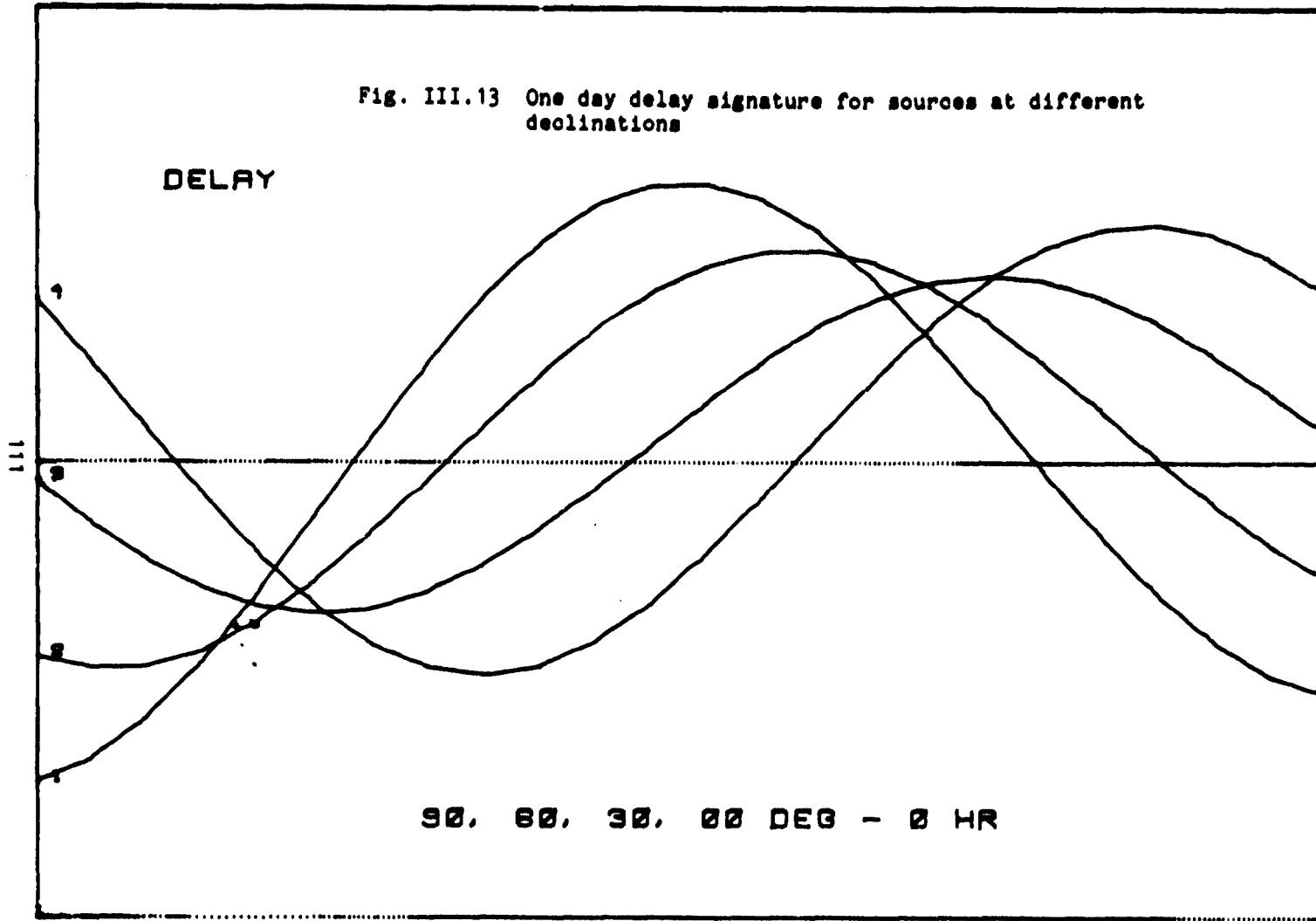
15 DEG - 0, 6, 12, 18 HR

Fig. III.12 One day delay signature for sources at different right ascensions for time that the sources are visible

-0.5 nsec

+0.5 nsec

Fig. III.13 One day delay signature for sources at different declinations



-0.5 nsec

+0.5 nsec

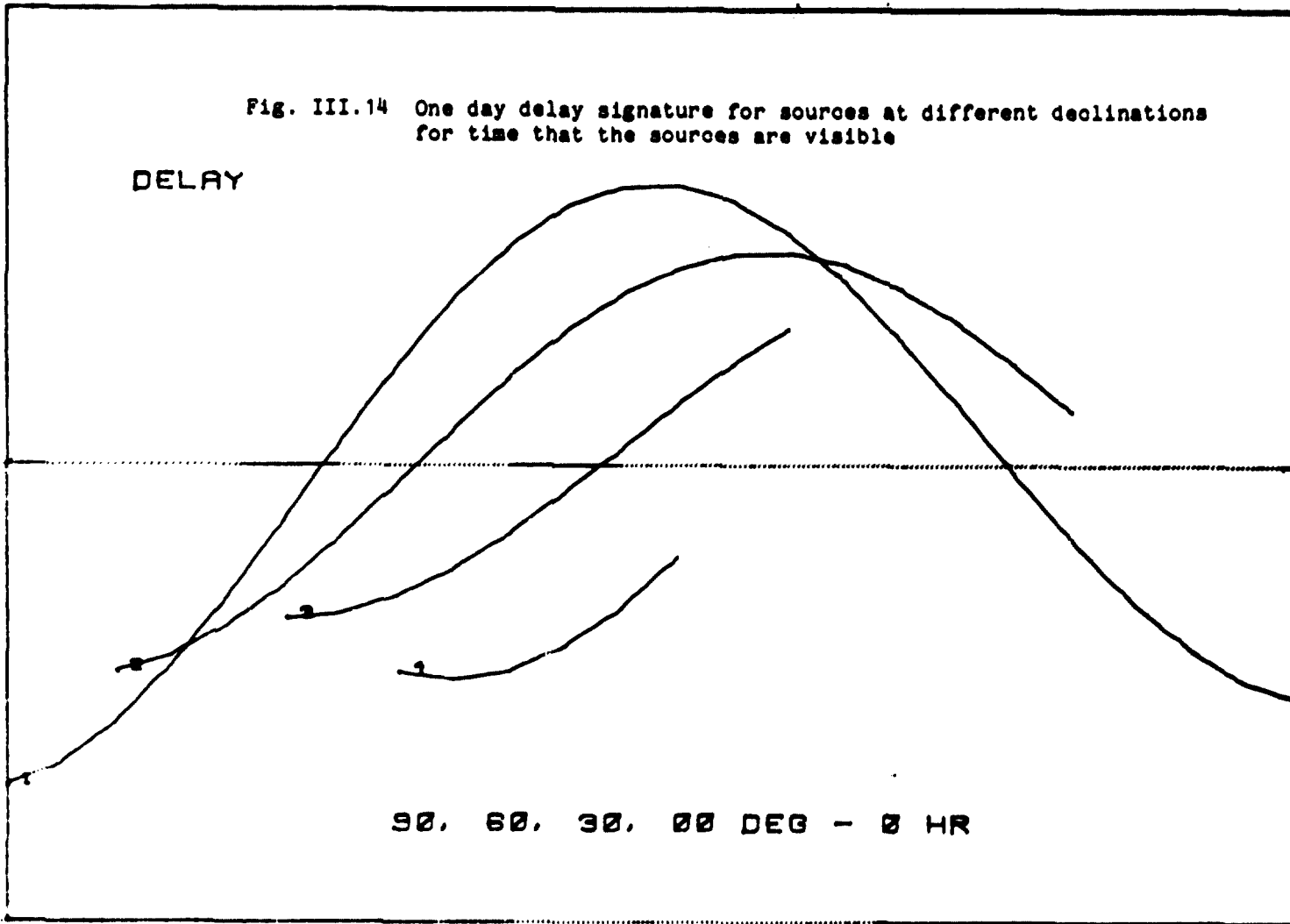
Fig. III.14 One day delay signature for sources at different declinations for time that the sources are visible

DELAY

112

90, 60, 30, 00 DEG - 0 HR

-0.5 nsec



visibility.

The Haystack-OVRO baseline is essentially east-west and illustrates the effect of diurnal polar motion for that component of baseline geometry. The behavior of a polar baseline is shown in figure III.15. Two differences emerge. First, a polar baseline is insensitive to rotations about the z-axis. The spin-angular momentum separation therefore has no effect. Second, the direction of the diurnal pole with respect to the slowly moving pole changes relatively slowly in the inertial reference frame. Consequently the projection of the polar displacement in the direction of a given source also changes slowly. Since there is no equatorial component of the baseline to give diurnal modulation, the north-south baseline sees a slowly changing effect on the delay observable.

The effect of diurnal polar motion on the observations of a complete VLBI observing session is too complex for a complete description. Figures III.16-20 show the effect on delay for five days of observations on the Haystack-OVRO baseline during 1976. The sources are 3C 84(7), 3C 120(14), 4C 39.25(28), 3C 273(33), 3C 279(35), 3C 345(43), PKS 2134(59), VRO 42.22.01(63), and 3C 454.3(67).

E. Observations and data preparation

The data for estimating the magnitude of diurnal polar motion were gathered from observations in the years 1972 through 1977 by VLBI groups at the University of Maryland, GSFC, Haystack Observatory, and

+0.5 nsec

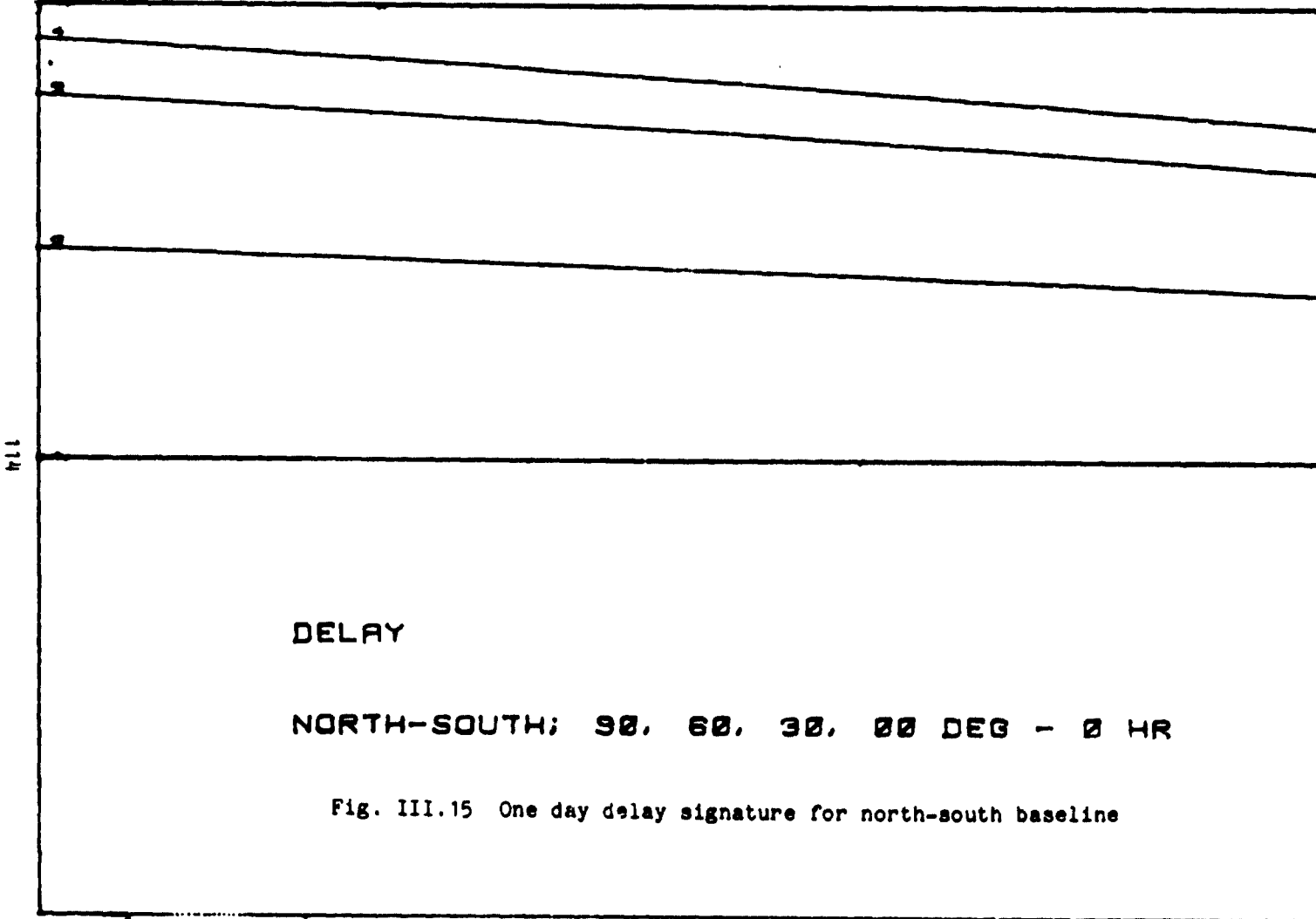


Fig. III.15 One day delay signature for north-south baseline

-0.5 nsec

+0.5 nsec

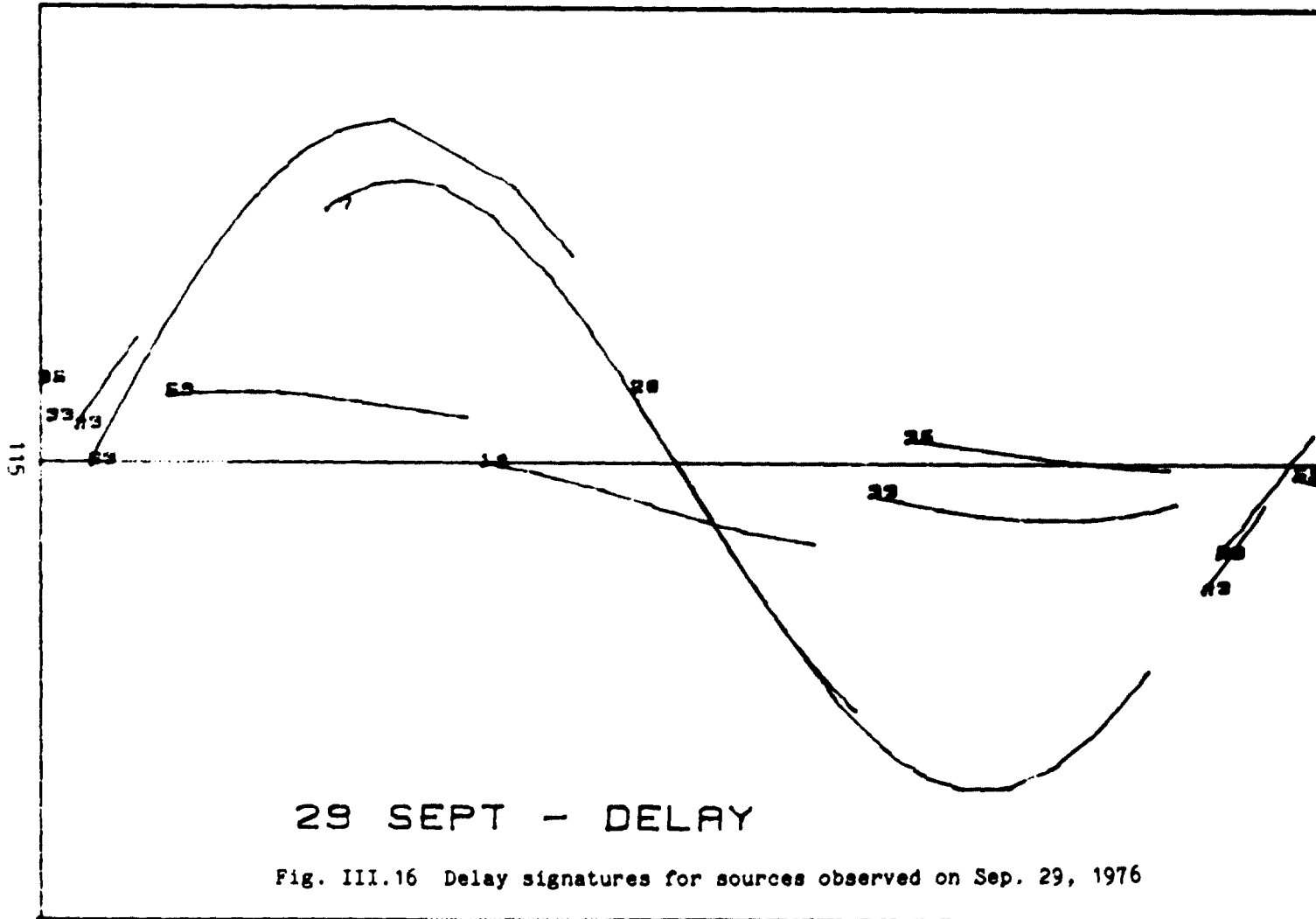
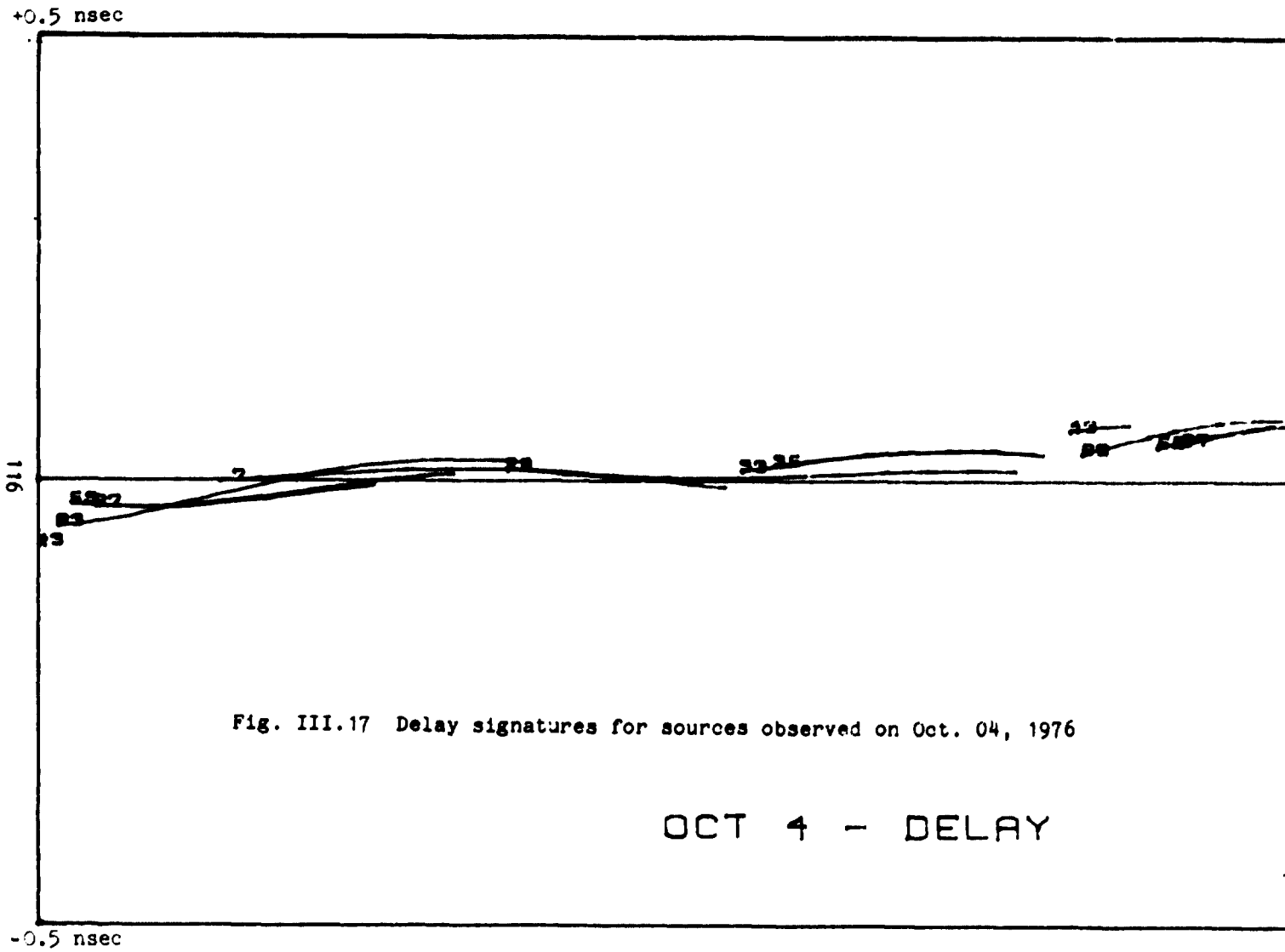
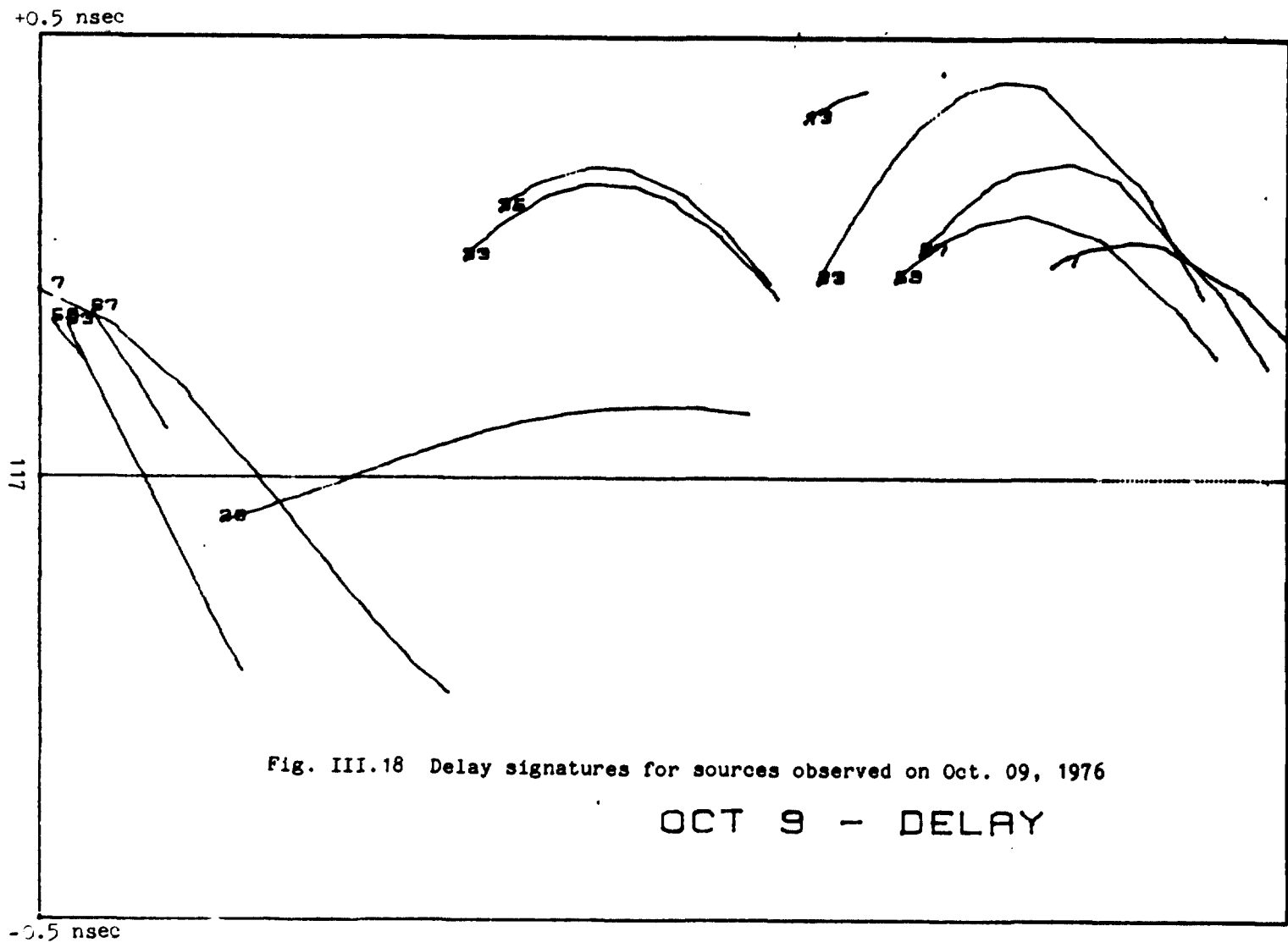


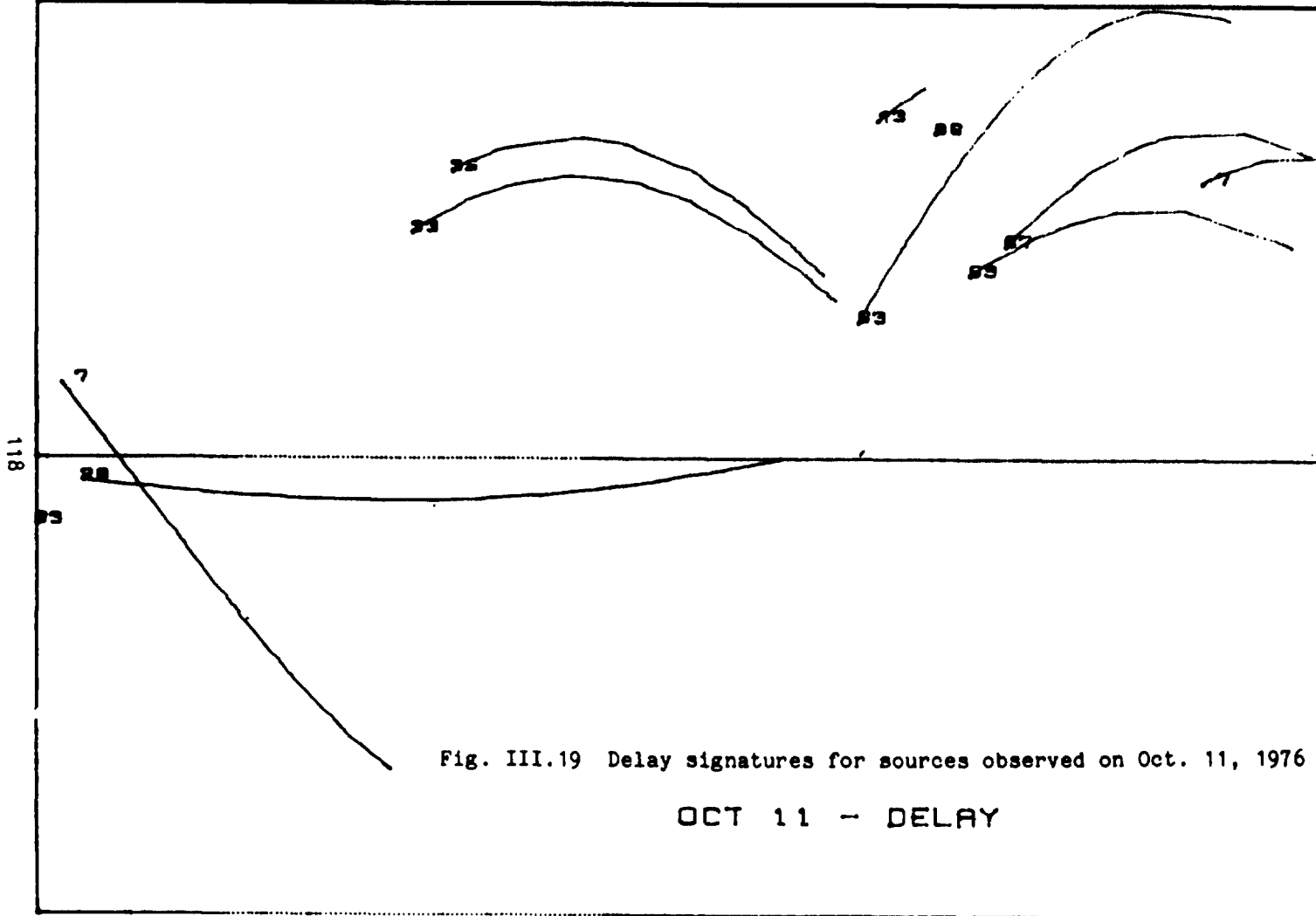
Fig. III.16 Delay signatures for sources observed on Sep. 29, 1976

-0.5 nsec





+0.5 nsec



-0.5 nsec

Fig. III.19 Delay signatures for sources observed on Oct. 11, 1976

OCT 11 - DELAY

-0.5 nsec

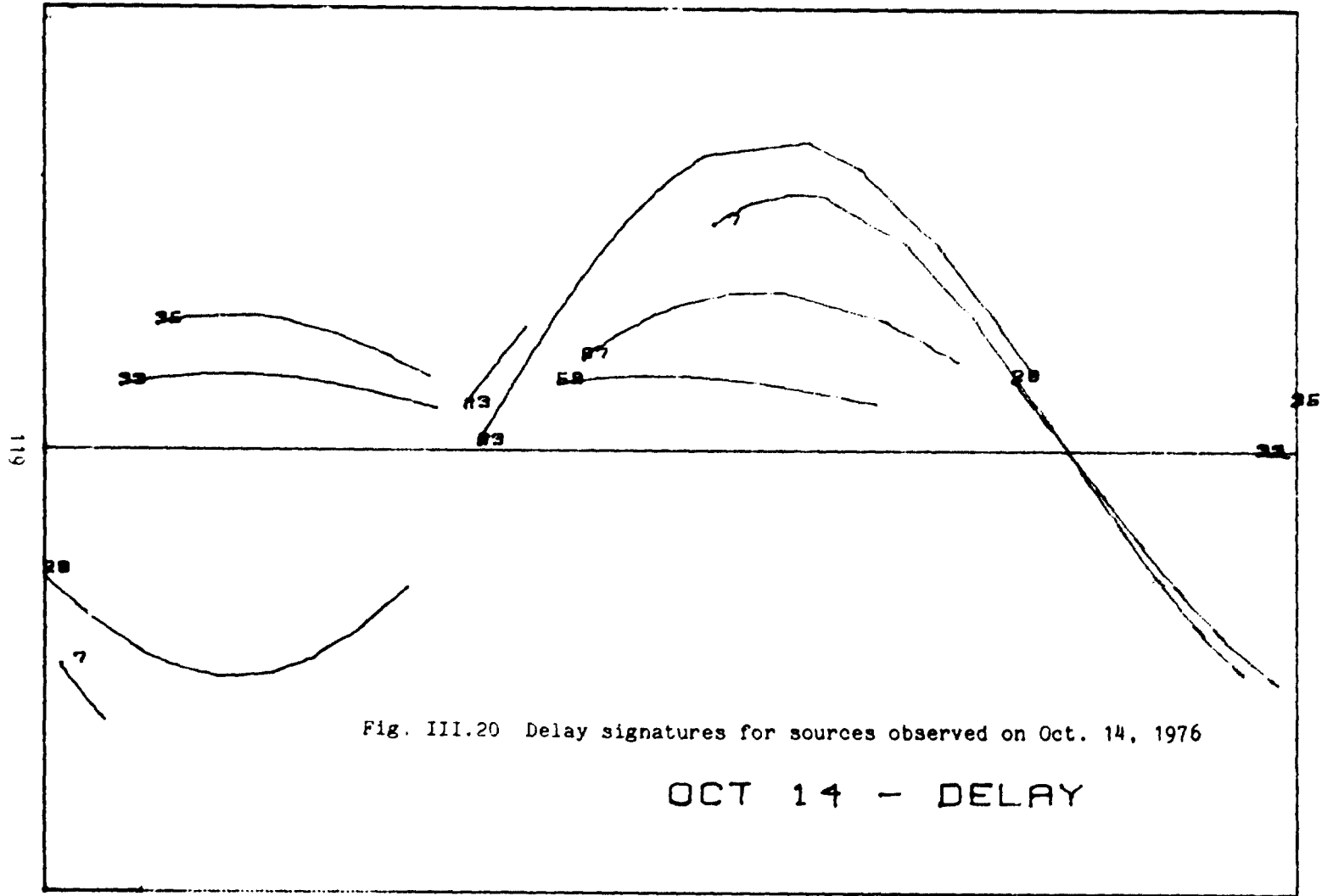


Fig. III.20 Delay signatures for sources observed on Oct. 14, 1976

OCT 14 - DELAY

-0.5 nsec

MIT. Switched frequency synthesized-bandwidth observations recorded and processed by the Mark I system were used throughout.

Four stations were operated during the period although no baseline was available for all observing sessions. The stations were Haystack, Goldstone, Sweden, and OVRO. Information about the antennas and receivers is given in table III.2. Haystack was used for all experiments and was the most reliable site. Because of its fast antenna slewing rate, it was rarely a limiting factor in observing schedules. It probably had the worst atmospheric conditions in terms of large scale and short term fluctuations. Goldstone had the coldest receiver and therefore allowed observations on weak sources. However, it had very slow slewing, limiting the number of runs that could be scheduled, and narrow observing bandwidth (30 MHz). Since the measurement uncertainty of the delay observable is inversely proportional to the observing bandwidth, the scatter in the data from Goldstone baselines is larger than from other baselines not limited by receiver bandwidth. Sweden suffered from extremely low (12%) antenna efficiency and limited mutual visibility with other sites. OVRO had slow slewing rates but a very wide observing bandwidth (300 MHz). The observations using OVRO have the lowest scatter.

The stations in use at different times break the data into four large sets summarized in table III.3.

Set A spans April 1972 through March 1973 when Haystack-Goldstone baseline was used. Each experiment lasted approximately one day and

Table III.2 Antenna and receiver information for diurnal polar motion data

| | a. | b. | c. | u. | e. | f. |
|---|----------------------|-------------|-----------------------------------|--|--------------------|-----|
| a. antenna diameter (meters) | | | | | | |
| b. mount | | | | | | |
| c. configuration | | | | | | |
| d. geodetic location - west longitude, north latitude, altitude (m) | | | | | | |
| e. receiver | | | | | | |
| f. approximate receiver temperature (degrees K) | | | | | | |
| g. location | | | | | | |
| h. organization | | | | | | |
| Name | a. | b. | c. | u. | e. | f. |
| Haystack | 37 | Cassegrain | az/el axes intersecting | 71 29 19.201 42 37 23.00 145 | cooled paramp | 70 |
| Goldstone | 64 | Cassegrain | az/el axes intersecting | 116 53 19.150 35 25 33.446 1030.85 | maser | 30 |
| Sweden | 26 | Cassegrain | equatorial offset 2.2 m | 348 04 47.2 57 23 36.10 14 | maser | 50 |
| OVRO | 40 | Prime focus | az/el axes intersecting | 118 16 54.36 37 13 53.49 1226.65 | uncooled paramp | 120 |
| | | g. | | h. | | |
| Haystack | Westford, Mass. | | Northeast Radio Observatory Corp | | | |
| Goldstone | Mojave, California | | Jet Propulsion Laboratory | | | |
| Sweden | Onsala, Sweden | | Chalmers University of Technology | | | |
| OVRO | Big Pine, California | | Owens Valley Radio Observatory | | | |

Table III.3 Number of observations by experiment and baseline for diurnal polar motion data

| | Haystack-Goldstone | Haystack-Sweden | Haystack-OVRO |
|---|--------------------|-----------------|---------------|
| Set A. April 1972 - March 1973: 1389 points | | | |
| 72/04/14-72/04/15 | 190 | | |
| 72/05/09-72/05/10 | 198 | | |
| 72/05/29-72/05/30 | 67 | | |
| 72/06/06-72/06/07 | 90 | | |
| 72/06/27-72/06/28 | 100 | | |
| 72/08/29-72/08/30 | 193 | | |
| 72/11/07 | 196 | | |
| 73/02/04-73/02/05 | 180 | | |
| 73/03/30-73/03/31 | 175 | | |
| Set B. August 1973 - July 1974: 2605 points | | | |
| 73/08/10-73/08/14 | 145 | | 370 |
| 73/10/12-73/10/16 | 161 | | 316 |
| 74/03/04-74/04/08 | 156 | | 372 |
| 74/04/29-74/05/03 | 212 | | 349 |
| 74/07/08-74/07/12 | 129 | | 394 |
| Set C. January 1975 - March 1976: 570 points | | | |
| 75/01/16-75/01/17 | 124 | | |
| 75/05/27-75/05/28 | 154 | | |
| 75/10/15-75/10/16 | 123 | | |
| 76/03/20-76/03/21 | 169 | | |
| Set D. September 1976 - June 1977: 1597 points | | | |
| 76/09/09-76/09/10 | | | 135 |
| 76/09/29-76/10/01 | | | 188 |
| 76/10/04-76/10/06 | | | 180 |
| 76/10/09-76/10/10 | | | 156 |
| 76/10/11-76/10/12 | | | 118 |
| 76/10/14-76/10/15 | | | 148 |
| 76/12/14-76/12/15 | | | 158 |
| 76/12/15-76/12/17 | | | 167 |
| 77/03/27-77/03/31 | | | 222 |
| 77/06/25-77/06/27 | | | 125 |

the clocks (frequency standards) at both sites were stable. A small number of observations were also made with an antenna at Fairbanks, Alaska, but the data are noisy and consequently not included.

From August 1973 through October 1974 the observing sessions consisted of a single day on the Haystack-Goldstone baseline scheduled during several continuous days involving Haystack and Sweden. Each four-day session is an individual data set in combined set B. The Haystack-Goldstone data show systematic trends caused by drifting of the Goldstone clock. The data on the Haystack-Sweden baseline are noisier but have less evidence of systematic errors. Data taken in October 1974 are not included because of processing difficulties. Two short sessions using only Haystack-Sweden are also not used.

After October 1974 the antenna in Sweden was no longer available. The absence of the Haystack-Sweden baseline was somewhat balanced by improvement in the Goldstone clock behavior. However, the schedules in set C are weakened in two cases because of time devoted to differential position measurements. Several hours were spent in May 1975 and March 1976 making continuous observations of 3C 345, PKS 1633+38 and NRAO 512. Since the observations were all in the same region of the sky and integrated for less than three minutes, the general observing geometry was weakened. All observing sessions in set C ran approximately one day. Data taken during August 1975 are not included because of a faulty frequency channel and a major contraction in the observing session.

The 40-m antenna at OVRO became available in Sept. 1976 after completion of a new receiver and arrival of a GSFC maser. The data from the Haystack-OVRO baseline form set D. 76/09/09 was the first test day on the baseline and used a peculiar observing schedule. Between 76/09/29 and 76/10/15 a major effort was made to acquire a large amount of data. However, the schedules used were complicated by incomplete analysis of the test results, inexperience with the OVRO antenna, and a desire to try many types of observations. While the time spanned by individual sets is not continuous, much of the intervening time was occupied doing other observations which could not be used for the present purpose. The sets from Dec. 1976 also represent a continuous period of observation broken by other work. Each set in Sept.-Dec. 1976 is approximately one day of data. Although there are gaps of several hours in the data from March 1977, the data are continuous enough to treat as a single four-day set. June 1977 is a short one-day session. An experiment was undertaken in Sept. 1977, but an undiagnosed electronics problem at OVRO apparently caused the baseline to fail completely.

During 1972-74 and 1976-77 the 43-m NRAO telescope at Green Bank, W. Va. was also in use. However the erratic behavior of its clock made the data on its baselines difficult to use, especially in 1973-74. In 1976-77 the clock was much improved, but the full observing bandwidth available at OVRO and Haystack was not possible on the NRAO receiver. The baselines with NRAO are similar to the baselines with Haystack while the Haystack-NRAO baseline is too short to be of much use. Because of the clock problems and the nature of the NRAO baselines, no

data from Green Bank are included.

The sources used in each combined set are given in table III.4.

The raw data tapes were processed on the Haystack Mark I correlator and passed through a series of programs (VLBI1, VLBI2, and VLBCARDS) to yield delay and delay rate observables. Measurement uncertainties were computed on the basis of correlation, observing bandwidth, and integration time. The data from each small set were edited and the delays were corrected for group delay ambiguity. The sessions in sets A and B were largely edited by D. S. Robertson at MIT and Haystack Observatory. Sets C and D were edited on the GSFC HP 21MX, again mostly by D. S. Robertson, using programs developed to support the Mark III system.

After the individual sets were edited, the measurement uncertainties were adjusted in order to prevent biases caused by incorrect relative weighting of single experiment data sets when combining several sets together. A multiplicative factor was used for experiments in sets A and B. A fit of baseline parameters, source positions, an atmosphere parameter for each site and day, and terms of the necessary clock polynomials was done for each small set. The sessions in set A generally required only a single clock offset and rate. The exception was 73/02/04 which needed a quadratic term. The experiments in set B all required a larger number of clock polynomials and more terms in each polynomial to fit the data at a adequate level. Each fit was done using only delay data. After fitting, the

Table III.4 Number of observations by source and combined data set for diurnal polar motion data

| source | Set A 72/4 - 73/3 | Set B 73/8 - 74/7 | Set C 75/1 - 76/3 | Set D 76/9 - 77/6 |
|--------------|----------------------|----------------------|----------------------|----------------------|
| 4C 67.05 | | | 10 | |
| 3C84 | 21 | 650 | 104 | 263 |
| NRAO 140 | 34 | | | |
| CTA 26 | 14 | | | |
| NRAO 150 | 9 | 180 | 47 | 95 |
| 3C 120 | 112 | 150 | 57 | 66 |
| OJ 287 | 86 | 82 | 17 | 3 |
| 4C 39.2 | 76 | 264 | 14 | 254 |
| 3C 273B | 219 | 234 | 29 | 146 |
| 3C 279 | 201 | 99 | 39 | 83 |
| OQ 208 | 38 | | 2 | |
| PKS 1633+38 | | | 61 | |
| NRAO 512 | 71 | 60 | 52 | |
| 3C 345 | 115 | 367 | 76 | 114 |
| 3C 418 | 30 | 27 | | |
| PKS 2134+00 | 92 | 132 | 23 | 180 |
| VRO 42.22.01 | 110 | 249 | 13 | 210 |
| 3C 446 | | | 2 | |
| CTA 102 | 11 | | | |
| 3C 454.3 | 150 | 110 | 24 | 183 |

measurement uncertainties of the delay points in a set were multiplied by a single factor to bring the root-scaled-mean-square post-fit residual (RSMS) to unity. The RSMS was computed by

$$RSMS = \left(\frac{\sum (wr)^2}{N} \right)^{1/2} \quad \text{III.E.1}$$

where

w = 1/measurement uncertainty

r = post-fit residual

N = number of included data points

The delay rate data were not used. Delay rate data when included properly do not reduce the formal error of the diurnal polar motion scaling factor by a large amount nor change the scaling factor significantly.

For the individual sets in combined sets C and D an additive constant was used to adjust the delay measurement uncertainties. An additive adjustment is more desirable than a multiplicative adjustment since it is more likely to represent the behavior of the actual scatter. However, an additive adjustment requires knowledge of the original measurement uncertainties, which was not available for sets A and B. A fit was done for each set adjusting baseline, source, atmosphere, and clock parameters. Only a single clock offset and rate were used for each day interval. An additive constant was calculated which, when root-sum-square added to the measurement uncertainty of each delay point, adjusted the RSMS to unity.

Both methods of adjusting measurement uncertainties represent heuristic approaches to the problem of determining the true uncertainties. The multiplicative factor is easy to compute since it leaves the relative weight of each point in a day's solution unchanged. Computing the additive term requires an iterative approach since the relative weight of the individual data points is changed. The latter is probably a better approach if the noise in the data is the result of random fluctuations which were not considered in calculating the original measurement uncertainties.

Although the Mark III programs were used in editing some data, the number of parameters to be adjusted simultaneously for each large data set was too large to be handled. The process of parameter estimation was accomplished on the GSFC IBM 360/91 using the least-squares estimation program VLBI3 developed by Robertson (1975) with modifications of the solid earth tide model by R. J. Cappallo. Instead of using a series tidal expansion, the tidal potential is calculated directly from lunar and solar positions. Both the series and direct models are given in section II.E.1. Additional changes were made to introduce the diurnal polar motion model and the partial derivative of the diurnal polar motion scaling factor. The partial derivative was checked by finite differences and by comparison with the derivative computed by program CALC.

While the combined data sets were grouped by baselines used, there is no theoretical restriction on treating all the data simultaneously when estimating diurnal polar motion. However the large

number of points and parameters made it impractical even using VLBI3. There is an advantage in treating the large sets separately. Since each set represents different geometries, equipment and observing schedules, independent estimates can be found. Consistency from different sets would strengthen the individual results. Some grouping of data is necessary. A single day's data cannot be used in estimating diurnal polar motion as the correlation between parameters is excessive. A longer time interval is necessary to separate the nearly diurnal signature of polar motion from other diurnal signatures. In addition, systematic effects caused by atmosphere and clock fluctuations tend to be absorbed in other parameter adjustments when using only one day of data.

The small data sets with measurement uncertainties rescaled were each passed through VLBI3 to check the rescaling procedure. The four combined sets were then grouped in a format to facilitate further processing. The original adjusted parameters used for the separate sets were retained and additional parameters for wobble and UT1 were added, a pair for each experiment. Wobble and UT1 were held fixed at the BIH values for the first experiment in each large data set to provide a reference. Wobble and UT1 had not been adjusted in the individual experiment fits since it is not possible to estimate all the baseline parameters and the earth's orientation simultaneously. Only the x-component of wobble was adjusted because the data for each day were generally strong in only one baseline. Since only delay data were used in adjusting the measurement uncertainties, the delay rate data were ignored in fitting the larger sets as well.

F. Estimation of the diurnal polar motion scale factor

The four large data sets were used to estimate the diurnal polar motion scaling factor. The set of adjusted parameters was varied in order to achieve a good fit. Different models for particular effects were used to test the stability of the parameter estimates.

The overall results are presented in table III.5. The table is divided by combined data set. Each set was analyzed in the same manner: 1) with the diurnal polar motion model disabled, 2) with the model applied and a unity scaling factor, and 3) with the scaling factor adjusted. The unity scale factor applies the McClure model without modification. The first group in each set is the result using only the parameters taken from the individual set estimates with the addition of wobble and UT1. The other results will be discussed in the next subsection. The root-weighted-mean-square post-fit residual (RWMS) is a measure of scatter in the data calculated by

$$RWMS = \left(\frac{\sum (wr)^2}{\sum (w)^2} \right)^{1/2} \quad \text{III.F.1}$$

where

$w = 1/\text{measurement uncertainty}$

$r = \text{post-fit residual}$

The RSMS defined in section III.E, on the other hand, compares the scatter to the data measurement uncertainties. The formal error is based only on the measurement uncertainty and the observation geometry

Table III.5 Estimate of diurnal polar motion scaling factor

- a. RWMS - root of weighted mean square delay residual (nsec)
- b. reduction from RWMS with model off (%)
- c. RSMS - root of scaled mean square delay residual (unitless)
- d. estimated diurnal polar motion scaling factor (unitless)
- e. formal error of diurnal polar motion scaling factor (unitless)
- f. formal error scaled by RSMS (unitless)

a. b. c. d. e. f.

Set A. 72/4 - 73/3

2 terms in each clock polynomial

| | | | | | | |
|----------------|------|------|-------|------|-----|-----|
| model off | .716 | | 2.638 | | | |
| model on | .699 | -2.4 | 2.576 | | | |
| model adjusted | .666 | -7.0 | 2.457 | 5.27 | .15 | .37 |

4 terms in each clock polynomial

| | | | | | | |
|----------------|------|------|-------|------|-----|-----|
| model off | .431 | | 1.587 | | | |
| model on | .417 | -3.2 | 1.537 | | | |
| model adjusted | .398 | -7.7 | 1.467 | 4.15 | .18 | .26 |

6 terms in each clock polynomial

| | | | | | | |
|----------------|------|------|-------|------|-----|-----|
| model off | .379 | | 1.396 | | | |
| model on | .364 | -4.0 | 1.343 | | | |
| model adjusted | .346 | -8.7 | 1.274 | 3.98 | .19 | .24 |

Set B. 73/8 - 74/7

2-4 terms in each clock polynomial

| | | | | | | |
|----------------|-------|------|-------|------|-----|-----|
| model off | 1.054 | | 1.433 | | | |
| model on | 1.044 | -0.9 | 1.419 | | | |
| model adjusted | 1.031 | -2.2 | 1.401 | 3.96 | .26 | .36 |

4 terms in each clock polynomial

| | | | | | | |
|----------------|------|------|-------|------|-----|-----|
| model off | .901 | | 1.225 | | | |
| model on | .891 | -1.1 | 1.211 | | | |
| model adjusted | .871 | -3.3 | 1.184 | 5.39 | .34 | .40 |

Set C. 75/1 - 76/3

2 terms in each clock polynomial

| | | | | | | |
|----------------|------|------|-------|------|-----|-----|
| model off | .547 | | 1.193 | | | |
| model on | .544 | -0.6 | 1.186 | | | |
| model adjusted | .542 | -1.0 | 1.181 | 2.96 | .71 | .84 |

4 terms in each clock polynomial

| | | | | | | |
|----------------|------|------|-------|------|------|------|
| model off | .478 | | 1.042 | | | |
| model on | .477 | -0.2 | 1.040 | | | |
| model adjusted | .477 | -0.2 | 1.040 | 2.81 | 1.32 | 1.37 |

Set D. 76/9 - 77/6

2 terms in each clock polynomial

| | | | | | | |
|----------------|------|-------|-------|------|-----|-----|
| model off | .416 | | 2.921 | | | |
| model on | .389 | -6.5 | 2.735 | | | |
| model adjusted | .361 | -13.2 | 2.535 | 3.42 | .06 | .15 |

4 terms in each clock polynomial

| | | | | | | |
|----------------|------|------|-------|------|-----|-----|
| model off | .284 | | 1.991 | | | |
| model on | .268 | -5.6 | 1.887 | | | |
| model adjusted | .256 | -9.9 | 1.800 | 3.02 | .09 | .16 |

8 terms in each clock polynomial

| | | | | | | |
|----------------|------|------|-------|------|-----|-----|
| model off | .242 | | 1.702 | | | |
| model on | .230 | -5.0 | 1.612 | | | |
| model adjusted | .219 | -9.5 | 1.541 | 2.92 | .10 | .15 |

while the scaled formal error includes the actual scatter of the data.

There is considerable variation in both RWMS and RSMS. Set D (1976-77) has the smallest RWMS. However, it has the largest RSMS indicating that errors were hidden in the individual set fits. Since the baseline and source coordinates are common to all points in the estimate, these parameters can no longer compensate for other errors as was possible in the individual set estimates. Set B (1973-74) has the largest RWMS but smaller RSMS, a sign that the original parameterization was more complete than for set D. Set A (1972-73) is intermediate in RWMS and RSMS while Set C (1975-5) has relatively small RWMS and RSMS.

Turning the model on and adjusting the scaling factor progressively improved the fit for all sets. The greatest change is in set D where a unity scaling factor reduces the RWMS by 6.5% compared to the model-off case and the adjusted scaling factor reduces the RWMS by 13.2%. If the same effects with different magnitudes were responsible for the scatter in all sets, it is reasonable that the least noisy set should have the greatest reduction when diurnal polar motion is applied. The improvement in residuals for set C is quite small and statistically insignificant. The formal error for the scaling factor is also more than twice that for any other data set. Set C therefore probably does not give a useful estimate of the scaling factor even though the RWMS is second smallest and the estimated scale factor is not greatly different from the other estimates. This lack of sensitivity is not unexpected since set C has the smallest number of

data points despite spanning the largest time interval. The data were also not well distributed within the individual days.

1. Clock parameterization

When the original parameters are used, the RSMS and residual plots provided by VLBI3 indicate that effects hidden in the individual experiment fits are being exposed. In many cases the residual for different sources with interleaved observations followed a similar trend. The probable cause is instability in the frequency standards over a few hours. Small amplitude fluctuations are easily absorbed in other adjusted parameters in a single day fit.

There are two methods for improving the parameterization of the clocks in VLBI3, both somewhat ad hoc. Additional short clock polynomials may be introduced so that each polynomial models the clock for a smaller time interval. The clock model is then a discontinuous function over a day. Alternately, the number of terms in each clock polynomial can be increased to model more complex clock fluctuations. The latter method was used largely for reasons of convenience. Adding more polynomials is more tedious and prone to error than adding more terms. In addition, the choice of epochs for the new polynomials in order to maximize the reduction of residuals depends on personal judgment and can lead to biases. The number of terms in the original clock polynomials, generally two, was increased in steps until either a program limit was reached or the scaled formal error of the diurnal polar motion scaling factor increased significantly. Expanding the

number of parameters in an estimate usually increases the formal error of any previously included parameters. At the same time the fit improves and the RMS decreases. If the scaled formal error of the parameter of interest is smaller, then the additional parameters model the data in some sense correctly. Even if the scaled formal error remains constant, the parameter estimate may still be improved as the new parameters redistribute the parameter corrections.

The results with additional clock terms are shown in table III.5.

In two cases, sets A and D, program limits restricted the number of terms in the clock polynomials. The scaled formal error or RWMS improves until the limit is reached. The improvement in RWMS is quite marked. For set A the RWMS decreases by 40% and 47% when the number of clock terms is raised from 2 to 4 and 6, respectively. The RWMS of set D decreases by 30% and 40% with 4 and 8 terms. The larger reduction in set A probably indicates that the clocks were less stable during 1972-73 than during 1976-77. As the number of clock terms is increased, the improvement in RWMS from first applying the polar motion model and then adjusting the scaling factor remains fairly constant. For set A the improvement is slightly enhanced as the number increases while the opposite occurs in set D. The diurnal polar motion scaling factor changes when new clock terms are added. However, the changes are considerably smaller than the change in RWMS for the first increment and are within the scaled formal error for the second step. In both cases the scaling factor decreases. If more clock terms had been added, it would be reasonable to expect the scaling factor to

reach an asymptotic value and the scaled formal error to rise sharply. The correlation between different terms in the same clock polynomial increases drastically with increasing number. The correlation between the diurnal polar motion scaling factor and other parameters remains small, always less than 0.45. The largest correlations are with some source declinations.

In the two other cases, sets B and C, the scaled formal error increased with additional clock terms. Since these two sets originally had the lowest RMS it could be expected that additional terms would produce less improvement. The decrease in RMS is insufficient to balance the increase in the number of adjusted parameters. The number of clock terms was therefore kept at the original number for later analyses.

2. Residual behavior

The behavior of the post-fit residuals plotted by VLBI3 differed considerably from set to set and within each set. A few general remarks can be made.

If the residuals for all the sources are considered as a group, the magnitude of drifting is greatly reduced by increasing the number of clock terms. The overall pattern appears random. Unfortunately the residual pattern for a given source has a systematic behavior which is usually different from that of other sources. Part of the trend can often be traced to the atmosphere model, which is less accurate at low

elevation angles. As the elevation decreases, the residuals for a source can show a systematic departure from the former behavior leading generally to larger residuals.

The residuals do not change appearance in any marked way when the diurnal polar motion model is activated or adjusted. While the overall scatter is reduced, the individual source trends are only slightly modified. There are a few cases where the residuals from different sources for an interval of hours are simultaneously brought nearer zero from both positive and negative values. The opposite also occurs. A comparison of the expected signature of diurnal polar motion for several days from figures III.16-20 with the actual residual plots shows no similarity. With a unity scaling factor the magnitude of the effect is under 0.5 nsec. The RMS is comparable or larger for all data sets. The individual source trends are often smaller, more frequently in set D. Since the effect of diurnal polar motion is relatively small, it is not surprising that the effect is masked in the residuals. Small corrections are easily absorbed by small adjustments in other fitted parameters.

The constituent small data sets are affected quite differently by the process of combination. If the data were all uniform in biases and noise sources, combining sets should affect the individual sets equally. However the RMS for individual sets varies by nearly a factor of three in set D. The variation in the other sets is much less. Since the individual sets are parameterized in fairly similar ways, the variation in RMS indicates that the errors present in the

data are quite different from day to day, at least in set D. Adjusting the diurnal polar motion scaling factor reduces the overall scatter but not uniformly over all small sets. While the scatter in most sets is smaller by varying amounts, the scatter on a few sets is larger although not substantially. This divergence occurs more frequently in set D. The effect of diurnal polar motion varies over the interval included in each combined set and it is to be expected that the degree of residual reduction should vary with experiment. It is not clear why the residuals should increase occasionally. One possibility is that the scaling factor is not constant and the model therefore introduces too much correction at some times.

3. Effect of phase variation

The model for diurnal polar motion defines a specific phase for the instantaneous angular momentum polar motion, i.e., a particular pole direction relative to the slowly moving pole. During a day this phase goes through approximately one turn. The phase is not affected by the scaling factor. There may be phase lag or lead that the model does not predict. A modification to program VLBI3 was made to examine this question.

There is another reason for considering the phase of diurnal polar motion. In a purely mathematical sense the model is a construct whose physical reality is open to question. The fitting process gives a value for the scaling factor which may represent only noise. If the model is entirely unphysical an arbitrary change in phase should cause

the fit to respond to different noise and give a scaling factor value which is not related in the manner which the model predicts.

The phase was investigated by changing the model rather than by introducing a new parameter. The choice was dictated largely by practical considerations but allows a more detailed analysis. The main disadvantage is that the formal error of the phase lag/lead cannot be determined directly. The terms in eq. III.C.14 and III.C.15, which give the cartesian components of the angular momentum pole position, all contain w (Greenwich mean sidereal time) as one of the arguments. A change in w directly changes the phase of the polar motion. The program was modified so that H_{1d} and H_{2d} were calculated using a new argument v in place of w , where v is the Greenwich mean sidereal time with an arbitrary phase added. For example, a phase addition of 180 deg would reverse the direction of the pole. The correction to the z-rotation in III.C.11 was unaffected.

Each large data set was re-analyzed using a series of values for the phase lead. The results for set D are presented in table III.6. The results from sets A and B are similar in character. The phase lead was incremented in steps of 30 deg. For each phase lead the scaling factor was estimated along with other parameters. Several points should be noted. The scale factor has a maximum between 300 and 330 deg and a minimum 180 deg away. The values separated by 180 deg are not of equal magnitude and opposite sign because the phase lag/lead does not affect the third rotation in the diurnal polar motion matrix related to the separation of the spin and angular momentum vectors.

Table III.6 Effect of phase on adjusted diurnal polar motion scaling factor using Set D and 8 terms in each clock polynomial

| phase lead degrees | RMS nsec | RMS | scale factor | error | scaled error |
|-----------------------|-------------|-------|--------------|-------|--------------|
| 0 | .219 | 1.541 | 2.92 | .101 | .156 |
| 30 | .237 | 1.662 | 1.50 | .101 | .168 |
| 60 | .242 | 1.702 | -0.12 | .099 | .169 |
| 90 | .237 | 1.663 | -1.36 | .097 | .162 |
| 120 | .231 | 1.622 | -1.99 | .096 | .156 |
| 150 | .232 | 1.626 | -1.98 | .098 | .159 |
| 180 | .239 | 1.676 | -1.22 | .101 | .169 |
| 210 | .242 | 1.702 | 0.23 | .103 | .175 |
| 240 | .234 | 1.641 | 1.85 | .101 | .166 |
| 270 | .216 | 1.519 | 3.05 | .099 | .150 |
| 300 | .203 | 1.423 | 3.66 | .098 | .139 |
| 330 | .204 | 1.430 | 3.66 | .099 | .142 |

90 deg removed from the extremes the scaling factor is nearest zero. The RMS and RSMS have minima at 300 deg and maxima at 60 and 210 deg.

The behavior of the various quantities is consistent with the geometry of the diurnal polar motion model assuming a phase lag of 44 deg. Since a negative scale factor reverses the direction of the pole, the negative values 180 deg away from the maximum value indicate that the estimated scale factors force the pole to the correct direction. If the phase effect is real, the scale factor at quadrature phase from the maximum should be zero as it is. The scatter is smallest when the scale factor is largest. If the model were unphysical, the minimum scatter and maximum scale factor would not necessarily be related. The scatter is largest at quadrature phase where the zero scaling factor disables the model. 180 deg away from the maximum scale factor the scatter has a local minimum. The direction of the pole is correct but the magnitude of displacement is smaller than it should be.

The results for the three sets A, B, and D are summarized in table III.7. The same procedure applied to set C does not give a smooth variation of scale factor with phase lead, a result consistent with the poor sensitivity of the data. Sets A and B have nearly identical phase leads of approximately 10 deg while set C diverges at -44 deg. The difference may be caused by the respective time intervals covered. Sets A and B both span one year fairly uniformly. Set C contains only ten months with a preponderance of data near the beginning. More than half the points are in the first month.

Table III.7 Diurnal polar motion scaling factor with phase corrected

| | clock terms | phase lead degrees | RWMS nsec | RSMS | scale factor | error | scaled error |
|--------|----------------|-----------------------|--------------|-------|--------------|-------|--------------|
| Set A. | 6 | 11 | .346 | 1.274 | 4.03 | .19 | .24 |
| Set B. | 2-4 | 10 | 1.029 | 1.398 | 4.12 | .26 | .36 |
| Set D. | 8 | -44 | .201 | 1.411 | 3.74 | .098 | .14 |

Weighted mean scaling factor: 3.84

4. Significance test

The statistical significance of adjusting the single additional parameter for diurnal polar motion can be tested using the F distribution. Bevington (1969) defines a quantity F_{χ} which measures the improvement in the fit caused by the introduction of a new parameter. The reduced chi-square χ^2 is used.

$$F_{\chi} = \frac{\chi^2(n-1) - \chi^2(n)}{\chi^2(n)/(N-n-1)} \quad \text{III.F.5.1}$$

where

n = number of parameters

N = number of data points

$\chi^2(n)$ = reduced chi-square with n parameters adjusted

The larger the value of F_{χ} , the smaller is the probability that the improvement in fit is accidental and the larger is the probability that the additional parameter is statistically significant. The results for the F_{χ} test are given in table III.8 for sets A, B, and D. The value of F_{χ} which has a given probability of chance occurrence depends on the number of degrees of freedom in the fit. For 120 degrees of freedom the probability (from Bevington table C-5) of F_{χ} exceeding 11.4 by chance is 0.1%. For an infinite number of degrees of freedom the 0.1% probability value of F_{χ} is 10.8. F_{χ} values with probabilities less than 0.1% would be larger, but table C-5 stops at 0.1%. The number of degrees of freedom exceeds 120 and F_{χ} is greater than 100 in all three cases. Since the value of F_{χ} is much larger than would occur by

Table III.8 F value significance tests for adjustment of diurnal polar motion scaling factor

| | Set A. 72/4 - 73/3 | Set B. 73/8 - 74/7 | Set D. 76/9 - 77/6 |
|---------------------------------|-----------------------|-----------------------|-----------------------|
| number of parameters | 131 | 159 | 177 |
| number of data points | 1389 | 2605 | 1597 |
| degrees of freedom | 1258 | 2446 | 1420 |
| chi-squared with model off | 2707 | 5351 | 4629 |
| chi-squared with model adjusted | 2253 | 5094 | 3181 |
| F_{χ} value | 254 | 123 | 646 |

For 120 degrees of freedom, the probability of F_{χ} exceeding 11 is 0.1%.

chance, the additional diurnal polar motion parameter is statistically significant. The level of confidence is considerably better than the 0.1% level. It should be noted that this test does not mean that the formal error of the diurnal polar motion scaling factor is 0.1%. The additional parameter is not significant in set C.

G. Comparison with literature

There is a dearth of literature on the topic of forced diurnal polar motion. The results of four investigations are given in table III.9. Only a single term, the fortnightly component proportional to $\sin(S - 2L)$, where S is the sidereal time of observation and L is the lunar longitude, has been studied. The data are exclusively optical based on visual zenith telescope and photographic zenith telescope observations taken by the IPMS-ILS, the U. S. Naval Observatory, and the Royal Greenwich Observatory. The various optical studies suffer from similar limitations. There is a problem of selection inherent in using transit, nighttime observations. Instrumental and observer personal equation errors are difficult to remove. The effect of diurnal and semi-diurnal earth tides on the vertical must be corrected. The methods of data reduction analyze the residuals of the individual observations relative to a smoothed set of data. The slowly changing signature of the lunar longitude rather than the diurnal signature is isolated in the data. Only a small set of parameters are adjusted, the source positions being fixed.

Even though there is an overlap in the data used in the different

Table III.9 Fortnightly diurnal polar motion

| Author | site | type | date | amplitude arcsec | error arcsec | phase deg | error deg |
|----------|--------------|------|---------|---------------------|-----------------|--------------|--------------|
| McCarthy | Washington | PZT | 1915-73 | | | | |
| | Richmond | PZT | 1949-73 | | | | |
| | Herstmonceux | PZT | 1958-70 | 0.0058 | 0.0002 | | |
| O'Hara | Herstmonceux | PZT | 1958-70 | 0.010 | 0.002 | 7.2 | 11. |
| Federov | Carloforte | VZT | 1900-34 | | | | |
| | Mizusawa | VZT | 1900-34 | | | | |
| | Ukiah | VZT | 1900-34 | | | | |
| | Pulkovo | VZT | 1915-28 | | | | |
| | Washington | PZT | 1931-51 | 0.009 | 0.001 | 14. | 6. |
| Morgan | Washington | PZT | 1931-51 | 0.0067 | 0.0013 | | |

PZT photographic zenith telescope

VZT visual zenith telescope

analyses, the results diverge. McCarthy (1976) has the smallest value for the amplitude of the fortnightly term (0.0058") but does not consider a phase offset. Federov (1963) gives a larger value (0.009") and a phase lead of 14 deg. Morgan (1952) presents a value (0.0067") consistent with rigid earth theory and considers it confirmation for the theory. O'Hara (1973) finds the largest value (0.010") but the corresponding period in the data is anomalous. Because of the substantial difference between the VLBI and optical studies in data (delay vs zenith angle), the interval of data (5 years vs 73 years), the distribution of data (wide hour angle and declination coverage vs fixed zero hour angle and station co-latitude), the number of diurnal polar motion terms considered (seven vs one), and the methods of analysis (simultaneous adjustment of all parameters vs stepwise adjustment of a few parameters), any comparison between the VLBI and optical results is difficult.

H. Interpretation of the estimated diurnal polar motion scaling factor

There are a number of phenomena which are related to diurnal polar motion and which might contribute to the large magnitude of the estimated scaling factor. These include solid earth tides, nutation, and core-mantle interactions.

1. Solid earth tides

The lunar and solar torques which drive diurnal polar motion also cause solid earth tides. McClure uses Doodson's tidal potential

development as a starting point in deriving the various diurnal polar motion terms. The periods of diurnal polar motion consequently have identical counterparts in the diurnal solid earth tides. The overall effects are quite different in character however. The solid earth tide has a strong semi-diurnal component as well as a diurnal component. The earth tide changes both the length and orientation of a baseline while diurnal polar motion only affects orientation. Nonetheless it is possible that the two effects are entangled in the data analysis. The relative effects of tides and diurnal polar motion and the effect of the tide model on estimates of the scaling factor were examined. The clock parameterization that previously had given the best results was retained.

The effects of solid earth tides are given in table III.10.

Table III.10 divides the data by large set. The measures of scatter, RWMS and RSMS, are given for five conditions: 1) both tide and diurnal polar motion set to zero, 2) tide model applied with diurnal polar motion zero, 3) polar motion applied with unity scaling factor and tide zero, 4) scaling factor adjusted with tide zero, and 5) scaling factor adjusted with tide model applied. In general the reduction in RWMS caused by the tide and polar motion models in the absence of the other are approximately equal. With the tide model disabled, adjusting the diurnal polar motion scaling factor (case 4) reduces the RWMS approximately twice as much as merely applying the model with unity scaling factor (case 3). The estimated scale factor with the tide model disabled (case 4) is higher than with the tide

Table III.10 Effect of solid earth tide on diurnal polar motion scaling factor

- a. RMS - root of weighted mean square delay residual (nsec)
- b. reduction from RMS with polar motion and tide off (%)
- c. RSMS - root of scaled mean square delay residual (unitless)
- d. estimated diurnal polar motion scaling factor (unitless)
- e. formal error of diurnal polar motion scaling factor (unitless)
- f. formal error scaled by RSMS (unitless)

- 1. tide and diurnal polar motion off
- 2. tide on, diurnal polar motion off
- 3. tide off, diurnal polar motion on
- 4. tide off, scaling factor adjusted
- 5. tide on, scaling factor adjusted

a. b. c. d. e. f.

Set A. 72/4 - 73/3

6 terms in each clock polynomial

| | | | | | | |
|----|------|-------|-------|------|-----|-----|
| 1. | .386 | | 1.422 | | | |
| 2. | .379 | -1.8 | 1.396 | | | |
| 3. | .371 | -3.9 | 1.368 | | | |
| 4. | .551 | -9.1 | 1.294 | 4.11 | .19 | .25 |
| 5. | .345 | -10.4 | 1.274 | 3.98 | .19 | .24 |

Set B. 73/8 - 74/7

2-4 terms in each clock polynomial

| | | | | | | |
|----|-------|------|-------|------|-----|-----|
| 1. | 1.054 | | 1.445 | | | |
| 2. | 1.054 | -0.9 | 1.435 | | | |
| 3. | 1.052 | -1.1 | 1.429 | | | |
| 4. | 1.033 | -2.9 | 1.404 | 4.47 | .26 | .37 |
| 5. | 1.031 | -3.1 | 1.401 | 3.96 | .26 | .36 |

Set C. 75/1 - 76/3

2 terms in each clock polynomial

| | | | | | | |
|----|------|------|-------|------|-----|-----|
| 1. | .543 | | 1.185 | | | |
| 2. | .547 | +0.7 | 1.193 | | | |
| 3. | .540 | -0.6 | 1.176 | | | |
| 4. | .536 | -1.3 | 1.169 | 3.42 | .71 | .83 |
| 5. | .542 | -0.2 | 1.181 | 2.96 | .71 | .84 |

Set D. 76/9 - 77/6

8 terms in each clock polynomial

| | | | | | | |
|----|------|------|-------|------|-----|-----|
| 1. | .242 | | 1.698 | | | |
| 2. | .242 | +0.0 | 1.702 | | | |
| 3. | .230 | -5.0 | 1.613 | | | |
| 4. | .221 | -8.7 | 1.550 | 2.79 | .10 | .16 |
| 5. | .219 | -9.5 | 1.541 | 2.92 | .10 | .15 |

model applied (case 5) except in one instance, an indication that the two effects can mix. However the RMS is larger in case 4 than in case 5 so that the diurnal polar motion adjustment cannot completely absorb the tide errors. The difference between the scale factor estimates in the two cases is less than 15%. Since the absence and presence of the tide model changes the scaling factor by only a small amount, it is unlikely that errors in the Love numbers, which scale the solid earth tide, account for the magnitude of the diurnal polar motion scaling factor.

2. Nutation

Nutation and diurnal polar motion are connected in two distinct ways. Kinematically, the amplitudes of nutation and diurnal polar motion have a theoretical fixed ratio given by Sasao (1977) as

$$M = - \frac{n}{\omega} N \quad \text{III.H.2.1}$$

where

M = diurnal figure polar motion

n = nutation frequency

ω = sidereal rotation frequency

N = nutation of the figure axis

For each term in a series development of nutation there is a corresponding term in diurnal polar motion. The factor n/ω reduces the amplitude of diurnal polar motion relative to nutation since $n \ll \omega$.

A geometrical relationship causes errors in nutation to map into false apparent diurnal polar motion. An error in any coefficient in the nutation series causes a separation between the celestial positions of the true celestial pole (the intersection of the spin axis with the celestial sphere, hereafter TCP) and the computed celestial pole (CCP). When projected back on the surface of the earth, the CCP will be removed from the spin pole (the projection of the TCP) by an angle equal to the error in nutation. The projection of the CCP follows a circle about the spin pole during the course of a day as the earth rotates. Since the CCP rather than the TCP enters into the models used to analyze the data, there is an apparent diurnal polar motion. Both the amplitude and phase of the apparent diurnal polar motion can change as the CCP moves relative to the TCP in the celestial reference frame over the period of the corresponding nutation. For example, if the nutation error is in a single term, either obliquity or longitude, the separation between the TCP and CCP is zero twice in each nutation period. At those times the amplitude of the apparent diurnal polar motion is also zero. If the errors in obliquity and longitude for a single nutation frequency are equal, the CCP moves in a circle about the TCP. The apparent diurnal polar motion is constant in amplitude but changes phase during a nutation period. The net effect of unrelated errors in obliquity and longitude in several nutation terms is consequently quite complicated.

The nutation series of Woolard (1953) is derived from a rigid earth. There are discrepancies which have been observed and corrections computed from more elaborate earth models. Melchior (1971)

has done extensive studies using vertical and horizontal earth tide measurements. The magnitude of a single nutation term is directly related to the magnitudes of a corresponding pair of diurnal earth tides. The total nutation is given by

$$\Delta\psi \sin \epsilon = -E \int \left[\frac{\omega}{d\omega_i} (A_i + A_{-i}) \sin(d\omega_i t) \right] \quad \text{III.H.2.2}$$

$$\Delta\epsilon = -E \int \left[\frac{\omega}{d\omega_i} (A_i - A_{-i}) \cos(d\omega_i t) \right] \quad \text{III.H.2.3}$$

where

$\Delta\psi \sin \epsilon$ = nutation in longitude

$\Delta\epsilon$ = nutation in obliquity

E = lunar or solar constant

ω = sidereal rotation frequency

$d\omega_i = \omega_i - \omega$

ω_i = tidal frequency

A_i, A_{-i} = amplitudes of the tidal pair

The pair of tidal terms associated with a nutation term has tidal frequencies which are the sum and difference of the nutation frequency and the sidereal rotation frequency. The semi-major and semi-minor axes for the ellipse of a particular nutation term can be found from the sum and difference of the two associated tidal amplitudes. Federov (1959, 1963), McCarthy (1972, 1976), and Wako (1976) give values for various nutation terms based on optical observations. Sasao (1977) discusses corrections using models by Jeffreys, Molodensky, Pederson, and Kakuta. While there are disagreements

between different theoretical models, there is general agreement on the experimental results. The errors quoted for the corrected values are less than 0.005".

Melchior (1972) proposes changes to four major terms in the nutation series: principal nutation, annual, semi-annual, and semi-monthly. The only large term missing has a 9.3 year period. The values, corresponding tides, and astronomical arguments are given in table III.11. These values were used to examine the effect of nutation errors on the diurnal polar motion scaling factor because they came from a single body of data.

The program VLBI3 uses values for nutation in obliquity and longitude interpolated from tabular entries on the MIT PEP ephemeris tape. The PEP tape was made with Woolard's nutation series. VLBI3 was modified to correct the interpolated values to Melchior's values by

$$\Delta\epsilon = -0''.0086 \cos \Omega + 0''.0056 \cos \ell' + 0''.0202 \cos 2L' + 0''.0022 \cos 2L \quad \text{III.H.2.4}$$

$$\Delta\psi = +0''.0442 \sin \Omega + 0''.0193 \sin \ell' - 0''.0412 \sin 2L' - 0''.0043 \sin 2L \quad \text{III.H.2.5}$$

where

Ω = mean longitude of the ascending node of the lunar orbit

ℓ' = mean solar anomaly

L' = mean solar longitude

L = mean lunar longitude

The effect of nutation corrections is summarized in table III.12.

Table III.11 Proposed values for nutation coefficients (Melchior 1972)

| period days | tide code | argument | $\Delta\psi$ sine arcseconds | $\Delta\epsilon$ arcseconds |
|----------------|-----------|----------|---------------------------------|--------------------------------|
| 6798 | 165.545 | Ω | -6.8408 | +9.2014 |
| | 165.565 | | | |
| 365 | 164.556 | $1'$ | +0.0579 | +0.0056 |
| | 166.554 | | | |
| 163 | 163.555 | $2L'$ | -0.5230 | +0.5724 |
| | 167.555 | | | |
| 13.7 | 145.555 | $2L$ | -0.0828 | +0.0906 |
| | 185.555 | | | |

Ω = mean longitude of the ascending node of the lunar orbit

$1'$ = mean solar anomaly

L' = mean solar longitude

L = mean lunar longitude

Table III.12 Effect of nutation corrections on diurnal polar motion scaling factor

- a. RWMS - root of weighted mean square delay residual (nsec)
- b. reduction from RWMS with no nutation corrections (%)
- c. RSMS - root of scaled mean square delay residual (unitless)
- d. estimated diurnal polar motion scaling factor (unitless)

a. b. c. d.

Set A. 72/4 - 73/3

6 terms in each clock polynomial

| | | | | |
|--------------|------|------|-------|------|
| old nutation | .346 | | 1.274 | 3.98 |
| new nutation | .348 | +0.6 | 1.283 | 1.53 |

Set B. 73/8 - 74/7

2-4 terms in each clock polynomial

| | | | | |
|--------------|-------|------|-------|------|
| old nutation | 1.031 | | 1.401 | 3.96 |
| new nutation | 1.028 | -0.3 | 1.397 | 2.29 |

Set C. 75/1 - 76/3

2 terms in each clock polynomial

| | | | | |
|--------------|------|------|-------|------|
| old nutation | .542 | | 1.181 | 2.96 |
| new nutation | .505 | -6.8 | 1.102 | 1.35 |

Set D. 76/9 - 77/6

8 terms in each clock polynomial

| | | | | |
|--------------|------|-------|-------|------|
| old nutation | .219 | | 1.541 | 2.92 |
| new nutation | .137 | -37.4 | .963 | 2.31 |

The combined data sets were re-analyzed using the best clock parameterization correcting nutation terms. The effects on RWMS and RSMS, which reflect the scatter of the residuals, for each set are quite different. In set A the RWMS increases slightly. In set B there is a slight decline in RWMS. Sets C and D are much improved by the nutation corrections. The reduction in RWMS in set D is quite startling, 37%. The improvement appears in all individual sets in set D but not uniformly. The four terms corrected are the largest terms in the nutation series except for the 9.3 year term, whose coefficients in obliquity and longitude are comparable to the semi-monthly term. A correction of proportional magnitude to the 9.3 year nutation term has negligible effect on the scaling factor when applied to set D.

The scale factors and phase angles for sets A, B and D are summarized in table III.13 together with the F_{λ} significance test for adjusting the scale factor in the presence of the nutation corrections. The diurnal polar motion scale factor is reduced in every data set when the nutation corrections are applied. The greatest change occurs in set A even though there is no reduction in the overall scatter of the residuals. The weighted mean scale factor from the three sets changes from 3.84 without nutation corrections to 2.26 with nutation corrections. However the new value is still significantly different from unity, which would represent the McClure model. The phase angle is also changed by nutation corrections and the scatter in phase is reduced. The deviation from 0 deg may not be significant. Although

Table III.13 Diurnal polar motion scaling factor with nutation corrected

| | clock terms | phase lead degrees | RWMS nsec | RSMS | scale factor | error | scaled error |
|--------|----------------|-----------------------|--------------|-------|--------------|-------|--------------|
| Set A. | 6 | -26 | .346 | 1.274 | 1.74 | .19 | .24 |
| Set B. | 2-4 | 22 | 1.026 | 1.394 | 2.55 | .26 | .36 |
| Set D. | 8 | 6 | .137 | .960 | 2.33 | .10 | .097 |

Weighted mean scaling factor: 2.26

E_{χ} : set A - 64
 set B - 48
 set C - 512

the F_{χ} values for the inclusion of diurnal polar motion are smaller when nutation corrections are applied, they indicate that the inclusion of the diurnal polar motion parameter is still statistically significant at the 0.1% level.

The introduction of nutation corrections does change the diurnal polar motion scaling factor. However the Melchior corrections alone cannot explain the large magnitude since a significant part greater than unity remains. It is possible, though unlikely, that the remaining discrepancy could be removed by other nutation corrections.

A correction to the precession constant of 1.1 arcsec per century (Fricke 1971) has a negligible effect on the diurnal polar motion scaling factor and the post-fit residual scatter.

3. Core-mantle interactions

The elaboration of the earth model to include distinct core and mantle leads to a free diurnal polar motion of the rotation pole. Debarbat (1972) and Yatskiv (1972) present evidence for its existence in latitude and time data with a magnitude of 0.13" and a period of 200 days. However, Toomre (1974) and Rochester et al (1974) point out that a much larger corresponding nutation with a period near 460 days must also occur but is not seen in their data, putting an upper limit of 0.0006" on the amplitude of the free diurnal polar motion. This motion is therefore probably not affecting the VLBI data because of its small amplitude and because of the long period of its corresponding

nutration.

Core-mantle interactions also affect the terms of diurnal polar motion directly. Since nutation and diurnal polar motion have a fixed kinematical relationship, proportional effects should occur in both. Sasao (1977) and Melchior (1971) list the scaling of various nutation terms for different earth models and nutation frequencies. The effect on the amplitude of nutation is less than 50% for all models and frequencies. The core-mantle effect is less than 20% except for a few frequencies where a resonance occurs. Since the change in the amplitude of diurnal polar motion is proportional, the change is too small to explain the large estimated scale factor.

McClure (1976) considers another core-mantle effect that is potentially important although the exact implications are far from clear. Using a generalized, rigid shell, inertial coupling model, he finds that both the free core mode and a resonant response to the 166.554 tide can lead to a large separation between the spin vector and angular momentum vector without a corresponding large nutation term. He calculates the separation to be 0.20" for the free mode and 0.006" for the resonant mode. When viewed in the inertial reference frame the spin vector rotates around the angular momentum vector with periods of 347 days and one year, respectively. The separation of spin and angular momentum leads to a correction in time given in III.C.11. Since the free mode separation is so large, it may affect the scaling of the time correction in the diurnal polar motion matrix D even though the celestial period is different from the periods of the terms in

diurnal polar motion. However, since the period is long compared to an observing day, the effect may be absorbed in the UT1 adjustment.

4. Other effects

There are other phenomena which affect the data and may influence the estimated diurnal polar motion scaling factor. These include effects which are not modeled or are poorly modeled. In the first category are source structure, the ionosphere, and hardware problems such as cable length variations, antenna flexure, and unknown characteristics of the electronics. In the second class are the dry and wet components of the atmosphere. It is impossible to assign exact numerical values to each effect. However, some very rough comparative estimates can be made. Cable lengths and antenna flexure tend to have solar diurnal signatures because of temperature and sunlight variations over a day. Their effects on the delay observable are not strongly dependent on the particular source. The unknown characteristics of the electronics should be largely independent of source and time of day. Since these effects are source-independent and do not have the same long term behavior as diurnal polar motion, they would be expected to have a very small effect on the scaling factor. Source structure affects delay depending on the size and complexity of the observed sources. Apparent changes in position over a day and over a year probably affect the data somewhat more than does the hardware. The ionosphere, while having wide variations, should be absorbed to a great extent in the much larger adjusted atmosphere parameters. It has a strongly solar diurnal signature in contrast to the sidereal signature

of diurnal polar motion. Consequently, the ionosphere should have an effect less than that of source structure. Variations of the atmosphere delay over a day, especially in stormy weather, are not adequately modeled in the present analysis. Such variations should not map strongly into the diurnal polar motion scale factor however. The atmosphere variations are independent of source and have irregular time scales. The effect of the atmosphere is greatest when a source is near the horizon while the effect of diurnal polar motion is quite often largest when the source is high. Because the overall atmospheric delay is large compared to the other phenomena, the effect of the dry and wet component variations is likely to be somewhat larger. The combined effect of all these phenomena on the diurnal polar motion scaling factor is probably an error of less than 10%.

5. Conclusions

Errors in the solid earth tide and nutation models do not fully explain the magnitude of the diurnal polar motion scaling factor, 2.3 +/- 10% compared to 1 for McClure's model. Rescaling of diurnal polar motion to account for simple core-mantle interaction is likewise inadequate to explain the observed effects. Investigation is required of more complex earth models perhaps incorporating dissipative and magnetic core-mantle coupling and of the effect of large spin-angular momentum separation described by McClure.

Chapter IV.

SIMULATION OF HIGH PRECISION INTERFEROMETRIC EXPERIMENTS

The purpose of experiment simulation is twofold: 1) to determine the necessary conditions for achieving a particular result and 2) to get the best results given particular conditions. The two are related but the emphasis is different. For the first the motivating interest is to study different configurations of stations, equipment, observation schedules, parameter sets, physical models, and external constraints to see if a particular parameter or set of parameters can be measured with a required precision. The latter is of interest when an actual experimental configuration exists and the remaining free conditions, usually the observation schedule and the parameter set, are optimized to achieve the best results for different parameters. In this chapter I will first review the mathematical foundation used for experiment simulation. I will then analyze three measurements for which high precision interferometry could be used: 1) determination of the relativistic light deflection parameter by WOVLBI observations near Jupiter, 2) monitoring of polar motion and UT1 using the Mark III system, and 3) baseline determination with optimized schedules.

A. Statistical theory

This section develops the mathematical basis for experiment simulation and error analysis.

The terms precision and accuracy will be used with the following meanings. The precision of a particular parameter is the formal error associated with it by statistical analysis of a set of observations. The accuracy of a parameter is its agreement with the actual physical value.

1. Least squares covariance analysis

A basic approach for simulating an experiment is to use least squares covariance analysis. One begins with N observations that can be modeled by

$$O = F(X) + e \quad \text{IV.A.1.1}$$

O = vector of measured observable values (dimension N)

X = set of parameters to be adjusted (dimension M)

F = mathematical models for the effect of X on O

e = vector of observation errors (dimension N)

The equations are linearized by expanding, for the ith equation,

$$F_i(X) = F_i(X_0) + \sum_j \frac{\partial F_i}{\partial X_j} x_j \quad \text{IV.A.1.2}$$

In matrix form,

$$F(X) = F(X_0) + Bx \quad \text{IV.A.1.3}$$

$F(X_0)$ = mathematical models evaluated at the nominal parameter values which are assumed to be close to the true values
 = computed values of the observables (dimension N)

B = matrix of observation partials (dimension N by M)

x = vector of parameter corrections (dimension M)

The N linearized equations for observed - computed are then

$$\begin{aligned} z &= 0 - F(X_0) && \text{IV.A.1.4} \\ &= Bx + e \end{aligned}$$

The least squares solution $x(ls)$ is identified by minimizing the mean square observation error.

$$J = \sum_{i=1}^N e_i^2 = e^T e \quad \text{IV.A.1.5}$$

Then

$$J(x) = (z - Bx)^T (z - Bx) \quad \text{IV.A.1.6}$$

If more than one x minimizes the mean square error J , then $x(ls)$ is further specified by minimizing the scalar length of x ,

$$|x| = (\sum x^2)^{1/2} \quad \text{IV.A.1.7}$$

$J(x)$ is non-negative and quadratic in components of x so that a necessary and sufficient condition for a minimum is that the first variation $dJ(x)$ equals zero. Differentiating the matrices and

rearranging the transposes,

$$\begin{aligned}
 dJ(x) &= d[(z - Bx)^T](z - Bx) + (z - Bx)^T d[z - Bx] & \text{IV.A.1.8} \\
 &= (-Bdx)^T(z - Bx) + (z - Bx)^T(-Bdx) \\
 &= dx^T(B^T Bx - B^T z) + [dx^T(B^T Bx - B^T z)]^T
 \end{aligned}$$

For $dJ(x)$ to vanish for all variations in dx , x must satisfy the normal equation

$$B^T Bx = B^T z \quad \text{IV.A.1.9}$$

If $N > M$ and $(B^T B)$ is non-singular, then

$$x(ts) = (B^T B)^{-1} B^T z \quad \text{IV.A.1.10}$$

If the observation errors are random variables with zero mean and the equations have been normalized, then

$$E[e] = 0 \quad \text{IV.A.1.11}$$

$$\text{COV}[e] = E[ee^T] = I = \text{unit matrix of order } N \quad \text{IV.A.1.12}$$

$E[\]$ = expectation operator

$\text{COV}[\]$ = covariance

The expectation operator is linear so that

$$E[Ax + By + Cz + D] = A E[x] + B E[y] + C E[z] + D \quad \text{IV.A.1.13}$$

$A, B, C, D =$ deterministic matrices

$x, y =$ random matrices

Substituting in the normal equation for z ,

$$B^T Bx(ts) = B^T z = B^T (Bx + e) = B^T Bx + B^T e \quad \text{IV.A.1.14a}$$

$$B^T B(x(ts) - x) = B^T e \quad \text{IV.A.1.14b}$$

$$x(ts) - x = (B^T B)^{-1} B^T e \quad \text{IV.A.1.14c}$$

Then

$$E[x(ts) - x] = E[(B^T B)^{-1} B^T e] = (B^T B)^{-1} B^T E[e] = 0 \quad \text{IV.A.1.15}$$

The expectation value of $x(ts)$ is the same as the expectation value of

x . The covariance of the estimate is given by

$$\begin{aligned} \text{COV}\{x(ts) - x\} &= E\{(x(ts) - x)(x(ts) - x)^T\} \quad \text{IV.A.1.16} \\ &= (B^T B)^{-1} B^T E\{e e^T\} B (B^T B)^{-1} \\ &= (B^T B)^{-1} B^T B (B^T B)^{-1} = (B^T B)^{-1} \end{aligned}$$

If the normalization is included explicitly, then

$$x(ts) = (B^T W B)^{-1} B^T W z \quad \text{IV.A.1.17}$$

$$\text{COV}\{x(ts) - x\} = (B^T W B)^{-1} \quad \text{IV.A.1.18}$$

where

$$W^{-1} = E[ee^T]$$

It should be noted that any correlation between observation errors is explicitly included in W . However, the case usually considered assumes that W is diagonal and that the errors are random. The difficulties in handling correlated noise will be mentioned in a section IV.A.3.

The least squares covariance adjusting only the parameters of interest and using observation errors based on the quality of the original observations gives the most optimistic values for the formal errors in estimating those parameters. The parameters of interest are those for which the experiment was performed, e.g., baseline length or UT1 offset. Essentially it is assumed that no other phenomena affecting the theoretical observables exist or that any other effects are perfectly modeled. Hence, simple covariance analysis can only be used for rough experiment simulation.

2. Enlarged parameter set

The next step to more realistic parameter estimates is to increase X , the set of adjusted parameters, to include parameters of perhaps no intrinsic interest but whose variation affects the value of the observables. For VLBI observations these include tropospheric delay and clock behavior polynomials. Another set of parameters to be added would be those from models of secondary interest whose nominal values may not be precisely known, e.g., precession, solid earth tides, polar motion, and UT1 variation. An experiment simulation based on

this larger parameter set would give a more reasonable estimate of the formal errors of the parameters of interest.

There are some difficulties which arise from a larger parameter set. As the covariance matrix expands, the ability to estimate any one parameter declines and the formal error increases. At worst, especially if the added parameters are strongly correlated with the initial set because of similar time signatures, the normal matrix $(B^T W B)$ may become ill-conditioned. The resulting estimates of the parameters would be distorted by relatively small errors and the formal errors would not be a good measure of the accuracy of the estimation. It is necessary to be somewhat restrictive in the choice of parameter set.

A second difficulty is related to possible biasing of the estimates of the parameters of interest. If the added parameters are ad hoc, e.g., additional clock polynomials or additional terms to a given clock polynomial, they may absorb corrections which physically belong in other models. While the post-fit residuals may improve, the parameter estimates for the parameters of interest may be less accurate. A simulation based on such a parameter set would not give the correct estimate of the accuracy that can be achieved from the data. The true accuracy might be considerably better.

3. Errors and error models

If it is not possible to adjust all the parameters that affect

the observables, it is necessary to predict how various error sources will affect the parameters that are adjusted. There are several types of errors and error models that should be distinguished.

The first type of uncertainty is measurement uncertainty, the precision with which an observable can be measured. In VLBI observations, this error is determined by signal to noise ratio, observing bandwidth, integration time, and ultimate clock stability. This error is inherent in the observable and can be improved by changing the physical experiment configuration. For example, the system noise temperature could be decreased and the recorded bandwidth increased. To some extent measurement precision is limited by the processing used to obtain observable values from the raw data and could be changed by different processing algorithms. This type of error will be referred to as the signal-to-noise error (SNE). The uncertainty associated with adjusted parameters when only measurement uncertainty is included in the analysis will be referred to as noise-only error (NOE). SNE is related to the original measurements while NOE is the result of parameter estimation.

Another type of error is a systematic error for which a mathematical model is not available. An example is variation in the length of the cable which carries the timing pulse to be injected with the incoming signal. Since there is no way of parameterizing the cable delay, the delay must be measured to account for the timing error and to reduce it to a measurement uncertainty. Other errors of this type include dispersion within the electronics and antenna geometry

distorsion.

An error may arise from random or correlated fluctuations in a physical effect. For example, patchiness in the atmosphere can cause correlated variations in the observables. Likewise, density variations over time can affect the observables. The station frequency standards probably also have identifiable fluctuations. While such effects can be characterized by coherence lengths and times, the resultant change in the observables is statistical rather than deterministic. The effect on a single observation cannot be modeled, only the effect of the correlation between observations. As a practical matter, it is desirable to measure such effects directly and reduce the error to a measurement uncertainty. Unfortunately the behavior of the frequency standards is not easy to monitor and cannot be treated in detail except statistically. Statistical error models are less tractable and will not be discussed further.

Inaccuracy or lack of precision in a parameter of a deterministic physical model causes a systematic error in the theoretical values of the observables. If the parameter is not adjusted, the error is absorbed by the parameters that are adjusted. A model error propagates into the parameter estimates in a manner different from measurement uncertainties. While a single uncorrelated measurement error only affects how strongly a particular observation enters into the final adjustments, a model error causes a systematic bias in the estimated parameters. A simple covariance analysis cannot take such systematic errors into account. Errors of this type include the Love numbers in

the solid earth tide model, the precession constant, and the geographic pole position. The term modeled error (MDE) will be used to describe the error in adjusted parameters caused by such errors in parameters which are not adjusted. The term model error will refer to the uncertainty in a parameter of a model.

Finally, errors may arise because of the inadequacy of a model. If a model is physically incorrect, there is no way of predicting the actual impact of the physical effect on the adjusted parameters. Errors of this type can only be eliminated by new models.

4. The effect of model errors on adjusted parameters

The statistical basis for the treatment of model errors (errors in the unadjusted parameters) is an extension of simple least squares covariance analysis. Corresponding to the simple case, the observations are modeled by

$$O = F(X,Y) + e \quad \text{IV.A.4.1}$$

O = vector of measured values for the observables (dimension N)

$F(X,Y)$ = model equations for the effect of X and Y on
the observables

X = set of M_1 adjusted parameters

Y = set of M_2 unadjusted parameters

e = vector of observation errors (dimension N)

For the i th equation,

$$F_i(X,Y) = F_i(X_0,Y_0) + \sum_j \frac{\partial F_i}{\partial X_j} x_j + \sum_k \frac{\partial F_i}{\partial Y_k} y_k \quad \text{IV.A.4.2}$$

In matrix notation,

$$F(X,Y) = F(X_0,Y_0) + Bx + Cy \quad \text{IV.A.4.3}$$

$F(X_0,Y_0)$ = model equations evaluated at the nominal parameter values which are assumed to be close to the true values
 = computed observable values

B = matrix of partials for adjusted parameters (dimension N by $M1$)

x = vector of parameter adjustments (dimension $M1$)

C = matrix of partials for unadjusted parameters (dimension N by $M2$)

y = vector of unadjusted parameter errors (dimension $M2$)

Then the linearized equations for observed - computed are

$$z = Bx + Cy + e \quad \text{IV.A.4.4}$$

The least squares variational requirement is unchanged since the variation is only in the vector x and the sum of the observation and modeled errors (MDE) is to be minimized. Therefore,

$$\begin{aligned} x(\text{ls}) &= (B^T B)^{-1} B^T z \\ &= (B^T B)^{-1} B^T (Bx + (Cy + e)) \end{aligned} \quad \text{IV.A.4.5}$$

$$= \mathbf{x} + (\mathbf{B}^T \mathbf{B})^{-1} \mathbf{B}^T (\mathbf{C} \mathbf{y} + \mathbf{e})$$

The error in estimating \mathbf{x} is

$$\mathbf{x}(\text{ls}) - \mathbf{x} = (\mathbf{B}^T \mathbf{B})^{-1} \mathbf{B}^T (\mathbf{C} \mathbf{y} + \mathbf{e}) \quad \text{IV.A.4.6}$$

The estimated covariance of $\mathbf{x}(\text{ls}) - \mathbf{x}$ is given by

$$\begin{aligned} \text{COV}[\mathbf{x}(\text{ls}) - \mathbf{x}] &= E[(\mathbf{x}(\text{ls}) - \mathbf{x})(\mathbf{x}(\text{ls}) - \mathbf{x})^T] && \text{IV.A.4.7} \\ &= E[(\mathbf{B}^T \mathbf{B})^{-1} \mathbf{B}^T (\mathbf{C} \mathbf{y} + \mathbf{e}) \{(\mathbf{B}^T \mathbf{B})^{-1} \mathbf{B}^T (\mathbf{C} \mathbf{y} + \mathbf{e})\}^T] \end{aligned}$$

Assuming that the unadjusted parameter errors are uncorrelated with the observation errors,

$$E[\mathbf{y} \mathbf{e}^T] = 0 \quad \text{IV.A.4.8}$$

and that the observation errors are zero mean, uncorrelated and normalized,

$$E[\mathbf{e}] = 0, \quad E[\mathbf{e} \mathbf{e}^T] = \mathbf{I} \quad \text{IV.A.4.9}$$

then,

$$\begin{aligned} \text{COV}[\mathbf{x}(\text{ls}) - \mathbf{x}] &= E\{[(\mathbf{B}^T \mathbf{B})^{-1} \mathbf{B}^T \mathbf{C} \mathbf{y} + (\mathbf{B}^T \mathbf{B})^{-1} \mathbf{B}^T \mathbf{e}] \\ &\quad \{[(\mathbf{B}^T \mathbf{B})^{-1} \mathbf{B}^T \mathbf{C} \mathbf{y} + (\mathbf{B}^T \mathbf{B})^{-1} \mathbf{B}^T \mathbf{e}]\}^T\} \\ &= (\mathbf{B}^T \mathbf{B})^{-1} \mathbf{B}^T E\{[\mathbf{C} \mathbf{y} \mathbf{y}^T \mathbf{C}^T + \mathbf{e} \mathbf{e}^T]\} (\mathbf{B}^T \mathbf{B})^{-1} \mathbf{B}^T \\ &= (\mathbf{B}^T \mathbf{B})^{-1} \mathbf{B}^T \mathbf{C} E\{[\mathbf{y} \mathbf{y}^T]\} \mathbf{C}^T (\mathbf{B}^T \mathbf{B})^{-1} \mathbf{B}^T \\ &\quad + (\mathbf{B}^T \mathbf{B})^{-1} \mathbf{B}^T E\{\mathbf{e} \mathbf{e}^T\} (\mathbf{B}^T \mathbf{B})^{-1} \mathbf{B}^T \\ &= (\mathbf{B}^T \mathbf{B})^{-1} \mathbf{B}^T \mathbf{C} \text{COV}[\mathbf{y}] \mathbf{C}^T (\mathbf{B}^T \mathbf{B})^{-1} \mathbf{B}^T + (\mathbf{B}^T \mathbf{B})^{-1} \mathbf{B}^T \mathbf{I} (\mathbf{B}^T \mathbf{B})^{-1} \mathbf{B}^T \end{aligned} \quad \text{IV.A.4.10}$$

$$\text{COV}[y] = E[yy^T] \quad \text{IV.A.4.11}$$

= covariance matrix associated with the unadjusted
parameter errors

If the normalization is included explicitly,

$$\text{COV}[x(ls) - x] = (B^T_{WB})^{-1} + (B^T_{WB})^{-1} B^T_{WC} \text{COV}[y] \{(B^T_{WB})^{-1} B^T_{WC}\}^T \quad \text{IV.A.4.12}$$

where

$$W^{-1} = E[ee^T]$$

The covariance of the adjusted parameters divides conveniently into two parts, one part identical to the covariance from a simple least squares analysis, the NOE covariance, and the other part related to model errors in the unadjusted parameters. In general the unadjusted parameter covariance, or MDE covariance, is dominant.

The algorithms developed in this section are implemented in the experiment simulation and error analysis program ESTIM described in appendix D. The output of ESTIM is the projected noise-only error (NOE), modeled error (MDE), and total error (the root-sum-square of NOE and MDE) of the adjusted parameters for the observing configuration and schedule under study.

B. Measurement of the gravitational light deflection parameter

Several experiments have been performed to measure gravitational light deflection using interferometers (Counselman et al 1974, Weiler et al 1975, Fomalant et al 1976). The Wide-Band Optical Very Long Baseline Interferometer described by Currie (1976 '1977) could be used to perform similar experiments. A number of simulations to test whether better results can be achieved are described in this section.

1. Occultations by Jupiter

The statistics of stellar distribution indicate that occultations of stars by Jupiter are rare but not unknown. The ESAENA lists twelve predicted occultations of stars brighter than ninth magnitude in the years 1955-61, inclusive. The SAO Star Catalog lists an average of 6 stars per square degree down to tenth magnitude with a maximum of 14.8 stars per square degree for the SAO grid rectangle in the direction of the galactic center. Jupiter travels approximately 45 degrees per year including retrograde motion. Using a figure of 5 stars per square degree and assuming a 90 arcsecond band (one Jupiter radius on either side), 5.6 events occur in a year. Since on the average half the events will occur during daylight at any particular location and therefore be unobservable, the number of possibly useful events per year is approximately two. When Jupiter is in the direction of the galactic center, the number of possible events could be doubled.

The effect of gravitational light deflection is to change a star's apparent position by

$$\alpha = 4 \frac{GM}{c^2 r}$$

IV.B.1.1

where

$$\frac{GM}{c^2} = \text{gravitational radius of the perturbing body}$$

M - mass

G = gravitational constant

c = speed of light

r = linear distance from star vector to center of deflecting body

On the limb of the sun $\alpha = 1.75$ arcseconds. Corona scintillation makes radio observations near the sun very difficult. For past VLBI observations the close limit has been approximately ten solar radii, where the deflection is one-tenth that at the limb. The mass of Jupiter is one-thousandth that of the sun while the radius is one-tenth that of the sun. Light deflection at the limb of Jupiter is then one-hundredth that at the solar limb. Since optical observations can be taken much closer to Jupiter than radio observations near the sun, the difference in observed effect may only be reduced by a factor of ten. In addition, Jupiter's average rate of motion is one-tenth the sun's. Consequently an observed object remains in the vicinity of the deflecting body for a longer time.

2. Algorithms for modeling the light deflection parameter

Two algorithms were used to model deflection to test different methods of data analysis. The first is a straightforward extension of the solar algorithm described in chapter II with the gravitational

radius of the sun (1476.64 m) replaced by the corresponding number for Jupiter (1.40988 m). The second is a three parameter model designed to exploit the symmetry of observations.

Assuming that a star moves by Jupiter with uniform velocity (figure IV.1), the motion can be characterized by an impact parameter p , a speed v , and a time of closest approach t_0 . At any given time the angular distance between the star and the center of Jupiter is d while the angular distance along the star's path to the point of closest approach is f . By symmetry, the scalar deflection at times $t_1 = t_0 - t$ and $t_2 = t_0 + t$ will be equal. The deflection will be maximum at $t = t_0$ and the magnitude will be inversely proportional to the impact parameter p . Estimating p and t_0 from the data eliminates the problem of measuring the impact parameter by other means.

The change in the star's apparent position is

$$\Delta s = gA \quad \text{IV.B.2.1}$$

where

g = magnitude of deflection

A = unit vector from Jupiter to the star

$$g = \frac{4(1+\gamma)}{2R_J r} \quad \text{IV.B.2.2}$$

where

γ = deflection parameter

R_J = gravitational radius of Jupiter

r = linear distance between center of Jupiter and star vector

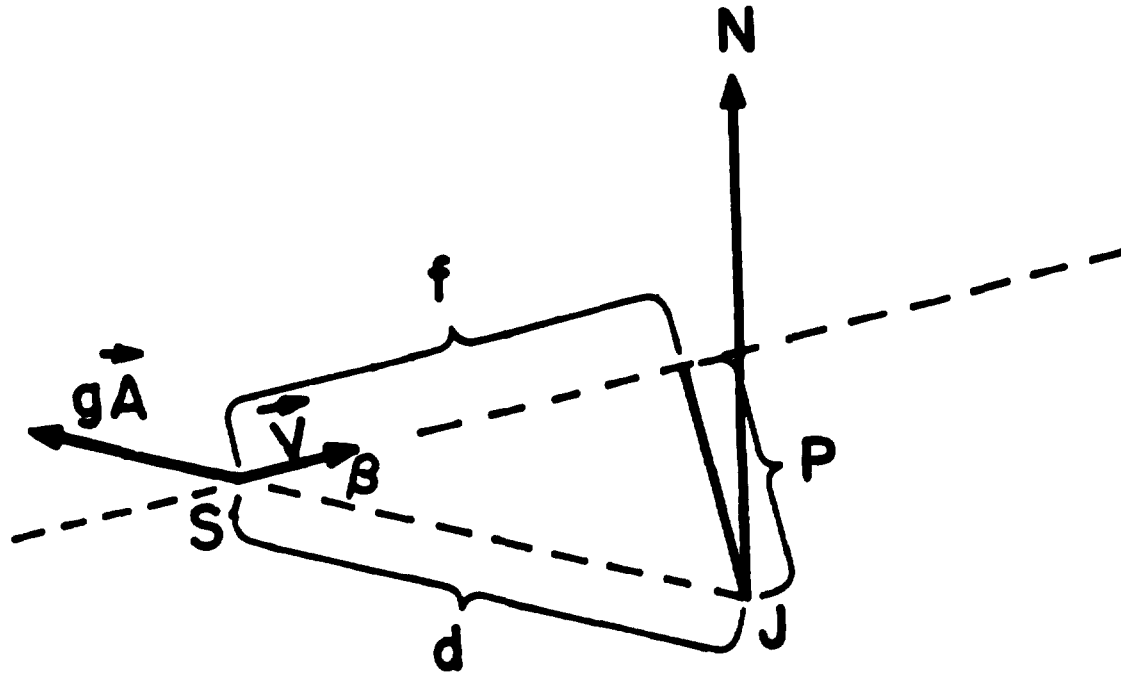


Fig. IV.1 Geometry of the three-parameter Jupiter deflection model

JRH
11-77

Then,

$$g = \frac{k(1+\gamma)}{2d} \quad \text{IV.B.2.3}$$

where

$$k = \frac{4GM}{c^2 D} \quad \text{IV.B.2.4}$$

D = distance from observer to Jupiter

d = angular distance from center of Jupiter to star

Ignoring the curvature of the celestial sphere,

$$d = (p^2 + f^2)^{1/2} \quad \text{IV.B.2.5}$$

With a constant linear velocity,

$$f = v(t - t_0) \quad \text{IV.B.2.6}$$

where

v = angular speed

t_0 = time of closest approach

Then,

$$f = -d \cos \beta \quad \text{IV.B.2.7}$$

$$p = d \sin \beta \quad \text{IV.B.2.8}$$

where

β = angle between the star's velocity vector relative to Jupiter
and the star-Jupiter vector

The delay observable is given by

$$\tau = b \cdot s \quad \text{IV.B.2.9}$$

where

b = instantaneous baseline vector in units of light time

s = unit vector in the direction of the star

With the effect of deflection included,

$$\begin{aligned} \tau &= b \cdot (s + \Delta s) & \text{IV.B.2.10} \\ &= b \cdot (s + gA) \end{aligned}$$

The partial derivatives of delay with respect to the deflection parameters are:

$$\frac{\partial \tau}{\partial \gamma} = (b \cdot A) \frac{\partial g}{\partial \gamma} = (b \cdot A) \frac{k}{2d} \quad \text{IV.B.2.11}$$

$$\begin{aligned} \frac{\partial \tau}{\partial p} &= (b \cdot A) k \frac{1+\gamma}{2} \frac{\partial}{\partial p} (p^2 + f^2)^{1/2} = (b \cdot A) k \frac{1+\gamma}{2} \left(\frac{-p}{d^3} \right) \\ &= -(b \cdot A) k \frac{1+\gamma}{2} \frac{\sin \delta}{d^2} \quad \text{IV.B.2.12} \end{aligned}$$

$$\begin{aligned} \frac{\partial \tau}{\partial f} &= (b \cdot A) k \frac{1+\gamma}{2} \frac{\partial}{\partial t_0} (p^2 + f^2)^{1/2} = (b \cdot A) k \frac{1+\gamma}{2} \left(\frac{-f}{d^3} \right) \frac{\partial f}{\partial t_0} \\ &= (b \cdot A) k \frac{1+\gamma}{2} \frac{\cos \delta}{d^2} (-v) \quad \text{IV.B.2.13} \end{aligned}$$

The units of γ , p , and t_0 are dimensionless, arcseconds, and seconds, respectively.

A subroutine was used to compute the apparent position and polar angular radius of Jupiter. Values of apparent right ascension and declination and true geocentric distance were obtained by fourth-difference Everett interpolation of daily tabulated values taken from the AENA for 1975. Fictitious stars were located in the sky to simulate occultations over a range of conditions. The times of occultation were approximated ignoring parallax and Jupiter's ellipticity. A star was considered occulted when the angular distance between the star and the center of Jupiter was less than the interpolated angular radius. Any observations scheduled during occultation were automatically ignored.

The parameters used in the following simulations based on suggestions by Prof. Currie are given in table IV.1. The five observation periods used are summarized in table IV.2. Each night's observations spanned approximately nine hours. The results for the one parameter deflection model are first described for all observation periods. The three parameter model results are then discussed.

3. Observations at Jupiter's stationary point

The period Dec 8 - 11, 1975 was chosen for minimum motion of Jupiter. During this time Jupiter moved only 2 seconds in right ascension and $34''$ in declination. At the epoch of occultation Jupiter

Table IV.1 Parameters for Jupiter occultation simulations

| | | | |
|----------------------------|---------------------|------------|---------------------|
| model errors: | | | |
| site cartesian coordinates | | | .01 mm |
| source right ascensions | | | .0667 millisecc |
| source declinations | | | 1. milliarcsec |
| earth tide Love h | | | .05 |
| earth tide Love l | | | .01 |
| diurnal polar motion scale | | | .2 |
| | | | |
| length of observation | | | 10 min |
| measurement uncertainty | | | .016 picosec |
| | | | |
| location of baselines | | | Greenbelt, MD |
| | | | |
| site | longitude | | latitude |
| north | 283 deg 9' 25.43" E | | 38 deg 59' 54.43" N |
| south | 283 deg 9' 25.43" E | | 38 deg 59' 22.09" N |
| east | 283 deg 10' 6.95" E | | 38 deg 59' 54.43" N |
| | | | |
| baselines | polar | equatorial | length |
| north-south | 775.106 m | 627.533 m | 997.290 m |
| north-east | 0. | 1001.281 m | 1001.281 m |
| south-east | -775.106 m | 1181.731 m | 1413.250 m |

Table IV.2 Observation period parameters for Jupiter occultations

| 1. number of observations | 7. initial declination of Jupiter | |
|---------------------------------------|---------------------------------------|-----------------------|
| 2. number of sources observed | 8. final declination of Jupiter | |
| 3. times observed | 9. motion in right ascension | |
| 4. elevation angle range | 10. motion in declination | |
| 5. initial right ascension of Jupiter | 11. source right ascension(s) | |
| 6. final right ascension of Jupiter | 12. source declination(s) | |
| | 13. epoch when central source on limb | |
| Dec 8-11 | Dec 8-11 | Mar 20 |
| 1. 162 | 162 | 54 |
| 2. 1 | 3 | 1 |
| 3. 12/8 20:00 - 12/9 04:50 | same | 3/20 12:51 - 21:41 |
| 12/9 20:00 - 12/10 04:50 | same | 3/20 12:52 - 21:42 |
| 12/10 20:00 - 12/11 04:50 | same | |
| 4. 15 deg - 56 deg | same | 17 deg - 50 deg |
| 5. 0 hr 56 min 31.696 sec | same | 0 hr 3 min 20.259 sec |
| 6. 0 hr 56 min 29.632 sec | same | 0 hr 3 min 39.902 sec |
| 7. 4 deg 30' 11.35" | same | - 48' 25.52" |
| 8. 4 deg 30' 45.73" | same | - 46' 18.04" |
| 9. 2.064 sec | same | 19.643 sec |
| 10. 34.38" | same | 127.48" |
| 11. 0 hr 56 min 29.632 sec | same | 0 hr 3 min 30.303 sec |
| | same | |
| | same | |
| 12. 4 deg 31' 6.40" | 4 deg 11' 6.40" | -0 deg 47' 35.78" |
| | 4 deg 31' 6.40" | |
| | 4 deg 51' 6.40" | |
| 13. 12/11 04:48 on N limb | same | 3/20 17:22 on S limb |
| Oct 12 | Oct 11-13 | |
| 1. 54 | 162 | |
| 2. 1 | 1 | |
| 3. 10/12 00:31 - 10/12 09:21 | 10/11 00:35 - 10/11 09:25 | |
| | 10/12 00:31 - 10/12 09:21 | |
| | 10/13 00:27 - 10/13 09:17 | |
| 4. 21 deg - 57 deg | same | |
| 5. 1 hr 15 min 49.660 sec | 1 hr 16 min 19.766 sec | |
| 6. 1 hr 15 min 38.538 sec | 1 hr 15 min 8.392 sec | |
| 7. 6 deg 16' 34.91" | 6 deg 19' 36.08" | |
| 8. 6 deg 15' 28.06" | 6 deg 12' 27.08" | |
| 9. 11.122 sec | 71.374 sec | |
| 10. 66.85" | 429.00" | |
| 11. 1 hr 15 min 44.026 sec | same | |
| 12. 6 deg 16' 24.27" | same | |
| 13. 10/12 05:00 on N limb | same | |

was stationary in right ascension, moving only 0.1 seconds during the interval from 12/10 20:00 to 12/11 04:50. The north-south baseline is more sensitive to deflections in declination. The fictitious source was therefore positioned to be on the north limb just prior to occultation to maximize the change in declination. During the last night of observation Jupiter moved northward at a rate of $20''$ or one semi-diameter per day. Since the distance between Jupiter and the source in right ascension was always less than the distance in declination, the north-south component of deflection always exceeded the east-west component. Three nights of observation were used to increase the time in which the deflection was measured.

The simulation results for a single relativity parameter are given in table IV.3. All the errors are unitless. Each column corresponds to a different set of adjusted parameters. Each row lists the MDE caused by the indicated model error. Taking only the measurement error of 0.016 picoseconds and adjusting only the relativity parameter, the projected NOE is 1.9%. Any improvement in measurement error would affect this number proportionally. Including the model errors, the projected MDE in the relativity parameter is 41%, an indication that an experiment represented by this set of model errors and parameters is not useful. The largest contribution to the MDE is the site y-coordinate. If the site coordinates are also adjusted, the equivalent of adjusting the baseline, the NOE is increased to 4.7% while the MDE drops to 7.9%. However, the estimation is poorly conditioned, and the four parameters may be inseparable. In the two previous cases it was assumed that the position of Jupiter

Table IV.3 Errors for relativity parameter, Dec 3-11, 1 source schedule

- A. relativity parameter adjusted
- B. relativity parameter and north site coordinates adjusted
- C. relativity parameter and source declination adjusted
- D. relativity parameter, source declination and right ascension adjusted

| Unadjusted parameter | A | B | C | D |
|-------------------------|-------|-------|-------|-------|
| north site x-coordinate | .086 | | -.185 | .003 |
| north site y-coordinate | -.343 | | -.076 | -.013 |
| north site z-coordinate | .035 | | -.000 | -.000 |
| source right ascension | .002 | .0 | -.060 | |
| source declination | .176 | .0 | | |
| Love h | -.078 | -.029 | -.021 | -.032 |
| Love l | .002 | -.001 | .008 | -.003 |
| diurnal polar motion | -.051 | -.073 | -.076 | -.072 |
| noise error | .019 | .047 | .045 | .047 |
| total modeled error | .407 | .079 | .223 | .080 |
| total error | .408 | .092 | .228 | .093 |

relative to the source was known from other data. Since ephemeris positions or optical determinations are unlikely to be better than 0.1", the assumed model error of 1 milliarcsecond is probably extremely optimistic. Increasing the assumed position model error to 0.1" would make it the dominant error source. Two simulations were done including declination and both declination and right ascension in the adjusted parameters to remove the source position as a source of MDE. The NOE in the relativity parameter remains 4.5% and 4.7% for the two cases. If only the declination is included, the total MDE in the relativity parameter is 22%. The largest error contributions are the equatorial coordinates of the site but the other errors are significant. Where both right ascension and declination are included, the MDE is 8% with the diurnal polar motion being dominant.

Another experimental configuration is to observe several sources and to use differenced observations. Although it was not possible to simulate this condition exactly, a series of simulations using three sources was examined to approximate the configuration. The results appear in table IV.4. The sources were positioned on a north-south line to enhance the measurement of deflection in declination and were observed in a regular sequence. The spacing of the sources was comparable to the star density assumed in estimating the number of usable events per year. The approximation should be fairly good. The algorithm for using differenced data requires that the corresponding partial derivatives be the differences of the partial derivatives of the original observations. If one source is much farther from Jupiter, its partial derivatives with respect to the relativity parameter are

Table IV.4 Errors for relativity parameter, Dec 8-11, 3 source schedule

- A. relativity parameter adjusted
- B. relativity parameter and north site coordinates adjusted
- C. relativity parameter and source declinations adjusted
- D. relativity parameter, source declinations and right ascensions adjusted
- E. relativity parameter, north site coordinates, source right ascensions (except for one source), and declinations adjusted

| Unadjusted parameter | A | B | C | D | E |
|--------------------------|-------|-------|-------|-------|-------|
| north site x-coordinate | .080 | | -.217 | -.000 | |
| north site y-coordinate | -.340 | | -.075 | -.001 | |
| north site z-coordinate | .305 | | -.000 | -.000 | |
| source 1 right ascension | -.001 | -.002 | -.000 | -.000 | .0 |
| source 1 declination | -.006 | -.083 | | | |
| source 2 right ascension | .000 | .000 | -.070 | | |
| source 2 declination | .175 | .163 | | | |
| source 3 right ascension | .000 | .002 | -.000 | | |
| source 3 declination | .005 | -.081 | | | |
| Love h | -.077 | -.007 | -.016 | -.032 | -.031 |
| Love l | .003 | .000 | .011 | -.001 | -.001 |
| diurnal polar motion | -.052 | -.017 | -.083 | -.080 | -.080 |
| noise error | .032 | .038 | .078 | .083 | .083 |
| total modeled error | .403 | .201 | .255 | .086 | .086 |
| total error | .404 | .205 | .267 | .120 | .119 |

small and hence the differenced partials vary only slightly from the partial derivatives of the close source observations. Differencing decreases the number of data points by a factor of m/n , where n is the number of sources observed and m is the number of reference sources, assuming all the sources are observed the same number of times. This effect is mimicked by including in the simulations the observations of the reference sources. Their contributions to the estimation of the relativity parameter is small because of their distance from Jupiter. Using differenced data weakens the estimation of the non-relativity parameters if they are included in the adjusted parameters. The sources cannot be very far apart so that the observing geometry is nearly the same. The partial derivatives which depend on the overall geometry will be comparable from source to source. Only the relativity partials differ markedly from observations of the distant reference source to the occulted source. Consequently the differenced partials for parameters such as declination and site position will be smaller than the partials from the individual observations, thus reducing their contribution to the normal matrix. The degradation of the non-relativity parameters is not considered in the three source simulations since the partials from the reference source observations were included.

If only the relativity parameter is adjusted, the NOE for the three source schedule is 3.2%, a factor of 3/2 worse than the one source schedule. The MDE remains essentially the same since the site coordinates again dominate. With the site coordinates also adjusted, the NOE is 3.8% with a 20% MDE. In this case the largest errors come

from the source declinations. The problem of determining the position of Jupiter relative to the sources remains. Adjustment of the relativity parameter and the source declinations leads to a NOE of 3.8% and a MDE of 26%. As in the one source case, the contribution of the site equatorial coordinates is the largest. If the source right ascensions are also included in the adjusted parameters, the NOE is 8.3% while the MDE is 8.6%. Including the site coordinates as well does not change the errors significantly. Diurnal polar motion contributes the largest MDE in the last two cases. Since the assumed error for diurnal polar motion is only 20%, the actual MDE may be considerably larger. The adjustment of a relativity parameter, the source positions and the site coordinates represents an almost complete estimation of the major parameters. Therefore the NOE of roughly 10% in the relativity parameter is the minimum error for this experimental configuration and method of analysis, given the assumed measurement and model errors.

A three site, three baseline configuration was examined to see if the addition of an east-west baseline and more observations would change the errors significantly. The results are shown in table IV.5. Both the one source and three source schedules were tried in simulations adjusting only the relativity parameter. While the NOE is reduced by one third to 1.3% and 2.3% respectively, the MDE increased slightly to 47%. The dominant errors are still the site coordinates. The other adjusted parameter sets were not pursued but probably would not give results much different from the corresponding one baseline results.

Table IV.5 Errors for relativity parameter, Dec 8-11, 3 site schedules

A. relativity parameter adjusted, 1 source observed
 B. relativity parameter adjusted, 3 sources observed

| Unadjusted parameter | A | B |
|--------------------------|-------|-------|
| north site x-coordinate | .062 | .058 |
| north site y-coordinate | -.205 | -.202 |
| north site z-coordinate | .021 | .021 |
| south site x-coordinate | -.073 | -.067 |
| south site y-coordinate | .336 | .332 |
| south site z-coordinate | -.034 | -.034 |
| east site x-coordinate | .011 | .008 |
| east site y-coordinate | -.131 | -.130 |
| east site z-coordinate | .013 | .013 |
| source 1 right ascension | .062 | -.003 |
| source 1 declination | .172 | -.306 |
| source 2 right ascension | | .060 |
| source 2 declination | | .171 |
| source 3 right ascension | | .003 |
| source 3 declination | | .006 |
| Love h | -.075 | -.073 |
| Love l | .011 | .012 |
| diurnal polar motion | -.035 | -.035 |
| noise error | .013 | .023 |
| total modeled error | .473 | .466 |
| total error | .473 | .467 |

4. Observations at Jupiter's maximum velocity point

On March 20, 1975 the motion of Jupiter was at an annual maximum, 53 seconds/day in right ascension and 346"/day in declination. An experiment was simulated for this period to examine the worst case occultation. A single baseline and source were used. Since Jupiter is within one radius of the source for less than two hours, the number of observations with substantial deflection is small and there is nothing to be gained by observing for more than one night. The results are given in table IV.6. The same adjusted parameter sets used in the December simulations were used for March. The NOE of the relativity parameter for all parameter sets is approximately 10% while the MDE exceeds 13% except when the site coordinates are adjusted. The problem of adjusting both the relativity parameter and the site coordinates makes the errors suspect in that case. The site coordinates are the largest source of error in all cases where they are not adjusted. This worst case analysis indicates that an occultation occurring when Jupiter is moving rapidly would not produce interesting results with the assumed system parameters.

5. Observations at intermediate velocity

The time around Oct. 12, 1975 was used to simulate an occultation which occurs while Jupiter is moving at half its maximum velocity. The results for a single baseline, single source schedule with the same adjusted parameter sets as above are shown in table IV.7. The errors

Table IV.6 Errors for relativity parameter, March 20

- A. relativity parameter adjusted**
- B. relativity parameter and north site coordinates adjusted**
- C. relativity parameter and source declination adjusted**
- D. relativity parameter, source declination and right ascension adjusted**

| Unadjusted parameter | A | B | C | D |
|-------------------------|-------|-------|-------|-------|
| north site x-coordinate | .168 | | .207 | -.029 |
| north site y-coordinate | .309 | | .170 | .123 |
| north site z-coordinate | .003 | | .000 | .000 |
| source right ascension | .071 | .0 | .073 | |
| source declination | -.070 | .0 | | |
| Love h | -.004 | -.009 | -.016 | -.022 |
| Love l | .015 | .007 | .020 | .035 |
| diurnal polar motion | -.012 | .001 | -.008 | .005 |
| noise error | .090 | .107 | .091 | .095 |
| total modeled error | .366 | .011 | .229 | .133 |
| total error | .377 | .108 | .293 | .163 |

in the relativity parameter for the cases in which the site coordinates are not adjusted are approximately 6% for NOE and exceed 12% for MDE. The site equatorial coordinates are again the largest source of error. When C.t. 11 and 13 are added to the data there is no substantial change. The NOE decreases from 5.7% to 5.6% while the MDE increases from 39% to 40% in the case of a single adjusted parameter. The three site, three baseline errors for this period are given in table IV.8. The NOE is approximately 3% in all cases. The MDE is greater than 25% in the cases where the site coordinates are not adjusted and is dominated by the south and east site equatorial coordinates. If the site coordinates of the north and south sites are included in the adjustment, the MDE is 2%. However, the estimates are probably ill-conditioned.

6. Simulations using three parameters

The problem of determining the position of Jupiter with respect to the occulted source is difficult. Jupiter itself is too large a source to be located by the same interferometer that observes the stars. It would be necessary to do simultaneous optical plate measurements or to extrapolate from a recently updated ephemeris. Both methods have inherent accuracies far worse than that of the optical interferometer. The method of using two additional parameters to characterize the motion of Jupiter which was described in section IV.B.2. avoids the direct problem of determining relative position. Results of three parameter modeling of gravitational deflection are presented in table IV.9. The observation sets are

Table IV.7 Errors for relativity parameter, Oct 12

- A. relativity parameter adjusted
- B. relativity parameter and north site coordinates adjusted
- C. relativity parameter and source declination adjusted
- D. relativity parameter, source declination and right ascension adjusted

| Unadjusted parameter | A | B | C | D |
|-------------------------|-------|-------|-------|-------|
| north site x-coordinate | -.114 | | -.191 | .027 |
| north site y-coordinate | -.349 | | -.151 | -.114 |
| north site z-coordinate | -.030 | | -.001 | -.001 |
| source right ascension | -.058 | .0 | -.067 | |
| source declination | .114 | .0 | | |
| Love h | -.020 | .006 | .007 | .009 |
| Love l | -.001 | -.003 | -.008 | -.032 |
| diurnal polar motion | -.019 | -.000 | .005 | -.003 |
| noise error | .057 | .088 | .060 | .066 |
| total modeled error | .391 | .007 | .253 | .122 |
| total error | .395 | .088 | .260 | .139 |

Table IV.8 Errors for relativity parameter, Oct 12, 3 site schedules

- A. relativity parameter adjusted
- B. relativity parameter and north and south site coordinates adjusted
- C. relativity parameter and source declination adjusted
- D. relativity parameter, source declination and right ascension adjusted

| Unadjusted parameter | A | B | C | D |
|-------------------------|-------|-------|-------|-------|
| north site x-coordinate | .057 | | .046 | .047 |
| north site y-coordinate | -.063 | | -.027 | .064 |
| north site z-coordinate | .008 | | .003 | -.009 |
| south site x-coordinate | .118 | | .141 | .108 |
| south site y-coordinate | .123 | | .049 | .047 |
| south site z-coordinate | -.008 | | .003 | .003 |
| east site x-coordinate | -.174 | .0 | -.187 | -.155 |
| east site y-coordinate | -.060 | .0 | .022 | -.111 |
| east site z-coordinate | -.000 | .0 | -.006 | -.000 |
| source right ascension | -.035 | .0 | -.056 | |
| source declination | .004 | .0 | | |
| Love h | .018 | .017 | .026 | .035 |
| Love l | .000 | -.006 | -.005 | -.004 |
| diurnal polar motion | -.008 | -.001 | .002 | -.001 |
| noise error | .024 | .035 | .024 | .025 |
| total modeled error | .268 | .018 | .254 | .258 |
| total error | .269 | .039 | .255 | .259 |

Dec. 8 - 11, March 20, Oct. 12, and Oct. 11 - 13. The additional parameters degrade the NOE considerably. The NOE range from 47% for Dec. 8 - 11 to 13% for Oct. 11 - 13. The December configuration suffers very badly from the slow movement of Jupiter, the factor which contributed highly to the small error in the one parameter analysis. The MDE arising from the equatorial site coordinates are the largest, exceeding 110% in all cases and reaching 200%. For December and March even the earth tide causes over a 40% MDE. The October observation periods have the lowest NOE and MDE. However, the one milliarcsecond model error in right ascension assumed for the source positions produces over 24% MDE in the relativity parameter for both sets of data. The analyses including other parameters in the adjustment were not done. It is difficult to increase the number of adjusted parameters since the estimation very soon becomes ill-conditioned. In any case, increasing the number of adjusted parameters can only increase the NOE in the relativity parameter, which is already considerably worse than for the one parameter analyses.

7. Baseline errors

Since in all cases the site coordinates contributed the largest MDE, a simulation was run for a north-south baseline using a schedule more suited to geodesy to see how well the coordinates could be estimated. The source positions used are given in table IV.10. They are spaced regularly on a grid four hours in right ascension by 60 degrees in declination. The sources were observed in numerical sequence as long as they were visible over a period of ten hours. The

Table IV.9 Errors in relativity parameter with 3 parameter modeling of gravitational deflection for 1 source, 1 baseline schedules

- A. Dec 8-11
- B. Mar 20
- C. Oct 12
- D. Oct 11-13

| Unadjusted parameter | A | B | C | D |
|-------------------------|-------|-------|-------|-------|
| north site x-coordinate | 1.35 | 1.10 | -.876 | -.768 |
| north site y-coordinate | -1.98 | -.147 | -.228 | -.276 |
| north site z-coordinate | .182 | -.011 | -.024 | -.011 |
| source right ascension | .265 | .317 | -.277 | -.248 |
| source declination | .919 | .287 | -.082 | -.033 |
| Love h | -.403 | -.609 | .024 | -.018 |
| Love l | -.077 | .023 | .029 | .032 |
| diurnal polar motion | .224 | -.030 | .045 | .068 |
| noise error | .473 | .194 | .139 | .133 |
| total modeled error | 2.629 | 1.337 | .952 | .857 |
| total error | 2.671 | 1.351 | .962 | .867 |

Table IV.10 Sources used for estimation of site coordinates

| source | right ascension | declination |
|--------|------------------|--------------|
| 1 | 1 hr 0 min 0 sec | 0 deg 0' 0" |
| 2 | 1 hr 0 min 0 sec | 30 deg 0' 0" |
| 3 | 1 hr 0 min 0 sec | 60 deg 0' 0" |
| 4 | 3 hr 0 min 0 sec | 0 deg 0' 0" |
| 5 | 3 hr 0 min 0 sec | 30 deg 0' 0" |
| 6 | 3 hr 0 min 0 sec | 60 deg 0' 0" |
| 7 | 5 hr 0 min 0 sec | 0 deg 0' 0" |
| 8 | 5 hr 0 min 0 sec | 30 deg 0' 0" |
| 9 | 5 hr 0 min 0 sec | 60 deg 0' 0" |

results are shown in table IV.11. Two parameter sets were used, the first adjusting only the site coordinates and the second adjusting both the site and source coordinates (except for the right ascension of a reference source). If only the site coordinates are adjusted, the NOE on all coordinates is 1.3 micrometers. If the source positions are not adjusted but come from conventional catalogues, the positions are unlikely to be better than 0.1", two orders of magnitude worse than the error assumed. Therefore the modeled error is rather optimistic. The analysis with source positions included in the adjusted parameters gives NOE ranging from 4.4 micrometers to 7.3 micrometers, an indication that the model error used in the previous simulations is feasible. Other effects like thermal expansion and tilting have been neglected.

8. Conclusions

These time delay simulations of WOVLBI experiments for measuring gravitational change in apparent position in the vicinity of Jupiter indicate that the configuration studied could yield interesting results for certain geometries with some improvement in the measurement uncertainty of the observations. However, there are a number of other possibilities that should be investigated. Alternate schedules using a different number and sequence of observations might reduce the effect of some modeled errors. More importantly, an analysis in which the observable is the angular distance between stars would more appropriately simulate a differential experiment. Estimates for a differential experiment could be made in the following way. One

Table IV.11 Errors in site coordinates for 1 km N-S baseline

A. site coordinates adjusted

B. site coordinates, source right ascensions (except one), and source declinations adjusted

| Unadjusted parameter | A | | | B | | |
|--------------------------|-----------------------|-------|-------|-------|-------|-------|
| | X | Y | Z | X | Y | Z |
| | error units = .0001 m | | | | | |
| source 1 right ascension | -.007 | -.001 | .003 | | | |
| source 1 declination | -.006 | .011 | .007 | | | |
| source 2 right ascension | -.005 | -.001 | .001 | | | |
| source 2 declination | -.001 | -.008 | -.004 | | | |
| source 3 right ascension | -.001 | -.001 | -.000 | | | |
| source 3 declination | -.004 | -.000 | -.013 | | | |
| source 4 right ascension | -.004 | .000 | .002 | | | |
| source 4 declination | -.005 | .009 | .006 | | | |
| source 5 right ascension | -.005 | -.002 | -.001 | -.030 | -.001 | .0 |
| source 5 declination | -.004 | .005 | -.003 | | | |
| source 6 right ascension | -.001 | -.001 | -.002 | | | |
| source 6 declination | .002 | -.001 | -.012 | | | |
| source 7 right ascension | -.003 | .001 | .002 | | | |
| source 7 declination | -.006 | .007 | .005 | | | |
| source 8 right ascension | -.003 | -.000 | -.001 | | | |
| source 8 declination | -.004 | .004 | -.002 | | | |
| source 9 right ascension | -.001 | -.002 | -.003 | | | |
| source 9 declination | .001 | -.001 | -.010 | | | |
| Love h | .011 | -.007 | .018 | .011 | -.006 | .023 |
| Love l | .003 | -.000 | -.002 | .011 | -.014 | .008 |
| diurnal polar motion | .007 | -.021 | .004 | -.010 | -.001 | -.003 |
| noise error | .013 | .013 | .013 | .044 | .049 | .073 |
| total modeled error | .022 | .029 | .030 | .035 | .015 | .025 |
| total error | .025 | .032 | .033 | .056 | .051 | .077 |

assumes that the modeled errors, canceling in first order, become negligible compared to the noise-only error. If calibration of the atmosphere is no longer necessary, a better signal-to-noise ratio is obtained leading to a reduction of the measurement uncertainty and, consequently, of the noise-only error. Assuming an improvement by a factor of 7 over the previously used measurement uncertainty, the noise-only error alone would amount to approximately 2% of the relativity effect. Further improvements in apparatus and data reduction techniques would have corresponding effects on the noise-only error. The observing configuration could also be simplified by constructing a completely polar baseline. Further studies of differential measurements using a polar baseline would be useful.

C. A comparison of two networks for measuring polar motion and UT1

1. Introduction

Polar motion and UT1 represent changes in the earth's orientation with respect to its spin axis. Polar motion is the motion of the spin pole with respect to the geographic pole. UT1 reflects the angular offset caused by changes in the spin rate.

Polar motion can be described by Euler's equations for a rotating body.

$$\frac{dI_i W_i}{dt} - (I_j - I_k) W_j W_k = N_i \quad i=1,2,3 \quad \text{IV.C.1.1}$$

where

I = moment of inertia

W = angular velocity

N = external torque

In the absence of torques and assuming $I_1 = I_2$,

$$I_1 \dot{W}_1 = (I_2 - I_3) W_2 W_3 \quad \text{IV.C.1.2}$$

$$I_2 \dot{W}_2 = -(I_1 - I_3) W_3 W_1 \quad \text{IV.C.1.3}$$

$$I_3 \dot{W}_3 = 0 \quad \text{IV.C.1.4}$$

where

$$\dot{W}_1, \dot{W}_2, \dot{W}_3 = \text{time derivatives of } W_1, W_2, W_3$$

Then taking a second time derivative and substituting,

$$I_1 \ddot{W}_1 = (I_1 - I_3) \dot{W}_2 W_3 \quad \text{IV.C.1.5}$$

$$\ddot{W}_1 = W_1 \left\{ W_3 \frac{(I_1 - I_3)}{I_1} \right\}^2 \quad \text{IV.C.1.6}$$

where

$$\ddot{W}_1 = \text{second time derivative of } W_1$$

The angular frequency $W_3(I_1 - I_3)/I_1$ determines the Euler period. From flattening measurements $(I_1 - I_3)/I_1$ is approximately -0.0033, which yields the classical Euler period of 300 days. The fact that a 14 month period rather than a 10 month period is observed is attributed to the earth's elasticity. The 12 month period also found in polar motion is attributed to the continuous redistribution of mass in meteorological and geophysical processes.

No simple analytical model for the variations in UT1 is known.

Variations in the position of the pole were suggested in the eighteenth century by Euler but not firmly identified until the end of the nineteenth century through the work of F. Kustner and S. C. Chandler. The secular retardation of the rotation rate was established by Adams and Delaunay in the middle of the nineteenth century. Irregular fluctuations were identified by S. Jones in 1939 and seasonal variations by K. Stoyko in 1937.

Interest in the position of the spin pole and rotational angle comes from two areas. High precision geodesy and astrometry are affected by both polar motion and UT1. Knowledge of UT1 is also necessary to maintain a close relationship between civil time, or UTC, and the sidereal angle of the earth. From a geophysical point of view, polar motion and UT1 variations may give insight into release of stress and mass transfer related to earthquakes, tectonic plate motion, core-mantle coupling, and atmospheric or oceanic circulation.

Polar motion has been monitored by five principal stations of the International Polar Motion Service (formerly the International Latitude Service) since 1899. The number of contributing observatories is now nearly 50. Determination of UT1 and the propagation of time are coordinated by the BIH, which uses data from approximately 90 instruments. The BIH also publishes an independent analysis of polar motion. There is an overlap in the contributors to the IPMS and the BIH.

The standard instruments for determining latitude and time are the visual zenith telescope, the photographic zenith telescope, the Danjon impersonal prismatic astrolabe and the visual transit circle. More recent work has been done with VLBI (Shapiro et al 1974), satellite laser ranging (Smith et al 1972), satellite doppler (Anderle 1976), and lunar laser ranging (Stolz et al 1976). However, none of these newer techniques has been established as a permanent service.

The National Geodetic Survey (NGS) has the responsibility for the operation of the two North American observatories of the IPMS, which are located at Gaithersburg, Maryland and Ukiah, California. The main optical device is the Horrebow-Talcott latitude instrument and Doppler Satellite Receivers are also installed. The NGS is also responsible for maintaining the North American Datum and for monitoring horizontal and vertical geodetic control. Because of recent requirements for even higher accuracy geodetic control, the NGS has decided to improve their operational capability for measuring polar motion and UT1 by the implementation of a three station VLBI network using the Mark III system. The network would also be used as a reference triangle in conjunction with portable VLBI terminals to establish a very high accuracy national and global survey grid. The POLARIS (POLar motion Analysis by Radio Interferometric Survey) project is proceeding in cooperation with the Goddard Space Flight Center and the Haystack Observatory.

There have been four sites proposed for the POLARIS network: Westford, Massachusetts; Fort Davis, Texas; Fairbanks, Alaska; and Richmond, Florida. All but Richmond have existing radio telescopes. It is expected that continuous observations would not be necessary. Westford and Fort Davis are likely to be included in the triangle but the third station must still be decided. The purpose of the following section is to compare the triangles containing the two undecided sites and to determine how well polar motion and UT1 can be measured by the POLARIS network.

2. Simulation configuration

A series of baseline configurations were simulated to determine the precision with which polar motion and UT1 could be monitored with VLBI measurements over the POLARIS network. The station parameters are shown in table IV.12. The sites were assumed to be equipped with Mark III recorders using 1.6 Mhz single channel bandwidth, 400 Mhz observing bandwidth and 16 minute observations. The station positions in the table are not given on the same datum nor are they necessarily accurate to better than a few kilometers. However, the positions are sufficiently good for simulation studies. The antenna at Fairbanks, Alaska actually has an X-Y mount, which could not be exactly simulated by the ESTIM program. The parameters for an az-el mount were used instead. Slewing time was not an important factor in the simulation schedules since the duty cycles are light and the telescopes are relatively small and quick. The difference between an X-Y mount and an

Table IV.12 Station configurations for wobble/UT1 simulations

| station | east longitude | | | north latitude | | | elevation |
|------------|----------------|-----|------------|----------------|-----|------------|-----------|
| Westford | 288 | deg | 30' 20.70" | 42 | deg | 36' 46.40" | 115.0 m |
| Richmond | 279 | | 37 4.20 | 25 | | 36 47.13 | 0. |
| Fort Davis | 256 | | 03 0. | 30 | | 38 0. | 1580.0 |
| Fairbanks | 212 | | 28 56.54 | 64 | | 58 36.02 | 299.5 |

| | diameter | type | slew rate 1 hr ang/elev | slew rate 2 declin/azim | minimum elevation | maximum hour angle |
|------------|----------|-------|----------------------------|----------------------------|----------------------|-----------------------|
| Westford | 18.3 m | az-el | 60 deg/min | 60 deg/min | 10 deg | 12 hr |
| Richmond | 25.9 | az-el | 60 | 60 | 10 | 12 |
| Fort Davis | 25.9 | equat | 60 | 60 | 10 | 5.5 |
| Fairbanks | 25.9 | az-el | 60 | 60 | 10 | 12 |

| | efficiency | system temperature | |
|------------|------------|--------------------|------------------------------|
| Westford | 60% | 120 deg K | integration time: 16 min |
| Richmond | 40 | 120 | observing bandwidth: 400 MHz |
| Fort Davis | 40 | 120 | recorded bandwidth: 1.6 MHz |
| Fairbanks | 30 | 120 | |

az-el mount would not affect the results significantly. The hour angle limit on the Fort Davis antenna is an important constraint. In particular, the limit reduces the importance of circumpolar or high declination sources which might otherwise have a long period of mutual visibility. The limited hour angle range of Fort Davis is more of a handicap in the Westford-Richmond-Fort Davis triangle where it is the westernmost station. The telescope listed for Richmond, Florida does not exist. It was included because of interest in locating an antenna at the site of the USNO photographic zenith telescope for logistical reasons.

The baseline parameters are given in table IV.13. The sources, positions and fluxes are shown in table IV.14. The source fluxes are approximate and cannot represent accurately the variations in correlated flux for different baselines and different observing geometries. Nevertheless, they do give some indication of the expected signal-to-noise ratio to be associated with individual observations.

The model errors used for the unadjusted parameters are shown in table IV.15. The site coordinate values are based on projected errors using the Mark III system. The atmosphere error is dependent on data from water vapor radiometers to calibrate the wet component. Errors for the source positions are an extrapolation of past determinations. The errors from solid earth tides and diurnal polar motion are based on results discussed in chapter III.

Five schedules were devised for Westford-Richmond-Fort Davis

Table IV.13 Baseline components for wobble/UT1 simulations

| station 1 | station 2 | X km | Y km | Z km | equatorial km | length km | long. deg E | decl. deg N |
|------------|------------|---------|---------|---------|------------------|--------------|----------------|----------------|
| Westford | Green Bank | 609 | 466 | 352 | 767 | 844 | 37.4 | 24.6 |
| Westford | Richmond | 531 | 1216 | 1556 | 1327 | 2044 | 66.4 | 49.5 |
| Westford | Fort Davis | 2817 | 874 | 1064 | 2949 | 3135 | 17.2 | 19.8 |
| Westford | Fairbanks | 3774 | -3005 | -1461 | 4825 | 5041 | -38.5 | -16.8 |
| Green Bank | Richmond | -79 | 750 | 1204 | 754 | 1420 | 96.0 | 57.9 |
| Green Bank | Fort Davis | 2207 | 408 | 712 | 2245 | 2355 | 10.5 | 17.6 |
| Green Bank | Fairbanks | 3165 | -3472 | -1813 | 4698 | 5035 | -47.6 | -21.1 |
| Richmond | Fort Davis | 2286 | -342 | -491 | 2311 | 2363 | -8.5 | -12.0 |
| Richmond | Fairbanks | 3244 | -4221 | -3016 | 5324 | 6119 | -52.5 | -29.5 |
| Fort Davis | Fairbanks | 958 | -3879 | -2525 | 3996 | 4727 | -76.1 | -32.3 |

Table IV.14 Sources used for wobble/UT1 simulations

| source | right ascension | | | declination | | flux | |
|--------------|-----------------|--------|------------|-------------|----|-------------------|-------|
| 4C 67.05 | 2 hr | 24 min | 42.900 sec | 67 deg | 8' | 6.00 ^m | 1.9 J |
| 3C 84 | 3 | 16 | 29.549 | 41 | 19 | 51.65 | 12.5 |
| NRAO 150 | 3 | 55 | 45.238 | 50 | 49 | 20.08 | 5.5 |
| 3C 120 | 4 | 30 | 31.586 | 5 | 14 | 59.40 | 4.0 |
| OJ 287 | 8 | 51 | 57.229 | 20 | 17 | 58.5 | 6.0 |
| 4C 39.25 | 9 | 23 | 55.294 | 39 | 15 | 23.73 | 7.5 |
| 3C 273 | 12 | 26 | 33.246 | 2 | 19 | 43.30 | 10.0 |
| 3C 279 | 12 | 53 | 35.833 | -5 | 31 | 8.00 | 10.0 |
| OQ 208 | 14 | 4 | 45.625 | 28 | 41 | 29.46 | 1.5 |
| 3C 345 | 16 | 41 | 17.635 | 39 | 54 | 10.97 | 4.5 |
| PKS 2134+00 | 21 | 34 | 5.225 | 0 | 28 | 25.00 | 6.0 |
| VRO 42.22.01 | 22 | 0 | 39.387 | 42 | 2 | 8.40 | 5.0 |
| 3C 454.3 | 22 | 51 | 29.535 | 15 | 52 | 54.25 | 8.0 |

Table IV.15 Unadjusted parameter errors for wobble/UT1 simulations

site cartesian coordinates: 5 cm
 atmosphere zenith thickness: 30 picosec
 source right ascension: .33 msec
 source declination: 5 marcsec
 love h: .05
 love l: .01
 diurnal polar motion scale: .2

(W-R-D) and Westford-Fort Davis-Fairbanks (W-D-F) using the mutual visibilities shown in figure IV.2 and figure IV.3, respectively. The schedules 00, 01, 02, and 03 have 24% duty cycles consisting of groups of four observations separated by four hours. The index indicates the hour of the starting time. The duty cycle was chosen as an approximation of an operational POLARIS network. Schedules beginning at staggered times are necessary because the mix of sources available during each hour of the day is quite different. If network operations require observations to begin at arbitrary times, different schedules are necessary and different results will be obtained. On the other hand, if the starting time is flexible, the best schedule can be used. The schedules indexed 24 use the entire day. An attempt was made to have as many observations on each source as possible. However, the random distribution of sources in right ascension and declination makes it impossible to have the same number of observations on all sources.

3. Comparison of networks using low duty cycle schedules

The results of the four short schedules for W-R-D are summarized in table IV.16 and IV.17 for W-R-D and W-D-F, respectively. The two sets of results for each table represent two modes of error. In the simulations labeled "S/N error only", the measurement uncertainty for each observation was determined from source flux, antenna size and efficiency, receiver temperature, recorder bandwidth, observing bandwidth and integration time. For the simulations marked "constant noise added", an external noise of 0.1 nsec was root-sum-square added to each measurement uncertainty derived above. The results with

**Figure IV.2 Mutual visibility for Westford-Richmond-Fort Davis
Time in UT for August 21, 1975**

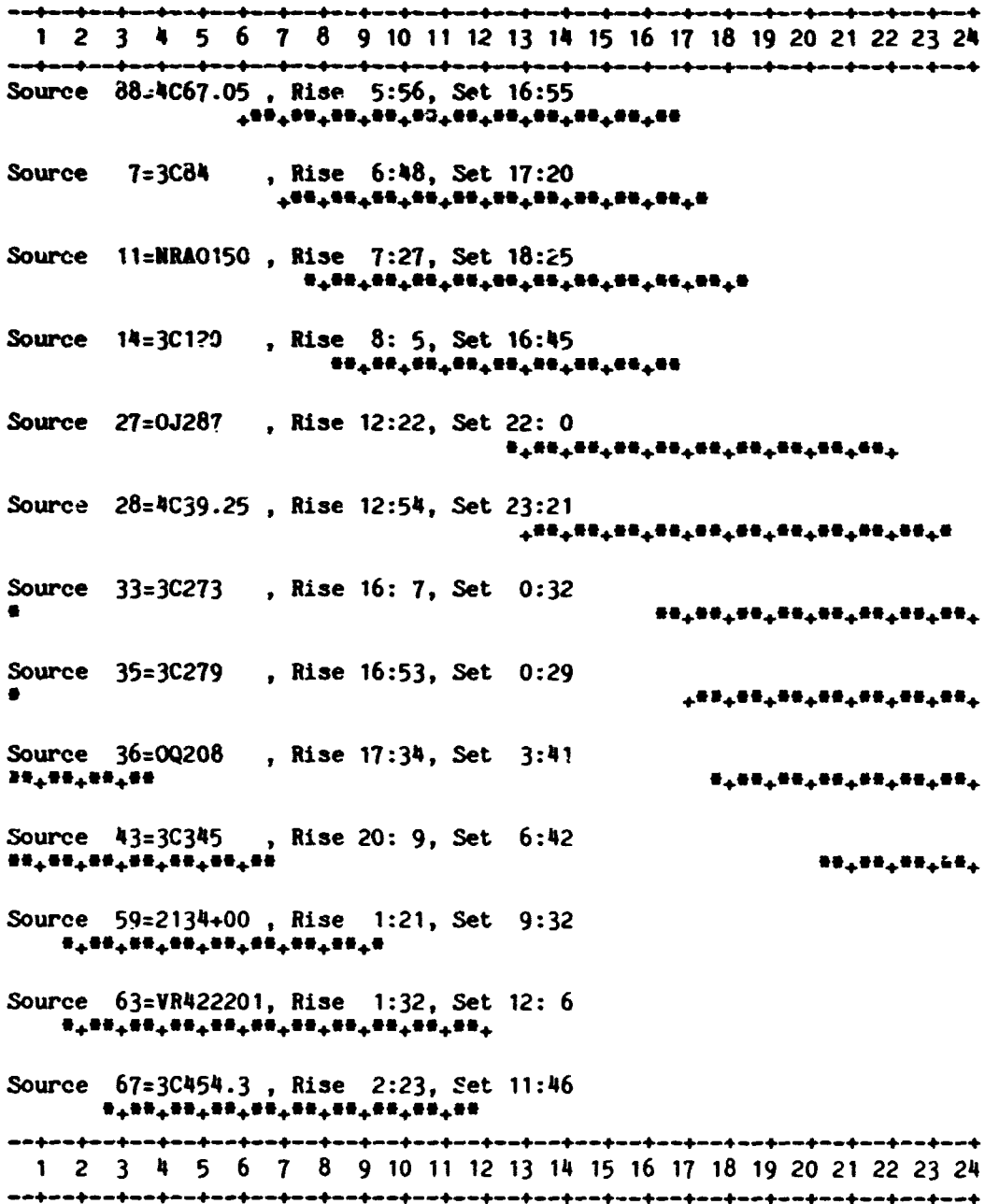


Figure IV.3 Mutual visibility for Westford-Fort Davis-Fairbanks
Time in UT for August 21, 1975

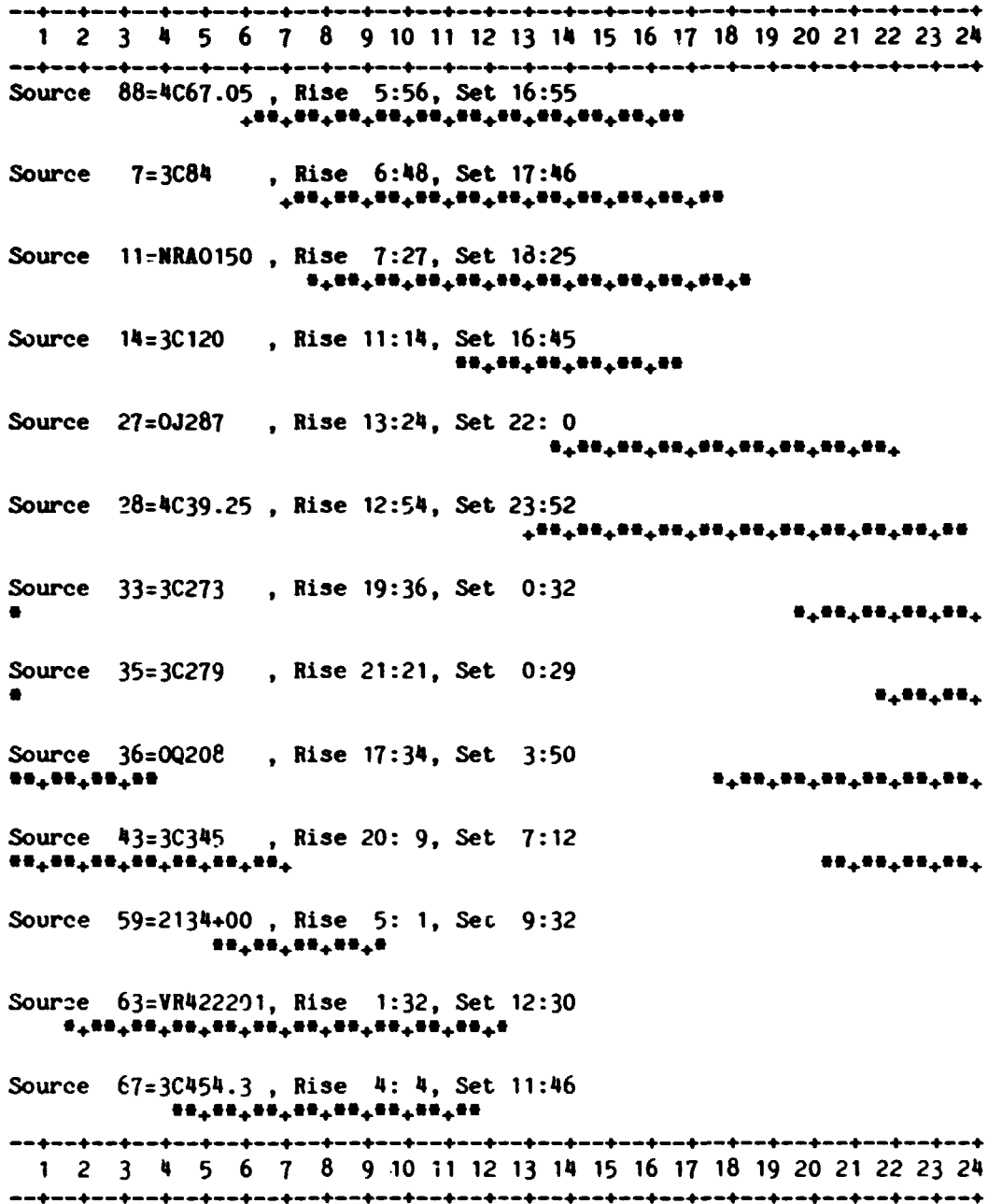


Table IV.16 Summary of errors from schedules WRD00, WRD01, WRD02, and WRD03

| schedule | constant noise added | | | S/N error only | | |
|-----------------------|----------------------|-----------------|-------------|---------------------|-----------------|-------------|
| | x-wob .01 arcsec | y-wob arcsec | UT1 msec | x-wob .01 arcsec | y-wob arcsec | UT1 msec |
| schedule WRD00 | | | | | | |
| noise error | .152 | .391 | .142 | .005 | .014 | .005 |
| total modeled error | .801 | 1.889 | .733 | .869 | 2.219 | .817 |
| total error | .816 | 1.929 | .747 | .869 | 2.219 | .817 |
| schedule WRD01 | | | | | | |
| noise error | .152 | .329 | .117 | .006 | .012 | .004 |
| total modeled error | .618 | 1.143 | .465 | .652 | 1.345 | .518 |
| total error | .636 | 1.190 | .480 | .652 | 1.345 | .518 |
| schedule WRD02 | | | | | | |
| noise error | .153 | .355 | .133 | .005 | .012 | .004 |
| total modeled error | .640 | 1.134 | .471 | .671 | 1.030 | .435 |
| total error | .658 | 1.189 | .489 | .671 | 1.030 | .435 |
| schedule WRD03 | | | | | | |
| noise error | .152 | .356 | .141 | .006 | .014 | .005 |
| total modeled error | .600 | 1.212 | .501 | .648 | 1.289 | .516 |
| total error | .619 | 1.263 | .520 | .648 | 1.289 | .516 |
| average | | | | | | |
| noise error | .152 | .358 | .133 | .006 | .013 | .005 |
| total modeled error | .665 | 1.345 | .543 | .710 | 1.471 | .572 |
| total error | .682 | 1.392 | .559 | .710 | 1.471 | .572 |

Table IV.17 Summary of errors from schedules WDF00, WDF01, WDF02, and WDF03

| | constant noise added | | | S/N error only | | |
|---------------------|----------------------|---------------|-------------|---------------------|---------------|-------------|
| | x-wob .01 arcsec | y-wob msec | UT1 msec | x-wob .01 arcsec | y-wob msec | UT1 msec |
| schedule WDF00 | | | | | | |
| noise error | .185 | .183 | .095 | .007 | .007 | .004 |
| total modeled error | .874 | .918 | .521 | 1.066 | 1.144 | .631 |
| total error | .893 | .936 | .530 | 1.066 | 1.144 | .631 |
| schedule WDF01 | | | | | | |
| noise error | .173 | .168 | .085 | .007 | .007 | .004 |
| total modeled error | .740 | .839 | .426 | .858 | 1.033 | .520 |
| total error | .760 | .856 | .434 | .858 | 1.033 | .520 |
| schedule WDF02 | | | | | | |
| noise error | .177 | .173 | .078 | .007 | .007 | .003 |
| total modeled error | .632 | .759 | .353 | .667 | .725 | .382 |
| total error | .656 | .779 | .362 | .667 | .725 | .382 |
| schedule WDF03 | | | | | | |
| noise error | .167 | .161 | .077 | .007 | .006 | .003 |
| total modeled error | .641 | .761 | .363 | .682 | .834 | .411 |
| total error | .662 | .778 | .371 | .682 | .834 | .411 |
| average | | | | | | |
| noise error | .175 | .171 | .084 | .007 | .007 | .004 |
| total modeled error | .722 | .819 | .416 | .818 | .934 | .486 |
| total error | .742 | .837 | .424 | .818 | .934 | .486 |

constant noise added give an indication of the precision presently possible with the Mark I system. Only the delay observable was used. The x and y components of polar motion, UT1, and clock offsets and rates at two sites were adjusted, a total of seven parameters.

Comparison of the W-R-D and W-D-F results indicates that the latter has errors between 20% and 40% smaller for the average polar motion component and UT1 offset in all cases. While the x-component is better determined by the baselines W-R-D, the y-component is sufficiently worse to make the average poorer. Given the particular values for the unadjusted parameter model errors, no single parameter stands out in the MDE of the adjusted parameters. All other things being equal, the network containing Fairbanks gives more precise measurements than the Richmond network when using low duty cycle schedules.

4. Comparison of two networks using 24 hr duty cycle

The results for the 24 hr schedules are shown in table IV.18. If the measurement uncertainty is determined by signal-to-noise limits, then the MDE for the two configurations are almost identical. With external noise added, the MDE for the W-D-F triangle are smaller than the errors for W-R-D by approximately 10%. Therefore the network containing Fairbanks gives better results even with a full day duty cycle, although the advantage is not so marked as with the low duty cycle schedules.

Table IV.18 Errors from wobble/UT1 schedules WRD24 and WDF24

| | constant noise added | | | S/N error only | | |
|---------------------|----------------------|-----------------|-------------|---------------------|-----------------|-------------|
| | x-wob .01 arcsec | y-wob arcsec | UT1 msec | x-wob .01 arcsec | y-wob arcsec | UT1 msec |
| schedule WRD24 | | | | | | |
| noise error | .083 | .187 | .069 | .003 | .007 | .002 |
| total modeled error | .554 | .984 | .409 | .580 | .997 | .416 |
| total error | .560 | 1.002 | .414 | .580 | .997 | .416 |
| schedule WDF24 | | | | | | |
| noise error | .094 | .091 | .044 | .004 | .004 | .002 |
| total modeled error | .661 | .700 | .367 | .746 | .837 | .414 |
| total error | .668 | .706 | .370 | .746 | .837 | .414 |

5. Comparison of networks using low duty cycles and complete adjustment

The simulations discussed above assume that only the polar motion and UT1 parameters are adjusted and that each day is adjusted separately. Another method of analysis is to combine the data from several days and adjust all the parameters possible simultaneously. The site coordinates and source positions are adjusted over all the data. Each day requires at least clock offsets and rates for two stations and an atmosphere parameter at each station. The polar motion and UT1 parameters must be left unadjusted for at least one day to provide a reference orientation. Using this method, between 65 and 70 parameters are required to handle four days of data. The results are presented in tables IV.19 and IV.20 for W-R-D and W-D-F, respectively. The 00, 01, 02 and 03 schedules were used. The 00 schedule was left unchanged and the wobble/UT1 parameters left unadjusted. The other schedules were slipped by 3 min 56 sec per day and moved to successive days to form a combined data set. The only models contributing to MDE are solid earth tides and diurnal polar motion. The NOE for W-D-F are generally at least 50% better than the NOE for W-R-D. An exception is the x-component if only the signal-to-noise error is included in the analysis, in which case the NOE are equal. However, it is evident that the W-D-F triangle is more susceptible to MDE caused by solid earth tides and diurnal polar motion. The x-component MDE is between 40% and 90% worse for W-D-F than for W-R-D while the advantage of W-D-F over W-R-D for the other parameters is also reduced. The average pole position is in fact determined better by the W-R-D configuration. It

Table IV.19 Westford-Richmond-Fort Davis four day estimate of wobble/UT1

| | constant noise added | | | S/N error only | | |
|---------------------|----------------------|---------------|-------------|---------------------|---------------|-------------|
| | x-wob .01 arcsec | y-wob msec | UT1 msec | x-wob .01 arcsec | y-wob msec | UT1 msec |
| schedule WRD00 | | | | | | |
| noise error | | | | | | |
| total modeled error | | | | | | |
| total error | | | | | | |
| schedule WRD01 | | | | | | |
| noise error | .562 | 1.27 | .516 | .022 | .053 | .021 |
| total modeled error | .055 | .105 | .085 | .078 | .113 | .127 |
| total error | .565 | 1.27 | .523 | .081 | .124 | .129 |
| schedule WRD02 | | | | | | |
| noise error | .669 | 1.35 | .683 | .025 | .055 | .026 |
| total modeled error | .082 | .058 | .120 | .115 | .104 | .159 |
| total error | .673 | 1.35 | .693 | .118 | .117 | .161 |
| schedule WRD03 | | | | | | |
| noise error | .571 | 1.32 | .574 | .023 | .056 | .023 |
| total modeled error | .084 | .094 | .112 | .077 | .109 | .113 |
| total error | .577 | 1.32 | .584 | .080 | .122 | .115 |
| average | | | | | | |
| noise error | .601 | 1.31 | .591 | .023 | .055 | .023 |
| total modeled error | .074 | .086 | .106 | .090 | .109 | .133 |
| total error | .605 | 1.31 | .600 | .093 | .121 | .135 |

Table IV.20 Westford-Fort Davis-Fairbanks four day estimate of wobble/UT1

| | constant noise added | | | S/N error only | | |
|---------------------|----------------------|-----------------|-------------|---------------------|-----------------|-------------|
| | x-wob .01 arcsec | y-wob arcsec | UT1 msec | x-wob .01 arcsec | y-wob arcsec | UT1 msec |
| schedule WDF00 | | | | | | |
| noise error | | | | | | |
| total modeled error | | | | | | |
| total error | | | | | | |
| schedule WDF01 | | | | | | |
| noise error | .416 | .405 | .235 | .020 | .020 | .012 |
| total modeled error | .060 | .035 | .023 | .073 | .067 | .028 |
| total error | .420 | .407 | .236 | .076 | .070 | .031 |
| schedule WDF02 | | | | | | |
| noise error | .439 | .473 | .233 | .022 | .022 | .012 |
| total modeled error | .127 | .090 | .029 | .208 | .095 | .091 |
| total error | .457 | .482 | .235 | .209 | .098 | .092 |
| schedule WDF03 | | | | | | |
| noise error | .450 | .446 | .233 | .022 | .022 | .011 |
| total modeled error | .141 | .110 | .057 | .251 | .112 | .108 |
| total error | .471 | .459 | .240 | .252 | .114 | .108 |
| average | | | | | | |
| noise error | .435 | .441 | .234 | .021 | .021 | .012 |
| total modeled error | .109 | .079 | .036 | .177 | .091 | .076 |
| total error | .449 | .449 | .237 | .179 | .094 | .077 |

should be noted that the results derived using only signal-to-noise measurement uncertainty are probably the most optimistic realistic estimate of the precision possible for either POLARIS network using low duty cycle schedules.

6. Effect of diurnal polar motion and solid earth tides

The same schedules may be used on different days provided the starting times are adjusted to offset the 3 min 56 sec daily slippage between solar time and sidereal time. The MDE contributions from site coordinates, atmosphere, and source positions are unaffected since the observing geometry is unchanged. The effects of the solid earth tide and diurnal polar motion, however, depend on the relative lunar and solar positions. These effects vary through a lunar cycle. Tables IV.21 and IV.22 show the effects of earth tides and diurnal polar motion for several different days using schedules WRD00 and WDF00, respectively. The days were spaced at five day intervals. The starting epoch for the schedules was altered to preserve the original observation geometry for the other effects. The first day was already presented in tables IV.16 and IV.17. The interval from 8/21 through 9/4 covers enough of a lunar cycle to give representative results. For measurement uncertainty from signal-to-noise only, the maximum root-sum-squared error contribution from earth tides and diurnal polar motion is 0.88 milliarcsec in the x-component, 1.93 milliarcsec in the y-component, and 0.119 msec in UT1. With constant external noise added the maximum effects are 0.30 milliarcsec, 0.92 milliarcsec, and 0.093 msec, respectively. Consequently these effects never dominate

Table IV.21 Errors from schedule WRD00 at 5-day intervals -
earth tide and diurnal polar motion modeled errors

| unadjusted parameter | constant noise added | | | S/N error only | | |
|------------------------|----------------------|-----------------|-------------|---------------------|-----------------|-------------|
| | x-wob .01 arcsec | y-wob arcsec | UT1 msec | x-wob .01 arcsec | y-wob arcsec | UT1 msec |
| starting 75/8/25 23:41 | | | | | | |
| Love h | .019 | .054 | .006 | .027 | .073 | .017 |
| Love l | .018 | .017 | .022 | .016 | .018 | .025 |
| diurnal polar motion | .001 | .054 | .050 | .004 | .171 | .075 |
| starting 75/8/30 23:22 | | | | | | |
| Love h | .004 | .048 | .010 | .028 | .014 | .022 |
| Love l | -.001 | .017 | -.008 | -.002 | .025 | -.009 |
| diurnal polar motion | .010 | -.018 | .019 | .051 | .118 | .077 |
| starting 75/9/4 23:02 | | | | | | |
| Love h | .001 | .027 | -.050 | -.004 | -.012 | -.083 |
| Love l | .019 | .032 | .027 | .028 | .019 | .036 |
| diurnal polar motion | -.021 | -.088 | -.073 | -.003 | -.196 | -.078 |

Table IV.22 Errors from schedule WDF00 at 5-day intervals -
earth tide and diurnal polar motion modeled errors

| unadjusted parameter | constant noise added | | | S/N error only | | |
|------------------------|----------------------|-----------------|-------------|---------------------|-----------------|-------------|
| | x-wob .01 arcsec | y-wob arcsec | UT1 msec | x-wob .01 arcsec | y-wob arcsec | UT1 msec |
| starting 75/8/25 23:41 | | | | | | |
| Love h | -.022 | .025 | -.008 | .002 | .006 | -.008 |
| Love l | .018 | .020 | .018 | .014 | .005 | .012 |
| diurnal polar motion | -.008 | .037 | .036 | -.020 | .120 | .036 |
| starting 75/8/30 23:22 | | | | | | |
| Love h | .020 | .043 | .020 | .053 | .075 | .044 |
| Love l | -.022 | -.016 | -.015 | -.028 | -.039 | -.023 |
| diurnal polar motion | .012 | .069 | .022 | .064 | .173 | .057 |
| starting 75/9/4 23:02 | | | | | | |
| Love h | .001 | .004 | -.001 | .018 | -.031 | -.015 |
| Love l | .001 | .038 | .013 | .019 | -.007 | .013 |
| diurnal polar motion | -.002 | -.003 | -.038 | .041 | -.076 | -.021 |

the MDE.

7. Conclusions

These results indicate that the network using Westford, Fort Davis and Fairbanks generally yields smaller errors in determining polar motion and UT1 than the network with Westford, Richmond, and Fort Davis. The longer lengths of the baselines in the first triangle give a better geometry while the problem of mutual visibility is not a major handicap. The results are valid only if the stations are essentially identical. If the antenna efficiencies or receiver temperatures are different, further analysis will be necessary.

D. The effect of scheduling on baseline parameter errors

1. Introduction

In most VLBI geodetic experiments there is relatively little flexibility in the physical observing configuration. The stations and times are set by observatory scheduling constraints. Antenna sizes are fixed. Once the frequency is decided, the effective collecting area cannot be altered. The receivers are those available at the selected frequency while integration time is limited by the recorders or frequency standard stability. Flexibility is only possible in the choice and sequence of sources to be observed. This section examines the effect of scheduling on the precision of baseline measurements using model errors in several small geophysical effects.

The analysis of scheduling would be simplified if sources were of equal flux with uniform distribution about the sky and if antennas could slew infinitely quickly. Observing all the visible sources simultaneously in all parts of the sky would give very strong geodetic results. To be at all realistic, however, it is necessary to consider the actual distribution of sources and the often infuriatingly slow movement of large telescopes. A number of single day, single baseline schedules were studied for three stations using sources observed in past VLBI experiments.

2. Simulation parameters

The station parameters are given in table IV.23 and the baseline components in table IV.24. The bandwidths and integration time reflect the capability of the Mark I VLBI system. Pioneer and Goldstone are two antennas in the Goldstone tracking complex of the Deep Space Network. The Haystack-Goldstone baseline has been used frequently in the past (Robertson 1975, Hutton 1976). The Haystack-Pioneer baseline has not been used and is discussed here for the purpose of simulations. The actual Pioneer antenna has an equatorial mount. The slewing times for an az-el mount were used in the following simulations so that a comparison with Goldstone would be more meaningful. The primary difference between an equatorial antenna and an az-el antenna, slewing rates and dish sizes being equal, is the ability to follow sources near or through transit. At transit the azimuth of a source changes rapidly, infinitely fast if the source passes through zenith, and an

Table IV.23 Station configurations for schedule tests

| station | east longitude | | north latitude | | elevation | | | |
|-----------|----------------|--------------------|----------------------------|------------------------------|----------------------|-----------------------|--|--|
| Haystack | 288 deg | 30' 40.86" | 42 deg | 37' 23.50" | 152.2 m | | | |
| Pioneer | 243 | 9 1.46 | 35 | 23 22.15 | 963.0 | | | |
| Goldstone | 243 | 6 37.84 | 35 | 25 33.34 | 977.5 | | | |
| | diameter | type | slew rate 1 hr ang/elev | slew rate 2 declin/azim | minimum elevation | maximum hour angle | | |
| Haystack | 36.6 m | az-el | 120 deg/min | 120 deg/min | 10 deg | 12 hr | | |
| Pioneer | 25.9 | az-el | 60 | 60 | 10 | 12 | | |
| Goldstone | 64.0 | az-el | 12 | 12 | 10 | 12 | | |
| | efficiency | system temperature | | integration time: 3 min | | | | |
| Haystack | 35% | 80 deg K | | recorded bandwidth: 360 kHz | | | | |
| Pioneer | 40 | 30 | | observing bandwidth: 330 MHz | | | | |
| Goldstone | 40 | 30 | | | | | | |

Table IV.24 Baseline components for schedule tests

| station 1 | station 2 | X km | Y km | Z km | equatorial km | length km | long. deg E | decl. deg N |
|-----------|-----------|---------|---------|---------|------------------|--------------|----------------|----------------|
| Haystack | Pioneer | 3844 | 188 | 623 | 3848 | 3899 | 2.8 | 9.2 |
| Haystack | Goldstone | 3846 | 184 | 620 | 3850 | 3900 | 2.7 | 9.1 |

Table IV.25 Sources used for schedule tests

| source | right ascension | | | declination | | | flux |
|--------------|-----------------|--------|------------|-------------|----|-------|-------|
| 4C 67.05 | 2 hr | 24 min | 42.900 sec | 67 deg | 8' | 6.00" | 1.9 J |
| 3C 84 | 3 | 16 | 29.549 | 41 | 19 | 51.65 | 12.5 |
| NRAO 150 | 3 | 55 | 45.238 | 50 | 49 | 20.08 | 5.5 |
| 3C 120 | 4 | 30 | 31.586 | 5 | 14 | 59.40 | 4.0 |
| OJ 287 | 8 | 51 | 57.229 | 20 | 17 | 58.5 | 6.0 |
| 4C 39.25 | 9 | 23 | 55.294 | 39 | 15 | 23.73 | 7.5 |
| 3C 273 | 12 | 26 | 33.246 | 2 | 19 | 43.30 | 10.0 |
| 3C 279 | 12 | 53 | 35.833 | -5 | 31 | 8.00 | 10.0 |
| OQ 208 | 14 | 4 | 45.625 | 28 | 41 | 29.46 | 1.5 |
| 3C 345 | 16 | 41 | 17.635 | 39 | 54 | 10.97 | 4.5 |
| PKS 2134+00 | 21 | 34 | 5.225 | 0 | 28 | 25.00 | 6.0 |
| VRO 42.22.01 | 22 | 0 | 39.387 | 42 | 2 | 8.40 | 5.0 |
| 3C 454.3 | 22 | 51 | 29.535 | 15 | 52 | 54.25 | 8.0 |

az-el telescope takes longer to move from source to source in this observing geometry. The problem is most acute if two sources being observed transit north and south of zenith in a short interval of time. While an equatorial mount can follow the sources easily, the large difference in azimuth may make it impossible for an az-el mount. For the purposes of these simulations the difference between Pioneer and Goldstone are antenna size and slewing rate. While Haystack is a relatively large az-el telescope, it is protected by a radome and can move extremely rapidly. It is not the limiting station in any schedule. One factor that is not included in the Haystack-Pioneer simulations is the constraint of cable wrap, the limit of an az-el antenna's continuous azimuth rotation clockwise and counterclockwise. In practice it is a serious limitation in scheduling large, slow-moving antennas and is considered in the Haystack-Goldstone schedule.

The sources used in the simulation schedules are listed in table IV.25. These are generally the strongest incompletely resolved sources visible in the northern hemisphere. The positions are for epoch 1950.0. The fluxes are approximate average values for the Haystack-Goldstone baseline taken from Wittels et al. (1975) except for the flux of 4C67.05, which is taken from more recent experiments. For some sources the visibility function has a complex behavior with deep nulls. In the following work such variations are ignored, leaving only the distinction between weaker and stronger sources. Table IV.25 shows clearly that there are gaps in distribution over the sky, particularly between 4 hr to 9 hr, 17 hr to 21 hr, and 23 hr to 2 hr in right ascension. There is only one high declination source, 4C67.05, because

of the scarcity of observable sources in this region. The sources used in each schedule are given in table IV.26. The mutual visibility of sources between Haystack and Pioneer/Goldstone is given in figure IV.4.

The schedules contain several realistic timing constraints. Two minutes were allowed in addition to the minimum slewing time for the mechanics of finding a source and doing radiometry. A minimum of three minutes was allowed between the end of one observation and the beginning of the next for rewinding and changing data tapes. The rewinding and changing time are drawn from Mark I practice. Mark II tapes typically record for several hours before rewinding. Mark III tapes can be filled in as little as 14 minutes or last for nearly two hours depending on the recording rate. Tape rewinding and changing time would be approximately 10 minutes.

The simulation geometry was computed with several simplifying assumptions. The source positions of 1950.0 were used unchanged. No corrections were made for precession, nutation, aberration, polar motion or UT1. The baseline geometry was computed directly from the site coordinates and not otherwise modified. The day was picked arbitrarily for proximity to an existing Haystack-Goldstone schedule.

Each schedule was run under three simulation configurations. In all cases only the delay observable was included in the normal matrix. Unless otherwise noted a pair of tapes was recorded each time a source was observed. In the first configuration the observations were weighted by the SNE measurement uncertainties, which were calculated

**Figure IV.4 Mutual visibility for Haystack-Pioneer/Goldstone
Time in UT for August 21, 1975**



Table IV.26 Sources used in schedules A - M

| schedule | A | | B | | C | |
|----------|--------------|-----|--------------|-----|----------|-----|
| | source | obs | source | obs | source | obs |
| | 3C 84 | 84 | 3C 84 | 31 | 3C 84 | 31 |
| | 3C 273 | 70 | 3C 273 | 25 | 3C 273 | 25 |
| | 3C 454.3 | 59 | 3C 454.3 | 27 | 3C 454.3 | 27 |
| | | | | | 4C 67.05 | 21 |
| schedule | D | | E | | | |
| | 3C 84 | 47 | 3C 84 | 41 | | |
| | 3C 120 | 32 | 3C 120 | 30 | | |
| | 3C 273 | 41 | 3C 273 | 37 | | |
| | 3C 345 | 48 | 3C 345 | 46 | | |
| | PKS 2134+00 | 22 | PKS 2134+00 | 20 | | |
| | VRO 42.22.01 | 38 | VRO 42.22.01 | 30 | | |
| | | | 4C67.05 | 24 | | |
| schedule | F | | G | | | |
| | 3C 84 | 38 | 3C84 | 36 | | |
| | 3C 120 | 24 | 3C 120 | 24 | | |
| | OJ 287 | 32 | OJ 287 | 28 | | |
| | 3C 273 | 32 | 3C 273 | 30 | | |
| | 3C 345 | 42 | 3C 345 | 38 | | |
| | PKS 2134+00 | 22 | PKS 2134+00 | 20 | | |
| | VRO 42.22.01 | 38 | VRO 42.22.01 | 28 | | |
| | | | 4C 67.05 | 24 | | |
| schedule | H | | I | | | |
| | 3C 84 | 36 | 3C 84 | 32 | | |
| | 3C 120 | 24 | 3C 120 | 24 | | |
| | OJ 287 | 26 | OJ 287 | 20 | | |
| | 3C 273 | 24 | 3C 273 | 24 | | |
| | OQ 208 | 30 | OQ 208 | 26 | | |
| | 3C 345 | 32 | 3C 345 | 32 | | |
| | PKS 2134+00 | 21 | PKS 2134+00 | 19 | | |
| | VRO 42.22.01 | 36 | VRO 42.22.01 | 28 | | |
| | | | 4C 67.05 | 24 | | |

| schedule | J | | K | | M | |
|----------|--------------|----|--------------|----|--------------|----|
| | 4C 67.05 | 16 | 4C 67.05 | 6 | 3C84 | 91 |
| | 3C 84 | 24 | 3C 84 | 22 | 4C 39.25 | 30 |
| | NRAO 150 | 28 | NRAO 150 | 23 | 3C 273 | 31 |
| | 3C 120 | 18 | 3C 120 | 23 | 3C 279 | 17 |
| | 4C 39.25 | 26 | 4C 39.25 | 22 | VRO 42.22.01 | 23 |
| | 3C 273 | 18 | 3C 273 | 15 | 3C 454.3 | 48 |
| | 3C 279 | 18 | 3C 279 | 20 | | |
| | 3C 345 | 24 | 3C 345 | 26 | | |
| | PKS 2134+00 | 16 | PKS 2134+00 | 22 | | |
| | VRO 42.22.01 | 26 | VRO 42.22.01 | 27 | | |
| | 3C 454.3 | 15 | 3C 454.3 | 23 | | |

from the source flux, antenna size and efficiency, receiver temperature, recorded and observing bandwidths, and integration time. This value of measurement uncertainty represents the minimum error achievable by the system, the limit set by signal-to-noise ratio. A full set of parameters was adjusted: 1) the coordinates of the western station, 2) a clock offset and rate, 3) an atmosphere zenith height for each station, and 4) the source right ascensions and declinations with the exception of the right ascension of 3C 273. Earth tides and diurnal polar motion were considered as source of MDE with model errors of 0.05 in Love h, 0.01 in Love l and 0.2 in the diurnal polar motion scaling. The results are given in table IV.27. The baseline longitude and latitude refer to the orientation of the baseline when translated to the origin of the geocentric coordinate system. The columns headed "noise-only error" show the parameter formal errors if only measurement uncertainty is included in the analysis. The columns headed "with modeled errors" show the total errors, i.e., the root-sum-square of NOE and MDE. In general the MDE is much larger than the NOE so that the total error is essentially equal to the MDE.

In the second configuration a constant external noise of 0.1 nanosec was root-sum-square added to the signal-to-noise measurement uncertainty to give the observation weight. The set of adjusted and unadjusted parameters was the same as above. These results, presented in table IV.28, represent the case where a large or dominant external random noise is present. The effect is to reduce the importance of the stronger sources.

Table IV.27 Baseline errors for Haystack-Pioneer/Goldstone schedules with measurement uncertainty determined by source and receiving parameters - full set of parameter adjustments

| schedule | noise-only error | | | with modeled errors | | |
|----------|------------------|--------------------------|----------|---------------------|--------------------------|----------|
| | length cm | longitude .001 arcsec | latitude | length cm | longitude .001 arcsec | latitude |
| A | .133 | .116 | .184 | 2.22 | 3.01 | 2.11 |
| B | .163 | .208 | .224 | 1.22 | 1.93 | 1.47 |
| C | .156 | .181 | .224 | 1.74 | 2.86 | 1.04 |
| D | .239 | .138 | .410 | 1.76 | 1.86 | 4.57 |
| E | .170 | .158 | .276 | .488 | 1.85 | 1.88 |
| F | .163 | .145 | .265 | .320 | 1.77 | 1.11 |
| G | .145 | .155 | .222 | .506 | 1.59 | .626 |
| H | .162 | .146 | .276 | .369 | 1.33 | .832 |
| I | .140 | .152 | .224 | .365 | 1.43 | .616 |
| J | .090 | .172 | .179 | .710 | 2.49 | 3.28 |
| K | .091 | .174 | .166 | .673 | 1.60 | 1.81 |
| L | .069 | .097 | .102 | 1.34 | 3.02 | 1.66 |
| M | 1.80 | .621 | .738 | 8.94 | 5.12 | 4.32 |

Table IV.28 Baseline errors for Haystack-Pioneer/Goldstone schedules with constant noise added to all observations - full set of parameter adjustments

| schedule | noise-only error | | | with modeled errors | | |
|----------|------------------|--------------------------|----------|---------------------|--------------------------|----------|
| | length cm | longitude .001 arcsec | latitude | length cm | longitude .001 arcsec | latitude |
| A | 2.59 | 2.53 | 3.49 | 3.52 | 4.17 | 4.36 |
| B | 3.21 | 3.99 | 4.39 | 3.61 | 4.97 | 4.75 |
| C | 2.63 | 3.75 | 3.33 | 3.09 | 5.00 | 3.59 |
| D | 2.84 | 2.47 | 4.90 | 3.40 | 2.71 | 6.12 |
| E | 1.76 | 2.64 | 2.32 | 1.81 | 2.94 | 2.40 |
| F | 2.19 | 2.48 | 3.54 | 2.35 | 2.82 | 3.63 |
| G | 1.75 | 2.60 | 2.20 | 1.88 | 2.95 | 2.31 |
| H | 1.93 | 1.57 | 3.26 | 1.96 | 2.11 | 3.32 |
| I | 1.54 | 1.65 | 2.05 | 1.56 | 2.18 | 2.08 |
| J | 1.57 | 2.90 | 2.72 | 1.61 | 3.57 | 3.55 |
| K | 1.53 | 3.01 | 2.57 | 1.63 | 3.17 | 2.66 |
| L | 2.23 | 3.71 | 2.61 | 2.43 | 4.15 | 2.71 |
| M | 38.6 | 13.3 | 15.7 | 39.2 | 14.0 | 16.1 |

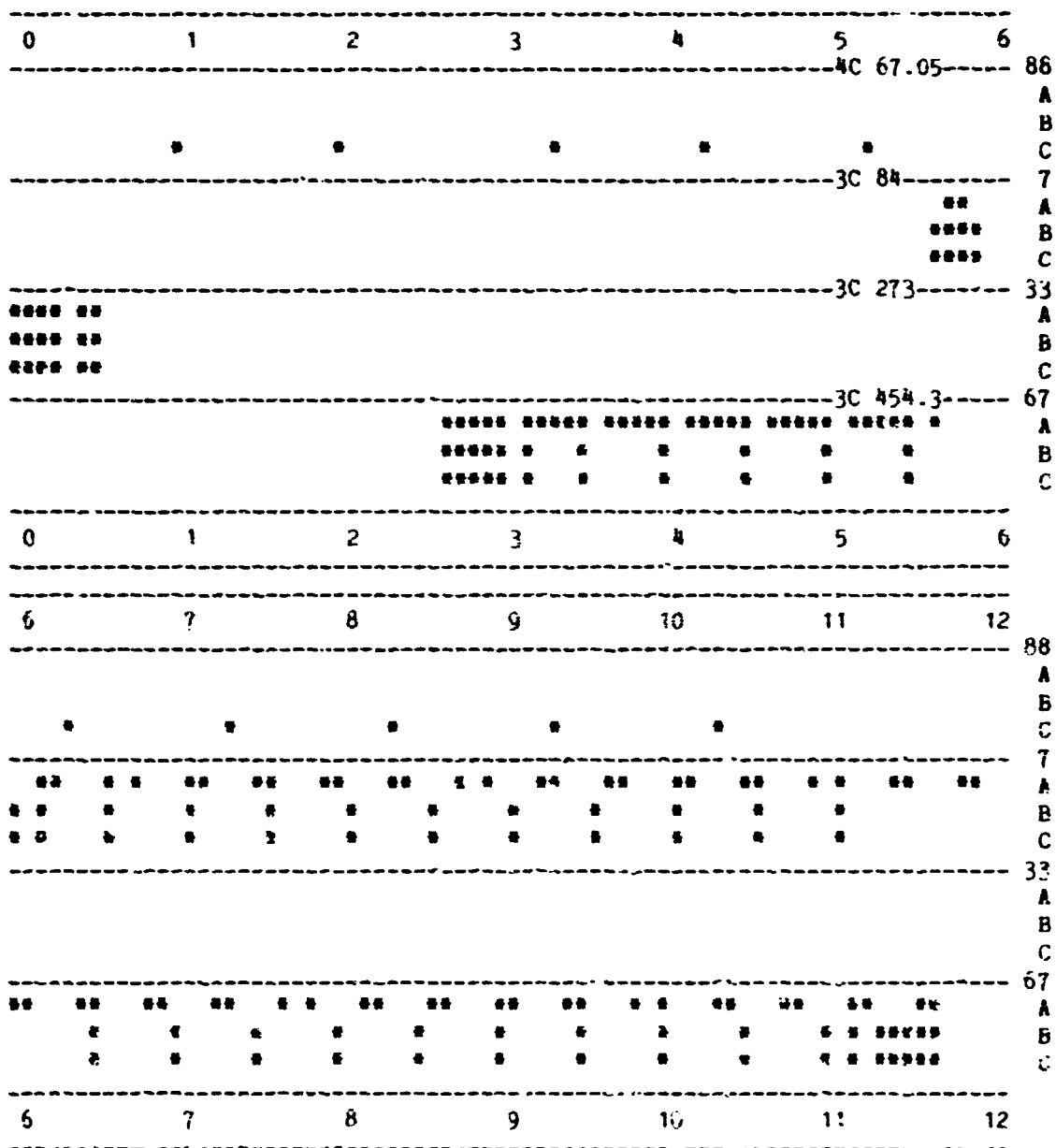
The third configuration used the signal-to-noise measurement uncertainty weighting but adjusted only the site coordinates and the two clock parameters. The atmosphere and source positions were included as unadjusted parameters with errors of 0.03 nanosec and 5 milliarcsec, respectively. Solid earth tides and diurnal polar motion are also included as unadjusted parameters. This configuration gives the most optimistic values for the baseline NOE and is rather unrealistic. The atmosphere must be calibrated to 1 cm while the source positions must be known from other measurements. The results are shown in table IV.29.

The simulations fall into three groups: 1) schedules A, B, and C; 2) schedules D - I; and 3) schedules J, K, and L. Schedule M is a special case. All the schedules except schedule L apply to the Haystack-Pioneer baseline.

3. Three and four source schedules

A comparison plot of schedules A, B, and C is presented in figure IV.5. The horizontal direction is UT observing time during one day. The asterisks in each band mark individual observations of the specified source. These schedules used the minimum number of sources possible to provide a reference for more complicated schedules. 3C 84, 3C 273, and 3C 454.3 were chosen because of source strength and distribution in right ascension and declination. Even so there is a gap of two hours after 3C 273 sets before 3C 454.3 rises. In schedule A each source was observed continuously when it was the only source

Figure IV.5 Comparison of schedules A, B, and C
Time in UT for August 21, 1975



| 12 | 13 | 14 | 15 | 16 | 17 | 18 | 96 |
|-------|-------|-------|-------|-------|-------|-------|----|
| | | | | | | | A |
| | | | | | | | B |
| | | | | | | | C |
| | | | | | | | 7 |
| ••••• | ••••• | ••••• | ••••• | ••••• | ••••• | ••••• | A |
| • | • | • | • | • | • | • | B |
| • | • | • | • | • | • | • | C |
| | | | | | | | 33 |
| | | | | | •• | •• | A |
| | | | | | | ••••• | B |
| | | | | | | ••••• | C |
| | | | | | | | 67 |
| | | | | | | | A |
| | | | | | | | B |
| | | | | | | | C |
| 12 | 13 | 14 | 15 | 16 | 17 | 18 | |
| 18 | 19 | 20 | 21 | 22 | 23 | 24 | 88 |
| | | | | | | | A |
| | | | | | | | B |
| | | | | | | | C |
| | | | | | | | 7 |
| •• | | | | | | | A |
| • | | | | | | | B |
| • | | | | | | | C |
| | | | | | | | 33 |
| ••••• | ••••• | ••••• | ••••• | ••••• | ••••• | ••••• | A |
| • | • | • | • | • | • | • | B |
| • | • | • | • | • | • | • | C |
| | | | | | | | 67 |
| | | | | | | | A |
| | | | | | | | B |
| | | | | | | | C |
| 18 | 19 | 20 | 21 | 22 | 23 | 24 | |

**Table IV.29 Baseline errors for Haystack-Pioneer/Goldstone schedules
adjusting only site coordinates and clocks**

| schedule | noise-only error | | | with modeled errors | | |
|----------|------------------|--------------------------|-------------------------|---------------------|--------------------------|-------------------------|
| | length cm | longitude .001 arcsec | latitude .001 arcsec | length cm | longitude .001 arcsec | latitude .001 arcsec |
| A | .0223 | .0244 | .0237 | 3.78 | 4.30 | 8.53 |
| B | .0257 | .0329 | .0364 | 3.86 | 4.50 | 7.63 |
| C | .0246 | .0329 | .0371 | 4.24 | 4.56 | 7.96 |
| D | .0246 | .0284 | .0279 | 5.61 | 4.13 | 6.87 |
| E | .0252 | .0308 | .0289 | 3.64 | 3.99 | 6.80 |
| F | .0251 | .0294 | .0296 | 3.32 | 3.74 | 6.55 |
| G | .0262 | .0299 | .0303 | 3.44 | 3.83 | 6.62 |
| H | .0261 | .0318 | .0309 | 3.55 | 3.79 | 6.62 |
| I | .0267 | .0327 | .0320 | 3.62 | 3.80 | 6.55 |
| J | .0249 | .0309 | .0278 | 2.82 | 3.29 | 4.90 |
| K | .0214 | .0315 | .0298 | 2.83 | 3.28 | 4.57 |
| L | .0120 | .0161 | .0170 | 3.53 | 3.21 | 5.76 |
| M | .0197 | .0259 | .0246 | 4.64 | 4.87 | 6.48 |

visible. Where two sources overlapped, pairs of observations on each source were interleaved. In schedule B the sources were observed once every half an hour except on rising and before setting. At those times the source was observed continuously for half an hour to have denser data at the extremes of the diurnal sinusoid. For schedule C one observation of 4C 67.05 at hourly intervals was added to schedule B to examine the effects of a weaker, high declination source.

Referring to table IV.27 for the SNE measurement uncertainty weighting results, it can be seen that schedule A produces the smallest baseline NOE. This is to be expected since schedule A has considerably more data than the other schedules in the group. Even though schedule B has less than half the number of observations on each source as schedule A, its NOE are only 20% worse than those of schedule A for length and latitude. The longitude error is 80% worse, somewhat worse than the reduction in the number of data points. Schedule C improves on schedule B in length and longitude NOE but somewhat surprisingly not in latitude. Apparently the additional adjusted parameters needed for 4C 67.05 weaken the solution sufficiently to make the high declination data less useful.

A different picture emerges when comparing the baseline MDE. Schedule B has between 30% and 45% smaller errors than schedule A with 60% fewer observations. While more observations of the same precision always decrease the NOE, the added data can increase the MDE. Schedule C has larger MDE than schedule B in baseline length and longitude and a smaller MDE in latitude. The additional observations degrade the

precision of the length and longitude more than they improve the latitude.

If the estimation is dominated by external noise as shown in table IV.28, the usefulness of a high declination source is more apparent. Schedule C is between 15% and 25% better than schedule B in baseline length and latitude for both NOE and total error while essentially the same in longitude. Schedule C is also better than schedule A in total length and latitude errors while worse in longitude. The differences are roughly 15%.

Schedule A is actually taking data 44% of the time while schedules B and C use 17% and 22%, respectively. Since the baseline length is usually the parameter of greatest geodetic interest, the results discussed above show that a sparse schedule is preferable if a small number of sources is observed and the signal-to-noise ratio is the limiting factor. Less tape is used and the total baseline error is smaller. If external noise is dominant the picture is less clear. The addition of a fourth source suitably placed can result in a smaller total baseline error than a completely filled schedule while giving the same NOE.

4. Six to nine source schedules

Schedules D through I used a larger number of sources. Schedule D comprised three pairs of sources distributed in right ascension and declination. Each pair included a low declination source (< 5 deg,

3C 120, 3C 273, PKS 2134+00) and a middle declination source (~ 40 deg, 3C 84, 3C 345, VMO 42.22.01). The right ascensions were chosen so that for all except one hour at least two sources were visible. There is a gap after 3C 84 sets when 3C 273 is the only source available. The sources were observed as often as possible with some emphasis on tracking them to the elevation limit. Schedule E is identical to schedule D except that a pair of observations of 4C 67.05 was substituted at one hour intervals. The number of observations on the other sources was consequently reduced.

In schedule F observations on OJ 287 were added to supplement the interval where 3C 273 was the sole source. OJ 287 falls in the gap in right ascension between 3C 120 and 3C 273. Observations on 3C 84, 3C 120, 3C 273 and 3C 345 were reduced to allow coverage of OJ 287. Schedule G is schedule F altered by the substitution of 4C 67.05 every hour.

OQ 208 was added to the previous schedules, filling the right ascension gap between 3C 273 and 3C 345, to give schedule H. The number of runs on all the other sources except 3C 120 was reduced. In a manner parallel to schedules E and G, schedule I was generated by adding 4C 67.05.

The schedules are plotted in figure IV.6.

Despite the fact that schedule D has more observations than schedule A, the baseline NOE with SNE measurement uncertainty weighting

Figure IV.6 Comparison of schedules D, E, F, G, H and I
Time in UT for August 21, 1975

| 0 | 1 | 2 | 3 | 4 | 5 | 6 | | |
|-------|----|----|----|----|----|----|---------------|----|
| ----- | | | | | | | 4C 67.05----- | 88 |
| ** | | ** | | ** | | | | D |
| ** | | ** | | ** | | | | E |
| ** | | ** | | ** | | | | F |
| * | | ** | | ** | | | | G |
| | | ** | | ** | | | | H |
| | | ** | | ** | | | | I |
| ----- | | | | | | | 3C 84----- | 7 |
| | | | | | | | ** | D |
| | | | | | | | ** | E |
| | | | | | | | ** | F |
| | | | | | | | ** | G |
| | | | | | | | ** | H |
| | | | | | | | ** | I |
| ----- | | | | | | | 3C 120----- | 14 |
| ----- | | | | | | | 0J 287----- | 27 |
| ----- | | | | | | | 3C 273----- | 33 |
| ** | ** | | | | | | | D |
| ** | ** | | | | | | | E |
| *** | ** | | | | | | | F |
| ** | ** | | | | | | | G |
| ** | ** | | | | | | | H |
| ** | ** | | | | | | | I |
| ----- | | | | | | | 0Q 208----- | 36 |
| ** | ** | ** | ** | ** | | | | D |
| ** | ** | ** | ** | ** | | | | E |
| ** | ** | ** | ** | ** | | | | F |
| ** | ** | ** | ** | ** | | | | G |
| ** | ** | ** | ** | ** | | | | H |
| ** | ** | ** | ** | ** | | | | I |
| ----- | | | | | | | 3C 345----- | 43 |
| *** | * | ** | ** | ** | ** | ** | ** | D |
| ** | ** | ** | ** | ** | ** | ** | ** | E |
| ** | ** | ** | ** | ** | ** | ** | ** | F |
| ** | ** | ** | ** | ** | ** | ** | ** | G |
| | ** | ** | ** | ** | ** | ** | ** | H |
| | ** | ** | ** | ** | ** | ** | ** | I |
| ----- | | | | | | | PKS 2134+00-- | 59 |
| | | ** | ** | ** | ** | ** | ** | D |
| | | ** | ** | ** | ** | ** | ** | E |
| | | ** | ** | ** | ** | ** | ** | F |
| | | ** | ** | ** | ** | ** | ** | G |
| | | ** | ** | ** | ** | ** | ** | H |
| | | ** | ** | ** | ** | ** | ** | I |

| | | | | | | VRO 42.22.01- 63 |
|----|----|----|----|----|----|------------------|
| •• | •• | •• | •• | •• | •• | D |
| •• | •• | •• | •• | •• | •• | E |
| •• | •• | •• | •• | •• | •• | F |
| •• | •• | •• | •• | •• | •• | G |
| •• | •• | •• | •• | •• | •• | H |
| •• | •• | •• | •• | •• | •• | I |
| 0 | 1 | 2 | 3 | 4 | 5 | 6 |

| 6 | 7 | 8 | 9 | 10 | 11 | 12 | |
|-------|----|----|----|----|----|----|----|
| ----- | | | | | | | 88 |
| ** | | ** | | ** | | * | D |
| ** | | ** | | ** | | * | E |
| ** | | ** | | ** | | | F |
| ----- | | | | | | | 7 |
| | ** | ** | ** | ** | ** | ** | D |
| | ** | ** | ** | ** | ** | ** | E |
| | ** | ** | ** | ** | ** | ** | F |
| | ** | ** | ** | ** | ** | ** | G |
| | ** | ** | ** | ** | ** | ** | H |
| | ** | ** | ** | ** | ** | ** | I |
| ----- | | | | | | | 14 |
| | | | ** | ** | ** | ** | D |
| | | | ** | ** | ** | ** | E |
| | | | ** | ** | ** | ** | F |
| | | | ** | ** | ** | ** | G |
| | | | ** | ** | ** | ** | H |
| | | | ** | ** | ** | ** | I |
| ----- | | | | | | | 27 |
| ----- | | | | | | | 33 |
| ----- | | | | | | | 36 |
| ----- | | | | | | | 43 |
| ** | ** | | | | | | D |
| ** | ** | | | | | | E |
| ** | ** | | | | | | F |
| ** | ** | | | | | | G |
| ** | ** | | | | | | H |
| ** | ** | | | | | | I |
| ----- | | | | | | | 59 |
| ** | ** | ** | ** | ** | | | D |
| ** | ** | ** | ** | ** | | | E |
| ** | ** | ** | ** | ** | | | F |
| ** | ** | ** | ** | ** | | | G |
| ** | ** | ** | ** | ** | | | H |
| ** | ** | ** | ** | ** | | | I |
| ----- | | | | | | | 63 |
| ** | ** | ** | ** | ** | ** | * | D |
| ** | ** | ** | ** | ** | ** | * | E |
| ** | ** | ** | ** | ** | ** | * | F |
| ** | ** | ** | ** | ** | ** | * | G |
| ** | ** | ** | ** | ** | ** | * | H |
| ** | ** | ** | ** | ** | ** | * | I |
| ----- | | | | | | | |
| 6 | 7 | 8 | 9 | 10 | 11 | 12 | |
| ----- | | | | | | | |

| 12 | 13 | 14 | 15 | 16 | 17 | 18 | |
|----|----|----|----|----|----|----|----|
| | | | | | | | 88 |
| * | | ** | | ** | | | D |
| * | | ** | | ** | | | E |
| ** | | ** | | ** | | | F |
| ** | ** | ** | ** | ** | ** | ** | G |
| ** | ** | ** | ** | ** | ** | ** | H |
| ** | ** | ** | ** | ** | ** | ** | I |
| ** | ** | ** | ** | ** | ** | ** | 7 |
| ** | ** | ** | ** | ** | ** | ** | D |
| ** | ** | ** | ** | ** | ** | ** | E |
| ** | ** | ** | ** | ** | ** | ** | F |
| ** | ** | ** | ** | ** | ** | ** | G |
| ** | ** | ** | ** | ** | ** | ** | H |
| ** | ** | ** | ** | ** | ** | ** | I |
| ** | ** | ** | ** | ** | ** | ** | 14 |
| ** | ** | ** | ** | ** | ** | ** | D |
| ** | ** | ** | ** | ** | ** | ** | E |
| ** | ** | ** | ** | ** | ** | ** | F |
| ** | ** | ** | ** | ** | ** | ** | G |
| ** | ** | ** | ** | ** | ** | ** | H |
| ** | ** | ** | ** | ** | ** | ** | I |
| ** | ** | ** | ** | ** | ** | ** | 27 |
| ** | ** | ** | ** | ** | ** | ** | D |
| ** | ** | ** | ** | ** | ** | ** | E |
| ** | ** | ** | ** | ** | ** | ** | F |
| ** | ** | ** | ** | ** | ** | ** | G |
| ** | ** | ** | ** | ** | ** | ** | H |
| ** | ** | ** | ** | ** | ** | ** | I |
| ** | ** | ** | ** | ** | ** | ** | 33 |
| ** | ** | ** | ** | ** | ** | ** | D |
| ** | ** | ** | ** | ** | ** | ** | E |
| ** | ** | ** | ** | ** | ** | ** | F |
| ** | ** | ** | ** | ** | ** | ** | G |
| ** | ** | ** | ** | ** | ** | ** | H |
| ** | ** | ** | ** | ** | ** | ** | I |
| ** | ** | ** | ** | ** | ** | ** | 36 |
| ** | ** | ** | ** | ** | ** | ** | D |
| ** | ** | ** | ** | ** | ** | ** | E |
| ** | ** | ** | ** | ** | ** | ** | F |
| ** | ** | ** | ** | ** | ** | ** | G |
| ** | ** | ** | ** | ** | ** | ** | H |
| ** | ** | ** | ** | ** | ** | ** | I |
| ** | ** | ** | ** | ** | ** | ** | 43 |
| ** | ** | ** | ** | ** | ** | ** | 59 |
| ** | ** | ** | ** | ** | ** | ** | 63 |
| ** | ** | ** | ** | ** | ** | ** | D |
| ** | ** | ** | ** | ** | ** | ** | E |
| ** | ** | ** | ** | ** | ** | ** | F |
| ** | ** | ** | ** | ** | ** | ** | G |
| ** | ** | ** | ** | ** | ** | ** | H |
| ** | ** | ** | ** | ** | ** | ** | I |

| 18 | 19 | 20 | 21 | 22 | 23 | 24 | |
|-------|-------|-----|-----|-----|-----|-----|----|
| ----- | | | | | | | 88 |
| .. | | . . | | . . | | | D |
| .. | | .. | | .. | | | E |
| | .. | . . | | .. | | | F |
| | | | | | | | G |
| | | | | | | | H |
| | | | | | | | I |
| ----- | | | | | | | 7 |
| .. | | | | | | | D |
| . | | | | | | | E |
| . | | | | | | | F |
| . | | | | | | | G |
| . | | | | | | | H |
| . | | | | | | | I |
| ----- | | | | | | | 14 |
| ----- | | | | | | | 27 |
| .. | . . | .. | . . | .. | . . | . . | D |
| | . . | .. | . . | .. | . . | . . | E |
| | | .. | . . | .. | . . | . . | F |
| | | | . . | .. | . . | . . | G |
| | | | | .. | . . | . . | H |
| | | | | | . . | . . | I |
| ----- | | | | | | | 33 |
| | | .. | . . | .. | . . | . . | D |
| | | .. | . . | .. | . . | . . | E |
| .. | .. | .. | .. | .. | .. | .. | F |
| .. | .. | .. | .. | .. | .. | .. | G |
| .. | .. | .. | .. | .. | .. | .. | H |
| .. | .. | .. | .. | .. | .. | .. | I |
| ----- | | | | | | | 36 |
| .. | .. | .. | .. | .. | .. | .. | D |
| .. | .. | .. | .. | .. | .. | .. | E |
| | | | | | | | F |
| | | | | | | | G |
| | | | | | | | H |
| | | | | | | | I |
| ----- | | | | | | | 43 |
| | .. | .. | .. | .. | .. | .. | D |
| | .. | .. | .. | .. | .. | .. | E |
| | .. | .. | .. | .. | .. | .. | F |
| | .. | .. | .. | .. | .. | .. | G |
| | .. | .. | .. | .. | .. | .. | H |
| | .. | .. | .. | .. | .. | .. | I |
| ----- | | | | | | | 59 |
| ----- | | | | | | | 63 |
| 18 | 19 | 20 | 21 | 22 | 23 | 24 | |
| ----- | | | | | | | |

(table IV.27) are considerably worse, more than twice as bad in baseline latitude. With MDE included, schedule D is better by 20% in length and 40% in longitude but a factor of two worse in latitude. All errors are smaller in schedule E than in schedule D, but the NOE still do not improve upon schedule A. The total errors for schedule E are a factor of 4.5 better in length, 40% better in longitude, and 11% better in latitude than those for schedule A. The total latitude error is not better than for schedules B and C, however.

In the case where external noise is present (table IV.28), schedule D is still worse than the four source schedule except for baseline longitude. Schedule E has roughly half the errors of schedule D in length and latitude but a slightly larger error in longitude. It is better than all the three and four source schedules by more than 30% in all parameters with the exception of longitude NOE.

The results from schedules D and E show that a considerable change in the projected errors can occur for a relatively small (12%) redistribution of observations to a high declination source. The length and latitude show the most improvement, up to a factor of 3.6. The longitude error generally increases but not by more than 14%. The increase in longitude error is caused by the dependence of the partial derivative of the longitude on the cosine of the source declination. The high declination source is both weaker than the sources it replaces and contributes less to the estimation of the longitude.

The addition of OJ 287 in schedule F produces large changes in

the uncertainties. With SNE measurement uncertainty weighting and considering the NOE, schedule F is better than schedule D by 30% in length and latitude while marginally worse in longitude. The total error is 5.5 and 4.1 times better in length and latitude although the longitude is only slightly improved. The baseline errors are also improved in the case of external noise not by as much. The larger improvement in the the case of SNE measurement uncertainty weighting arises from the high source flux of OJ 287. The fact that the improvement also occurs with external noise indicates that the observing configuration is actually strengthened.

The relationship between schedule F and schedule G (4C 67.05 included) is similar to the relationship between schedules D and E. In three cases (baseline NOE from SNE measurement uncertainty weighting and both NOE and total error with constant external noise added) the errors for length and latitude are improved by the high declination source while the longitude is slightly worse. In the case of total error with SNE measurement uncertainty weighting, schedule G has a worse uncertainty in length but a smaller error in longitude than schedule F.

A comparison of schedules E and F is instructive. Both are variations on schedule D with the addition of another source. With SNE measurement uncertainty weighting and considering the NOE, schedule F is a slight improvement over schedule E in all parameters. The total error is between 30% and 40% better in length and latitude while the longitude is only marginally improved. Most of the effect is caused by

the relative strength of OJ 287 compared to 4C 67.05, 6 J instead of 1.9 J. This conclusion is supported by the fact that the baseline errors with external noise are essentially the same for schedules E and G. OJ 287 does not contribute significantly to the observing coverage when 4C 67.05 is already included. In the presence of noise schedule F is between 25% and 50% worse than schedule E in length and latitude for both NOE and total error. The longitude error in schedule F is slightly less. The usefulness of expanding the schedule to include OJ 287 is therefore dependent on whether external noise is present. If the system is limited by the signal-to-noise ratio, then OJ 287 strengthens the baseline estimation. Otherwise it is better to use 4C 67.05.

Although OJ 208 is a weak source, it does have some effect on the errors. Looking at schedule H in table IV.27, there is no significant change in the baseline NOE derived from SNE measurement uncertainty weighting compared to schedule F. However, there is a 25% improvement in the total longitude and latitude errors. The total length error is 15% worse. The effect of adding OJ 208 can be more readily seen in the case of external noise as shown in table IV.28. There is a decrease of 10% to 30% for all errors with the largest change in the longitude.

The addition of both OJ 208 and 4C 67.05 is not significantly better than the previous schedules if only signal-to-noise measurement uncertainty is important. The baseline NOE are almost the same for schedule I and schedule G. There is a 35% improvement in the total length error but the total longitude and latitude errors show little

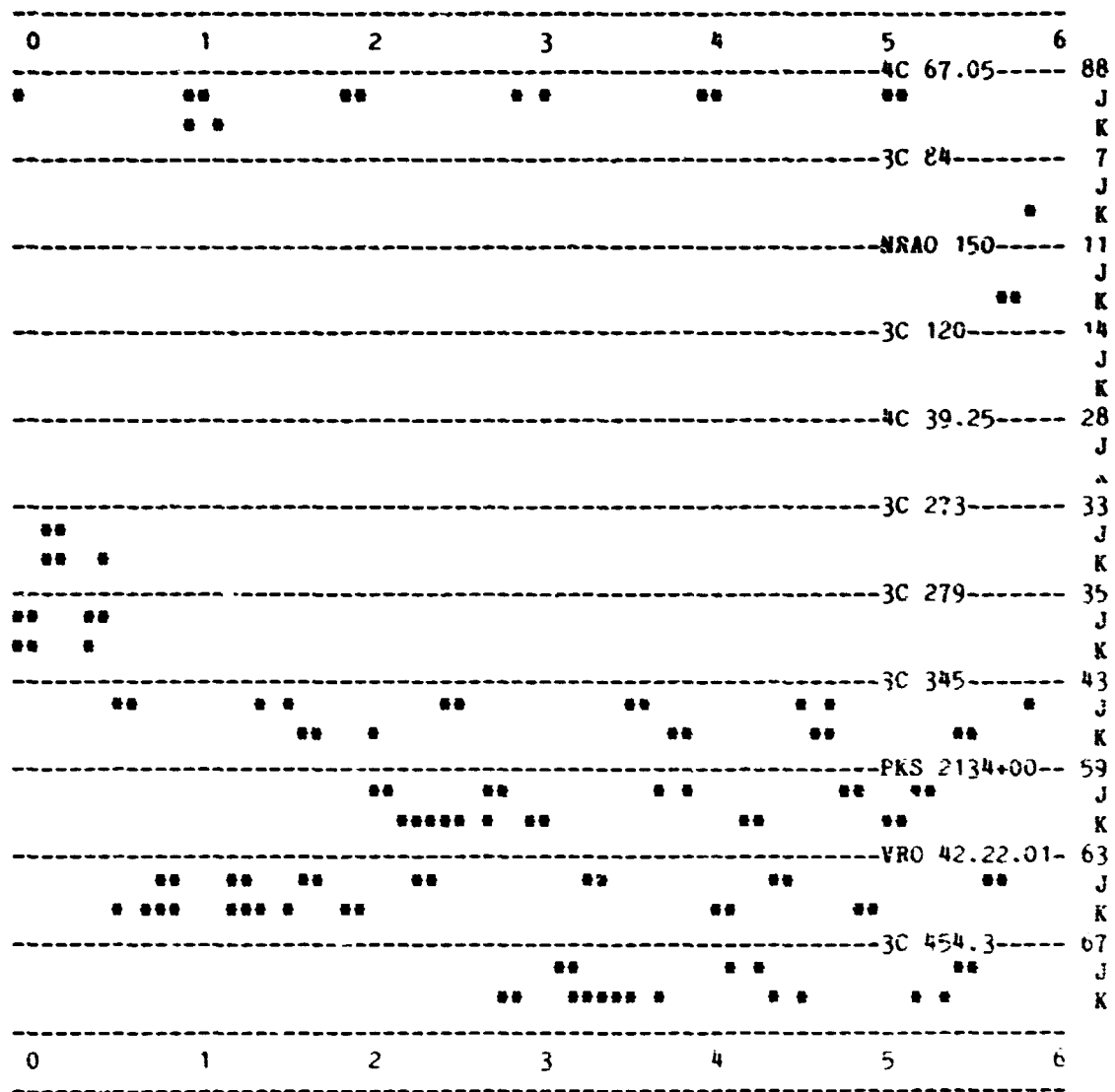
improvement. Part of the difficulty lies in taking time from stronger sources to observe two weaker sources. If source strength is not the primary factor in determining the observation errors, then the geometry of OQ 208 and 4C 67.05 are useful. In table IV.28 there is a 10% improvement in length and latitude from schedule G to schedule I and a 30% improvement in longitude for both NOE and total error. As in the other schedules, the addition of 4C 67.05 weakens the longitude estimation slightly while improving the length and latitude.

5. Eleven source schedules

It is possible to continue adding sources to the schedule. However, the additional parameters required for extra sources begin to weaken the entire estimation. This problem can be seen in schedules J and K, which are shown in figure IV.7. These schedules use eleven sources compared to a maximum of nine for the previous schedules. NRAO 150, 4C 39.25 and 3C 454.3 are added and OQ 208 is dropped. The three new sources are quite strong with fluxes ranging from 4 J to 8 J. As a result the baseline NOE using measurement uncertainty weighting are improved by 35% in length and 25% in latitude compared to schedule I. The longitude is 10% worse. The total errors are considerably worse however. In particular, schedule J has roughly twice the total length and longitude error and five times the latitude error of schedule I.

There is a large difference between schedules J and K in total baseline errors which is caused by the observing strategy. Both

Figure IV.7 Comparison of schedules J and K



| 6 | 7 | 8 | 9 | 10 | 11 | 12 | |
|------|-----|----|------|------|------|------|----|
| | •• | •• | | | | | 88 |
| | | | | | | | J |
| | | | | | | | K |
| • • | •• | •• | •• | • • | •• | | 7 |
| • •• | •• | •• | | | •• | | J |
| | | | | | | | K |
| •• | •• | •• | • • | •• | •• | | 11 |
| •• | | •• | | | •• | | J |
| | | | | | | | K |
| | | | •• | •• | •• | •• | 14 |
| | | | •• | •••• | •• | •• | J |
| | | | | | | | K |
| | | | | | | | 28 |
| | | | | | | | J |
| | | | | | | | K |
| | | | | | | | 33 |
| | | | | | | | J |
| | | | | | | | K |
| | | | | | | | 35 |
| | | | | | | | J |
| | | | | | | | K |
| • | •• | •• | | | | | 43 |
| | •• | •• | | | | | J |
| | | | | | | | K |
| | • • | •• | •• | •• | | | 59 |
| | | •• | •••• | •• | ••• | | J |
| | | | | | | | K |
| •• | | •• | •• | • • | •• | •• | 63 |
| | •• | •• | | | •• | | J |
| | | | | | | | K |
| • | | •• | | •• | •• | •• | 67 |
| | | •• | | | •••• | •••• | J |
| | | | | | | | K |
| 6 | 7 | 8 | 9 | 10 | 11 | 12 | |

| 12 | 13 | 14 | 15 | 16 | 17 | 18 | |
|----|------|-----|-----|-----|----------|-----|----|
| | | | | | | | 88 |
| | | | | | | | J |
| | | | | | | | K |
| | | | | | | | 7 |
| •• | • • | • • | • • | • • | •• | •• | J |
| | •• | •• | •• | | •• | • • | K |
| | | | | | | | 11 |
| •• | •• | •• | •• | •• | •• | •• | J |
| | •• | •• | •• | •• | | | K |
| | | | | | | | 14 |
| | •• | •• | •• | •• | •• | • • | J |
| | • • | • • | • • | • • | •••••••• | • | K |
| | | | | | | | 23 |
| •• | •• | •• | •• | •• | •• | •• | J |
| •• | •••• | •• | •• | •• | | | K |
| | | | | | | | 33 |
| | | | | | | • • | J |
| | | | | | •• | •• | K |
| | | | | | | | 35 |
| | | | | | | | J |
| | | | | | | | K |
| | | | | | | | 43 |
| | | | | | | | J |
| | | | | | | | K |
| | | | | | | | 59 |
| | | | | | | | J |
| | | | | | | | K |
| | | | | | | | 63 |
| | •• | | | | | | J |
| •• | ••• | | | | | | K |
| | | | | | | | 67 |
| | | | | | | | J |
| | | | | | | | K |
| | | | | | | | 12 |
| | | | | | | | 13 |
| | | | | | | | 14 |
| | | | | | | | 15 |
| | | | | | | | 16 |
| | | | | | | | 17 |
| | | | | | | | 18 |

| 18 | 19 | 20 | 21 | 22 | 23 | 24 | |
|------|------|------|------|----|----|------|----|
| | | | | | | | 88 |
| | | | •• | | •• | • | J |
| | | | | | | | K |
| | | | | | | | 7 |
| | | | | | | | J |
| | | | | | | | K |
| | •• | •• | •• | | | | 11 |
| | | •••• | •• | | | | J |
| | | | | | | | K |
| | | | | | | | 14 |
| | | | | | | | J |
| | | | | | | | K |
| | •• | •• | •• | •• | •• | •• | 28 |
| | | | •• | •• | •• | •••• | J |
| | | | | | | | K |
| | •• | •• | •• | •• | •• | •• | 33 |
| | | | •• | •• | •• | •• | J |
| | | | | | | | K |
| | •• | •• | •• | •• | •• | •• | 35 |
| •••• | •••• | | •• | •• | •• | | J |
| | | | | | | | K |
| | | •• | •• | •• | •• | •• | 43 |
| | | •• | •••• | •• | •• | •• | J |
| | | | | | | | K |
| | | | | | | | 59 |
| | | | | | | | J |
| | | | | | | | K |
| | | | | | | | 63 |
| | | | | | | | J |
| | | | | | | | K |
| | | | | | | | 67 |
| | | | | | | | J |
| | | | | | | | K |
| 18 | 19 | 20 | 21 | 22 | 23 | 24 | |

schedules attempt to maximize coverage on all sources except 4C 67.05. Schedule J distributed the observations on a source fairly uniformly over the period of visibility while schedule K observed each source continuously for half an hour at rising and setting. 4C 67.05 was not observed as frequently because of its low flux. The total length errors are approximately the same for both schedules, but the total longitude error is 30% less and the latitude error 45% less in schedule K even though 4C 67.05 was observed fewer times.

In the case of constant external noise schedules J and K are clearly worse than schedule I in longitude and latitude. The length errors are comparable. Schedule K has smaller total longitude and latitude errors than schedule J but they are still larger than the errors for schedule I by roughly 35%.

The comparison of schedules A through K shows that it is necessary to select sources judiciously even out of the limited number available. Observations on a minimum or maximum number of sources can give deceptively good results if MDE and external noise are ignored. Contrary to the expectation that the largest set of sources is best, the best results are generated by observing a moderate number of sources. Even relatively small model errors in the solid earth tide and diurnal polar motion cause modeled errors which are several times the noise-only error if signal-to-noise measurement uncertainty is the limiting factor. The length and latitude total errors are at least twice the noise-only error while the longitude error is nine times larger. Since the modeled errors are relatively unaffected by changes

in the observation weighting, they would not be reduced substantially by improvements in the measurement uncertainties.

6. Haystack - Goldstone schedule

Schedule L is grouped with schedules J and K in observing strategy, i.e., using a large number of sources. It differs in being developed from an actual observing schedule for the Haystack and Goldstone antennas. Because of the slow slewing rate of the Goldstone antenna and cable wrap constraints, the number of observations is reduced. As can be seen from table IV.27, the larger collecting area reduces the baseline NOE if SNR measurement uncertainty weighting is used. Schedule L is 20% better in length, 10% better in longitude, and 60% better in latitude than the best values from the previous schedules. The total errors are worse than most of the schedules, however. In comparison to the best values, the total length error is larger by a factor of 4.2, the longitude by 2.3 and the latitude by 2.7. It would be necessary to reduce the model errors considerably before the high sensitivity of the larger antenna is usable. If in fact the system is dominated by external noise, the smaller number of observations forced by the slower slewing causes even the NOE to be poor. One factor that is not considered here is the threshold of detection. A larger antenna may be necessary in order to find any fringes at all for weak sources. Once the fringes are detected, the measurement uncertainty computed from the signal-to-noise ratio can be used to weight the observations in the analysis.

7. Baseline length optimized schedule

Schedule M was generated by a completely different algorithm. The previous schedules attempted to provide complete hour angle coverage of all the sources observed. For schedule M the observations were picked to maximize the partial derivative with respect to the baseline length. Each observation was weighted by the signal-to-noise measurement uncertainty. As a result the strongest source visible was usually picked. From tables IV.27 and IV.28 it can be seen that this strategy leads to a very poor schedule if a full set of adjusted parameters is used. Table IV.29 shows the results if only the Pioneer site and clock parameters are adjusted. The other parameters were included as contributions to the MDE. In this case the baseline length NOE is in fact less than that for any other Haystack-Pioneer schedule. The total errors are poor, however. The length and longitude total errors are greater than the corresponding errors for the other Haystack-Pioneer schedules. The total latitude error is better than schedules A-I but worse than schedules J and K. It is clear that this type of simple approach does not give good results.

8. Conclusions

These simulations indicate that although there are general trends, it is difficult to select a schedule which gives the best estimate of the baseline parameters. Neither the strategy of maximum sources nor the selection of maximum baseline length derivative yields the best results. Based on the antenna parameters and schedules

studied, it appears that a good number of sources to observe for geodetic purposes is approximately ten. Since it is the entire schedule which determines the NOE and MDE for the adjusted parameters, it is unlikely that any method of scheduling which picks observations one at a time will give the optimum schedule.

E. Comparison of simulated and actual experiments

The data taken on the Haystack - OVRO baseline between Sept. 29, 1976 and Oct. 15, 1976 form a useful set for comparison of simulations with actual experiments. The observations were scheduled using the program ESTIM. However, because of insufficient time, schedule complexity, schedule changes, and the novelty of the baseline, the final observing schedules were not optimized. After the Mark I data tapes were processed at Haystack Observatory, the reduced data were transferred to data base files at GSFC using a series of temporary programs. Parameter estimation was done with the SOLVE program described in appendix B.

A summary of the observations for each session is given in table IV.30. Each set covers approximately one day. The data for 10/09 and 10/11 are the parts of a longer observing session which produced useful results for baseline measurements, the other time being used for source structure, occultation, and lunar ALSEP observations. The observations included as "scheduled" are those in the original schedule between the first and last times, inclusive, for which good data were taken. Consequently, runs lost because of initial setup and

**Table IV.30 Individual experiment statistics for Haystack - OVRO observations
from 76/09/29 - 76/10/14**

| | scheduled | taken | good | taken/sch. | good/sch. | good/taken |
|----------|------------------|--------------|-------------|-------------------|------------------|-------------------|
| 76/09/29 | 231 | 212 | 188 | .92 | .81 | .89 |
| 76/10/04 | 247 | 230 | 180 | .93 | .73 | .78 |
| 76/10/09 | 226 | 222 | 156 | .98 | .69 | .70 |
| 76/10/11 | 171 | 163 | 118 | .95 | .69 | .72 |
| 76/10/14 | 228 | 201 | 148 | .88 | .65 | .74 |

early shutdown are not included in the statistics. Runs "taken" include those tape pairs actually processed on the Mark I correlator. "Good" data are those which contributed to baseline solutions. As shown in the fourth column, the fraction of runs taken is high but far from perfect. The causes of loss were equipment failure, operator errors, and, less commonly, disappearance in shipping.

The fraction of good data for 09/29 is quite different from the other days. The cause can be seen more easily in table IV.31 where the observations are divided by source. The data from 3C 279 varied widely in quality over the different days because of the source's occultation by the sun during the period. Scintillations in the corona usually preclude useful Mark I observations when 3C 279 is less than ten solar diameters away from the sun. 09/29 is the only day on which most of the 3C 279 runs were good.

3C 120 was observed only on 09/29. It was dropped from subsequent schedules because data taken earlier in September and processed after the 09/29 schedule was made indicated that the source would not be detectable. In fact 3C 120 was one of the most reliable sources. 3C 454.4, which partially replaced 3C 120, was also reliable. The schedules would have been strengthened if both had been included. Of the other sources the least reliable were 3C 279, VRO 42.22.01, and 3C 84. The latter two sources had varying visibility functions which fell below the sensitivity threshold of the baseline. The low region for VRO 42.22.01 caused it to be undetectable for several hours. 3C 84 had much sharper dips which removed the source from several parts of

Table IV.31 Individual source statistics for Haystack - OVRO observations from 76/09/29 - 76/10/14

s - number of times scheduled
t - number of observations processed
g - number of data points used in parameter estimations

| | 09/29 | | | 10/04 | | | 10/09 | | | 10/11 | | | 10/14 | | |
|--------------|-------|----|----|-------|----|----|-------|----|----|-------|----|----|-------|----|----|
| | s | t | g | s | t | g | s | t | g | s | t | g | s | t | g |
| 3C 84 | 36 | 36 | 33 | 36 | 34 | 26 | 42 | 42 | 30 | 29 | 29 | 21 | 42 | 40 | 28 |
| 3C 120 | 21 | 19 | 17 | | | | | | | | | | | | |
| 4C 39.25 | 33 | 28 | 25 | 39 | 35 | 27 | 39 | 39 | 33 | 37 | 32 | 30 | 47 | 41 | 29 |
| 3C 273 | 23 | 21 | 19 | 22 | 18 | 14 | 22 | 22 | 17 | 20 | 18 | 11 | 27 | 20 | 16 |
| 3C 279 | 19 | 18 | 16 | 19 | 14 | 5 | 19 | 19 | 0 | 17 | 17 | 0 | 21 | 12 | 7 |
| 3C 345 | 18 | 18 | 16 | 12 | 12 | 10 | 9 | 9 | 8 | 6 | 5 | 3 | 9 | 9 | 7 |
| PKS 2134+00 | 33 | 31 | 29 | 32 | 31 | 26 | 25 | 24 | 20 | 18 | 18 | 17 | 20 | 19 | 16 |
| VRO 42.22.01 | 48 | 41 | 33 | 48 | 47 | 36 | 38 | 38 | 23 | 28 | 28 | 21 | 35 | 33 | 20 |
| 3C 454.3 | | | | 39 | 39 | 36 | 32 | 29 | 25 | 16 | 16 | 15 | 27 | 27 | 25 |

| | scheduled | taken | good | good/sched. | good/taken |
|--------------|-----------|-------|------|-------------|------------|
| 3C 84 | 185 | 181 | 138 | .75 | .76 |
| 3C 120 | 21 | 19 | 17 | .81 | .89 |
| 4C 39.25 | 195 | 175 | 144 | .74 | .82 |
| 3C 273 | 114 | 99 | 77 | .68 | .78 |
| 3C 279 | 95 | 80 | 28 | .29 | .35 |
| 3C 345 | 54 | 53 | 44 | .81 | .83 |
| PKS 2134+00 | 128 | 123 | 108 | .84 | .88 |
| VRO 42.22.01 | 197 | 187 | 133 | .68 | .71 |
| 3C 454.3 | 114 | 111 | 101 | .89 | .91 |

the schedule.

Absence of fringes was the most frequent cause for runs actually taken to be useless for baseline estimations. Other problems were excessive parity errors and short records.

Each day was analyzed separately with SOLVE. The OVRO station coordinates, all source coordinates except the right ascension of 3C 273, a single atmosphere parameter for each station, and clock offset and rate were adjusted. The atmosphere parameter at Haystack was a scale factor for the Marini model based on actual weather data. OVRO's atmosphere parameter was the zenith thickness. Solutions from delay data only were used to calculate the normalizing error needed to bring the root-scaled-mean-square residual to unity.

The average measurement uncertainties (calculated from correlation coefficients and bandwidths) and normalizing errors are presented in table IV.32. The measurement uncertainty averages include only those points used in the solutions. Several other data sets are included for illustrative purposes. As can be seen from the last two columns, the normalizing error is larger than the measurement uncertainty, dominatingly so for delay rate. The source of the additional error is most likely to be short term clock and atmosphere fluctuations. There is no strong correlation with large scale atmosphere effects, at least with Haystack weather. Even though a storm passed through the Haystack area with pressure minima during 10/09 and 10/14, the normalizing errors for those days and the day

Table IV.32 Haystack - OVRO observations: average measurement uncertainties over good data points and normalizing errors

| | measurement uncertainty | | normalizing error | | ratio (n/d) | |
|----------|-------------------------|-----------|-------------------|-----------|-------------|------|
| | delay ns | rate ps/s | delay ns | rate ps/s | delay | rate |
| 76/09/29 | .0819 | .0254 | .111 | .216 | 1.36 | 8.50 |
| 76/10/04 | .0825 | .0263 | .203 | .192 | 2.46 | 7.30 |
| 76/10/09 | .0805 | .0241 | .199 | .169 | 2.47 | 7.01 |
| 76/10/11 | .0677 | .0207 | .077 | .103 | 1.14 | 4.98 |
| 76/10/14 | .0847 | .0260 | .187 | .137 | 2.21 | 5.27 |
| 76/12/14 | .0620 | .0195 | .068 | .086 | 1.10 | 4.41 |
| 76/12/15 | .0763 | .0232 | .129 | .090 | 1.69 | 5.55 |
| 77/03/27 | .0798 | .0238 | .127 | .112 | 1.59 | 4.71 |
| 77/06/26 | .0829 | .0286 | .145 | .143 | 1.75 | 5.00 |
| average | .0776 | .0242 | .138 | .139 | 1.75 | 5.86 |

between are less than the error for 10/04. Weather data at OVRO was not available at the time of processing.

In order that the simulations cover the same periods as the actual experiments, the original schedules were truncated to the intervals of time included in the "scheduled" observations of table IV.30. Each experiment was simulated with delay only using the source parameters in table IV.34 and the Haystack parameters in table IV.32. The antenna diameter, antenna efficiency, and receiver temperature for OVRO were 39.6 m, 60%, and 120 deg K, respectively. The effects contributing to modeled error (MDE) were solid earth tides and diurnal polar motion with uncertainties of 0.05 for Love h, 0.01 for Love l, and 0.2 for the diurnal polar motion scaling factor. Two simulations were done for each experiment. In the first the measurement uncertainty for each observation was calculated from source and system parameters. In the second a constant noise of 0.1 nsec was root-sum-square added to the previous measurement uncertainty.

The results for the actual and simulated baseline formal errors are shown in table IV.33. The first column is the formal error from parameter estimations using the actual delay data weighted by the root-sum-square of the measurement uncertainty and the normalizing error. The second and third columns come from the simulations using only source/system measurement uncertainties. The fourth and fifth columns are derived from simulations in which the constant noise was included. Two comments can be made here. In the absence of constant noise the MDE dominates the simulated errors. With constant noise

Table IV.33 Comparison of actual and simulated parameter formal errors for baseline length, longitude, and latitude from Haystack - OVRO observations using delay only

- col. 1 - formal error from actual data
- 2 - simulated error from S/N measurement uncertainty only
- 3 - simulated error from S/N uncertainty and modeled error (MDE)
- 4 - simulated error with constant 0.1 nsec noise added
- 5 - simulated error with constant noise and modeled error (MDE)
- 6 - ratio of formal error to simulated error from constant noise + MDE
- 7 - error ratio scaled by experiment normalizing error
- 8 - scaled error ratio adjusted by fraction of good data

| Length | 1 cm | 2 cm | 3 cm | 4 cm | 5 cm | 6 | 7 | 8 |
|-----------|-----------|-----------|-----------|-----------|-----------|------|------|------|
| 76/09/29 | 3.2 | .12 | .53 | 2.0 | 2.1 | 1.48 | 1.33 | 1.05 |
| 76/10/04 | 4.9 | .11 | .93 | 1.7 | 2.0 | 2.48 | 1.22 | .87 |
| 76/10/09 | 6.1 | .11 | .84 | 1.9 | 2.0 | 3.12 | 1.57 | 1.07 |
| 76/10/11 | 4.0 | .13 | .55 | 2.2 | 2.3 | 1.72 | 2.23 | 1.56 |
| 76/10/14 | 5.0 | .11 | .55 | 1.9 | 2.0 | 2.47 | 1.32 | .84 |
| average | | | | | | 2.25 | 1.53 | 1.08 |
| Longitude | 1 ".01 | 2 ".01 | 3 ".01 | 4 ".01 | 5 ".01 | 6 | 7 | 8 |
| 76/09/29 | .65 | .022 | .06 | .38 | .39 | 1.68 | 1.51 | 1.19 |
| 76/10/04 | .82 | .018 | .20 | .31 | .42 | 1.93 | .95 | .67 |
| 76/10/09 | .79 | .019 | .16 | .31 | .41 | 1.90 | .95 | .65 |
| 76/10/11 | .55 | .024 | .18 | .44 | .49 | 1.13 | 1.47 | 1.03 |
| 76/10/14 | .80 | .019 | .05 | .32 | .33 | 2.43 | 1.30 | .83 |
| average | | | | | | 1.81 | 1.24 | .87 |
| Latitude | 1 ".01 | 2 ".01 | 3 ".01 | 4 ".01 | 5 ".01 | 6 | 7 | 8 |
| 76/09/29 | .76 | .028 | .10 | .46 | .47 | 1.62 | 1.46 | 1.15 |
| 76/10/04 | .87 | .020 | .22 | .34 | .43 | 2.01 | .99 | .70 |
| 76/10/09 | .99 | .021 | .19 | .35 | .43 | 2.30 | 1.16 | .79 |
| 76/10/11 | 1.02 | .028 | .17 | .52 | .54 | 1.87 | 2.43 | 1.70 |
| 76/10/14 | .89 | .021 | .08 | .35 | .37 | 2.43 | 1.30 | .83 |
| average | | | | | | 2.05 | 1.47 | 1.03 |

included the MDE is generally not an important additional term.

The sixth column of table IV.35 is the ratio of actual formal errors to the simulated errors of the fifth column. The ratio averages for the three baseline parameters are roughly 2, but there is wide variation over the several days. A component of the variation can be attributed to the range of the normalizing errors. The seventh column is computed by scaling the sixth column by the ratios of the individual day normalizing errors to the constant 0.1 nsec noise. 10/11 is the only day for which the seventh column is larger since its normalizing error is less than 0.1 nsec. This day is anomalously clean and stands out in the seventh column under length and latitude. If 10/11 is ignored, the variation in length is considerably reduced while the variations in longitude and latitude are not substantially changed.

The eighth column is the seventh column adjusted by the fraction of data for each day actually included in the parameter estimations. The average values come closer to unity, an indication that part of the discrepancy between actual and simulated errors is caused by data loss. However, the variation between experiments is not reduced.

The fact that the sixth column shows wide departures from unity indicates that the individual day formal errors are poorly predicted. The fact that the normalizing errors are large compared to the average measurement uncertainties and have considerable variation is an indication that it would be difficult to predict individual day formal errors. Another consequence of the large, scattered normalizing errors

is that schedules whose simulated errors differ by less than 50% probably would not give significantly different results.

The scatter of the baseline estimates between minimum and maximum values is 15 cm in length, 0.036 arcsec in longitude, and 0.027 arcsec in latitude. These values are 2.9, 4.9, and 3.0 times the average actual formal errors in length, longitude, and latitude, respectively, and 7.1, 8.7, and 5.9 times the corresponding average simulated errors. The scatter is fairly consistent with the actual errors but much larger than the simulated errors. The accuracy of the prediction of scatter could be improved in several ways: 1) constant external noise closer to the average normalization error derived from experience, 2) inclusion of atmosphere and clocks as sources of modeled error, and 3) construction of schedules to improve the fraction of good data. The effect of data loss because the original observing schedules cannot be followed as a result of slow setup or equipment failure is largely unpredictable. The problem could be alleviated by more reliable, permanently installed VLBI terminals.

CONCLUSION

A. Summary

This work has dealt with several aspects of high precision interferometry. Several improved algorithms, including diurnal polar motion and solid earth tides, were developed as part of the models necessary for parameter estimation and experiment simulation. VLBI data have been used to estimate diurnal polar motion. It was found that McClure's model does not fully explain the effect seen. The size of the diurnal polar motion scaling factor was significantly changed by Melchior's corrections to the standard nutation series. It is conceivable that further refinements of nutation would yield results for diurnal polar motion more consistent with McClure's model. An experiment simulation and error analysis program was developed and applied to an optical test of relativity, measurement of polar motion and UT1, and optimization of baseline errors. It was found that the optical configuration studied could produce interesting results given some improvement in measurement uncertainty. It was also found that the Westford-Fort Davis-Fairbanks triangle is the better choice for the POLARIS polar motion network and that geophysical effects should be a small error source. The strategy of observing the largest number of sources was found to be a non-optimal method of reducing baseline errors.

B. Remaining problems

The remaining problems may be divided into two areas:

1) instrumentation and physical effects, and 2) data and experiment integration structure.

1. Instrumentation and physical effects

The frequency standards have been and continue to be a difficult problem. New hydrogen masers under development at GSFC should alleviate this problem in the future. However, better methods of treating old data - either by numerical filtering or improving clock models, are still necessary.

The atmosphere is probably the largest error source affecting current VLBI observations. The meteorological sensors and radiometers which are part of the Mark III system will presumably eliminate this problem in the future. More work is required on radiometer instrumentation and physical models before the wet component can be accurately monitored. The existing data can be improved by using the best available meteorological records and modeling both the dry and wet components.

The ionosphere has been a hidden effect in most past VLBI analyses. Dual frequency observations were recorded in October 1976, but the second frequency data were too noisy to be useful. There is no fundamental difficulty in using two frequencies and better feed horn and amplifier designs should improve the data considerably.

Mark III VLBI observations since September 1976 have suffered from low sensitivity. The Mark III recorder will increase the recorded bandwidth. Other steps must be taken to improve antenna efficiencies and receiver system temperatures.

While a number of source structure maps have been made, the results have not been entered into the data base for use in correcting the delay and delay rate observables. As other errors are reduced, this effect will become more important.

The currently used values of the precession constant and the nutation coefficients are not the best available. Since VLBI uses a fundamentally different celestial reference frame from optical studies, it would be desirable to estimate these parameters simultaneously so that errors in the theory of the earth's motion do not propagate into other parameters.

The effect of ocean loading displacement has been ignored in the past and should be modeled if precision at the 2 cm level is desired.

2. Data and experiment integration structure

The largest bottleneck in the Mark III data and experiment integration structure is its incompleteness. Several large sections have not been implemented including the scheduler, the field controller, and a data editor. Very little of the older data has been entered into the data base. A large data base is necessary for many

astrometric and geophysical studies. These are not fundamental problems but do severely limit the usefulness of the system. In addition, the data base handler is annoyingly slow in operation. Some work must be done to increase its speed. A simpler, more controlled system for transferring the data base from one machine to another must be developed.

The section of the Mark III system for parameter estimation could be improved. The number of adjustable parameters is currently limited to 55. A much higher number (200-500) is required to work with large data sets. There is no capability for differencing or filtering data to remove the effects of erratic clock behavior. The current system of saving solutions is not adequate for recovering the exact configuration of data and parameters used initially. It would be desirable to save normal equations for both global (e.g., station coordinates, source positions, or Love numbers) and experiment-specific (e.g., clock polynomials or atmosphere zenith thicknesses) parameters so that additional data could be treated incrementally.

The experiment simulation and error analysis program also lacks the capability for treating differenced observations. Some algorithms for handling statistical error models and correlated observations are needed. Source visibility data should be included to give more realistic measurement uncertainties. The program now exists outside the data base structure and must be integrated.

C. Future projects and possibilities

The value found for diurnal polar motion disagrees with theory. Different parameterizations and other models such as dissipative core-mantle coupling should be tried. A longer span of data should be used as new data are taken and better methods for handling old data are developed. The study of diurnal polar motion should be broadened so that nutation and solid earth tide parameters can be simultaneously adjusted since all these effects have a common origin.

While the interferometer configuration which was studied for an optical test of relativity would require some improvement in measurement uncertainty, other baseline configurations and analytical approaches should be investigated. In particular, differential measurements with a polar WOVLBI should be examined. At radio frequencies the Mark III system will permit group delay observations closer to the sun than previous experiments. This geometry should be investigated to see if the earlier phase delay result can be improved upon.

The simulation of polar motion and UT1 measurements indicated that the POLARIS network should be able to perform from two to ten times better than conventional optical techniques. The routine processing of POLARIS observations should provide daily polar motion and UT1 values with considerably less time lag than the present BIH and IFMS distributions.

The precision which is possible with baseline measurements can be

applied in several areas. Intercontinental measurements can establish a world-wide geodetic network independent of local azimuth and vertical. The various datums can be joined to provide direct measurements of the figure of the earth. The question of glacial rebound, which is now dependent on gravimetric and geological data, could be addressed with direct displacement measurements.

Appendix A.

MARK III INSTRUMENTATION

The following description has been compiled from meetings, memoranda, and discussions of the Mark III design group. A. R. Whitney was particularly helpful in correcting and updating the material.

1. Mark III field system

The Mark III field system may be thought of in four connected parts, the receiver front end, the recorder back end, the environmental sensors, and the VLBI controller. The entire system is diagrammed in figure A.1. The system is run by the controller, which is an HP 21MX minicomputer with a 32K word core-based operating system. Using schedule input, the controller sets the receiver and recorder configuration, directs the telescope to position, starts and stops the data tape drive, monitors the system's functions, and logs all necessary information. It interfaces with the other components of the system through a series of ASCII transceivers. The ASCII transceivers are control devices that can be addressed individually or as a group. Each unit has 32 bits of input, 32 bits of output, and 8 to 10 control lines. There is also an alarm line and an auxiliary line, which set an interrupt in the controller and the data rate, respectively. Each transceiver, or all of them together, can be commanded to send a message to its device, return a message to the controller, pulse a control line, interrogate its device, or ready itself for input from

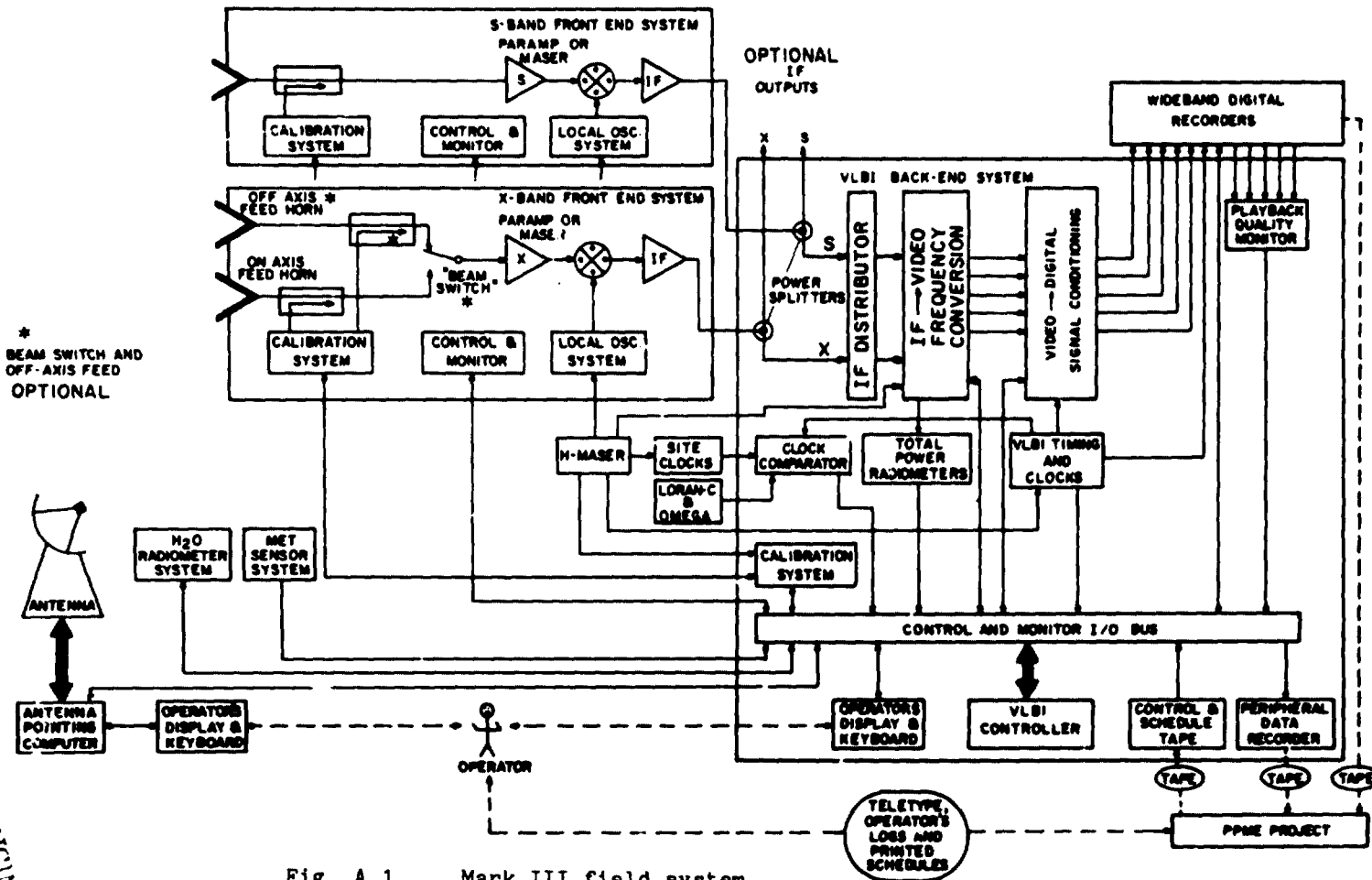


Fig. A.1 Mark III field system

ORIGINAL PAGE IS OF POOR QUALITY

its device. The input and output buffers in each transceiver are separate.

The receiver has separate systems for X band (8 GHz) and S band (2 GHz). While several receiver boxes have been built specifically for the Mark III system, other receivers can be used if the calibration system and the control/monitor port are added. The phase calibration system injects timing pulses into the receiver along with the received signal. Since the epoch of the data is determined directly from the phase calibration signal rather than from the station clock, the calibration system also measures the electrical length of the cable which carries the phase calibrator signal up to the receiver. The correct operation of the local oscillator chain can also be checked by detecting the phase calibrator signal in the IF frequency. The control/monitor port is used to control the beam switch and to check the receiver performance. Both the calibration system and the control/monitor are interfaced with the controller via an ASCII transceiver.

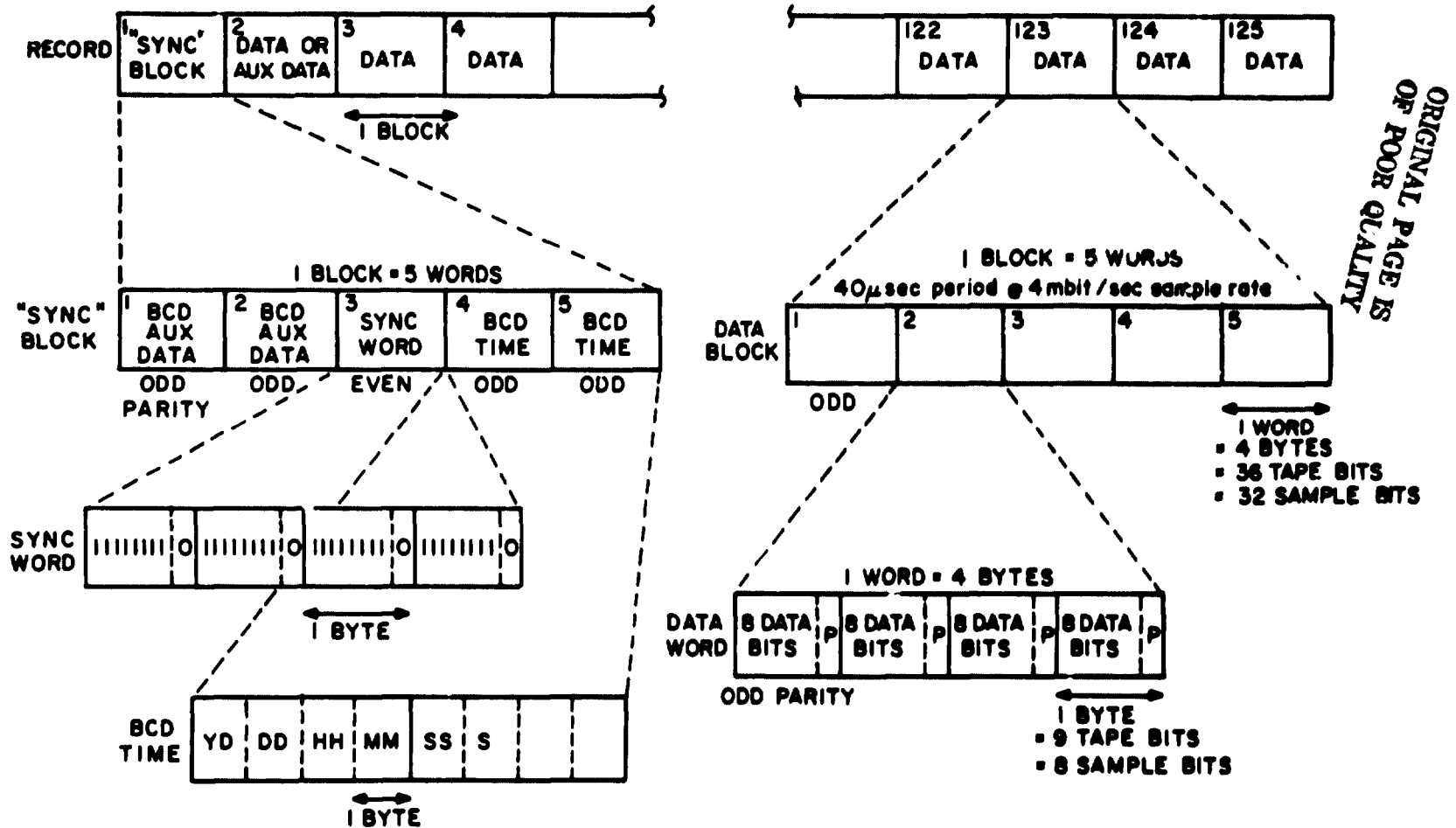
The recorder back end is organized around a Honeywell 96 instrumention tape drive which records 28 parallel tracks on one-inch wide tape. The normal reel size is 9200 feet but reels up to 12800 feet are available. The drive records in both directions and has read-after-write capability in one direction. The recording speed is controlled by an external reference frequency and can be set at 135, 67.5, 33.75, 16.875, and 8.4375 inches per second. The recording density is approximately 33000 bpi.

For each track there is a separate IF to video frequency converter producing both upper and lower sidebands and a video to digital formatter synched to the station 1 PPS and driver VLBI clock. Each track is independently encoded with time code, auxiliary data, data bit and parity bits. Each frame is 22500 bits long, divided into 125 blocks of five 36 bit words. The first block contains auxiliary data such as station name and tape reel identification, synchronization bits, and the time code. The rest of the frame is data. See figure A.2. The data sampling rates are 4, 2, 1, 0.5, and 0.25 Mbits/sec. The writing of each track is controlled independently by the formatter ASCII transceiver.

Each IF to video converter module contains a synthesizer and a total power integrator. The output bandwidths are 2, 1, 0.5, 0.25, and 0.125 MHz with both upper and lower sideband outputs. There is an external spigot if a filter for an unusual bandwidth is necessary. The local oscillator can be set between 100 MHz and 500 MHz in 10 kHz steps so that the sampled observation frequencies can be adjacent or widely separated in the total passband. The position of the phase calibrator signal in the passband is determined by this local oscillator setting. The total power integrator converts the square law detector output to a frequency and counts it for a specified time interval. The upper and lower sideband outputs, the IF input, or the LO power can be measured. The synthesizer can be set manually or via the ASCII transceiver. The power readings can likewise be read via the ASCII transceiver. The LO setting and the power readings are also displayed on the module front

MARK III TAPE FORMAT (longitudinal)

1 RECORD = 125 BLOCKS (5 msec period @ 4 Mbit / sec sample rate)



ORIGINAL PAGE IS OF POOR QUALITY

274
A-4

Fig. A.2

Mark III tape format

panel. To minimize the number of special filters required if only a few tracks are recorded at a time (as in spectral line work), several video converters are multiplexed to access all the formatter track inputs.

The IF distribution box has 42 output channels, 21 for each RF band, to allow an unequal split of the number of tracks assigned to each of the two RF bands. The bands are normally S and X band. There are four inputs, two for each observing frequency. There are two output ports for each channel, high and low IF. Each output channel has a single step attenuator and a total power detector. The port selected for a particular channel is connected to its video converter by a jumper cable.

The VLBI timing and clock module is set with the date and time of day at the beginning of an experiment with an external clock pulse. It provides the time code for writing on the data tapes.

The clock comparator monitors the behavior of the internal and external clocks. Each clock generates one pulse per second and the comparator checks the time interval between pulses from different clocks against the internal clock. It is controlled and read by an ASCII transceiver.

The playback quality monitor contains two read channels with two full decoders. The channels are controlled and read by an ASCII transceiver and can access any track on the tape drive immediately

after writing or during playback. The data read back is used by the controller to check formatting, bandpass shape, and phase calibrator behavior.

The environmental sensors are also read and controlled by an ASCII transceiver. The meteorological sensors return the ambient temperature, humidity, and barometric pressure. The water vapor radiometer measures the brightness temperature on the shoulders of two water vapor lines. The ASCII transceiver points the radiometer in various directions and reads back the brightness temperatures.

2. The Mark III processor

The Mark III processor is a hard-wired correlator controlled through an HP 21MX minicomputer with a disk-based operating system. A block diagram of the processor is given in figure A.3 while the external arrangement is shown in figure A.4. The processor contains a set of parallel modules, each working on a single track pair and producing eight complex delays for the correlation function. For a three station, 28 track observation, 84 modules are in operation. Each module runs asynchronously and is serviced independently by the correlation program (COREL). Since the modules are entirely independent, they all can be directed to a single track for 672 auto-correlation points or to a single pair of tracks for 336 simultaneous auto-correlation and cross-correlation points. For spectral line precessing, the number of auto-correlation points need only be half of the number of cross-correlation points, however. COREL

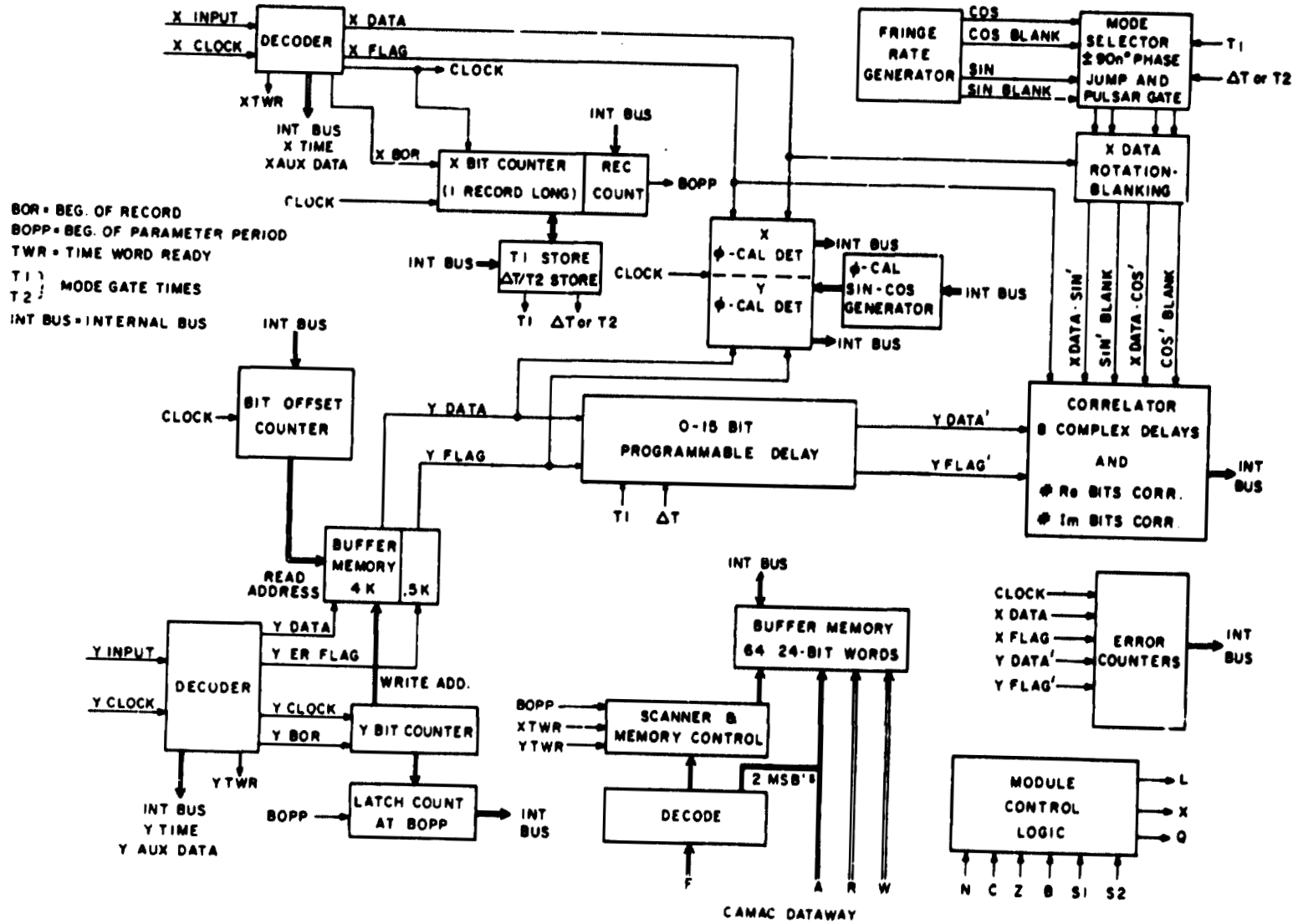


Fig. A.3 Mark III processor internal block diagram

JRM
10-77

278

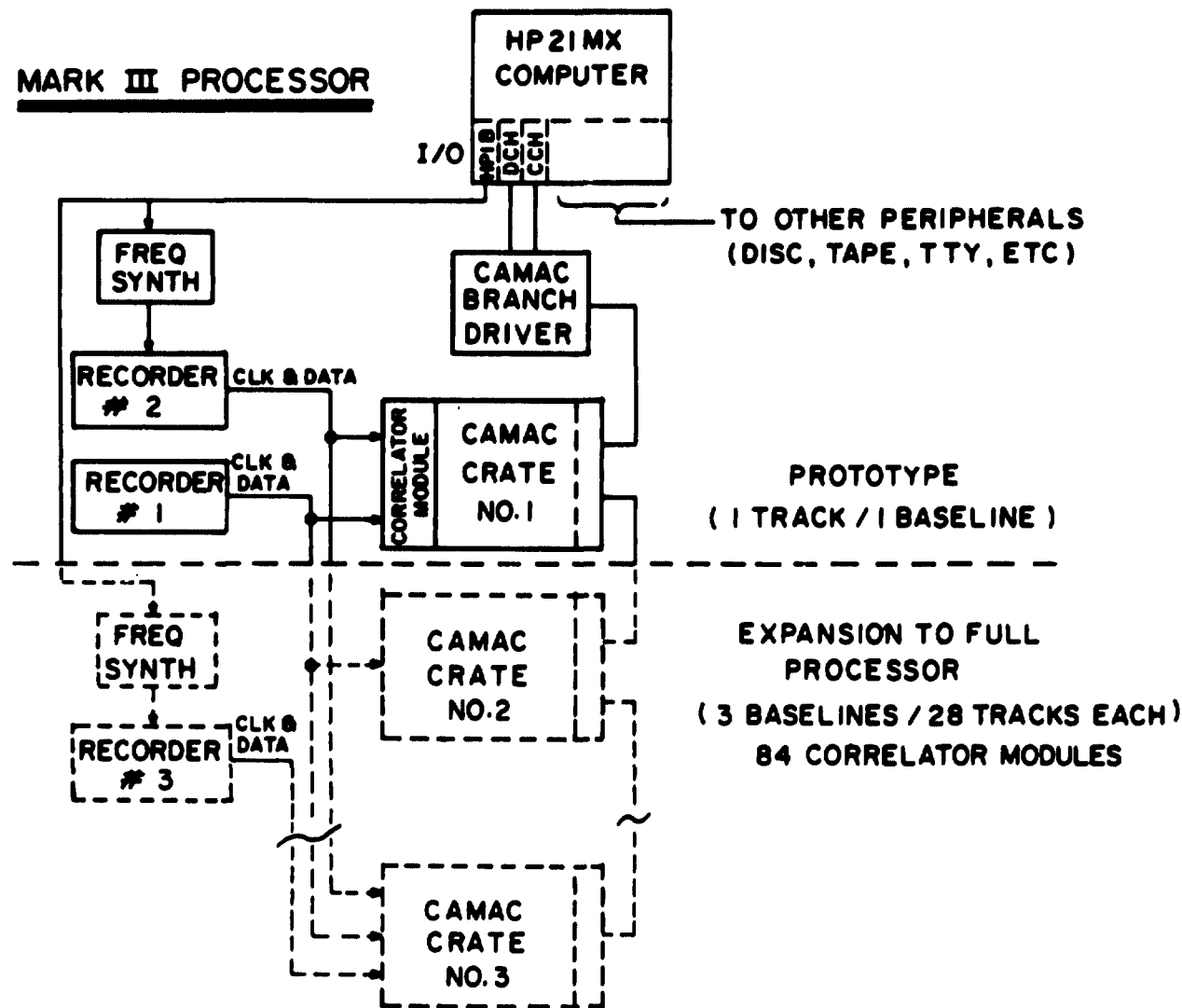


Fig. A.4 Mark III processor external block diagram

ORIGINAL PAGE IS
OF POOR QUALITY

interpolates the delay, fringe rate, and fringe phase from an input file and updates values to each module as needed. Up to 15 bits of offset and 2 seconds are allowed between updates. The correlation program also sends the correct rotator rates for extracting the phase calibration signal in each channel and gating information if pulsar data is being processed. COREL controls the tape drive playback speeds to keep the module bit buffers in step. When a module has summed data for the prescribed accumulation period, COREL reads out the time, eight complex delays of the correlation function, and tape error counts and puts them in another external file for archiving and further processing.

The modules of the processor communicate with COREL using CAMAC dataways, over which processing parameters are received and complex delays, buffer status, time, and auxiliary data are returned. A module accepts data from two inputs, which may be a pair of tracks or a single track. The data from the first track are decoded and rotated by an a priori fringe rate. The data from the second track are decoded and placed in a 4000 bit buffer. At the same time the buffer is being filled, the data with the proper delay are read out for correlation with the first bit stream. The speed of the tape drive which is supplying the second bit stream is controlled by a frequency synthesizer programmed by COREL to keep the buffer write and read rates equal. The fringe rate rotator uses a 24 bit phase register. The phase of the fringe rate rotator is updated every n th data bit, where n can be set under program control to 1, 2, 4, 8, or 16. The maximum fringe rate that can be handled is $1/n$ times the recording bandwidth.

Under normal processing n is chosen to give a fringe rate resolution of 15 MHz for bandwidths less than 4 MHz and 30 MHz for possible 4 MHz recording. The correlator produces eight complex delays for the correlation function in a 23 bit accumulation register. At 4 Mbit/sec the maximum accumulation period is 2.1 sec before the register must be emptied. The correlation parameters can be changed for each data frame or held constant for up to 512 frames. The correlator can be gated for pulsar processing so that only the expected pulse window is integrated. The phase calibration signal is extracted from each data stream by a pair of single channel correlators.

Appendix B.

MARK III EXPERIMENT INTEGRATION AND DATA BASE SYSTEM

The development of new techniques which have the potential of generating large amounts of high quality data aggravates two problems which have only been nuisances in the past. In the first place, a piece of equipment may produce excellent data but is of little use if excessive time, effort, or money is required for operation. Secondly, even if a large amount of raw data is available, the results derived from the data may be misleading or outdated if the data reduction and analysis process is too cumbersome or poorly controlled. Of course the use for which the final results are intended is an important factor. A research group may be willing to expend the effort for a while if the results are unavailable by any other means. An organization which needs the results on a timely and continuous basis might be forced to consider quicker, more reliable, easier to operate, or cheaper alternatives. Since it is hoped that wider use will be made of the new VLBI techniques, it is necessary to address these problems.

Minicomputers provide a tool for alleviating both these difficulties. By appropriate monitoring and internal testing, the need for manual adjustments during data acquisition can be virtually eliminated. As described in section A.1, ASCII transceivers are used to control and read the calibration instruments. If the schedule of an experiment is available in machine-readable form, the sequence of operations can be automated and human intervention, as well as human

error, can be minimized. A complex sequence of events can be programmed to replace a long check list of manual operations. Computer control removes the need for continuous attention, improves reliability, and increases flexibility.

Before and after the observation phase of an experiment, minicomputers can be used to facilitate planning, direct data reduction, and control information flow. The steps in the reduction and analysis procedure can be monitored so that data is not lost or misprocessed. A data base has been developed as part of the Mark III system to integrate experiments and to assure data integrity. My contributions have been in the development of the data base structure (the files and programs which control the flow of information from conception of an experiment to the final results) and in the design of several programs that use the data base. I will describe the overall concept and follow the programs which operate on the data through the different stages of an experiment.

1. Data base structure

The data base was originally motivated by problems in passing data from one program to another and in keeping track of what programs actually had done. Because of the complexity of VLBI data processing, a number of programs were written, each by different people at different institutions. Each program's input and output were in unique, fixed formats. To avoid an impossible amount of human labor, the output of one program was available in machine-readable form as

input to the next, often by way of a small (but not necessarily trivial) intermediate program. Data could still be lost by accident, e.g., card mutilation, or be confused by reprocessing. The continual development of the programs led to three distinct problems. First, if the output of a program changed, the input to the next program was affected at the level of the program code. Sometimes new data was put in empty slots in the old format and the space of obsolete data was left blank. At worst, the entire interface format might be changed. Second, a multiplicity of output archive formats developed. It was necessary to know not only that a tape was written by a given program but also what version of the output format was used. Finally, programs evolved in ways which left the input/output formats unchanged but changed the results for a given input. It became difficult to recover what version and hence what algorithm had been used to produce a particular result.

When a new set of programs for parameter estimation became necessary, the questions of data integrity, interfacing, and program accountability were raised based on past experience. There were to be three programs. The first would take delay and delay rate data and combine them with meteorological, polar motion/UT1, and planetary ephemeris information. The second would calculate the theoretical values of delay and delay rate using the assembled data and output theoreticals, partial derivatives, and model contributions. The last would permit interactive selection and estimation of parameters. The form of several items was either unknown or known to be variable: the meteorological data, the state of the polar motion and UT1 data, the

number of parameters and partial derivatives. It was decided to adopt a flexible, format-free, permanent information transfer scheme, and the data base was born (but not named or recognized). The problem of program accountability was reduced by requiring each program to write into the data base an identifier describing the program, program version, programmer, and date of last modification.

Credit for conceiving of the data base as the information structure for integrating VLBI experiments must be given to Dr. T. A. Clark. During a trip to Green Bank we discussed the scheme that had been hatched and he described his ideas for extending it throughout the Mark III system. To use his simile, the data base is like a stream flowing past all the programs and processors which deal with the numbers of an experiment. At each bend some water is tasted and some water is added. The analogy should not be pushed too far since one guiding principle is that new data must not pollute information that is already there.

After preliminary discussions with J. W. Ryan, I designed the structure of the data base files and then designed, coded, and tested the data base handling programs (DBH) on the UNIVAC 1108 at the University of Maryland. The logic and code of the programs were developed in a top-down, structured fashion and were intended to be machine-independent. The success of the approach was shown by the ease with which I implemented the data base on the GSFC IBM 360/91 and HP 21MX, computers with quite different organization and capability. A second version of the data base handler has been written by J. W. Ryan

to include features not available in the initial design. Both versions have been used in data analysis done at GSFC and Haystack.

The data base itself consists of a series of programs and files. All access to the files is through the DBH programs.

A single data base file typically contains the data related to one experiment. As new information is added the file expands. Actual physical files are not changed but new versions containing the additional data are created. The file structure is essentially transparent to users. Each physical file consists of four parts: 1) a file identifier, 2) history entries, 3) tables of contents, and 4) data records.

The file identifier contains the file name (internal and external), the date of creation, a short file description, a version number, the name of the file from which the file was created, and a DBH identifier indicating the DBH revision used and the machine on which the file was made. The internal file name uniquely identifies the physical file. The external name associates the physical file with other physical files which form one data base file.

The history entries track the progress of a data base file. A data base file cannot be altered unless a history entry is made so that all changes in a file have associated history entries. Unfortunately it is impossible to prevent users from entering nonsense but at least such nonsense will be immediately evident.

As many as 99 different types of data record can be defined within a single data base file. Each existing data record type in a file has its own table of contents. Within each data record each data element is identified by an access code, text description, dimensions, and file version number when the element was initially added or last changed. Data elements can be real (floating point), integer, or alphameric.

The data records contain the values of the data elements defined in the tables of contents. Typically one data record type has information applicable to an entire experiment and only one data record of that type exists in the file. A second data record type contains information derived from observations so that each observation corresponds to a separate data record of this type. The data records are stored in sequence and are not cross-linked.

Beyond the fact that information must be real, integer, or alphameric, the data base is entirely format-free. It is also machine-independent as long as different word lengths do not lose significant digits. Each data record and each data element is independently accessible through type number and access code, respectively. The entry of new values, elements, records, or record types does not affect the existing information or structure. The amount of information that can be put in a single data record or data base file is limited only by the available space on physical storage devices. Since the version number associated with each data element is

updated when the value of the element is changed, the flow of data through the file can be monitored.

Associated with the entire data base is the data base catalog. The catalog is a linked-list structure which keeps track of the physical files which compose the data base files. Each physical file has a separate entry. The entries of all the versions of a data base file are linked or chained in sequence to the external file name. Chains also track the files which exist on specific storage devices, either disks, magnetic tapes, or diskettes.

The user-called programs fall into two categories: 1) access to the data base files and 2) access to the catalog.

The group of file access programs is the data base handler proper. They enable a user to:

1. open a data base file to creation, reading, or updating
2. make history entries
3. add to or delete from tables of contents
4. create, destroy, or move to data records
5. put values into data records
6. get values from data records
7. query the table of contents for existing data elements

A detailed description of these user-called programs is given in appendix C.

The catalog access programs enable a user to search the chains in the catalog, create and destroy chains, link entries to a chain and unlink entries from a chain. As these programs are not fully implemented, a detailed description is not possible.

In addition to the user-called programs, there are independent programs which use the catalog to move files from one storage device to another and from one computer's data base to another. The catalog can also be displayed and corrected. These programs operate interactively, prompting the user for type of action and data base files required. While working versions of these programs exist, they were conceived and executed in haste and are to be replaced shortly.

The information flow through the integrated Mark III VLBI system is shown in figure B.1. For each section I will describe the function within the system, the programs, and the scientific output. The programs for each stage are presently in considerably different states of completion. It is anticipated that all programs will be operational by the end of 1978.

2. Experiment scheduling

An experiment must begin with an idea of what is to be accomplished. Since VLBI is an observational technique, the experimenter must decide what to look at, when, how and why. The purpose of the SKED program is to assist in making a schedule that will

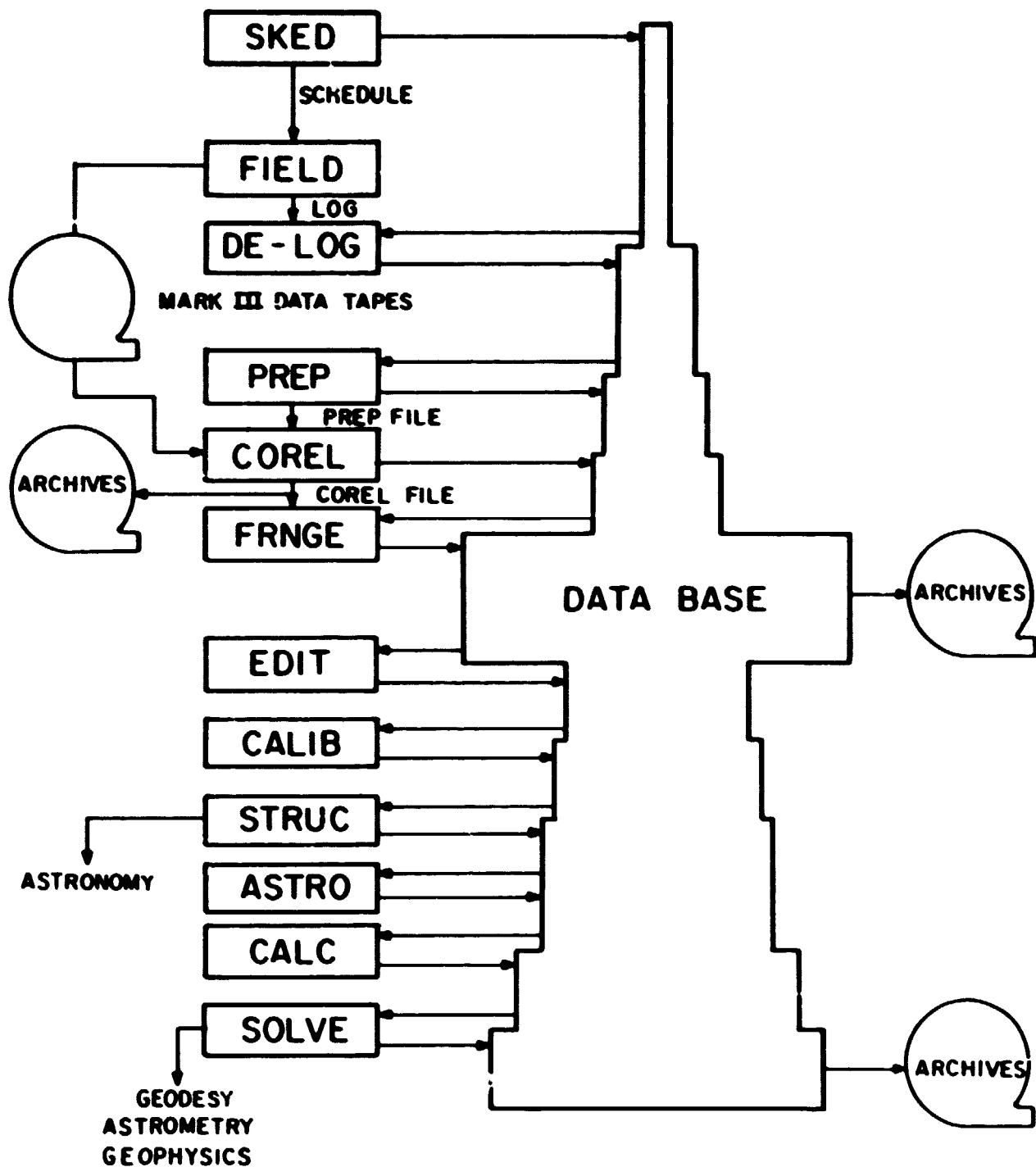


Fig. B.1 Mark III information flow

JRH
10-77

best accomplish the scientific objective. Unfortunately the requirements of different types of experiments sometimes conflict. For studying source structure, it is desirable to follow a source continuously with maximum sensitivity in order to get a complete, accurate fringe visibility function. The need for continuous observation is especially important for complex sources whose fringe visibility functions vary rapidly. For geodesy, maximum sky coverage for a set of sources using maximum synthesized bandwidth is desirable. Spectral line work does not require large bandwidths so that it may be possible to trade bandwidth for tape usage. I will concentrate on the requirements of geodesy.

One specific requirement of geodesy is a precise baseline determination. The word precise is used here to mean minimum formal error after the estimation of the baseline components. There are two steps in reaching the "best" schedule: making a schedule and determining if the schedule is leading in the direction of minimizing the baseline errors. The first is a function of the SKED program. The second is accomplished through the data base. As soon as a schedule is put in the data base, another program can perform an error analysis. By a series of schedule simulations, the schedule can be improved. The details of schedule optimization are discussed in section IV.D.

There are a number of programs used for generating VLBI schedules. Those that run on the Haystack Observatory CDC 3300 and the University of Maryland UNIVAC 1108 are interactive while the GSEC IBM 360 version is basically a schedule verifier and printer. The best

features of all three have been combined in the specifications of the SKED program which is part of the integrated Mark III system. SKED runs on the GSFC disk-based HP 21MX using a CRT terminal with line plotting capability. It begins with a skeleton data base file which contains a list of observing stations and radio sources. The file also has: 1) station cartesian positions, 2) telescope parameters such as diameter, receiver temperature, efficiency, axis type and slewing rates, and 3) source positions and flux densities. The scheduler sets the time of the experiment and selects the stations and sources to be used. SKED then provides information to allow the scheduler to select a sequence of sources to make a schedule: 1) a list of sources currently visible, their hour angle, elevation and azimuth at each station and the time to slew to position; 2) the last few observations scheduled; 3) a complete mutual visibility plot for the day with a mark for the current time, 4) a polar plot of the sky at each or a specified station; 5) the status of cable wrap at the az-el antennas, and 6) a summary of the schedule so far. After the scheduler selects a source, SKED schedules the observation taking into account slewing, pointing, and radiometry time requirements and updates the visual display. The default values for observation length, dead time between runs, frequencies, and bandwidth can be changed at any time as can the stations and sources. The scheduler may also back up in the schedule and change a block of time or repeat a previous sequence on a different day. Special requirements for particular observations, e.g., pulsar gating, can be indicated. As shown in figure B.1, SKED produces two types of output, a data base file containing the schedule in time order, one record for each baseline-source observation, and an

operating schedule for each site field controller. The data base file is used for error analysis and later processing. It contains two types of records: 1) a header with information applicable to the entire experiment, and 2) observation records with data pertinent to individual observations. The operating schedule controls a station's operation and is described in the next section.

The program SKED is being written by N. R. Vandenberg.

3. Observations

The second stage of a VLBI experiment is taking data. The logistics of shipping schedules and data tapes to distant stations remains a problem. However, the Mark III field system is designed to automate data acquisition as much as possible. Once the equipment is running (and as long as it continues running), the only manual intervention is loading and unloading tapes. The field hardware is described in section A.1. The following paragraphs will concentrate on the software requirements. Since the programs that control the field operations are not yet completely defined, the functions required will be described rather than the exact implementation. The entire field system including instrumentation and control programs is expected to be ready in late 1978.

The three main functions of the field program are: 1) to direct the sequence of events set by the schedule, 2) to monitor the system behavior, and 3) to log information pertaining to the state and

environment of the experiment.

The experiment schedule is a file which controls the operation of a specific station for a specific length of time. At the beginning of a schedule file is information that remains constant for the interval covered by the file: 1) descriptive text, 2) the station name, 3) the date, 4) the beginning and end times for the file, 5) the type and epoch of the source positions, and 6) the intervals for scheduling various operations. After the header come data for observations and special operations, each with a time associated. The start time, source name, source position, duration, synthesizer settings, sideband, bandwidth, tracks to be recorded, and direction of tape travel are given for the observations in the domain of the schedule file. The sequence of events which constitute an observation are defined. These include moving the telescope to the correct position, peaking on the source, doing radiometry, starting and stopping the data tape. Special operations are those not related to a particular observation. These include rewinding the data tapes and operator messages requesting manual operations. If the schedule must be changed after the schedule files have arrived at the station, the operator can make the change manually.

The field program reads the schedule file and directs the hardware to perform the operations at the time and in the sequence called for. While operations are in progress, the program monitors the equipment to detect problems. If any equipment difficulties are discovered, the operator is alerted.

The log records the actual conduct of an experiment. Four types of information are logged: 1) schedule verification, 2) data quality, 4) system and environmental conditions, and 5) operator notes. The header of the log contains general information about the experiment including the station name and date. The information that specifies an observation is copied into the log so that all schedule changes are recorded. The number of the data tape containing the observation is also kept. For each observation the bandpass shape, phase calibrator signal strength and phase and number of parity errors are logged. Since only two tracks can be read back at one time, complete checking is not possible. Internal timing checks are also recorded. These numbers give some indication about the performance of the receiving and recording system. Also associated with an observation are the source temperature, the system temperature, the phase calibrator cable length, pointing corrections, and output from the water vapor radiometer. Some information is monitored and recorded at fixed intervals: the meteorological sensors, the station clocks, the phase calibrator cable length, and internal Mark III switch settings. At any time the operator can enter comments into the log.

After an experiment is finished, the data tapes are sent to the Mark III processor at the Haystack Observatory. The logs are merged and entered into the experiment data base file by the program DELOG. DELOG has not been written.

4. Evaluation of VLBI observables

Reduction of the mass of raw data bits to a smaller set of useful numbers, the VLBI observables, is accomplished through a set of programs operating with the data base and the Mark III processor. Referring again to figure B.1, these programs are PREP, COREL, FRNGE, and EDIT, which are (to be) implemented on the Haystack HP 21MX. Preliminary version COREL and FRNGE have been written and tested by A. E. E. Rodgers and A. R. Whitney. PREP and EDIT are in the design stage.

The data base is augmented by output of DELOG describing the experiment as it was actually run. PREP gets information from the data base on the observations that were made. Using clock data, a simple atmosphere model, start times, frequencies, tracks, station and source positions, it prepares an external file, i.e., not in the data base, which contains a priori delays, fringe rates, and fringe phases needed by COREL. The frequency of the phase calibration signal in each channel is also retrieved and placed in the PREP file.

The function of COREL was described in section A.2 with the operation of the Mark III processor.

FRNGE reads the COREL file and integrates the individual accumulation period values for an entire observation. For each track it computes the residual delay and fringe rate. Individual accumulation period fringe amplitudes and phases for each track are calculated and put into an intermediate file or into the data base.

EDIT is an interactive program for editing reduced data from FRNGE and producing VLBI observables. The fringe amplitudes and phases for each channel of an observation are displayed graphically. The phase calibration amplitude and phase, residual delay and fringe rate, averaged fringe amplitudes for selected integration periods, and error counts are also displayed for each channel. The user selects the start time, stop time, and coherent integration length for each channel based on a judgment of the data's quality. EDIT then integrates the selected channels to get average fringe amplitudes and phases corrected for residual fringe rate. The fringe phase over the channels is used to calculate the residual group delay and the residual delay rate is corrected for phase calibration rate. The residual delay and rate are added to the a priori values in the data base to produce total delay and delay rate. The epoch associated with the delay and delay rate may not coincide with the original schedule but depends on how the bits from the observation are processed. A single continuous observation can, for example, be divided into several parts. The editing parameters and the output from EDIT are put into the data base. After the geometric and source structure observables for an entire experiment have been put in the data base, the data base file is archived.

Another step is necessary to reduce the subsidiary data from the logs. The cable length and meteorological data are used to calculate the respective effects on the VLBI observables at the epochs associated with the observables. The corrections are entered in the data base for each observation.

5. Estimation of parameters

Even though the machinery for taking and reducing raw data is complex and expensive, the immediate output is not of scientific interest. The system described so far is designed to reduce the burden of running an experiment and to produce data of higher quality. Part of the improvement is in the new hardware, which is more sensitive and more complete. Another part comes from increased flexibility in planning an experiment and executing a schedule. The programs which extract scientifically interesting numbers combine flexibility and completeness to facilitate the final data analysis. Instead of sitting around waiting for computer runs to percolate through a long job queue, a researcher can sit in front of a television screen and work with the data interactively.

There are three principal programs for data analysis as shown in figure B.1, STRUC, CALC, and SOLVE. All of them operate from information in the data base and put their results into the data base. The graphical and interactive parts of STRUC and the whole of SOLVE are implemented on the disk-based HP 21MX. For reasons of speed and size the "number crunching" parts of STRUC and all of CALC run on the IBM 360/91. CALC and SOLVE are operational while STRUC has yet to be written.

STRUC analyzes the data for source structure. It uses the source temperatures, system temperatures, fringe amplitudes, and projected

baselines to calculate and plot the fringe visibility function for each source observed. If there are three or more baselines which form closed triangles, the fringe phases are combined to make closure phase observables for each simultaneous set of observations. From the fringe visibility function and closure phase a milliarcsecond source map is made and displayed. Corrections to the delay and delay rate are computed from the projected baselines and observed source structure. The source maps are put into the data base as brightness grids while the corrections are entered as contributions to the observables from source structure.

CALC generates theoretical delays and delay rates, partial derivatives, and model contributions. Its organization is based on the ESTIM error analysis program, which is described in appendix D. Using my detailed design, CALC was coded by D. Markham with assistance from D. S. Robertson and J. W. Ryan.

CALC is divided into thirteen sections, one for each physical or geometrical model now used. These are:

1. troposphere
2. antenna axis offset
3. corona
4. diurnal polar motion
5. solid earth tides
6. nutation
7. ocean loading displacement

8. precession
9. gravitational deflection of light
10. station position
11. source position
12. UT1
13. polar motion

The algorithms used in the model are given in chapter II. Each section includes several parts: 1) additions to the data base tables of contents, 2) initialization, 3) observation geometry, 4) parameter partial derivatives, and 5) model contributions. Each part gets the data it needs from the data base using the data base handler. The various parts of a section are separate programs which communicate through a labeled common area unique to the section. A schematic diagram of a section is shown in figure B.2.

The part of a section which modifies tables of contents adds entries for information which is put in the data base by other parts of the section. A message identifying the section is added to the header. Partial derivatives and contributions are added to each observation record. This part is called once.

The initialization part puts the section text message into the data base header. The message includes the model version and status during the present run. The part gets from the header necessary information such as a priori parameter values and initializes variables for use within the section. This part is also called once.

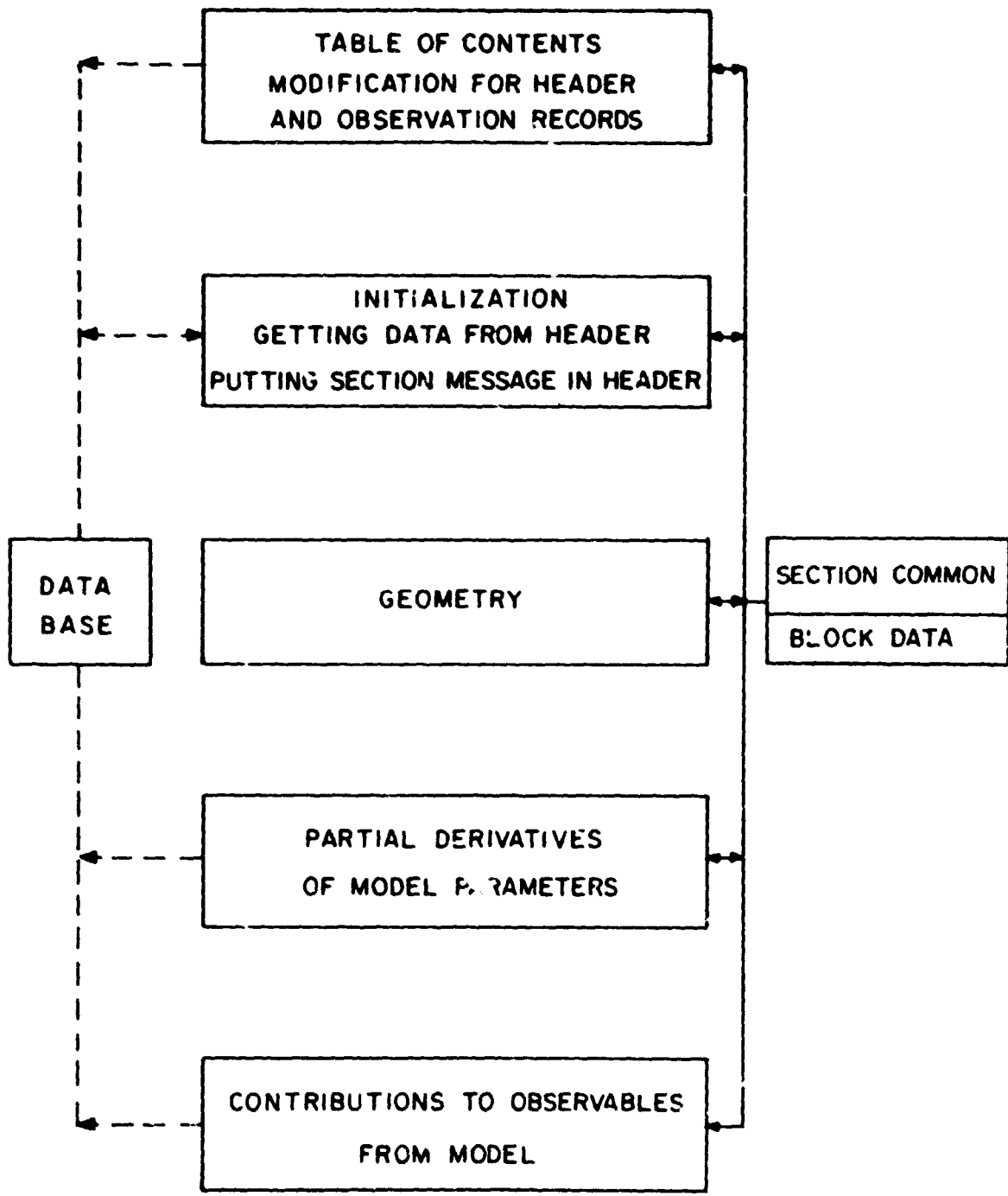


Fig. B.2 CALC section block diagram

JRH
11-77

The observation geometry part calculates the effect of the model on the instantaneous source-baseline configuration at the nominal epoch of an observation. The site and source sections return cartesian coordinates in terrestrial and fundamental VLBI coordinate systems, respectively. The nutation, precession, diurnal polar motion, and polar motion sections return coordinate rotation matrices. The UT1 section returns the offset between UT1 and atomic time. The earth tide and ocean loading sections return corrections to the station positions. The corona and relativity sections return corrections to the source position. The troposphere and axis offset sections do not return corrections since these models do not affect the source-baseline orientation. Each geometry part is called once for every observation.

The partial derivative part calculates the partial derivatives of the theoretical delay and delay rate with respect to the model parameters and puts them in the data base observation record. This part is called once for each observation.

The contribution part calculates the contribution of a model to the theoretical delay and delay rate and puts it in the data base observation record. The contributions from models which do not enter into the observation geometry are later added to the theoretical delay and rate. These are troposphere and axis offset. The contributions from models which affect the geometry are calculated by linear approximation from the partial derivatives. These are diurnal polar motion, earth tides, ocean loading, gravitational light deflection, and

polar motion. The purpose of calculating individual model contributions is to allow models to be selectively subtracted at the SOLVE phase of parameter estimation. The contribution part is also called once for each observation.

The overall structure of CALC is shown in figure B.3. There are a series of executive routines which call the section parts in the correct order. TOCUP calls the table of contents modification parts. INITAL calls the initialization parts. DRIVRG, DRIVRP, and DRIVRC call the geometry, partial derivative, and contribution parts, respectively.

Four routines provide the connections to get observation data from the data base and put the theoretical values into the observation records. START reads input to CALC and opens the data base. OBSENT positions the data base file for each observation so that the section parts can access the observation record. THEORY uses the geometry and model contributions to calculate the total theoretical delay and delay rate and puts the values in each observation record. MAIN calls all the executive subroutines in the proper sequence.

PEP calculates from the ephemeris tape geocentric position and velocity of the sun and moon and solar system barycentric position, velocity, and acceleration of the earth if this data is not present in the data base. It also interpolates nutation in longitude and obliquity for each epoch of observation. UTCTME, ATIME, and CTIME calculate UTC time, atomic time, and coordinate time, respectively, of each observation as the fraction of day.

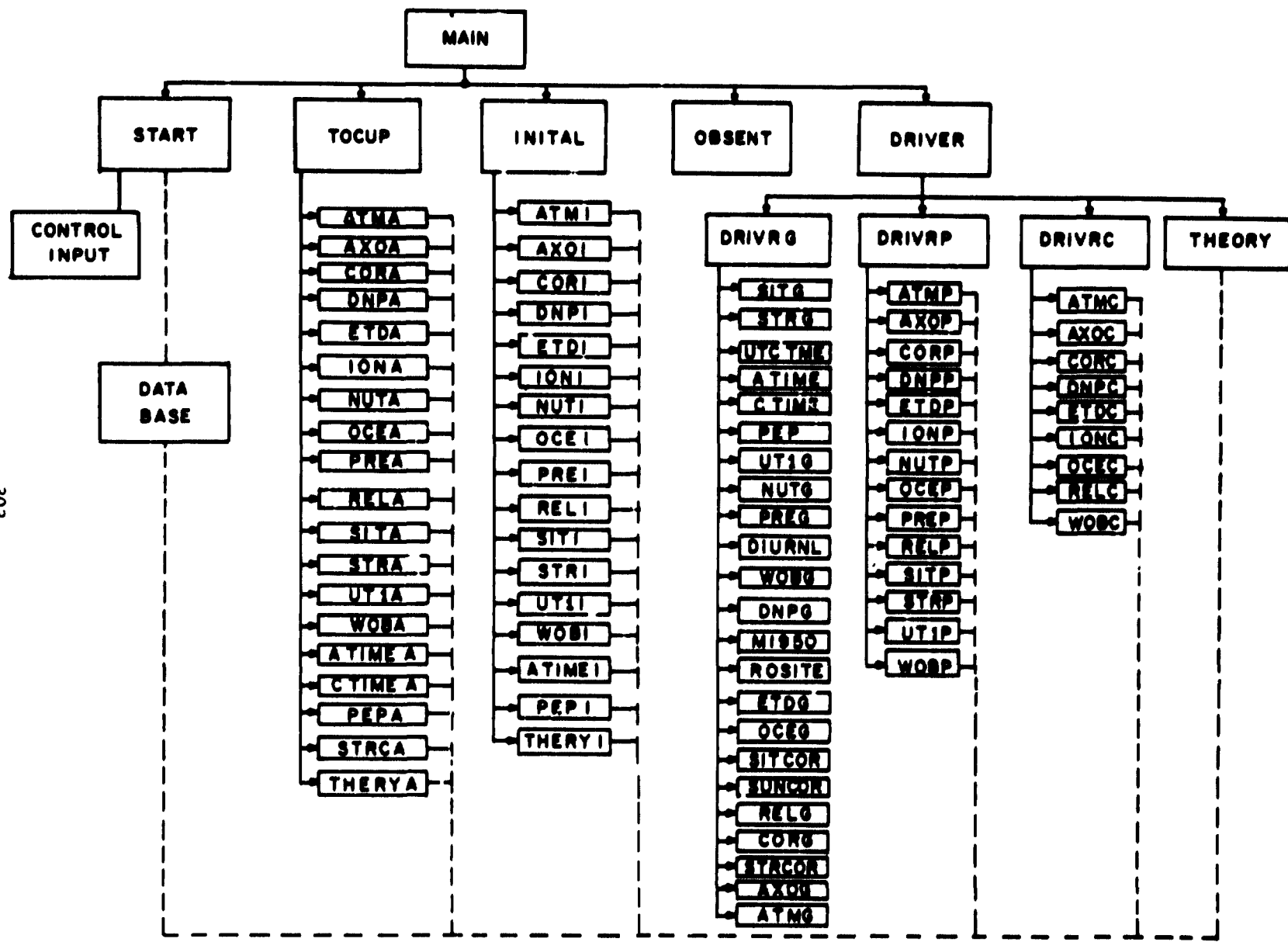


Fig. B.3 CALC block diagram

It should be noted that CALC is critically dependent only on SKED. CALC can be run as soon as a schedule is made and put in a data base file. The partial derivatives produced can be used by SOLVE to do preliminary covariance analyses of the schedule. After an experiment has been processed by EDIT, preliminary and final data for UT1, polar motion, and source structure can be entered as they become available in order to refine the theoretical values computed by CALC.

The final stage in the data analysis is SOLVE. This program was developed by D. S. Robertson based on his experience with an older CDC 3300 version. Sitting at the console of the HP 21MX the user can call for an experiment data base file, combine it with others, select the parameters to be estimated, select epochs for parameters that vary (such as clock polynomials), select either the delay observable, the delay rate observable, or both, and run a solution. The post-fit residuals are plotted on a TEKTRONIX 4012 CRT and the parameter corrections and formal errors are printed. The user can then alter the plotting limits, examine particular points, change observation weights, delete faulty data points, move delay points by an integral number of delay ambiguities, and produce a hard copy of the plot. After the data are edited the solution can be run again with the same or different parameters selected. The data base may be updated to save the editing information or to rescale the observation measurement errors. A file is kept of all the adjusted parameters with enough information to recreate any particular solution. The saved parameter values from solutions based on data spanning a length of time can then be analyzed

for dispersion and drift.

The scientific results possible from the analysis described above cover a large area in present VLBI research. The output of STRUC is source maps which can be used to study the evolution of radio source structure. The source positions estimated in SOLVE are important in astrometry while the baseline results can be used in geodesy. A test of general relativity theories is possible with refinement of the gravitational light bending parameter. Love numbers from earth tide and diurnal polar motion solutions give geophysical information. Determination of UT1 and polar motion is applicable to time and navigation while estimating the precession constant is of interest to general astronomy.

6. Archiving data

In the same way that the data base serves as the information stream between programs, it is also functions as the primary archiving medium. Fundamentally there is no reason why all versions of all data base files could not be kept on mass storage simultaneously. However, for reasons of security and practical disk usage, the data base is archived on tape periodically and earlier file versions are purged from the active area. The format of an archive tape is ASCII characters in blocked card images. Files which may be read back frequently, e.g., various stages of SOLVE processing, are also kept on binary tapes to save reformatting time. Since each data base file contains both history entries and tables of contents for the data, it should always

be possible to reconstruct the data reduction and analysis procedure used. There is one place where information is archived outside the data base. The COREL file that contains the single accumulation period complex correlation values is too large to fit practically in a data base file. Since the file is passed from COREL to FRNGE on tape, the tape itself is later archived.

Appendix C.

USER GUIDE TO DATA BASE HANDLER VERSION 2C AS OF NOV. 1977

The following documentation applies specifically to the currently operational version of the data base handler on the GSFC HP 21MX. However, the IBM 360 and Haystack HP 21MX versions do not differ in any essential details. Familiarity with the basic file structure and vocabulary given in appendix B will be assumed.

The following terms will have specific technical meanings:

element - a unit of information. The term **element** subsumes two related concepts: 1) the name and meaning of a piece of information, e.g., epoch of observation, and 2) the number(s) or literal character(s) which are the specific representation of the information, e.g., 77/11/22/08/15. An element can contain only a single number or may be stored as an array.

access code - the 8-character string used to identify an element. The access code is required for all operations with a specific element and corresponds to the name of the element.

value - the number(s) or literal character(s) which are the specific representation of an element within a particular data record. The values of an element may (and usually do) differ from data record to data record. The access code of an element is fixed

within the entire data base file.

table of contents (TOC) - the arrays in core and in the data base file which are used to locate element values within data records. Each type of data record has an independent table of contents. Each element has an entry in the proper table of contents.

data record - a set of values organized according to the table of contents for the applicable data record type. Data records of the same type contain the same elements but the element values are generally different. Each data record is independently accessible.

data record type - a number from 1 to 99, inclusive, which identifies a particular table of contents and hence a subset of all the data records in a data base file.

private file - a data base file which is identified by a 6-character FMGR file name. At present all data base files are private files.

catalogued file - a data base file which is identified by a 10-character experiment name and whose versions are tracked by the data base catalogue. There are currently no catalogued files in this sense since the proper catalogue does not exist.

version - a physical copy of a data base file differing from other

copies of the same data base file in having different values and/or elements. While one experiment now gives rise to a string of private files, the term version does not properly apply. Versions in this sense will not exist until the proper catalogue is developed.

data base catalogue - a file which tracks the versions of the data base files. This catalogue does not yet exist.

provisional catalogue - a file which tracks the existing private files.

The current CATLG/CATLF programs keep track of all existing data base files. CATLF is used to update the provisional catalogue as new files are created. Operations with CATLF are not automatic but require the data base handler user to reply to prompts which ask for the file just created, the position at which to place the file in the provisional catalogue, and a file description.

real element - an element whose values are floating point numbers. The precision of real elements is limited to 11 significant figures because of HP 21MX machine requirements. On both the HP 21MX and the IBM 360 real elements are double precision numbers.

integer element - an element whose values are integers. The values of integer elements are limited to $-32768 \leq N \leq 32767$ because of the HP 21MX. On the IBM 360 integer elements are I#4 numbers.

alphanumeric element - an element whose values are characters drawn from

the full ASCII set. The dimensions of alphabetic elements are as they appear in the user program. On the HP 21MX alphameric elements are stored in single 16-bit words, two characters per word. On the IBM 360 alphameric elements are stored in I*2 words, two characters per word.

history entry - a descriptive text of up to 160 characters appended to the data base file each time a new file or version is created with new information.

The data base handler has three modes of operation: 1) read, 2) update, and 3) create. In the first mode information, i.e., the existence of elements and the values of elements, can be retrieved from a data base file. Information cannot be changed. In update mode the elements and values in a file can be changed. A new file or version is made incorporating the changes. In create mode a data base file is created from scratch. Each mode has a different sequence of operations.

Read mode is the simplest since the tables of contents are not changed. The sequence is as follows with (XXX) indicating an optional operation.

1. IRWIN
2. (GHIST)
3. (ASK)
4. (MVREC)----! loop

5. (GET)-----; loop

6. FINIS

IRWIN establishes the connections to the desired data base file. GHIST retrieves history entries. ASK interrogates the tables of contents about specific access codes. A loop over MVREC and GET accesses successive data records and gets values from the records. FINIS terminates data base operations cleanly. Except for the indicated loop, the operations must be done in the continuous sequence shown without branching backwards. GHIST and ASK may be called as many times as necessary at the proper time.

Update mode is used when an existing data base file is to be changed. The change can be any or all of the following: 1) changing the values of existing elements, 2) introducing new elements and the corresponding values, 3) creating new data records of already existing types and putting in new values, 4) deleting existing elements and the corresponding values, 5) deleting existing data records, 6) adding a new type of data record and creating the corresponding data records. Values can be changed in any or all of the existing or created data records. The sequence of operations is:

1. IRWIN

2. (GHIST)

3. PHIST

4. (ASK), ADD, DEL

5. OPREC, MVREC----; loop

6. (GET), (PUT)----; loop
7. WRIDR, DELDR----; loop
8. FINIS

IRWIN opens the input file and creates the output file. PHIST enters one or more new history entries. The history entries should include the user name and the changes/additions to be done. ADD changes the tables of contents. A separate call to ADD must be made for each element whose values are to be changed or introduced. A new TOC entry is made if the element (as indicated by the access code) does not already exist in the specified table of contents. If there is already an entry corresponding to the access code, the entry is updated to indicate that the element description, dimensions, or values will be changed. DEL deletes the entry of an element and removes the element and its values from the file. All calls to ADD and DEL must be done before proceeding in the sequence. OPREC and MVREC operate with the data records. OPREC creates a new data record of a specified type while MVREC activates existing records. Once OPREC or MVREC is executed, GET and PUT can get values from the data record and put values into the record, respectively. Each data record in which a change is to be made must be accessed by OPREC or MVREC. After operations on the active data record are finished, WRIDR is used to write that record. If the record is not wanted, DELDR deletes the entire data record. The loop over OPREC, MVREC; GET, PUT; and WRIDR, DELDR is used to move through the data base file, changing and creating data records as desired. FINIS terminates the data base operations. FINIS then schedules CATLF which prompts the user for a file name,

position in catalogue, and a file description to be entered into the provisional catalogue.

Create mode is not often used except to begin the data base file or string of private files related to a particular experiment. The operations are a subset of those used in update mode.

1. IRWIN
2. PHIST
3. ADD
4. OPREC---| loop
5. PUT-----| loop
6. WRIDR---| loop
7. FINIS

IRWIN creates the file. PHIST appends the initial history entry. The calls to ADD create the tables of contents and insert the entries for all the elements whose values are to appear in the data base at the beginning. It is not necessary to call ADD for elements which will not be entered until some later version. The loop over OPREC, PUT, and WRIDR creates data records, fills the data records with the desired values, and writes the data records to the file. FINIS terminates data base operations and enters the output file in the provisional catalogue. As in the other modes, the sequence of operations must be followed, i.e., all calls to PHIST before any call to ADD and all calls to ADD before any call to OPREC.

Restrictions and notes:

At present the size of an element is limited to 500 HP 21MX words, i.e., 1000 characters, 500 integers, or 166 real numbers.

Certain elements are entered as two values in order to increase precision. These include the mathematical constants and the delay.

The first data record in all data base files is a type 1 record, which is called the header. There is only one type 1 record. The header contains information pertaining to the entire file.

The data pertaining to particular observations are contained in type 2 data records.

Each program which updates data base files is expected to put into the header a message indicating program version, programmer, last modification date, and internal options taken.

Only one data base file can be opened at a time in the present implementation. This restriction applies within a single program and to two separate programs executing simultaneously.

The data base files are to be in strict time order. Data records which have no epoch associated will be at the beginning or the end of the file. There is no set order for data records of different types with the same time tag.

In update mode, if the dimensions of an element are changed, it is necessary to GET the old values and PUT them for all data records in which the values are not actually changed. Any data record which is made active in update mode, even if no change is made, must be written to the output file using WRIDR before operations on another data record can begin.

While an access code is 8 characters or 4 words, each time it is passed to a routine an array of 7 words must be passed. The 3 additional words are used by the data base handler for rapid searching in the data record and should never be altered by the user.

A program which uses the data base handler on the HP 21MX should not be terminated by OF. Typing BR,DBASE in system mode will cleanly terminate both the data base handler and the user program.

Alphabetized listing of the data base handler routines and arguments

1. ADDA, ADDI, ADDR
2. ASK
3. DELA, DELI, DELR
4. DELDR
5. FINIS
6. GETA, GETI, GETR
7. GHIST
8. IRWIN

- 9. MVREC
- 10. OPREC
- 11. PHIST
- 12. PUTA, PUTI, PUTR
- 13. WRIDR

1. ADDA

ADDI

ADDR

ADD(A/I/R) enters or changes the entry of an (alphanumeric/integer/real) element in the table of contents of a specified type of data record. ADD(A/I/R) must be called for each element whose values are to be entered or changed and is applicable only in update and create modes. All calls to ADD must be completed before moving to or creating a data record.

calling sequence - CALL ADDA(NTOC,LCODE,LTEXT,ND1,ND2,ND3)

CALL ADDI(NTOC,LCODE,LTEXT,ND1,ND2,ND3)

CALL ADDR(NTOC,LCODE,LTEXT,ND1,ND2,ND3)

input variables:

1. NTOC the data record type to which this element is to be added where $0 < NTOC < 100$.

2. LCODE(7) the 8-character access code in the first four

words followed by three words which should never be altered by the user. The same seven word unit must be passed each time the element is accessed. The three additional words are used by the data base handler to store rapid search parameters.

- 3. LTEXT(16) the 32-character text description of the element.

- 4. ND1 the first dimension of the element being defined (0 or 1 if singled-valued element)

- 5. ND2 the second dimension (0 or 1 if element is single-valued or a one-dimensional array)

- 6. ND3 the third dimension (0 or 1 if element is single-valued or a one/two-dimensional array)

2. ASK

ASK determines if a specific access code already exists in the table of contents of a particular data record type. ASK returns a flag indicating if the code exists and, if so, information about the element associated with the code.

calling sequence - CALL ASK(LCODE,NTOC,ND1,ND2,ND3,NVER,LTEXT,

KTYPE,KERR)

input variables:

1. LCODE(4) the 8-character access code to be interrogated.
2. NTOC the data record type to be checked where
0 < NTOC < 100.

output variables:

1. ND1,ND2,ND3 the dimension of the element associated with
LCODE.
2. NVER the version number when the element entry in
the table of contents was last updated.
3. LTEXT(16) the 32-character text description associated
with LCODE.
4. KTYPE element type (1 - real, 2 - integer,
3 - alphanumeric)
5. KERR return flag (0 - element found, 1 - the
requested data record type (NTOC) was found but
the LCODE was not in it, 2 - the requested data
record type was not found)

3. DELA

DELI

DELR

DEL(A/I/R) deletes an (alphanumeric/integer/real) element from the table of contents of a specified type of data record. The element and its values are removed from the file. DEL(A/I/R) is applicable in update mode. All calls to DEL must be made before moving to any data record.

calling sequence - CALL DELA(NTOC,LCODE)

- CALL DELI(NTOC,LCODE)

- CALL DELR(NTOC,LCODE)

input variables:

1. NTOC the data record type from which the element is to be deleted where $0 < NTOC < 100$.
2. LCODE(7) the 8-character access code in the first four words followed by three words which should never be altered by the user. The same seven word unit must be passed each time the element is accessed. The three additional words are used by the data base handler to store rapid search parameters.

4. DELDR

DELDLDR deletes the active data record. It is applicable in update mode.

calling sequence - CALL DELDR

5. FINIS

FINIS terminates data base operations. It must be called in all modes for proper termination.

calling sequence - CALL FINIS(KFIN)

input variable:

1. KFIN 0 - normal stop. In the read mode, the input file is closed. In the create mode, the output file is closed and entered in the catalogue. In update mode, the remainder of the input file is copied to the output file. The input and output files are closed and the output file is entered into the catalogue.

 1 - normal crash termination. The output file (if any) is purged, and the input is closed.

The catalogue is not changed.

2 - legal in update mode only. The output file is closed. The remainder of the input file is not copied. The catalogue is updated.

6. GETA

GETI

GETR

GET(A/I/R) retrieves (alphanumeric/integer/real) values from the active data record.

restrictions: The dimensions passed in the call to GET do not have to be the same as the dimensions specified in the table of contents. However, when a dimension in the call is less than the dimension in the table of contents, some values will not be transferred to the user's array. Where the dimension in the call is larger than the dimension in the table of contents, the data base handler will pass as much as possible. In any case the data base handler assumes that the user's array is organized according to the dimensions in the call statement and never exceeds that array.

calling sequence - CALL GETA(LCODE,LLEM,ND1,ND2,ND3,NDO,KERR)
CALL GETI(LCODE,ILEM,ND1,ND2,ND3,NDO,KERR)
CALL GETR(LCODE,RLEM,ND1,ND2,ND3,NDO,KERR)

input variables:

1. LCODE(7) the 8-character access code is the first four words followed by three words which should never be altered by the user. The same seven word unit must be passed each time the element is accessed. The three additional words are used by the data base handler to store rapid search parameters.

2. (L/I/R)LEM(*) the variable or array into which the (alphanumeric/integer/real) value(s) are to be transferred.

3. ND1 the first dimension of the user array (0 or 1 if single value)

4. ND2 the second dimension of the user array (0 or 1 if single value or one-dimensional array)

5. ND3 the third dimension of the user array (0 or 1 if single value or one/two dimensional array)

output variables:

1. NDO(3) the element dimensions from the table of

contents.

- 2. KERR error condition flag (0 - normal return,
 2 - data successfully retrieved but passed
 dimensions did not equal the dimensions in the
 table of contents, 1 - data not found)

7. GHIST

GHIST gets information from the history entries in the data base file.

calling sequence - CALL GHIST(KC,IMAX,LHIST,JMAX,IHDT,NVER,KERR)

input variables:

- 1. KC input control variable (0 - get the next
 history entry, 1 - get the last history entry)
- 2. IMAX the maximum number of (16 bit) words of history
 text to be passed back to the user.

output variables:

- 1. LHIST(*) the array in the user program where the output
 history text is to be placed.

2. JMAX the number of words of history text actually placed in L HIST.

3. IHDT(5) the year/day-of-year/hour/minute/second that the returned history entry was put into the data base.

4. NVER the number of the version when this history text was added.

5. KERR output information flag (0 - no error, 1 - this is the last history item, -1 - the last call to ghist returned the final history item; nothing returned this time)

8. IRWIN

IRWIN opens the data base handler and the data base files. IRWIN performs the following functions:

1. For catalogued data base files it resolves the file name and version number into a FMGR file name or a file number of a tape. If the data base file is on the 21MX disk it opens the file. If the file is on tape it requests that the operator dump the file to the disk and suspends itself until that action is completed. Once the file is on the disk IRWIN opens it.

2. For private (uncatalogued) data base file, it opens the file.
In the create or update mode it obtains the name for the output file and opens that file.
4. IRWIN reads from the input file the identification records.
These records contain the FMGR file name, the 80-character descriptor of the file, and the date/time of the creation of the file.
5. The identification records are written into the output file, if any.
6. Various data base handler control variables and arrays are initialized.

calling sequence - CALL IRWIN(KRUC,IIN,IOUT,LFCI,LFVI,LFTO,
LFCO,KTYPE,ISTP,IDATE,LFIO,KERR)

input variables:

1. KRUC mode control flag (1 - read, 2 - update,
 3 - create)
2. IIN input logical unit. On the HP 21MX 0, 21, 51,
 52, and 53 are acceptable. If 0 is used, the
 entire disk is searched.
3. IOUT output logical unit. On the HP 21MX 0, 21, 51,
 52, and 53 are acceptable. If 0 is used, the
 output file is created on LU 51.

4. LFCI(5) the input file code name. This is a ten-character code. For a catalogued file it must be constructed in a form that is yet to be specified. In the case of a private file the first six characters of LFCI must contain the precise FMGR file name.
5. LFVI for a catalogued file, the version number desired; zero for the latest version.
6. LFTO(40) This is a 80-character output file descriptor. In the update mode if LFTO(1) is zero, then the text descriptor from the input file is transferred to the output file. The user may therefore code a zero directly in the calling sequence for IRWIN at the position for LFTO.
7. LFCO(3) In the case of a private output file this must contain the FMGR name of the output file.
8. KTYPE set to 'PP' for private input and output files, set to 'PC' private input but catalogued output file, and set to 'CP' for catalogued input but private output. Set KTYPE to any other value for both catalogued input and output.

9. ISTD the logical unit on which error messages are to
 be written.

output variables:

1. IDATE(5) the date the input file was created in the form
 Y.M.D.H.M.

2. LFIO(40) the 80-character descriptor from the input
 file.

3. KERR error flag (0 - no error, 1 - input file not
 found in the catalogue, 3 - no room on the disk
 to open the output file, 4 - KRUC invalid)

9. MVREC

MVREC is used to access data records existing in the data base
file. Once a data record is made active, the user can get values
from it and put values into it. Using MVREC the user can access
the data records sequentially. MVREC is applicable in read and
update modes.

calling sequence - CALL MVREC(NTOC,KMODE,KNUM,KERR)

input variables:

1. NTOC data record type to be made active
(0 < NTOC < 100 - access data record of type
NTOC, 0 - access the next data record in the
input file regardless of type)
2. KMODE relative/absolute flag (1 - move relative to
the current position in the input file,
2 - move to an absolute record number of type
NTOC)
3. KNUM move count (In the relative mode, move ahead
(or backward) KNUM records of type NTOC. In
the absolute mode, move to the KNUM'th record
of type NTOC counting records of type NTOC from
the beginning of the file.)

Note 1. If NTOC is 0, then KMODE and KNUM are ignored.
However, this mode is not yet implemented.

Note 2. The absolute mode (KMODE = 2) is not currently
implemented and attempting to use it will
generate an error stop. Also relative moves
may only move forward through the data base.
An attempt at a backward move will generate an
error stop. Both these capabilities will be
implemented in the data base in the future.

output variable:

1. KERR execution status flag (0 - normal return,
1 - end of file encountered, 2 - requested data
record type does not exist, 3 - attempted to
move backwards beyond first data record)

10. OPREC

OPREC creates and makes active an empty data record of a specified type. Once OPREC is executed, PUT's may be performed to put values into the data record. OPREC must be used to create data records in create mode and can be used in update mode to create new data records.

calling sequence - CALL OPREC(NTOC)

input variable:

1. NTOC the type of empty data record to be created
where $0 < NTOC < 100$.

11. PHIST

PHIST makes history entries in a data base file. PHIST must be called in update and create modes and can be called as many times as needed.

calling sequence - CALL PHIST(NHIST,LHIST)

input variables:

1. NHIST the number of (16 bit) words in the history
 entry being passed from LHIST where
 $0 < \text{NHIST} \leq 80$.

2. LHIST(*) the history entry to be appended to the output
 file.

12. PUTA

PUTI

PUTR

PUT(A/I/R) inserts (alphanumeric/integer/real) values into the active data record. All elements for which a PUT is executed must have had corresponding calls to ADD. PUT(A/I/R) is applicable only in update or create mode.

restrictions: The dimensions passed through to PUT(A/I/R) must be less than or equal to the dimensions defined for the element corresponding to LCODE. Also, ND1 and ND2 must be actual dimensions defined in the user program dimension statement. Finally, the dimensions defined for the element in the table of contents will be used to put the values into the data

record. For example, if the dimensions of an element in the table of contents are (4,5,6), but the user passes dimensions of (2,2,2) in the call to PUT(A/I/R), the values will be stored in the upper left-hand portion of the array in the data record.

calling sequence - CALL PUTA(LCODE,LLEM,ND1,ND2,ND3)
CALL PUTI(LCODE,ILEM,ND1,ND2,ND3)
CALL PUTR(LCODE,RLEM,ND1,ND2,ND3)

input variables:

1. LCODE(7) the 8-character access code in the first four words followed by three words which should never be altered by the user. The same seven word unit must be passed each time the element is accessed. The three additional words are used by the data base handler to store rapid search parameters.

2. (L/I/R)LEM(•) the (alphanumeric/integer/real) variable or array from which the value(s) are to be transferred.

3. ND1 the first dimension of the user area (0 or 1 if single value)

4. ND2 the second dimension (0 or 1 if single value or

one-dimensional array)

5. ND3 the third dimension (0 or 1 if single value or
 one/two dimensional array)

13. WRIDR

WRIDR writes the active data record to the output file. It is the last action applicable to the currently active data record and must be called before another data record can be made active. WRIDR must be called for each data record in update and create modes. In read mode WRIDR is not used.

calling sequence - CALL WRIDR

Appendix D.

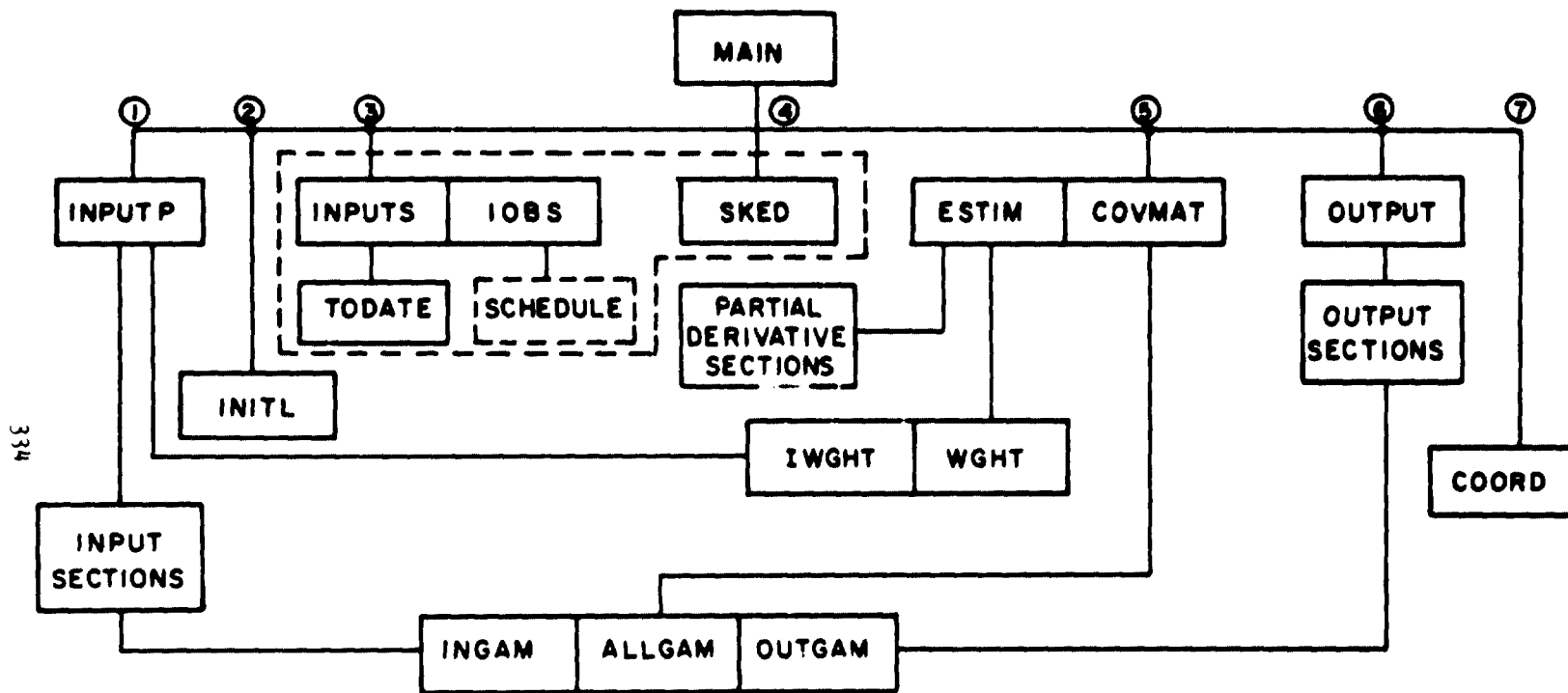
EXPERIMENT SIMULATION PROGRAM (ESTIM)

This appendix describes the experiment simulation and error analysis program. The overall organization of the program, particular features of individual sections, and modes of operation are covered.

The algorithms developed in section IV.A are implemented in a program called ESTIM. The output of the program is the projected noise-only error (NOE), modeled error (MDE), and total error (the root-sum-square of NOE and MDE) of the adjusted parameters for the observing configuration under study. ESTIM includes three components: 1) mathematical models for physical effects, 2) computation of observation configuration, and 3) error analysis. A block diagram of the organization is given in figure D.1.

1. The models of physical effects

There are nine models implemented in ESTIM: 1) atmosphere, 2) clock behavior, 3) diurnal polar motion, 4) solid earth tides, 5) relativistic gravitational ray deflection, 6) station position, 7) source position, 8) UT1, and 9) wobble (long period polar motion). The algorithms used are described in Chapter II. Each model is contained in a three part program section. The first part handles input and initialization. The second part computes the partial derivatives of the model parameters needed for the normal matrix. The



334

Fig. D.1 ESTIM block diagram

third part handles output. At the input phase control information and parameter error values are entered. Each model parameter can be included in the simulation, as either an adjusted or an unadjusted parameter, or ignored completely. Those models requiring specific sites, sources, and starting epochs to be associated with particular parameters receive this information through the input part. In the computation part the partial derivatives of the desired observables (delay, rate, or both) for the included parameters are calculated. The observation geometry is available to each computation part in identical format: the Julian date, UT time, Greenwich mean sidereal time, rotation matrix from date to 1950.0, the time derivative of the rotation matrix, and indices for the source and two sites involved. Control information received at the input phase determines where the computed partials are stored in order to enter the simulation as adjusted or unadjusted parameters. The output part has two functions. For unadjusted parameters it lists the formal error used. For adjusted parameters it indexes the computation of the various errors which are the output of the simulation program. All the sections have similar internal structure and identical interfaces so that new or different models can be introduced with little difficulty. Each section operates with control flags to make intermediate results available for reference or checking.

The atmosphere section works with only one type of parameter, the zenith troposphere thickness in seconds of travel time. Up to twenty atmosphere parameters can be included, each associated with a specific site and starting epoch. The multiplicity of parameters is necessary

for realistic simulation of actual data analysis. A different zenith parameter is needed at each site since distant VLBI antennas do not look through the same atmosphere. Usually a different parameter is used for each day of an experiment. If the weather changes radically, a single parameter for a day may not adequately model the air mass above the station and more must be used. The interval over which a single parameter is adequate cannot be predicted in practice. It is desirable to limit the number of atmosphere parameters to avoid weakening estimates of the parameters of interest, but it is useful to see how badly the estimation will be degraded. The introduction of meteorological and radiometric data for more complex modeling of the atmosphere changes the actual data analysis and hence the simulation. In particular, the zenith angle dependence may be different. This complication is not yet included. The simple atmosphere parameters have always been adjusted in actual data analysis and are generally included as adjusted parameters in simulations.

The clock section uses a polynomial to model the behavior of station frequency standards. Twenty polynomials of up to five terms, each associated with specific sites and starting epochs, can be included in a simulation. The argument of the polynomials is elapsed time from the starting epoch. The units of the coefficients are sec, sec/sec, sec/sec², etc. It has been the experience that clocks can be modeled well by a two or three term polynomial, i.e., offset, drift, and curvature, or not at all. The higher order terms are not a good model for erratic clock behavior. When the clock behavior is not linear or slightly curved, it is necessary either to use more

polynomials for a given time interval or to difference successive data points on different sources. Differencing data removes the clock offset entirely and reduces the drift behavior to the time between observations. Both methods weaken the solution, the first by adding more uninteresting adjusted parameters, the second by discarding information. For well-behaved data the clocks for a one-day experiment can be modeled by a single offset and rate at all stations but one. The clock at one station must be considered error-free as a reference. Since polynomials are rather ad hoc models mimicking actual data analysis, the clock parameters are generally included as adjusted parameters. Including higher order terms as unadjusted parameters, besides being unphysical, leads to numerical difficulties.

The diurnal polar motion section applies a single parameter, the dimensionless scaling factor for the radius of the diurnal path of the angular momentum pole with respect to the terrestrial coordinate system. Summation of the time series derived by McClure (1973) is done by two subsidiary routines. To save computational time and program space, the mean obliquity is used instead of the true obliquity in calculating the correction to sidereal position, $\text{delpsi}(rD) \cos(\text{eps})$. The error is insignificant. Since diurnal polar motion has almost the same time signature as apparent source motion, it is virtually impossible to include both source positions and diurnal polar motion as adjusted parameters in a normal one-day experiment. Consequently, diurnal polar motion is usually included as an unadjusted parameter. The effect has been difficult to measure and the parameter model error could be quite large.

The earth tide section contains two parameters, the Love numbers h and l . The Love number h scales vertical tidal displacement while l scales horizontal displacement. Computation of the time series taken from Melchior (1966) is done in a separate subroutine. For simplicity, geodetic latitude rather than geocentric latitude is used. As with diurnal polar motion, the time signature makes it difficult to include both source positions and Love numbers as adjusted parameters for a single day of observation and the tidal parameters are generally taken as unadjusted parameters.

The section for relativistic gravitational light deflection uses the single dimensionless parameter γ . There are two versions of the section to model the sun and Jupiter. The position of the mean sun is calculated in a subsidiary program. Since the corona makes it difficult in practice to follow fringes at approaches closer than ten solar radii, the difference between mean and true position is not important. Past observations of solar occultations were done using phase delay because of the recording scheme used by the Mark I VLBI system. Samples over the spanned bandwidth are recorded sequentially instead of simultaneously. Consequently the group delay is badly affected by phase fluctuations caused by the corona. With Mark III there will be simultaneous recording of wider single frequency channels so that it may be possible to follow a source closer to the sun. A more accurate solar position model may be needed for correct simulation of Mark III occultation experiments using group delay. The Jupiter version of the deflection section uses a separate program to compute

Jupiter's apparent position and polar radius based on tabulated values for 1975. During most experiments the observed sources are not close to the sun or Jupiter so that the deflection effect is small. There is little reason to expect that the value of γ differs from unity. For these two reasons the parameter is usually not included in simulations of other measurements. There is more interest in testing configurations for their usefulness in estimating γ .

The site section controls which stations are included in the observation configuration as well as computing the partial derivatives of the site position components. Five stations can be treated in a single simulation. The sites can be parameterized using cartesian or cylindrical coordinates, both coordinates referenced to a right handed system aligned by the geographic pole and the Greenwich meridian. For cartesian components the units are in meters. The units for cylindrical radius, east longitude and z-component are in meters, arcseconds, and meters, respectively. If all the components of a site are adjusted, the choice of cartesian or cylindrical does not affect the baseline errors. In both data analysis and simulation the position of at least one station must be held fixed. Any errors in the reference site position will appear directly in the positions of the adjusted stations and should not affect the baseline errors. Since the site positions are basic to VLBI geodesy, the position parameters usually appear as adjusted parameters.

The source position section computes partial derivatives of source right ascension and declination for up to twenty sources. Units

are seconds of time and seconds of arc, respectively. The right ascension of one observed source must be held fixed in order to determine the origin of right ascension. While the reference source is usually 3C273, the choice of another source does not affect parameter adjustments. The NOE and MDE of the adjusted parameters may change as a result of different parameter correlations, however. In practice, source positions are usually adjusted to refine their error bars. It is implausible that many of the sources will show true displacement.

The UT1 section parameterizes the offset between UTC and UT1 by a polynomial of up to three terms. Ten polynomials with associated starting epochs can be included. The units for the coefficients are sec, sec/hr, and sec/hr². The UTC-UT1 offset for at least one observation must be held fixed in order to determine an origin of time. In practice UT1 is not adjusted unless several days of data are available. The values of UTC-UT1 are taken from an empirical model, usually BIH one-side-smoothed ten-day tabular points, for one of the days in the set and a different offset is fit for each of the remaining days. The adjustment is to the difference between the BIH values and the true values. Higher order terms in the polynomials have rarely been used. A constant error in UTC-UT1 will be absorbed in the longitude of the adjusted sites without affecting the adjustments of other parameters. Variations in UTC-UT1 or sudden jumps will bias the adjusted parameters in a more complex way.

The wobble section models the offset between the slowly moving spin pole and the geographic pole as two polynomials in the x and y

displacement. Each polynomial can have up to three terms and ten sets of polynomials can be included. The units for the coefficients are arcsec, arcsec/hr and arcsec/hr². As with UT1 the pole displacement for at least one data point must be held fixed. The adjustment to the displacement is to the difference between the true values and the BIH values used as the empirical model. Only one component can be adjusted if only a single baseline is included, and higher order terms are not generally used. Since the displacement of the pole is slow, the wobble parameters are not adjusted unless several days of data are included, in which case a single offset may be fit for each day except the reference day. It is not possible to adjust the complete set of station coordinates and the wobble/UT1 parameters simultaneously as the normal matrix becomes ill-conditioned.

2. The observation configuration

The observation configuration is determined by a table of default conditions and the schedule section. Certain information is contained internally but can be overridden:

physical constants for the speed of light, the radius of the earth, and the flattening factor;

source names, right ascensions, declinations, and fluxes at different frequencies;

station names, geodetic coordinates, antenna sizes, efficiencies, slewing rates and limit stops, receiver temperatures, and index codes;

observing frequencies;

recorded and spanned bandwidth, fractional relative frequency stability for the clocks, and integration time;
default measurement errors for delay and delay rate.

The schedule section consists of the routines INPUTS, TODATE, IOBS, and SKED. INPUTS enters the starting epoch and any new values for observation timing. If source position updating is required, TODATE is used. IOBS enters a source index for each observation. If desired, the starting epoch, integration time, waiting time, and cable wrap direction can also be entered. SKED computes the observation geometry.

The schedule section has both interactive and batch modes of operation. In the interactive mode, a schedule for the selected stations and starting epoch is created to simulate a particular experiment. The user selects a source to be observed. SKED checks the station horizons and limits stops to ensure that the source can be seen at all sites. If the observation is acceptable to the scheduler, the orientation of the antennas and the time of day are updated to reflect the observation. As subsequent sources are entered, the program calculates the appropriate observation starting epochs based on antenna slewing rates, the types of telescope mounts, the integration time, and any waiting time required for other functions. An observation can be specified to begin at a particular epoch, in which case the program checks that there is sufficient time for the antennas to reach the desired position. Each observation is accepted or rejected by the scheduler. However it is possible to jump back to an

earlier point in the schedule and start again. This feature is necessary to untangle problems that are caused by cable wrap on slow-moving alt-az mounted telescopes. The partial derivatives of the included parameters are accumulated by the error analysis section as the schedule is made. When the schedule is considered complete, the total observing and slewing times of the telescopes and the number and distribution of observations for each source are summarized. The error analysis section finishes its calculations and the results are printed. The complete schedule is saved so that it can be re-analyzed with different parameter sets or with a subset of the initial stations.

In batch mode a previously created schedule is analyzed. The schedule section calculates the geometry of each observation and flags those that cannot be made because of slewing or pointing constraints. The partial derivatives for all the observations entered are accumulated and the necessary matrix operations performed by the error analysis section to produce the desired covariances. In batch mode measurement errors for each observation can be entered

3. The error analysis section

A few terms are defined here for use in the following sections. The normal matrix and the adjusted/unadjusted cross partials matrix are given by

$$N = B^T W B \quad (\text{dimension } m_1 \text{ by } m_1) \quad D.3.1$$

$$K = E^T W C \quad (\text{dimension } m_1 \text{ by } r_2) \quad D.3.2$$

where

B = matrix of partials for adjusted parameters (dimension n by m_1)

C = matrix of partials for unadjusted parameters (dimension n by m_2)

n = number of observations

m_1 = number of adjusted parameters

m_2 = number of unadjusted parameters

The weight matrix is defined as

$$W = E[ee^T]^{-1} \quad (\text{dimension } n \text{ by } n) \quad D.3.3$$

where

e = vector of observation errors

and is assumed to be diagonal. The unadjusted parameter formal error vector, S_y , is defined as the square root of the diagonal of the covariance of y , $COV[y]$, where y is the vector of unadjusted parameter errors. It is assumed that the unadjusted parameter errors are uncorrelated and therefore that only the diagonal elements exist. Each element of S_y is the uncertainty of a particular model parameter. The gain matrix is

$$G = (B^T W B)^{-1} B^T W C \quad (\text{dimension } m_1 \text{ by } m_2) \quad D.3.4$$

The sensitivity vector is defined as

$$S = (B^T W B)^{-1} B^T W C S_y \quad (\text{dimension } m_1) \quad D.3.5$$

The error analysis section consists of routines ESTIM, WGHT, COVMAT, GAM, and COORD.

ESTIM is called for each acceptable observation. It prompts the computation part of each model section to enter values into the vector of adjusted parameter partials, B, and into the vector of unadjusted parameter partials, C. The WGHT routine is called to calculate the measurement error. The vector B is scaled by the weighting value, giving $(B^T W)$, multiplied by B and C to give $(B^T W B)$ and $(B^T W C)$, and summed with the accumulating normal matrix N and cross-partial matrix K.

The input part of WGHT (IWGHT) accepts control data on what source fluxes to use and which error sources to include. A number of options are available. The weight may default to a fixed value or a value entered for each observation. The weight may also be calculated from source fluxes with antenna, receiver, and recording information. Alternatively, the weight can be derived from the atmosphere or clock error or a sum of several error sources. A fixed external error can be added to whatever other errors are included. WGHT returns values for both delay and delay rate. Each weighting number applies to a single observation and no correlation between measurement errors can be included.

COVMAT is called when a schedule is complete. The normal matrix is inverted and multiplications are performed to produce the gain

matrix and the sensitivity vector. If desired, various correlation and covariance matrices are computed and printed.

The routine GAM has three parts. INGAM forms the unadjusted parameter formal error vector S_y . ALLGAM prints S_y for reference. OUTGAM is called by the output part of each model section. It calculates for each adjusted parameter the MDE contribution from each unadjusted parameter. The individual modeled errors are root-sum-squared to give a total MDE. The individual MDE contributions, the noise-only error, the total modeled error, and the root-sum-square of the NOE and modeled errors are printed for each adjusted parameter.

COORD transforms the covariance associated with the station components to the covariance of the baseline parameters. Errors and correlations for the baseline length, longitude, and latitude are computed based on the noise-only covariance and the total error covariance.

4. Driver sections

The driver routines form the structure that links the three computational pieces. The MAIN program calls in turn INPUTP, INITL, INPUTS, SKED, COVMAT, OUTPUT, and COORD. INPUTP prompts the input parts of WGHT and the model sections. INITL converts angular quantities stored internally as hours-minutes-seconds or degrees-minutes-seconds to radians and computes cartesian coordinates

for source and site positions. It also prints default information of the sources and stations. INPUTS accepts data defining the starting epoch and new schedule timing parameters for waiting time and minimum cycle time. INPUTS also updates source positions to epoch of date if more accurate geometry is required. OUTPUT prompts the output parts of the model sections.

5. Coordinate system and time

Because the observing geometry need not be so accurately computed for error analysis as for parameter estimation, a number of simplifications can be made. The basic coordinate system is nominally the geocentric 1950.0 reference frame in which the source positions are given. Two rotation matrices, $(P N S)$ and $(P N \dot{S})$, are calculated to give the delay and delay rate at each observation epoch.

$$\tau = (PNSb) \cdot S \quad D.5.1$$

where

P = precession matrix from mean of date to 1950.0

N = nutation matrix from true of date to mean of date

S = diurnal rotation matrix

b = baseline vector terrestrial coordinates (light-seconds)

s = unit vector in the direction of the source

$$\dot{\tau} = (PNS\dot{b}) \cdot S \quad D.5.2$$

where

\dot{S} = time derivative of the diurnal rotation matrix

The precession/nutation matrix is calculated for each observation epoch. The diurnal rotation matrix is computed from Greenwich apparent sidereal time for each observation.

$$S = R_z(-GAST) \quad D.5.3$$

where

$$GAST = GMST(0 \text{ hr UT}) + UT W + \Delta T \quad D.5.4$$

GMST = Greenwich mean sidereal time

UT = UTC epoch of observation

W = diurnal rotation rate

ΔT = equation of the equinoxes

GMST and W are computed from the standard expression in ESAENA (1961) while ΔT is computed using only the largest term in the nutation series and the mean obliquity.

For special purposes, particularly in scheduling an actual experiment, it is desirable to use more accurate source positions. In that case the source positions are updated with aberration, precession, and the largest two terms in nutation in obliquity and longitude. The source positions are good within two arcseconds. All geometric calculations then proceed in the true of date coordinate system.

All other distortions of the simple geometry are ignored.

Appendix E

EXPERIMENTS SCHEDULED

The ESTIM program described in appendix D has been used to schedule a number of VLBI experiments. This appendix briefly summarizes the purpose and outcome of these experiments.

The Haystack-NRAO baseline was scheduled in October 1974 for a survey of high declination sources not previously observed or rarely observed at X band. The sources were selected by L.K. Hutton from general surveys on the basis of spectrum and type. Most of the sources did not give fringes. The data are being prepared for publication by C.A. Knight and J.J. Wittels.

A geodesy schedule was used in August 1975 on the Haystack-Goldstone baseline. An attempt was made to optimize the schedule for minimum baseline length error on the basis of expected source fluxes and system parameters. The original 26 hr span was shortened to approximately 12 hr because of Viking launch operations. In addition, one frequency channel in the synthesized bandwidth was faulty and the resulting group delays were extremely noisy. The data from this experiment have not proved to be useful.

An extensive experiment was scheduled using Haystack, NRAO, and Owens Valley Radio Observatory (OVRO) during September and October 1976. A number of different activities were included. During the time

only Haystack and NRAO were available, a single-frequency source structure schedule was used, concentrating on 3C 84. An attempt was made to observe a lunar occultation of CTA 21, which did not give fringes. Several geodesy schedules were used including and excluding 3C 120, which a preliminary test had shown to be very weak. Geodesy schedules for successive days were staggered so that sources would not be observed at the same hour angles, a desirable feature for source structure studies. The data have been reduced for astronomical use by J.J. Mittels. D. Roberston and J. Ryan have analyzed the data for geodesy and wobble/UT1.

A geodesy schedule was prepared for several days in March 1977 using Haystack, NRAO, and OVRO. The schedule attempted to increase the number of useful observations by scheduling each station somewhat individually. In particular, the effect of the slow slewing rate of the OVRO telescope was reduced by allowing Haystack and NRAO to make additional observations while OVRO was engaged in long pointing motions. OVRO and Haystack also made additional observations when the hour angle limit at NRAO prevented that telescope from observing. The data are being analyzed at GSFC, MIT and Haystack.

Haystack, NRAO, OVRO, and Onsala were scheduled in September 1977. Approximately 40 hr were used for the first test of Mark III. Both strong sources normally used such as 3C 84 and weak sources below the sensitivity of Mark I such as the galactic center and Algol were observed simultaneously with Mark I, Mark II, and Mark III. Mark III was only available on the Haystack-NRAO baseline. Two days of

conventional geodesy schedules followed the Mark III test. The schedules were prepared for Haystack-NRAO-OVRO while Onsala observed whatever it could. Fringes were detected with all three recording systems on the Haystack-NRAO baseline. No fringes were found on the OVRO baselines. The cause has not been conclusively determined but may have been a faulty local oscillator.

Appendix F.

MEASUREMENT OF SOLID EARTH TIDES FROM GRAVIMETER DATA

Fundamental astronomy has long been dominated by measurements of zenith angle. Consequently the effect of earth tides on the local vertical has been of some concern. More recent techniques such as interferometry and laser ranging are affected by earth tides in a different way. The delay and range observables are determined by the position of the observing sites relative to the source or the reflector. Displacements caused by earth tides rather than deflection of the vertical change the observing geometry. The question arises how the displacement can be measured or modeled. The problem is more difficult than monitoring changes in local vertical. Tiltmeters are available to measure deflection directly but no instruments are capable of measuring displacement relative to the earth's barycenter. It is possible, however, to measure the gravity tide (Kuo et al 1970). Since the response of the earth to the displacement tide is similar to the response to the gravity tide, variations in gravity should be reflected in displacement. From the Love numbers h , k and l the displacement tide can be inferred.

A brief study was made of the gravity tide in the vicinity of Goddard Space Flight Center to see how well the gravity tide, and indirectly the displacement tide, could be modeled from theory. The measurements were made in the basement of the Physics Building at the University of Maryland with a Lacoste and Romberg gravity meter, model

E-T, serial number 9. Voltage output was recorded at 5 minute intervals on magnetic tape using a Monitor Lab analog scanner and a PEC incremental tape drive. The time during which useful data were taken lasted from August to November 1975. After November both the scanner and the tape drive failed to function properly. Throughout the period of observation the gravimeter was subject to disruptions caused by strong seismic events. The pendulum beam would go off scale and remain out of range for periods of hours to days.

The data tapes were copied, edited, and decimated to one hour intervals for processing. A program ETIDE written by G. Epstein was used to fit and plot the data. The fitting procedure consisted of two steps. In the first step the data were least-squares fit with an equation

$$V = aT + b_0 + b_1t + b_2t^2 + \dots \quad \text{F.1}$$

where

V = voltage

a = scaling factor (volts/microgal)

T = gravity tide

b_0 = constant voltage offset

t = time in hours

b_1, b_2, \dots = coefficients of the time polynomial

A modification of J. C. Harrison's program for the gravity tide was used. Jumps in voltage caused by zero adjustments and spikes resulting from seismic events or faulty recording were then marked in the plotted

post-fit residuals. For each step discontinuity a new set of time coefficients was introduced. Spikes were removed by linear interpolation. The data were then fit with an equation

$$\begin{aligned}
 V = aT + b_{01} + b_{11}t + b_{21}t^2 + \dots & \quad \text{F.2} \\
 + b_{02} + b_{12}t + b_{22}t^2 + \dots & \\
 + \dots &
 \end{aligned}$$

where

b_{01} = constant voltage offset at t_1

b_{02} = constant voltage offset at t_2

b_{11}, b_{21}, \dots = coefficients of time polynomial starting at t_1

b_{12}, b_{22}, \dots = coefficients of time polynomial starting at t_2

The coefficients were estimated by least squares, the residuals plotted, and root-mean-squared residual computed.

The results are presented in tables F.1-5. Table F.1 shows seventeen days of data beginning on day 220 of 1975. One step was necessary at point 237 to account for resetting the gravimeter zero. The data were fit with the scaling factor, a constant, and from one to three time coefficients indicated by A, B, and C. The addition of a quadratic term reduces the rms residual by 28% from the value using only a linear rate. The cubic term has little effect. The scaling factor is unaffected by additional terms.

The behavior of the residuals is quite different before and after the gravimeter adjustment. Tables F.2 and F.3 show the two parts fit

Table F.1 Fit to 400 gravity data points beginning 75/220 18:00

| start point | a V/microgal | b0 V | b1 V/hr | b2 V/hr ² | b3 V/hr ³ | rms residual |
|-------------|-----------------|---------|------------|-------------------------|-------------------------|----------------|
| A. 1 | .01368 | .78 | .0083 | | | 6.062 microgal |
| 237 | | -.24 | .0047 | | | |
| B. 1 | .01367 | .94 | .0040 | .000018 | | 4.384 |
| 237 | | -.25 | .0049 | -.000001 | | |
| C. 1 | .01367 | .93 | .0048 | .9-5 | .20-7 | 4.326 |
| 237 | | -.21 | .002 | .4-4 | -.16-7 | |

Table F.2 Fit to 236 gravity data points beginning 75/220 18:00

| start point | a V/microgal | b0 V | b1 V/hr | b2 V/hr ² | rms residual |
|-------------|-----------------|---------|------------|-------------------------|----------------|
| A. 1 | .01368 | .78 | .0083 | | 7.190 microgal |
| B. 1 | .01365 | .95 | .0040 | .000018 | 4.687 |

Table F.3 Fit to 175 gravity data points beginning 75/230 14:00

| start point | a V/microgal | b0 V | b1 V/hr | b2 V/hr ² | rms residual |
|-------------|-----------------|---------|------------|-------------------------|----------------|
| A. 1 | .01369 | -.25 | .0048 | | 3.868 microgal |
| B. 1 | .01369 | -.25 | .0047 | .0000009 | 3.863 |

Table F.4 Fit to 400 gravity data points beginning 75/220 18:00

| start point | a V/microgal | b0 V | b1 V/hr | rms residual |
|-------------|-----------------|---------|------------|----------------|
| 1 | .01368 | .97 | .0041 | 3.121 microgal |
| 81 | | 1.41 | .0080 | |
| 195 | | 2.22 | .0194 | |
| 237 | | -.24 | .0048 | |

separately with one and two time coefficients indicated by A and B. The coefficients do not differ greatly from the combined fit, but the rms residual is 20% larger for the first set than for the second. The fit for the first set is considerably improved by the inclusion of a quadratic term, indicating a less linear drift than in the second part. The behavior of the residuals in the first set indicated that additional steps or polynomial terms were necessary. The fit of all 400 points with steps at points 81, 195, and 237 is shown in table F.4. The scaling factor is consistent with the previous results. The drift rate of the gravimeter is not stable over the seventeen days and ranges from .0041 to .0194 V/hr or from 7.2 to 34 microgals per day. The root-mean-square residual for the span is only 3.121 microgals.

After a gap caused by a large seismic disturbance, a 37-day span was recorded. The results of fitting are shown in table F.5. A single step was used at point 250 for a zero adjustment. This is shown as solution A. The behavior of the residuals indicated that many terms in the time polynomial would be required to remove the instrumental drift. The interval was instead divided in solution B using steps at points 125, 250, 320, 360, 560, 800, and 835 where the curvature of the residual plot changed. The erratic drift of the gravimeter can be seen in the rates for each interval which vary from -.0063 to .0116 V/hr. Nonetheless the rms residual is only 4.235 microgals.

According to Farrell (private communication) the M2 and O1 ocean tides should contribute 2.54 and .47 microgals, respectively, to the gravity tide in the Goddard Space Flight Center area because of ground

Table F.5 Fit to 900 gravity data points beginning 75/241 17:00

| start point | a V/microgal | b0 V | b1 V/hr | rms residual |
|----------------|-----------------|---------|------------|----------------|
| A. 1 | .01365 | 1.52 | .0033 | 8.031 microgal |
| 250 | | -1.05 | .0019 | |
| B. 1 | .0373 | 1.38 | .0056 | 4.235 |
| 125 | | 2.04 | .0015 | |
| 250 | | -1.04 | -.0007 | |
| 320 | | -1.14 | .0113 | |
| 360 | | -.83 | .0018 | |
| 560 | | -.34 | .0016 | |
| 800 | | -.10 | .0116 | |
| 835 | | .19 | -.0063 | |

loading and Newtonian attraction. The rms residual gravity tide from the two sets of data is not inconsistent with Farrell's calculations. However, gravity measurements cannot separate the displacement effect from the Newtonian attraction of the oceans. Only displacement affects the observing geometry of interferometers and laser ranging. If the entire gravity tide residual were caused by displacement, the displacement error indicated by the gravimeter data would be between 1 cm and 1.4 cm. It should be noted that the effect of oceans on an island site could be much larger.

The necessity of measuring or modeling the displacement tide is dependent on the accuracy required. The displacement tide cannot be directly measured. The previous gravity meter measurements indicate that observations are necessary only if accuracy better than 2 cm is desired. For lesser accuracy a solid earth tidal model and an ocean loading model should be sufficient.

REFERENCES CITED

- The American Ephemeris and Nautical Almanac 1975 (Washington, D.C.: GPO, 1973).
- Anderle, R. J., "Polar motion determined by Doppler satellite observations" 1976, Bull. Geod. 50, 377.
- Ash, M. E., Determination of Earth Satellite Orbits, Lincoln Laboratory Tech. Note 1972-5, 1972.
- Atkinson, R. d'E., "On the 'dynamical variations' of latitude and time" 1973, A. J. 78, 147.
- Atkinson, R. d E., "On the Earth's axes of rotation and figure" 1975, M. N. R. A. S. 171, 381.
- Bare, C., Clark, B. G., Kellerman, K. I., Cohen, M. H., Jauncey, D. L., "Interferometer experiment with independent local oscillators" 1967, Science 157, 189.
- Bevington, P. R., Data Reduction and Error Analysis for the Physical Sciences, (New York: McGraw-Hill, 1969).
- BIH Annual Report for 1976, Bureau International de l'Heure, 1977.
- Brotten, N. W., Legg, T. H., Locke, J. L., McLeish, C. W., Richards, R. S., Chisolm, R. M., Gush, H. P., Yen, J. L., Galt, J. A., "Long baseline interferometry: A new technique" 1967, Science 156, 1592.
- Chao, C. C., A Preliminary Estimation of Tropospheric Influence on the Range and Range Rate Data during the Closest Approach of the MM/1 Mars Mission, Jet Propulsion Laboratory Tech. Memo 391-129, 1970.
- Clark, T. A., Hutton, L. K., Marandino, G. E., Counselman, C. C.,

- Robertson, D. S., Shapiro, I. I., Wittels, J. J.,
 Hinteregger, H. F., Knight, C. A., Rogers, A. E. E.,
 Whitney, A. R., Niell, A. E., Ronnang, B. O., Rydbeck, O. E. H.,
 "Radio source positions from very-long-baseline interferometry
 observations" 1976, A. J. 81, 599.
- Coates, R. J., Clark, T. A., Counselman, C. C., Shapiro, I. I.,
 Hinteregger, H. F., Rogers, A. E., Whitney, A. R., "Very long
 baseline interferometry for centimeter accuracy geodetic
 measurements" 1975, Tectonophysics 29, 9.
- Cohen, M. H., "Accurate positions for radio sources" 1972, Astrophys.
 Letters 12, 81.
- Counselman, C. C., Kent, S. M., Knight, C. A., Shapiro, I. I.,
 Clark, T. A., Hinteregger, H. F., Rogers, A. E. E.,
 Whitney, A. R., "Solar gravitational deflection of radio waves
 measured by very-long-baseline interferometry" 1974,
 Phys. Rev. Letts. 33, 1621.
- Counselman, C. C., "Radio Astrometry" in Annual Review of Astronomy and
 Astrophysics, Vol. 14, edited by G. R. Burbidge (Palo Alto:
 Annual Reviews, 1976).
- Currie, D. G., Knapp, S. L., Liewer, K. M., "Four stellar diameter
 measurements by a new technique: amplitude interferometry" 1974,
 Ap. J. 187, 131.
- Currie, D. G., "Detection of extra solar planets using optical
 amplitude interferometry" presented at the Conference on Extra
 Solar Planetary Detection, U. of C. at Santa Clara, 1976.
- Currie, D. G., The Development, Fabrication, and Astronomical
 Application of a Wide-Band Long Baseline Optical Amplitude

- Interferometer, U. of Maryland Tech. Report 77-075, 1977.
- Dahlen, F. A., "Passive influence of oceans upon rotation of the earth" 1976, Geophys. J. R. A. S. 46, 363.
- Debarbat, S., "Nearly diurnal nutation derived from the observations of time and latitude" in Rotation of the Earth, IAU Symposium No. 48, edited by P. Melchior and S. Yumi (Dordrecht: D. Reidel, 1972).
- Explanatory Supplement to the Astronomical Ephemeris and the American Ephemeris and Nautical Almanac (London: Her Majesty's Stationery Office, 1961).
- Farrell, W. E., "Gravity tides" 1970, U. of C. at San Diego (Ph.D. thesis).
- Federov, E. P., "Nutation as derived from latitude observations" 1959, A. J. 64, 81.
- Federov, E. P., Nutation and Forced Motion of the Earth's Pole (New York: MacMillan, 1963).
- Fomalant, E. B., Sramek, R. A., "Measurements of solar gravitational deflection of radio-waves in agreement with general relativity" 1976, Phys. Rev. Letts. 36, 1475.
- Fricke W., "Determinations of precession" 1971, Celestial Mech. 4, 150.
- Gubbay, J. S., Legg, A. J., Robertson, D. S., "Position solution of compact radio sources using long coherence VLBI" in New Problems in Astrometry, IAU Symposium No. 61, edited by W. Gliese, C. A. Murray, and R. H. Tucker (Dordrecht: D. Reidel, 1974).
- Hazard, C., Mackey, M. B., Shimmins, A. J., "Investigation of the radio source 3C 273 by the method of lunar occultations" 1963, Nature 197, 1037.

- Hinteregger, H. F., "Precision geodesy via radio interferometry" 1972,
M. I. T. (Ph.D. thesis).
- Hinteregger, H. F., Shapiro, I. I., Robertson, D. S., Knight, C. A.,
Ergas, R. A., Whitney, A. R., Rogers, A. E. E., Moran, J. M.,
Clark, T. A., Burke, B. F., "Precision geodesy via radio
interferometry" 1972, Science 198, 396.
- Hutton, L. K., "Fine structure in 3C 120 and 3C 84" 1976,
U. of Maryland (Ph.D. thesis).
- Jeffreys, H. in Nutation and Forced Motion of the Earth's Pole by
F. P. Federov, translated by B. S. Jeffreys (New York: MacMillan,
1963).
- Kolaczek, B., Weiffenbach, G., eds., On Reference Coordinate Systems
for Earth Dynamics, IAU Colloquium No. 26 (Warsaw, 1975).
- Kuo, J. T., Jachens, R. C., "Transcontinental tidal gravity profile
across the United States" 1970, Science 168, 968.
- Lieske, J., Expressions for the Precession Quasiperiods and Their Partial
Derivatives, Jet Propulsion Laboratory Technical Report 32-1044,
1967.
- McCarthy, D. D., "Analysis of Washington latitude variations from 1915
to 1972 using the photographic zenith tube" 1972, University of
Virginia (Ph.D. thesis).
- McCarthy, D. D., "Observations of the fortnightly nutation terms and
the 'dynamical variation of latitude' with photographic zenith
tubes" 1976, A. J. 81, 482.
- McClure, P., Diurnal Polar Motion, NASA Goddard Space Flight Center
X-592-73-259, 1973.
- McClure, P., "Core-resonance effects on the earth's angular momentum

- vector and rotation axis - a generalized model" 1976, Bull. Geod. 50, 262.
- Melchior, P., The Earth Tides (Oxford: Pergamon Press, 1966).
- Melchior, P., "Precession-nutations and tidal potential" 1971, Celestial Mech. 4, 190.
- Melchior, P., Introduction to Rotation of the Earth, IAU Symposium No. 48, edited by P. Melchior and S. Yumi (Dordrecht: D. Reidel, 1972).
- Moran, J. M., Crowther, P. P., Burke, B. F., Barrett, A. H., Rogers, A. E. E., Ball, J. A., Carter, J. C., Bare, C. C., "Spectral line interferometry with independent time standards at stations separated by 845 kilometers" 1967, Science 157, 676.
- Moran, J. M., "Some characteristics of an operational system for measuring UT1 using very-long-baseline-interferometry" 1973, Space Research XIII 1, 73.
- Moran, J. M., Penfield, H., Test and Evaluation of Water Vapor Radiometers and Determination of their Capability to Measure Tropospheric Propagation Path Length, report prepared for NASA Goddard Space Flight Center, 1976.
- Morgan, H. R., "The short period terms in nutation as given by observation" 1952, A. J. 57, 232.
- Moyer, T. D., Mathematical Formulation of the Double-Precision Orbit Determination Program (DPODP), Jet Propulsion Laboratory Tech. Report 32-1527, 1971.
- Mueller, I. I., Spherical and Practical Astronomy as Applied to Geodesy (New York: Frederick Ungar, 1969).
- Munk, W. H., Macdonald, G. J. F., The Rotation of the Earth (London:

Cambridge University Press, 1960).

- O'Hara, N. P. J., "Fortnightly terms in PZT observations" 1973, A. J. 78, 1115.
- Ong, K. M., MacDoran, P. F., Thomas, J. E., Fliegel, H. F., Skjerve, D. J., Spitzmesser, D. J., Batelaan, P. D., Paine, S. T., Newsted, M. G., "A demonstration of radio interferometric surveying using DSS14 and the project Aries transportable antenna" 1976, J. Geophys. Res. 81, 3587.
- Poma, A., Proverbio, E., "The secular motion of the pole from BIH results" 1976, Astron. Astrophys. 47, 105.
- Resch, G. M., "Comparison of microwave radiometric and in-situ measurements of tropospheric water vapor" presented at the annual meeting of the U. S. Nat. Comm. International Union of Radio Science, Boulder, 1975.
- Robertson, D. S., "Geodetic and astrometric measurements with very-long-baseline interferometry" 1975, M. I. T. (Ph.D. thesis).
- Rochester, M. G., Jensen, O. G., Smylie, D. F., "A search for the Earth's 'nearly diurnal free wobble'" 1974, Geophys. J. R. A. S. 38, 349.
- Rogers, A. E. E., "Very-long-baseline interferometry with large effective bandwidth for phase-delay measurements" 1970, Radio Science 5, 1239.
- Rogers, A. E. E., Counselman, C. C., Hinteregger, H. F., Knight, C. A., Robertson, D. S., Shapiro, I. I., Whitney, A. R., Clark, T. A., "Extragalactic radio sources: accurate positions from very-long-baseline observations" 1973, Ap. J. 186, 801.
- Rogers, A. E. E., Knight, C. A., Hinteregger, H. F., Whitney, A. R.,

- Counselman, C. C., Shapiro, I. I., Gourevich, S. A.,
 Clark, T. A., "Geodesy by radio interferometry: determination of
 a 1.24-km base line vector with approx. 5-mm repeatability" 1978,
 J. Geophys. Res. 83, No. B1, 325.
- Sasao, T., Okamoto, I., Saki, S., "Dissipative core-mantle coupling and
 nutational motion of the Earth" 1977, Publ. Astron. Soc. Japan
 29, 83.
- Shapiro, I. I., "New method for the detection of light deflection by
 solar gravity" 1967, Science 157, 806.
- Shapiro, I. I., Robertson, D. S., Knight, C. A., Counselman, C. C.,
 Rogers, A. E. E., Hinteregger, H. F., Lippincott, S.,
 Whitney, A. R., Clark, T. A., Niell, A. E., Spitzmesser, D. J.,
 "Transcontinental baselines and the rotation of the earth
 measured by radio interferometry" 1974, Science 186, 920.
- Smart, W. M., Textbook on Spherical Astronomy (London: Cambridge
 University Press, 1965).
- Smith, D. E., Kolenkiewicz, Dunn, P. J., Plotkin, H. H.,
 Johnson, T. S., "Polar motion from laser tracking of artificial
 satellites" 1972, Science 178, 405.
- Smithsonian Astrophysical Observatory Star Catalog (Washington D.C.:
 Smithsonian Institution, 1966).
- Stolz, A., Bender, P. L., Faller, J. E., Silverberg, E. C.,
 Mulholland, J. D., Williams, J. G., Carter, W. E., Currie, D. G.,
 Kaula, W. M., "Earth rotation measured by lunar laser ranging"
 1976, Science 193, 997.
- Thomas, J. B., Fanselow, J. L., MacDoran, P. F., Spitzmesser, D. J.,
 Skjerve, L. J., "Radio interferometry measurements of a 16-km

- baseline with 4-cm precision" 1976, J. Geophys. Res. 81, 995.
- Toomre, A., "On the 'nearly diurnal wobble' of the Earth" 1974, Geophys. J. R. A. S. 38, 335.
- Wako, Y., "Nutation terms derived from time and latitude observations" presented to XVI General Assembly of IAU, 1976.
- Walter, H. G., "Precision estimation of precession and nutation from radio interferometric observations" 1977, Astron. Astrophys. 59, 433.
- Weiler, K. W., Ekers, R. D., Raimond, E., Wellington, K. J., "Dual frequency measurement of the solar gravitational microwave deflection" 1975, Phys. Rev. Letts. 35, 134.
- Whitney, A. R., "Precision geodesy and astrometry via very long baseline interferometry" 1974, M. I. T. (Ph.D. thesis).
- Whitney, A. R., Rogers, A. E. E., Hinteregger, H. F., Knight, C. A., Levine, J. I., Lippincott, S., Clark, T. A., Shapiro, I. I., Robertson, D. S., "A very-long-baseline interferometer system for geodetic applications" 1976, Radio Science 11, 421.
- Wittels, J. J., Knight, C. A., Shapiro, I. I., Hinteregger, H. F., Rogers, A. E. E., Whitney, A. R., Clark, T. A., Hutton, L. K., Marandino, G. E., Niell, A. E., Ronnang, B. O., Rydbeck, O. E. H., Klempner, W. K., Warnock, W. W., "Fine structure of 25 extragalactic sources" 1975, Ap. J. 196, 13.
- Woolard, E. W., Theory of the Rotation of the Earth around Its Center of Mass, Astronomical Papers prepared for the use of the American Ephemeris and Nautical Almanac XV, Part I, 1953.
- Yatskiv, Ya. S., "On the comparison of diurnal nutation derived from separate series of latitude and time observations" in Rotation of

the Earth, IAU Symposium No. 48, edited by P. Melchior and
S. Yumi (Dordrecht: D. Reidel, 1972).

BIBLIOGRAPHIC DATA SHEET

| | | | |
|---|---|--|-------------------|
| 1. Report No. | 2. Government Accession No. | 3. Recipient's Catalog No. | |
| 4. Title and Subtitle Very Long Baseline Interferometry Applied to Polar Motion, Relativity, and Geodesy (VLBI, Polar Motion, Relativity, Geodesy) | | 5. Report Date | |
| | | 6. Performing Organization Code | |
| 7. Author(s) Chopo Ma | | 8. Performing Organization Report No. | |
| 9. Performing Organization Name and Address NASA/Goddard Space Flight Center Laboratory for Extraterrestrial Physics Greenbelt, MD 20771 | | 10. Work Unit No. | |
| | | 11. Contract or Grant No. | |
| | | 13. Type of Report and Period Covered | |
| 12. Sponsoring Agency Name and Address | | 14. Sponsoring Agency Code | |
| | | 15. Supplementary Notes | |
| 16. Abstract <p>The causes and effects of diurnal polar motion are described. An algorithm is developed for modeling the effects on very long baseline interferometry observables. Five years of radio-frequency very long baseline interferometry data from stations in Massachusetts, California, and Sweden are analyzed for diurnal polar motion. It is found that the effect is larger than predicted by McClure. Corrections to the standard nutation series caused by the deformability of the earth have a significant effect on the estimated diurnal polar motion scaling factor and the post-fit residual scatter.</p> <p>Simulations of high precision very long baseline interferometry experiments taking into account both measurement uncertainty and modeled errors are described. It is found that the Wide-Band Optical Very Long Baseline Interferometer may be useful in studying gravitational deflection near Jupiter. A selection is made between two three-station networks for monitoring polar motion. The effects of scheduling and the number of sources observed on estimated baseline errors are discussed. It is found that a moderate number of sources should yield the best results. A comparison of actual and simulated experiments indicates that the present</p> | | | |
| 17. Key Words (Selected by Author(s)) VLBI, Polar Motion, Relativity, Geodesy | | 18. Distribution Statement | |
| 19. Security Classif. (of this report) | 20. Security Classif. (of this page) | 21. No. of Pages | 22. Price* |